

Radiative flux divergence in the surface boundary layer

A study based on observations at Summit, Greenland

Sebastian W. Hoch



Diss. ETH No. 16194

DISS. ETH NO. 16194

Radiative flux divergence in the surface boundary layer

**A study based on observations at Summit,
Greenland**

A dissertation submitted to the
SWISS FEDERAL INSTITUTE OF TECHNOLOGY (ETH)
ZURICH

for the degree of
DOCTOR OF NATURAL SCIENCE

presented by

Sebastian Wilhelm Hoch

Dipl. Natw. ETH

born 17.11.1973

citizen of Germany

accepted on the recommendation of

Prof. Dr. A. Ohmura, examiner

Dr. P. Calanca, co-examiner

Prof. Dr. M. Kuhn, co-examiner

2005

Licht

Als ich den verdorrten Hang
hinabstieg durch den Staub,
der Bus war weg, vorbei
mit festgeklemmten Türen,
sah ich die Insel treiben
weit im Dunst, kein Laub,
ich sah das Wasser funkeln
durch Geschlossenheiten
von Stille, Licht und Nachmittag,
ich sah die Wellen,
aufgeblättert sacht vom Wind.

Der Sommer ging und blieb
in diesem Augenblick
noch für ein nächstes Jahr.
Ich ging, ich stand, war da
und hatte nichts dabei,
kein Brot, kein Wasser,
keinen Beutel Trauben,
nur diesen Anblick,
dieses fernenleichte Blau
in Räumen, in den Augen.

Jürgen Theobaldy

Acknowledgments

First of all I would like to thank my supervisor, Atsumu Ohmura. He gave me the chance to actively take part in a field campaign on the Greenland ice sheet, and the freedom to follow my scientific interests in the frame of this project.

I am thankful for the scientific and personal advice of Pierluigi Calanca, my co-advisor. He drew my attention to the problem of radiative flux divergence.

I am indebted to Prof. Michael Kuhn, who kindly agreed to co-examine my work. His feedback based on his wide knowledge on radiation in the polar regions will be very much appreciated.

Without Karl Schrott and Hansjörg Frei, who provided all the infrastructure, the instrumentation and organizational skill, the field campaigns at Summit would have been far less successful.

I want to thank my colleges from the 'Greenland-Group', Peter Schelander and Saskia Bourgeois. Peter kept all the instrumentation running during the long dark phase, and Saskia spent long summer 'nights' with me during intensive observational periods.

Rolf Philipona visited Summit Camp and helped me with the task of calibrating eight pyrgeometers relative to each other. He gave me valuable advice regarding the radiation instrumentation.

The scientific discussions with Hendrik Huwald, Ludwig Zraggen and Guido Müller were always a source of motivation.

I am thankful for all the support that was given to me, by the Veco support teams at Summit Camp, by the computer administrators Vlado Nesporek and Daniel Lüthi, and by our secretaries Esther Jampen and Rosmarie Widmer.

And of course a big thank you to all my colleges and friends at the Irchel Campus and beyond, for all the badminton matches, hikes, lunch and coffee breaks ...

This work was financed by the Swiss National Science Foundation, grants 21-57249 and 20-66760.

Abstract

The stability of the Greenland ice sheet largely depends on the existence of the dry snow zone. In this zone, which covers approximately 40 % of the ice sheet, 57 % of the annual net accumulation takes place. As the Greenland ice sheet incorporates an ice volume equivalent to a potential sea level rise of 6.7 m, detailed knowledge of the energy and mass balance in the dry snow zone is of greatest importance to evaluate the response of the ice sheet to a warming global climate.

The dry snow zone of the Greenland ice sheet is characterized by a homogeneous and smooth surface and has an almost unlimited fetch. With the frequent occurrence of stable conditions, it is an ideal site for studying fundamental processes in the stable atmospheric boundary layer. One of these processes, the divergence of the longwave radiative fluxes, has never been investigated in great detail. Although recognized as an important component of the thermodynamics of the stable atmospheric boundary layer, measurements of longwave radiative flux divergence are rare. Especially the vertical distribution of the induced radiative heating and cooling is largely unknown.

From June 2001 to July 2002, an extensive field campaign was carried out by ETH Zurich at the Greenland Summit Environmental Observatory, which lies in the center of dry snow zone (72°35'N, 38°28'W, 3203 m.a.s.l.). This thesis deals with two of the main objectives of the field program.

The first objective is the evaluation of the components of the surface energy balance over the entire 14-month period, covering all seasons. The main focus lies on the radiative fluxes that were monitored following the high standards set by the Baseline Surface Radiation Network (BSRN). The characteristic features of the radiation regime of the dry snow zone are determined. The annual mean albedo is as high as 0.82, and the annual mean net radiation amounts to -7 Wm^{-2} . Subsurface heat fluxes are inferred from firn temperatures and fluxes of sensible and latent heat are derived from measurements of temperature, humidity and wind speed on eight levels of a 50 m meteorological tower. Positive net radiation during the three summer months leads to a development of a diurnal stability cycle, and sensible heat fluxes are directed upward on up to twelve hours per day.

The second part of this thesis deals with the process of longwave radiative flux divergence, which is derived from longwave fluxes measured at up to six levels within the lowest 50 m of the boundary layer. A careful relative calibration of the pyrgeometers reduces the uncertainty of net longwave flux differences to within $\pm 0.75 \text{ Wm}^{-2}$. The influences of the tower structure on the measurements are corrected. The cooling and heating rates that are induced by the divergence of the longwave radiative flux are in the order of the observed temperature change. Longwave radiative flux divergence thus effectively influences the evolution of the temperature profile. Measurements clearly indicate a dominating effect of the divergence of the outgoing flux for most situations. Between 2 m and 50 m, the mean diurnal variation of longwave radiative flux divergence in summer ranges from 0.14 Wm^{-3} (-13 Kd^{-1}) at night to -0.05 Wm^{-3} (4.8 Kd^{-1}) at noon. During summer nights with fog formation, longwave radiative flux divergence of up to 0.55 Wm^{-3} (-53 Kd^{-1}) are observed. During stable conditions in winter, daily means of longwave radiative flux divergence as

large as 0.31 Wm^{-3} (-30 Kd^{-1}) are recorded. Monthly means of longwave radiative flux divergence vary between 0.03 Wm^{-3} (-3 Kd^{-1}) during summer and 0.13 Wm^{-3} (-12 Kd^{-1}) in fall, winter and early spring.

Longwave radiative flux divergence varies with height. During the summer months, when a diurnal stability cycle develops, observations reveal a characteristic profile of longwave radiative flux divergence related to stratification. When the surface is colder (warmer) than the overlying air, a thin layer (0.5 m-2 m) of heating (cooling) is induced. Above this layer, the sign of the divergence changes, and radiative cooling (heating) results. The sign change of radiative flux divergence within the first meters above the surface can be attributed to a changing relative importance of the divergence of the incoming and outgoing flux components. Model calculations with the radiative transfer model MODTRAN agree well with the observations and reveal the spectral characteristics of the process.

The observed fine structure of the temperature profile exhibits a characteristic pattern. During daytime, an elevated surface inversion is observed within the lowest meter, while nighttime inversions exhibit a layer of reduced stability between 0.3 m and 5 m. The profile of longwave radiative flux divergence is suggested to play a significant role in the formation of these patterns.

Zusammenfassung

Die Stabilität des grönländischen Eisschildes steht in engem Zusammenhang mit der Existenz der Trockenschneezone. In dieser Zone, die 40% der Fläche Grönlands ausmacht, kommt es zu 57% der Jahresnettoakkumulation. Das Eisvolumen Grönlands entspricht einem theoretischen Meeresspiegelanstieg von 6.7m. Daher ist es sehr wichtig, den genauen Energie- und Massenhaushalt in der Trockenschneezone zu kennen, um eine Reaktion des Eisschildes auf das sich global erwärmende Klima abschätzen zu können.

Die Trockenschneezone Grönlands zeichnet sich durch ihre sehr flache Oberfläche aus. Da zusätzlich sehr häufig stabile Schichtungen auftreten, ist sie der geeignete Ort zur Untersuchung grundlegender Prozesse in der stabilen Grenzschicht. Einer dieser Prozesse, die Strahlungsstromdivergenz, wurde bis anhin noch nie detailliert untersucht. Obwohl die Bedeutung der langwelligen Strahlungsstromdivergenz als wichtige Komponente der Thermodynamik der stabilen Grenzschicht gilt, wurde sie selten gemessen. Insbesondere die Höhenverteilung der induzierten Strahlungserwärmung und -abkühlung ist nur in Ansätzen bekannt.

Von Juni 2001 bis Juli 2002 fand eine umfassende Messkampagne der ETH Zürich am Greenland Summit Environmental Observatory statt, welches sich im Zentrum der Trockenschneezone befindet (7235'N, 3830'W, 3203 m.ü.M.). Die vorliegende Arbeit behandelt zwei der Zielsetzungen des Projektes.

Das erste Ziel dieser Arbeit ist die Bestimmung aller Komponenten der Energiebilanz für die 14-monatige Zeitspanne, welche alle Jahreszeiten einschliesst. Der Schwerpunkt liegt hierbei auf den Strahlungsflüssen, die den hohen Standards des Baseline Surface Radiation Network (BSRN) entsprechend gemessen wurden. Die Messungen ergeben ein umfassendes Bild des Strahlungsregimes der Trockenschneezone. Die jahresmittlere Albedo beträgt 0.82, die Nettostrahlung -7 Wm^{-2} . Der Bodenwärmestrom wurde aus Firntemperaturen ermittelt und die fühlbaren und latenten Wärmeflüsse wurden anhand von Messungen der Temperatur, der Feuchte und der Windgeschwindigkeit an acht Niveaus eines 50 Meter hohen meteorologischen Mastes hergeleitet. Aufgrund der positiven Nettostrahlung während den drei Sommermonaten entwickelt sich ein Tagesgang des Stabilitätszustandes. An bis zu 12 Stunden ist daher ein nach oben gerichteter fühlbarer Wärmefluss zu beobachten.

Der zweite Teil dieser Arbeit beschäftigt sich mit der langwelligen Strahlungsstromdivergenz. Diese wurde aus Messungen des langwelligen Strahlungsstromes ermittelt, welcher an bis zu sechs Höhen innerhalb der untersten 50 m der planetaren Grenzschicht gemessen wurde. Die Unsicherheit der Messung der Differenzen zweier Nettostrahlungsflüsse konnte durch eine sorgfältige Relativeichung auf $\pm 0.75 \text{ Wm}^{-2}$ reduziert werden. Der Einfluss des Mastes auf die Messungen wurde berücksichtigt. Die Heiz- und Kühlraten, die aus der Strahlungsstromdivergenz hervorgehen, sind von gleicher Grössenordnung wie die beobachtete Temperaturänderung. Die langwellige Strahlungsstromdivergenz wirkt sich deshalb deutlich auf die zeitliche Veränderung des Temperaturprofils der bodennahen Grenzschicht aus. In den meisten Situationen zeigt sich ein dominierender Effekt der Divergenz des ausgehenden Strahlungsflusses. Zwischen 2m und 50m überhalb der Oberfläche liegen die täglichen Schwankungen der langwelligen Strahlungsstromdivergenz im Sommer im

Mittel zwischen 0.14 Wm^{-3} (-13 Kd^{-1}) in der Nacht und -0.05 Wm^{-3} (4.8 Kd^{-1}) am Mittag. In Sommernächten mit Nebelbildung werden langwellige Strahlungsstromdivergenzen von bis zu 0.55 Wm^{-3} (-53 Kd^{-1}) beobachtet. Im Winter können bei stabilen Bedingungen tagesmittlere Werte von bis zu 0.31 Wm^{-3} (-30 Kd^{-1}) erreicht werden. Im Monatsmittel schwankt die Strahlungsstromdivergenz zwischen 0.03 Wm^{-3} (-3 Kd^{-1}) im Sommer und 0.13 Wm^{-3} (-12 Kd^{-1}) im Herbst, Winter und Frühling.

Die langwellige Strahlungsstromdivergenz variiert mit der Höhe. Wenn sich während den Sommermonaten ein Tagesgang des Stabilitätszustandes ausbildet, ergibt sich ein charakteristisches Bild des Profils der Strahlungsstromdivergenz. Dieses steht im Zusammenhang mit der Stabilität. Ist die Oberfläche wärmer (kälter) als die darüberliegende Luft, so ist in einer dünnen Luftschicht (0.5-2 m) Strahlungserwärmung (-abkühlung) zu beobachten. Darüber ändert das Vorzeichen der Strahlungsstromdivergenz und bewirkt Strahlungsabkühlung (-erwärmung). Der beobachtete Vorzeichenwechsel innerhalb der ersten Meter überhalb der Oberfläche beruht auf einem Wechsel des Einflusses der Divergenz des einfallenden bzw. ausgehenden langwelligen Strahlungsstromes. Berechnungen mit dem Strahlungstransfermodell MODTRAN stimmen gut mit den Beobachtungen überein und zeigen die spektralen Charakteristiken des Prozesses auf.

Die beobachtete Feinstruktur des Temperaturprofils zeigt charakteristische Muster. Tagsüber kann eine abgehobene Bodeninversion innerhalb des untersten Meters beobachtet werden, während die nächtliche Inversion eine Schicht mit reduzierter Stabilität zwischen 0.3 m und 5 m aufzeigt. Das Profil der langwelligen Strahlungsstromdivergenz deutet auf seine wichtige Rolle bei der Ausbildung dieser Muster hin.

Contents

Acknowledgments	v
Abstract	vii
Zusammenfassung	ix
I Motivation	1
II Climate of the dry snow zone at Summit, Greenland	5
1 Meteorological Conditions	6
1.1 Temperature	6
1.2 Wind	7
1.3 Pressure	8
1.4 Humidity	8
1.5 Subsurface temperatures	9
2 Radiation Regime	11
2.1 Instrumentation and observations	12
2.2 Calibrations and accuracy	13
2.3 Problems, corrections and quality control	15
2.4 Results	15
2.4.1 Cloud conditions	16
2.4.2 Monthly means and annual cycles	16
2.4.3 Diurnal cycles	17
2.4.4 Example days under clear and cloudy conditions	20
2.4.5 Cloud forcing	25
2.5 Summary	26

3	Energy balance	28
3.1	Subsurface heat flux	28
3.2	Sensible and latent heat flux	29
3.3	Mean diurnal cycles of the energy balance at Summit, Greenland . . .	30
3.4	Energy and mass balance	34
III	Radiative flux divergence	37
4	Introduction	38
4.1	Fluxes, divergence and heating: Definitions	42
4.2	Shortwave and longwave radiative flux divergence	42
4.3	Infrared radiative transfer	43
5	Measurements of longwave radiative flux divergence	49
5.1	Experimental setup	49
5.1.1	Deployments patterns	49
5.1.2	Instrument setup	50
5.1.3	Instrumentation: Pyrgeometers and their calibration	51
5.1.4	Tower influence correction	62
5.1.5	Data analysis	68
5.2	Observational Results	68
5.2.1	Summer conditions	70
5.2.2	Longwave radiative heating under clear and overcast conditions	72
5.2.3	Longwave radiative heating under calm and windy conditions	76
5.2.4	Heating rates at night with and without fog formation	79
5.2.5	Longwave radiative heating and temperature gradient	84
5.2.6	Longwave radiative heating and humidity	93
5.2.7	Year-round measurements of bulk divergence between 2 m to 50 m	95
6	Model calculations	98
6.1	MODTRAN Radiative transfer model	98
6.1.1	Model input	98
6.1.2	Model output	99
6.2	Results from model calculations	99
6.2.1	Stable nighttime and unstable daytime conditions	100

6.2.2	Shape of temperature profile	103
6.2.3	Longwave radiative heating, temperature gradient and humidity	105
6.2.4	Longwave radiative heating and surface emissivity	111
6.2.5	A spectral viewpoint	113
6.2.6	The causes for heating and cooling	114
6.2.7	Spectral radiative flux divergence under clear sky and fog conditions	119
7	Comparison of detailed measurements with model calculations	123
7.1	Unstable day	123
7.2	Stable night	126
7.3	Fog situation	126
8	Discussion	130
8.1	Divergence of the incoming and outgoing flux	130
8.2	Vertical structure of longwave flux divergence	131
8.3	Longwave radiative flux divergence and fog	133
8.4	Detailed comparisons between observation and model	134
8.5	Causes for longwave radiative flux divergence	134
8.6	Flux divergence, temperature gradient and humidity	136
8.7	Flux divergence under different meteorological conditions	138
8.8	Fine structure of the temperature profile	140
IV	Summary and conclusions	143
	Appendices	150
A	Shortwave radiative heating	150
B	Temperature measurements	152
C	Shortwave leaking and down-facing pyrgeometers	153
	Bibliography	155

Part I

Motivation

The Greenland ice sheet is the second most intensely glaciated land mass after Antarctica. It occupies a latitude band from 60°N to 80°N, and covers 1.76 million square kilometers. The ice volume contained within the ice sheet is approximately 2.62 million cubic kilometers (Weidick, 1995). This corresponds to an equivalent sea level rise of 6.7 m. Precipitation in the interior of Greenland is small. The existence of the ice sheet therefore depends on its large accumulation area, which covers 90.5 % of its area (Ohmura et al., 1999). The high elevation part of the accumulation area belongs to the dry snow zone. This zone is characterized by a high surface albedo. The accumulation in this zone is rather small. With 195 mm y⁻¹ it corresponds to only 25 % of the entire winter accumulation. Nevertheless, it is of vital importance for the existence of the ice sheet, as this amount is equivalent to 57 % of the total net accumulation (Ohmura et al., 1999). While Benson (1962) found that 40 % of the ice sheet falls under the dry snow zone, recent satellite analyses have shown a gradual decrease of its area since 1980 (Abdalati and Steffen, 1995; Abdalati and Steffen, 2001). Future projections based on numerical climate models have shown that the Greenland ice sheet is more vulnerable to climate change than the Antarctic ice sheet (Ohmura et al., 1996; Wild et al., 2003). Thus, the investigation of the energy and mass balance of the dry snow zone is of greatest importance for the understanding of the role of the Greenland ice sheet in a changing global climate.

A summary of the surface climate of the Greenland ice sheet has been presented by Putnins (1970). Field observations of the full energy balance, however, and especially the energy balance in the dry snow zone, are rare. The existing studies on the energy balance such as Ambach (1963), Ambach (1977) and Obleitner (1995) are limited to short periods during the year. Extensive year-round studies of the radiation budget and the temperature and wind profiles in a similar environment as the dry snow zone of Greenland are available for Plateau Station, Antarctica. The observations by Kuhn et al. (1977), Lettau et al. (1977) and Riordan (1977) offer valuable insight into the high elevation surface climate of an ice sheet. The automatic weather stations from Greenland Climate Network (GC-Net) (Steffen et al., 1996; Steffen and Box, 2001) give a good overview over the surface climate of Greenland, especially regarding the spatial variation of the energy balance. The quality of automatic measurements in such a harsh environment is limited, however. Shortwave fluxes are measured using photo-diodes with an accuracy of 5-15 %, and net radiometers have an accuracy of 5-50 % (Box and Steffen, 2000). More reliable year-round measurements of the full radiative balance and of the additional components of the surface energy balance (sensible, latent and subsurface heat flux) are needed in high temporal resolution to allow for a thorough analysis of their relative importance and of their interactions.

The atmospheric boundary layer above the dry snow zone is often characterized by a very stable stratification (Putnins, 1970). In the winter months, this inversion may persist for many days to weeks. In summer, a diurnal stability cycle develops reflecting the diurnal variation in net radiation. Then, unstable conditions are often observed during the day, while intense inversions occur at night. Thus, the dry snow zone of Greenland is the perfect site for studying the stable atmospheric boundary layer and the processes that lead to the formation and destruction of surface inversions.

The process of longwave radiative flux divergence has been recognized to play an important role in the thermodynamics of the boundary layer (Robinson, 1950; Kondratyev, 1969; Garratt and Brost, 1981). An interplay of both the divergence of the radiative and the sensible heat fluxes must lead to the diurnal variation of the near surface air temperature and to the formation of nocturnal and persistent winter inversions. Nevertheless, observations of longwave radiative flux divergence are rare, and especially the shape of the profile of the induced radiative cooling or heating is still unknown (Stull, 1988).

Calculations of the longwave flux profile have been widely used to investigate radiative heating and cooling. The calculations range from basic radiation charts to narrow band radiation schemes. Most of the model approaches indicate a cooling within elevated air layers under stable conditions, but the conclusions on the near-surface profile are very contradictory. Theoretical considerations by Fleagle (1953) predict a sign change in the longwave radiative heating rate profile above black body surfaces that are colder (stable conditions) or warmer (unstable conditions) than the overlying air. In a shallow layer in contact with the colder (warmer) surface, a heating (cooling) due to the convergence (divergence) of the net longwave flux is indicated.

Measurements of radiative flux divergence are extremely rare and usually cover only one atmospheric layer for a limited time. Observed longwave radiative heating rates range from -290 Kd^{-1} in the evening (Funk, 1960) to 480 Kd^{-1} during the day (Eliseev et al., 2002). An observational confirmation of the theoretical predictions of model results has not been available. Up to now, no coherent picture of the profile of radiative flux divergence could be drawn based on observations.

In May 2001, ETH Zurich started an extensive field program at the Greenland Summit Environmental Observatory. This site is centered in the dry snow zone of the Greenland ice sheet ($72^{\circ}35'N$, $38^{\circ}30'W$, 3203 m.a.s.l.). For a period of 14 consecutive months, covering all seasons, the components of the surface energy balance were determined. In addition, profiles of temperature, humidity, wind speed and longwave radiation were collected at up to eight levels from a 50 m meteorological tower.

The objectives addressed in this thesis are twofold. In the first part, the observations of the climatic conditions, the radiation regime and the surface energy balance of the dry snow zone are described. Radiation measurements were performed under the high standards of the Baseline Surface Radiation Network (BSRN) (McArthur, 1998). Together with calculations of the subsurface heat flux from temperature measurements within the firn layers, and turbulent fluxes determined with the profile method, the surface energy balance is calculated for all seasons. In addition, observations of accumulation allow an estimation of the seasonal mass balance at Summit.

The second part of this thesis focuses on the divergence of the longwave radiative fluxes in the surface boundary layer. During the field campaign, incoming and outgoing longwave radiative fluxes were measured with pyrgeometers at up to six levels on a 50 m meteorological tower. So far, only a few experiments have tried to directly measure the divergence of radiative fluxes. The reason is the high accuracy required in the determination of the individual fluxes. In this work it is shown how accurate and reliable profiles can be obtained by a careful relative calibration of

the instruments and by correcting the measurements for external influences such as the longwave emission of the tower structure. The experimentally derived profiles of radiative flux divergence are then discussed in relation to meteorological conditions, the vertical temperature structure and humidity.

In addition to the measurements, simulations of the radiation profile were carried out with the state-of-the-art radiative transfer model MODTRAN. The model could be driven by the observed temperature and humidity profiles from tower measurements and radiosonde ascents. Aim of these simulations was to investigate aspects such as the spectral characteristics of the vertical flux variations and the role of the individual components of the outgoing flux (path thermal, surface emitted, reflected). The shape of the flux profile near the surface can be resolved with a high vertical resolution by the model calculations. The spectral characteristics of the radiative flux divergence are shown to be particularly important for understanding the interactions between fog and radiative cooling.

Part II

Climate of the dry snow zone at Summit, Greenland

1 Meteorological Conditions at Summit, Greenland

The Greenland Summit Environmental Observatory (former GISP II drilling site) lies in the center of the dry snow zone of the Greenland ice sheet, at 72.58°N and 38.46°W at an elevation of 3203 m above the sea level. This is 29 km west of the highest point of the ice sheet. The polar night lasts from November 11th to January 31st. The sun is above the horizon from May 9th to August 2nd. At Summit, the difference between local standard time (LST) and universal time coordinated (UTC) is 3 hours (LST=UTC-3).

Our detailed observations of temperature and other climatic variables are summarized in this chapter. They are limited to the period from June 2001 to July 2002, unless stated differently.

1.1 Temperature

Annual mean air temperature (2 m) at Summit is -28.4°C. The coldest month is February 2001 with -47.3°C, the warmest is July with -12.4°C. The coldest 10-minute mean temperature was recorded on February 21st, 2002, at 4:50 UTC, with -65.3°C. The highest temperature of 0.1°C was recorded on June 29th, 2001, at 16:30 UTC.

Monthly mean temperature, monthly absolute maximum and minimum temperatures, and monthly mean daily maximum and minimum temperatures are shown in Figure 1.1. A wide range between the daily maximum and minimum is seen in the winter months. Large scale flows occasionally break up the strong wintertime inversions which leads to high temperatures. The variation of the monthly mean diurnal cycle of temperature is greatest in spring, when total cloud amount is low (see Section 2.4.1), and the sun still sets. A secondary peak of this variation is observed in August (Figure 1.1). The range between monthly mean daily maximum and minimum temperatures includes the effect of advection on temperature variation. It demonstrates the importance of advective processes in the winter months.

Strong surface inversions are observed throughout the winter months. In summer however, a diurnal stability cycle develops when net radiation turns positive. Unstable conditions occur throughout long periods in the day, while surface inversions develop during the night. The strong and persistent inversion in the colder months can be seen in the monthly mean profiles of temperatures from the tower

profile measurements in Figure 1.1 and in the results of the upper air soundings in Figure 1.2.

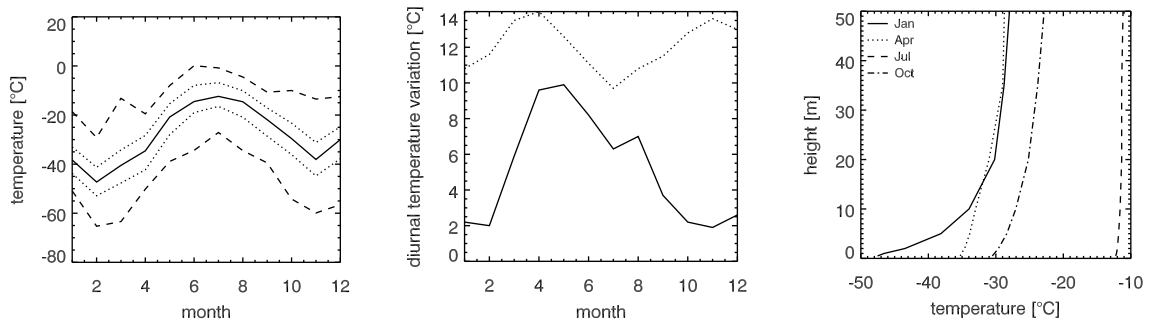


Figure 1.1: Left panel: Monthly mean (solid line), monthly absolute maximum and minimum (dashed line), and monthly mean daily maximum and minimum air temperature (dotted line) at 2m. Middle panel: Variation of the monthly mean diurnal cycle of air temperature (solid line) and difference between the monthly mean daily maximum and minimum temperatures (dotted line). Right panel: Monthly mean temperature profiles for the four mid-season months measured on the 50 m meteorological tower at Summit, Greenland.

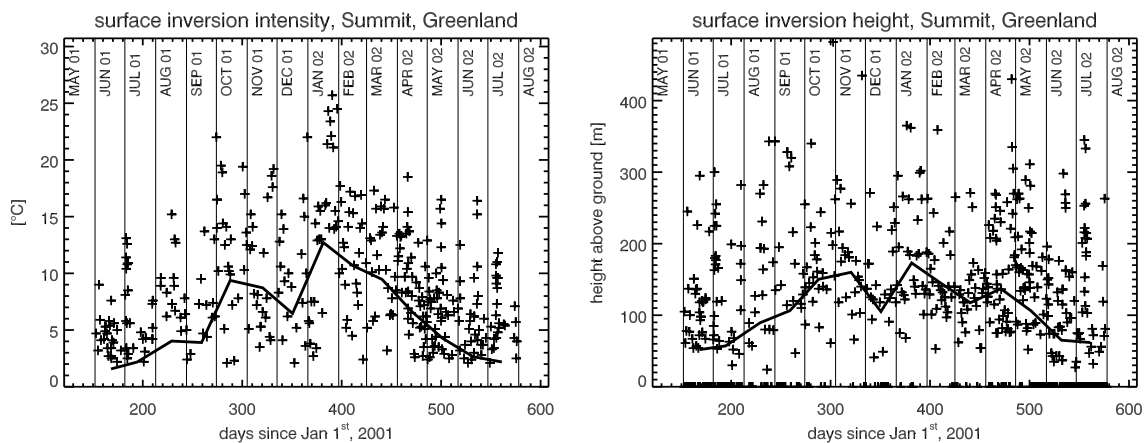


Figure 1.2: Variation of intensity and height of the surface inversion determined from radio-soundings, Summit, Greenland. Thick line connects monthly means of the individual soundings.

1.2 Wind

The prevailing wind direction at Summit is SSW. In 27% of the time winds are from the S-SW sector, while positive northerly components occur in only 15% of the time. Wind roses for the entire time of the field campaign, for the summer months June through August, and for December are shown in Figure 1.3. During the summer months the prevailing winds are from SSE, while winter conditions are characterized by persistent wind directions that last for several days. Monthly mean

wind speeds (Figure 1.4) are slightly larger in November and December, when also the highest maximum wind speed were recorded. Monthly mean wind speed profiles (middle panel in Figure 1.4) show a variation over the year. In wintertime the wind maximum is often observed within the lowest 50 m.

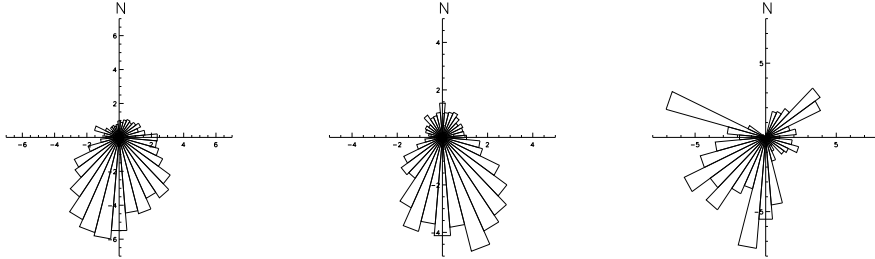


Figure 1.3: Wind roses for Summit, Greenland. For all seasons (June 2001 to July 2002), for the summer months (JJA), and for December.

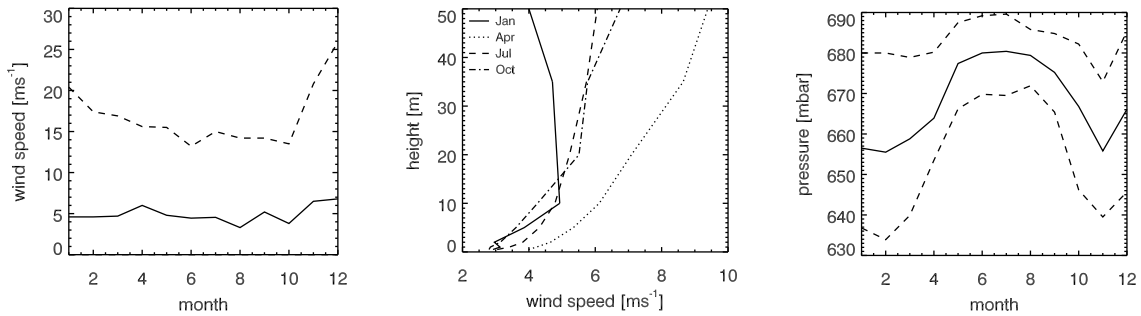


Figure 1.4: Monthly mean and maximum wind speed at 10 m, and selected monthly mean profiles of wind speed. Right panel: Monthly mean, maximum and minimum pressure, for Summit, Greenland.

1.3 Pressure

Monthly mean pressure is shown in Figure 1.4. During the summer months, a mean pressure of 680 hPa is observed, while 660 hPa is a typical value for winter. The annual cycle of mean pressure correlates very well with the annual cycle of temperatures.

1.4 Humidity

Absolute humidity is low at Summit. The monthly mean, maximum and minimum values of specific humidity from measurements with a dew point mirror hygrometer are shown in the left panel of Figure 1.5. In the summer months June and July a mean specific humidity of only 2 g kg^{-1} is observed. From September through May, specific humidity amounts to only 1 g kg^{-1} or less. Total column water vapor

was also calculated from radiosonde ascents, and are shown in the right panel of Figure 1.5. Less than 1 mmWE (millimeter water equivalent) are contained within the atmosphere above Summit between November and April.

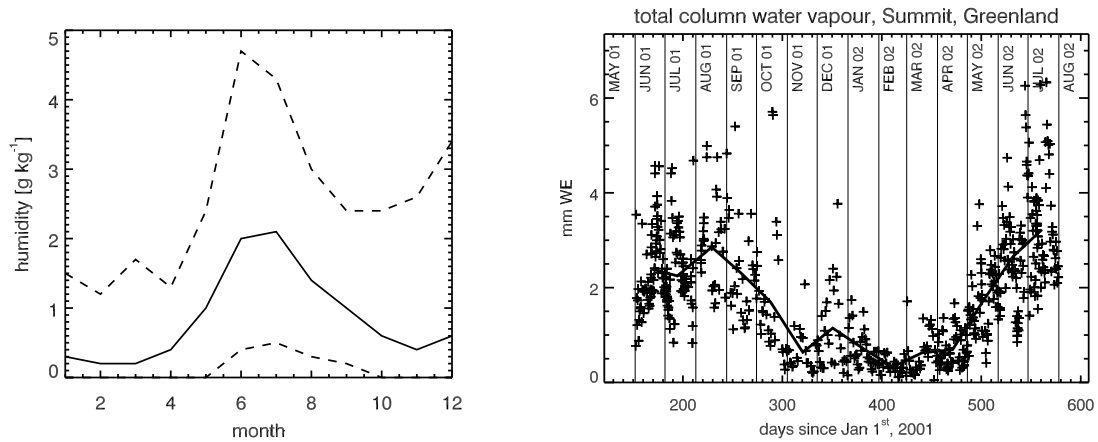


Figure 1.5: Monthly mean, maximum and minimum specific humidity at 2 m, for Summit, Greenland. Right panel: Variation of total column water vapor from radiosoundings.

1.5 Subsurface temperatures

The subsurface temperatures in the firn show a strong annual cycle to a depth of about 10 m below the surface. The monthly mean tautochrones are presented in Figure 1.6.

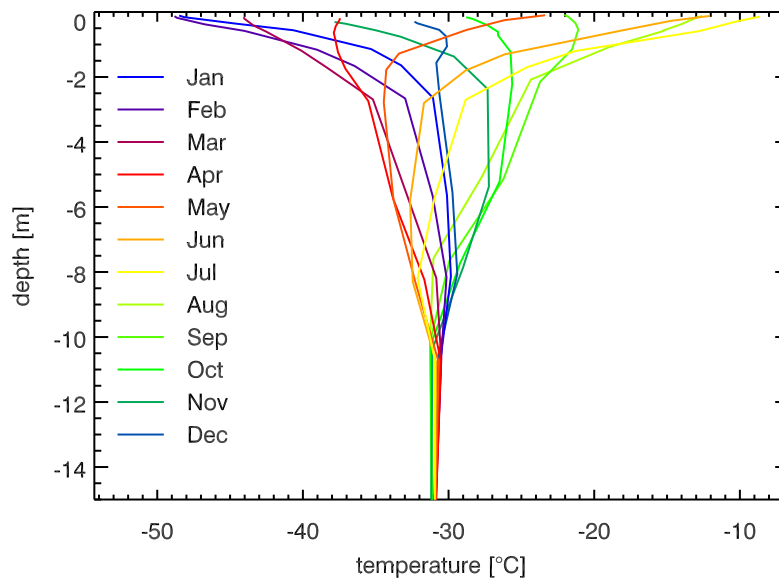


Figure 1.6: Monthly tautochrones at Summit, from June 2001 to May 2002.

The strongest variations can be seen above 2.5 m depth. Below 10 m the variation of the annual cycle is small. At the lowest measurement depth of 15 m, the standard deviation of the monthly means is only 0.1°C. The annual mean temperature at 15 m depth is -31.1°C. This temperature is lower than the annual mean screen level temperature. If one assumes a uniform heat exchange between the firn and the atmosphere, one could assume the temperature at 15 m depth to represent the annual mean temperature. However, some heat exchange mechanisms might occur unhomogenously distributed over the year. Heating of the snow cover due to the absorption of penetrating shortwave radiation is limited to the summer months. Enhanced wind pumping might occur when the air is warmer than the monthly mean, when storms advect warmer air from lower regions of the ice sheet. December 2001 was warmer than the other winter months. It is characterized by strong winter storms, advecting warm and moist air to central Greenland. This led to a warming of the topmost meter of snow compared to November 2001.

2 The radiation regime at Summit, Greenland

This chapter focuses on detailed measurements of the radiative energy fluxes that were started in July 2000 at Summit, Greenland. A comprehensive picture of the radiative fluxes and their annual and diurnal variations is presented for all four seasons. The observations reveal the relative importance of the shortwave and longwave fluxes for the radiation balance. Cloud observations that were made parallel to the radiation measurements allow a thorough analysis of the impact of cloudiness on the radiative fluxes on this high elevation arctic site.

The dataset is suitable for satellite ground truthing and validation for general circulation models (GCMs). The urgent need for comparisons between GCM and observations, particularly for sites at high latitudes, has been expressed by Wild et al. (2001). It has been demonstrated that GCM calculations of both shortwave (Wild et al., 1998) and longwave fluxes (Wild et al., 2001) show differences of 10-20 Wm^{-2} to observations. To allow for the assessment of model accuracy, the highest radiation measuring standards need to be adopted. Therefore the measurements conducted at Summit follow, with some exceptions, the Baseline Surface Radiation Network (BSRN) conventions (Ohmura et al., 1998).

In the past, several investigations have taken place to infer the radiative energy budget of the Greenland ice sheet. Measurements have been conducted in the ablation zone (Ambach, 1963), at the equilibrium line altitude (Konzelmann and Ohmura, 1995) and in the accumulation area (Ambach, 1977; Ambach and Markl, 1983). Most of these studies, however, were limited to the summer months between May and August. The full radiative balance has not been measured for an entire annual cycle, with the exception of the measurements of the automatic weather stations (AWS) from GC-Net (Steffen et al., 1996; Steffen and Box, 2001). At these AWS stations, shortwave and net fluxes are measured using photo-diodes and net radiometers which have an accuracy of 5-15 % and of 5-50 %, respectively (Box and Steffen, 2000). The GC-Net measurements offer valuable information about the spatial distribution of radiative fluxes. The measurements in this work are of BSRN quality and recorded in high temporal resolution. This allows a more accurate assessment of the radiative fluxes, their relative importance for the radiation balance, and of the interactions.

2.1 Instrumentation and observations

The radiative fluxes determined by direct measurements at Summit, Greenland, are: direct solar irradiance (D), diffuse sky irradiance (d), shortwave reflected irradiance ($SW_{refl.}$), global irradiance (Gl), longwave incoming irradiance (LW_{in}) and longwave outgoing irradiance (LW_{out}). The albedo (α) and net radiation (NR) were derived from the relevant measured fluxes. The radiation balance (net radiation) as part of the surface energy balance is given as

$$NR = D + d - SW_{refl.} + LW_{in} - LW_{out}. \quad (2.1)$$

Global irradiance and diffuse irradiance were measured by pyranometers (Kipp & Zonen, CM21). The pyranometer measuring the diffuse irradiance was constantly shaded by a shading disk. Shortwave reflected irradiance was measured by a Kipp & Zonen CM11 pyranometer. Direct solar irradiance was measured with a thermopile pyrhelimeter (Kipp & Zonen CH1). Longwave irradiances were measured by two pyrgeometers (Eppley Precision Infrared Radiometer, PIR). They were modified with three dome thermistors to monitor the temperature of the silicon dome of the instrument as suggested by Philipona et al. (1995) and discussed in Section 5.1.3. The up-facing instrument is shaded by a shading disk.

All instruments taking hemispheric measurements (pyranometers, pyrgeometers) are installed at a height of approximately 1.8 m on a boom on top of a semi-intelligent INTRA solar tracker manufactured by BRUSAG, Switzerland. The shading of the pyranometer measuring the diffuse irradiance and the up-facing pyrgeometer and the accurate pointing of the pyrhelimeter is ensured by the trackers active solar positioning feedback sensor. A pointing accuracy of better than 0.1° is guaranteed. These shaded up-facing hemispheric instruments, together with the unshaded pyranometer measuring the global irradiance are mounted close to the vertical rotation axis of the solar tracker. The down-facing instruments are mounted on each end of the boom, in a distance of 115 cm from the rotation axis. All hemispheric instruments are ventilated with an air-stream slightly heated above ambient temperature. This keeps the instrument domes free of depositing rime. Without these measures, long-term measurements of radiation would inevitably fail in an environment as harsh as Summit. The setup of the instrumentation is shown in Figure 2.1.

To ensure radiation measurements of the highest quality, the guidelines of the BSRN (McArthur, 1998) were followed as much as possible. However, a few exceptions had to be made. To ensure longer lifetime of the multiplexer used in data retrieval, the measurement frequency was reduced from the requested 1 Hz to one measurement every six seconds. BSRN requires a combination of a cavity radiometer and a thermopile pyrhelimeter for measurements of direct solar irradiance. Due to the harsh environment with the frequent occurrence of blowing snow and ice crystal precipitation, measurements with a cavity radiometer (PMO6) are limited to clear sky days in the summer months only.

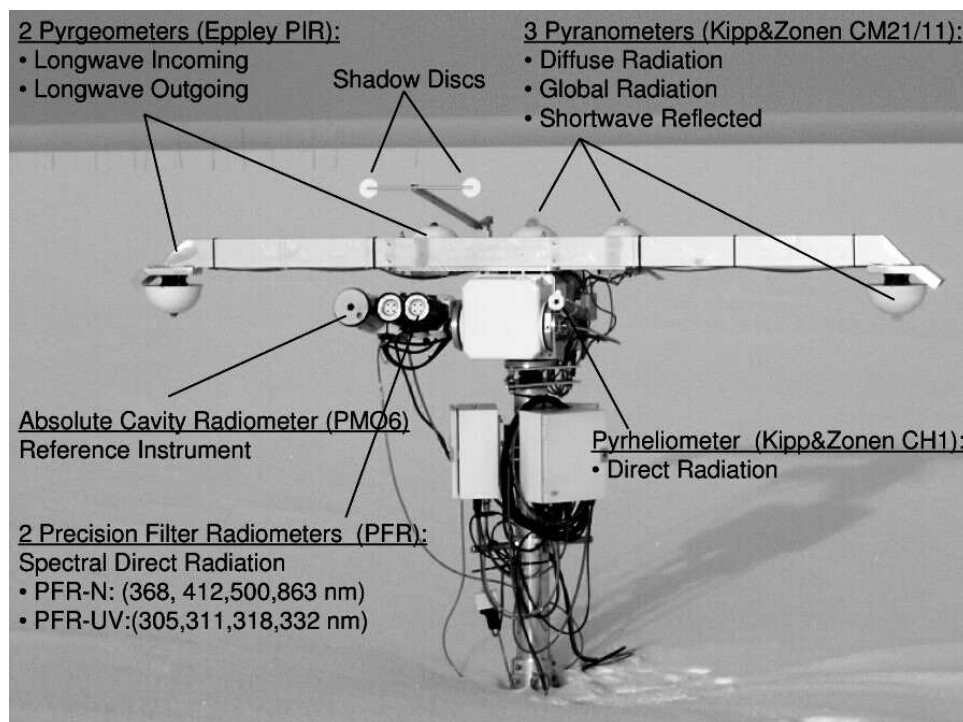


Figure 2.1: Radiation monitoring tower at Summit, Greenland, 2002.

The down-facing hemispheric instruments are not equipped with shadow-bands and are mounted at approximately the same height as the up-facing instruments. BSRN requires the use of shadow-bands and measurements of up-welling quantities should be done from a high tower. Also, pyranometer body temperatures are not recorded. Data-logger clocks are set every week. A mean offset of -2 ± 10 s is observed. Thus, the time accuracy of better than 1 s required by the BSRN standards is not met.

Detailed cloud observations of amount and type according to the codes of the World Meteorological Organization were made between June 2001 and July 2002. The frequency of observation ranged from seven times a day (May to July 2001, July 2002) to two observations in the dark months (November 2001 to January 2002). February and March 2002 and September and October 2001 are covered by three daily observations, April through June 2002 by six observations. Five daily cloud observations are available for August 2001. Observations are made on the synoptic hours, but limited to the light part of the day. As exception from the WMO code, cloud amounts were observed in tenths instead of eights.

2.2 Calibrations and accuracy

The pyranometers and pyrgeometers were calibrated at the Physikalisch-Meteorologisches Observatorium Davos and World Radiation Center (PMOD/WRC) in spring 2000 prior to their installation in the field. The pyrheliometer was calibrated in late 1996, but never engaged in any measuring

activity. It was re-calibrated to a traveling standard at Summit in summer 2001 and 2002. The traveling standard, an absolute cavity radiometer (PMO6) was directly compared to the World Standard Group (WSG) at PMOD/WRC Davos, in spring 2001 and 2002.

Uncertainties and accuracy of the involved instruments are given by the manufacturer and have been, for measurements performed following the standards described by McArthur (1998), estimated by BSRN scientists. The latter are given by Ohmura et al. (1998) and are summarized in Table 2.1. They were estimated from the standard deviations of the calibration coefficients, and represent the capability achieved by 1995. Similarly, the accuracy of the shortwave instruments used at Summit is estimated using the standard deviations of calibration coefficients during the calibrations and the maximum monthly mean irradiance levels of each radiation component. These values are given in Table 2.2.

Table 2.1: BSRN measured irradiances, instrumentation and estimated capabilities, estimated from standard deviations of the calibration coefficients, from Ohmura (1998).

component	instrument type	estimated capability by 1995
global, diffuse (G_l, d)	pyranometer	$\pm 5 \text{ Wm}^{-2}$
direct solar (D)	pyrheliometer	$\pm 2 \text{ Wm}^{-2}$
longwave incoming (LW_{in})	pyrgeometer	$\pm 10 \text{ Wm}^{-2}$

The accuracy of measurements of longwave irradiances has been intensively studied (Philipona et al., 1995; Philipona et al., 1998). Pyrgeometers that have been calibrated at PMOD/WRC participated in the two International Pyrgeometer and Absolute Sky-scanning Radiometer Comparisons (IPASRC) in Oklahoma (Philipona et al., 2001) and Barrow, Alaska (Marty et al., 2003). They may be considered as representative for the pyrgeometers used in this study at Summit, Greenland. The comparison in Oklahoma indicates a high level of accuracy (uncertainty of 3.4 Wm^{-2}) that is reached in longwave irradiance measurements using modified pyrgeometers and the data reduction formula by Philipona et al. (1995). The cold and dry conditions during the second field comparison in Barrow, Alaska, in March 2001 resembled the atmospheric conditions at our field site. It was shown that the pyrgeometers calibrated with the blackbody source at PMOD/WRC have an uncertainty of $\pm 6 \text{ Wm}^{-2}$. Field calibrations to a standard instrument however could significantly decrease the uncertainty to $\pm 2 \text{ Wm}^{-2}$. A comparison with a traveling standard pyrgeometer of PMOD/WRC took place at Summit in May 2002. The comparison confirmed the calibration coefficients of the pyrgeometers that were determined in a blackbody calibration in Davos in spring 2000.

Table 2.2: Measured irradiances at Summit, Greenland, instrumentation type, serial numbers and manufacturer and their accuracy. Accuracy is estimated from the standard deviations of calibration coefficients from calibrations at PMOD/WRC Davos and at the field site and maximum monthly mean irradiance levels.

component	instrument type, manufacturer, model, serial nr.	accuracy
direct solar (D)	pyrheliometer, Kipp CH1, # 940063	$\pm 1 \text{ Wm}^{-2}$
global (G_l)	pyranometer, Kipp CM21, # 920090	$\pm 3 \text{ Wm}^{-2}$
diffuse (d)	pyranometer, Kipp CM21, # 960308	$\pm 1 \text{ Wm}^{-2}$
shortwave reflected ($SW_{refl.}$)	pyranometer, Kipp CM11, # 935142	$\pm 4 \text{ Wm}^{-2}$

2.3 Problems, corrections and quality control

In times of strong winds and drifting or blowing snow, the pyrheliometer was sometimes blocked by a layer of hard packed snow. The direct component was then calculated as the difference between the measured global and diffuse radiation. On some mornings after extreme riming events, a very thin layer of rime had formed on the windward side of the outer glass dome of the pyranometers. Usually it did not persist for a long time or it was removed by wiping the dome with a soft cloth.

Negative pyranometer signals during the night, called 'zero offset' or 'nighttime offset' are caused by the temperature gradient between the dome and the body of the instrument. During clear nights the dome often cools off faster than the instrument body, leading to a negative signal. The ventilation system used with our instrumentation was introduced by PMOD/WRC, and is designed to reduce the disturbing temperature gradient. Nevertheless, nighttime offsets occur in the extremely cold environment during clear nights at Summit. Efforts have been undertaken to estimate and correct for the error introduced through the thermal infrared exchange to pyranometer measurements (Dutton et al., 2001). They are, however, limited to shaded instruments measuring the diffuse sky irradiance. Negative nighttime offsets recorded at Summit are therefore simply set to zero. Pyranometer measurements presented in this study are not corrected for thermal infrared exchange induced offsets that might occur during the day.

2.4 Results

In this section radiation measurements collected between June 2001 and July 2002 are presented. This was the main period of the ETH Greenland Summit Experiment. Radiation measurements started as early as in July 2000, and have, with an interruption from August 2002 to June 2003, continued until today (July 2005). In some of the graphs, all data collected between July 2000 to July 2002 is included.

Daily averages are calculated for all components when 96.5 % of the daily minute averages are available. Monthly means are calculated from daily mean diurnal cycles.

The monthly mean albedo is calculated as the ratio of the monthly mean shortwave reflected radiation and the monthly mean global radiation.

2.4.1 Cloud conditions

Cloud observations are available for the 14 months between May 2001 and July 2002. They are summarized in Table 2.3. In 2001, total cloud amounts increased from 62 % in May and June to a maximum amount of 83 % in September. Between October and January, total cloud amount is about 60 % with a slightly higher value in December (67 %). Then, a decrease in total cloud to a minimum of 39 % in April is observed. In the summer months, from May to June 2002, an increase from 63 % to 80 % is seen. Low cloud cover shows a minimum from March to May, and a maximum in September, November and December. The most frequently observed low cloud types are stratus and stratocumulus. High and middle clouds are most often observed in the summer months. Annual cycle of total and low cloud amount are shown in the top right panel of Figure 2.2.

Table 2.3: Monthly means of cloud amount in tenths at Summit, Greenland, for May 2001 to July 2002

year	month	total cloud	low cloud	middle cloud	high cloud
2001	05	6.3	2.0	1.0	4.6
2001	06	6.2	3.6	1.3	3.3
2001	07	7.3	4.9	2.2	3.1
2001	08	7.6	4.4	2.6	4.3
2001	09	8.3	6.2	3.0	4.2
2001	10	6.1	2.7	1.5	3.6
2001	11	6.0	5.3	0.6	3.1
2001	12	6.7	5.7	1.5	2.5
2002	01	6.0	4.5	0.4	2.1
2002	02	5.2	2.7	0.5	3.1
2002	03	4.2	1.1	1.7	2.2
2002	04	3.9	0.9	2.3	1.4
2002	05	6.3	1.1	1.4	5.3
2002	06	6.7	2.4	2.7	4.3
2002	07	8.0	4.6	3.3	4.2

2.4.2 Monthly means and annual cycles

The monthly means of the radiative fluxes, total cloud amount and temperature are presented in Table 2.4. The annual cycle of selected variables are shown in Figure 2.2.

Direct solar irradiance and global irradiance reach their maximum in June, with 202 Wm^{-2} and 382 Wm^{-2} , respectively (values for 2001). Diffuse sky irradiance peaks with 192 Wm^{-2} in July. Monthly mean global irradiance shows the expected symmetry to the June mean value, when solar elevations are greatest. The composition of the global irradiance in terms of diffuse sky radiation and direct radiation

varies over the year. From March until June, the direct solar irradiance component dominates. From July on, the larger contribution to the global irradiance comes from the diffuse sky irradiance. This reflects the distribution of cloudiness over the year, with smaller cloud amounts in spring and early summer (top right panel). Shortwave net radiation peaks in June with 68 Wm^{-2} . The ratios of global, direct and diffuse irradiance to the radiation at the top of the atmosphere (TOA) are shown in the middle left panel of Figure 2.2. The largest ratios of G_I/TOA , between 0.75 and 0.8 are observed in April, May and June. The June values are higher than the value of 0.71 that has been previously reported for Summit by Konzelmann (1994). Albedo shows an increase between March and October (middle right panel). This has two causes. The first cause is the increase in cloudiness, which leads to an increase in albedo (c.f. Section 2.4.4). The second cause is the changing character of the snow surface. The increase in precipitation in fall leads to a higher albedo, while the greater surface roughness and surface topography (sastruga) observed in the early year leads to a lower albedo (Table 3.3). The influence of solar elevation, which is observed in the diurnal cycle of clear sky days, plays only a secondary role. With a higher reflectance at low zenith angles, this effect would lead to lower albedo in summer and higher albedo in both fall and spring. The longwave incoming irradiance reaches its maximum in August with 220 Wm^{-2} and its minimum of 141 Wm^{-2} in January and February. The range of longwave outgoing irradiance lies between 161 Wm^{-2} in January and 253 Wm^{-2} in August. Longwave net radiation is lowest in May and June (-50 Wm^{-2}) and is highest in December and January (-17 Wm^{-2}). Net radiation is clearly positive in the summer months May, June and July, and is close to zero in April and August. A minimum net radiation of -21 Wm^{-2} is observed in January and February. The annual radiation balance is only slightly negative with -7 Wm^{-2} .

2.4.3 Diurnal cycles

Monthly mean diurnal cycles of selected radiative quantities are presented in Figures 2.3 to 2.5. Figure 2.3 shows the monthly mean diurnal cycles of the shortwave incoming fluxes: direct solar, diffuse and global irradiance. After the polar night which lasts from November 11th to January 31st, a diurnal cycle develops. While the magnitude of global irradiance grows with higher solar elevation angles, the relative importance of the diffuse and direct irradiance components reflects the annual and diurnal variation of cloudiness. In February, when solar elevation angles are still very small, the diffuse irradiance component dominates the shortwave fluxes. From March until June, when total cloud amount is lowest, the direct component dominates during most of the day. From July on, when total cloud amount has increased, the diffuse component dominates. This leads to the maximum monthly mean of diffuse irradiance in July. All other shortwave fluxes reach their maximum in June, when the maximum solar elevation angles are reached. June and August show a special pattern in the diurnal cycle of the shortwave fluxes: In June, the diffuse component reaches its peak at 14 TST (true solar time), the direct component between 11 and 12 TST. In August, the direct component is highest around 13 TST, while the diffuse component peaks at 11 TST. This is caused by the diurnal variation of cloud cover.

Table 2.4: Monthly means of total cloud amount (%), air temperature at 2 m ($^{\circ}\text{C}$), and radiative variables (Wm^{-2}) for July 2000 through July 2002 at Summit, Greenland: Direct solar irradiance D , diffuse sky irradiance d , global irradiance Gl , shortwave reflected irradiance SW_{refl} , albedo α , net shortwave radiation SW_{net} , longwave incoming irradiance LW_{in} , longwave outgoing irradiance LW_{out} irradiances, net longwave radiation LW_{net} and net radiation NR . Temperatures from July 2000 to May 2001 are from the Summit AWS from GC-Net.

year	month	cloud	T_{2m}	D	d	Gl	SW_{refl}	α	SW_{net}	LW_{in}	LW_{out}	LW_{net}	NR
2000	Jul	-	-14.9	111	204	315	258	0.82	56	217	258	-40	16
2000	Aug	-	-14.7	61	150	211	179	0.85	32	224	252	-27	4
2000	Sep	-	-21.3	22	58	80	67	0.84	13	202	223	-20	-7
2000	Oct	-	-36.3	9	14	23	19	0.81	4	143	166	-22	-18
2000	Nov	-	-37.5	0	1	1	0	-	0	154	170	-15	-16
2000	Dec	-	-39.7	0	0	0	0	-	0	142	160	-17	-17
2001	Jan	-	-39.1	0	0	0	0	-	0	141	161	-19	-19
2001	Feb	-	-41.0	2	7	10	8	0.83	1	141	163	-21	-19
2001	Mar	-	-42.1	52	30	82	66	0.81	16	127	157	-29	-14
2001	Apr	-	-31.9	112	85	198	160	0.81	37	150	187	-37	0
2001	May	63	-24.8	198	127	326	265	0.82	60	162	213	-51	8
2001	Jun	62	-16.7	202	179	382	313	0.82	68	192	245	-52	16
2001	Jul	73	-14.3	136	192	328	273	0.83	55	208	251	-43	12
2001	Aug	76	-14.6	84	131	216	181	0.84	35	220	253	-32	2
2001	Sep	83	-21.9	30	70	100	85	0.85	15	197	221	-24	-8
2001	Oct	61	-29.6	8	17	26	22	0.88	3	172	193	-20	-17
2001	Nov	60	-38.1	0	0	0	0	-	0	144	164	-19	-19
2001	Dec	67	-30.0	0	0	0	0	-	0	168	186	-17	-17
2002	Jan	60	-38.3	0	0	0	0	-	0	137	155	-17	-17
2002	Feb	52	-47.3	4	6	11	9	0.82	1	114	139	-24	-22
2002	Mar	42	-40.5	44	33	78	63	0.81	14	130	157	-27	-12
2002	Apr	39	-34.6	134	69	203	162	0.80	41	134	179	-44	-2
2002	May	63	-20.8	179	136	316	261	0.83	54	175	223	-47	7
2002	Jun	67	-12.3	189	184	373	307	0.82	66	205	258	-52	15
2002	Jul	80	-10.5	115	204	319	267	0.84	51	229	264	-35	17
7/2000-	7/2002			65	71	137	112	0.82	24	167	198	-30	-6

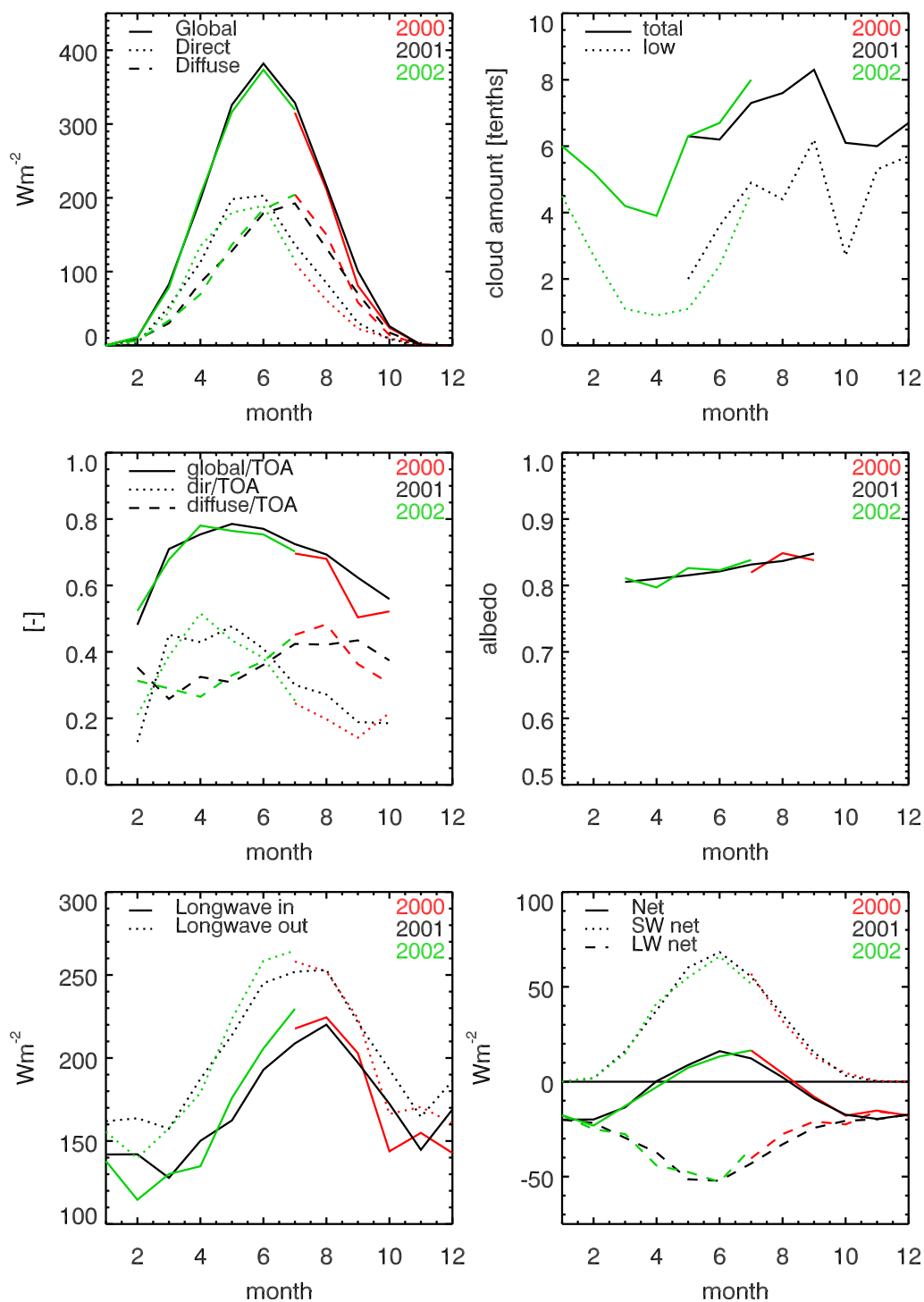


Figure 2.2: Annual cycle of the main radiative quantities for Summit, Greenland, 2000-2002. Top left panel: Global irradiance (solid), direct solar irradiance (dotted) and diffuse sky irradiance (dashed); Top right panel: total cloud amount (solid), low cloud amount (dotted); Middle left panel: ratio of global (solid line), direct (dotted) and diffuse (dashed) radiation to radiation at the top of the atmosphere (TOA); Middle right panel: albedo; Lower left panel: Longwave incoming irradiance (solid) and longwave outgoing irradiance (dotted); Lower right panel: net radiation (solid), shortwave net radiation (dotted) and longwave net radiation (dashed).

In August 2001, the observed mean total cloud amount is lowest between 12.30 TST and 15.30 TST. This is when the direct component reaches the same magnitude as the diffuse.

Longwave irradiances are presented in Figure 2.4. The longwave outgoing irradiances show a developing diurnal cycle reflecting the diurnal temperature cycle of the snow surface during the summer months. The maximum of the diurnal cycle is reached around 13.30 TST. Incoming longwave irradiance shows no significant diurnal variation, but shows a strong flicker. This is due to large changes in longwave incoming irradiance occurring on individual days. These fast changes in incoming longwave irradiance occur when low cloud amount is changing rapidly.

The diurnal cycles of net radiation (Figure 2.5) show the increasing importance of the shortwave component with higher solar elevations reached at noon. On the other hand, the enhancement of energy loss due to longwave emission with higher surface temperatures around 13.30 TST plays an important role for the diurnal net radiation. In August 2001, for example, net radiation reaches its maximum as early as 10.30 TST. Longwave net radiation drops to a minimum at 13.30 TST, due to the highest surface temperatures and the minimum in cloud cover. The maximum of the shortwave net irradiance is reached at 11.30 TST. The lag between the maximum shortwave net radiation and the minimum net longwave shifts the maximum of net radiation to the pre-noon hour.

2.4.4 Example days under clear and cloudy conditions

In this section, the differences in the radiative fluxes under clear and cloudy skies are presented. Net fluxes observed on two selected summer days are shown in Figure 2.6.

June 29th represents an overcast day. Stratus clouds with an estimated base height of 300 to 400 m above ground were observed. The solar disk was sometimes visible through the cloud cover. The daily mean global irradiance amounted to 328 Wm^{-2} , the daily mean net radiation to 33 Wm^{-2} (longwave net: -18 Wm^{-2} , shortwave net: 51 Wm^{-2}). It is remarkable that net radiation was positive throughout most of the day. Only between 0 UTC and 1 UTC the cloud cover must have opened up. This led to a negative net radiation due to a reduced incoming longwave irradiance.

Two days later, on July 1st, a clear sky day was observed. Only one tenth of cirrostratus was visible at the horizon before 12 UTC. Global irradiance reached a daily mean of 417 Wm^{-2} , nearly 4/3 of the value observed on the overcast day. Due to the clear sky, mean net longwave radiation was as low as -77 Wm^{-2} . This energy loss compensated the positive shortwave net radiation, leading to a daily mean net radiation of 0 Wm^{-2} .

In Figure 2.7, the short term variation of selected radiative quantities are shown for the two example days, June 29th and July 1st, 2001. Global and longwave irradiances are very smooth on the clear sky day, whereas the minute to minute variability can be quite large on an overcast day like June 29th. The strong variation is most likely due to a variation in cloud thickness. For the longwave irradiances, the minute to minute variability is less than 0.5 Wm^{-2} for the clear sky case, but amounts to more than 1.5 Wm^{-2} beneath the cloud cover. The albedo on the overcast day shows

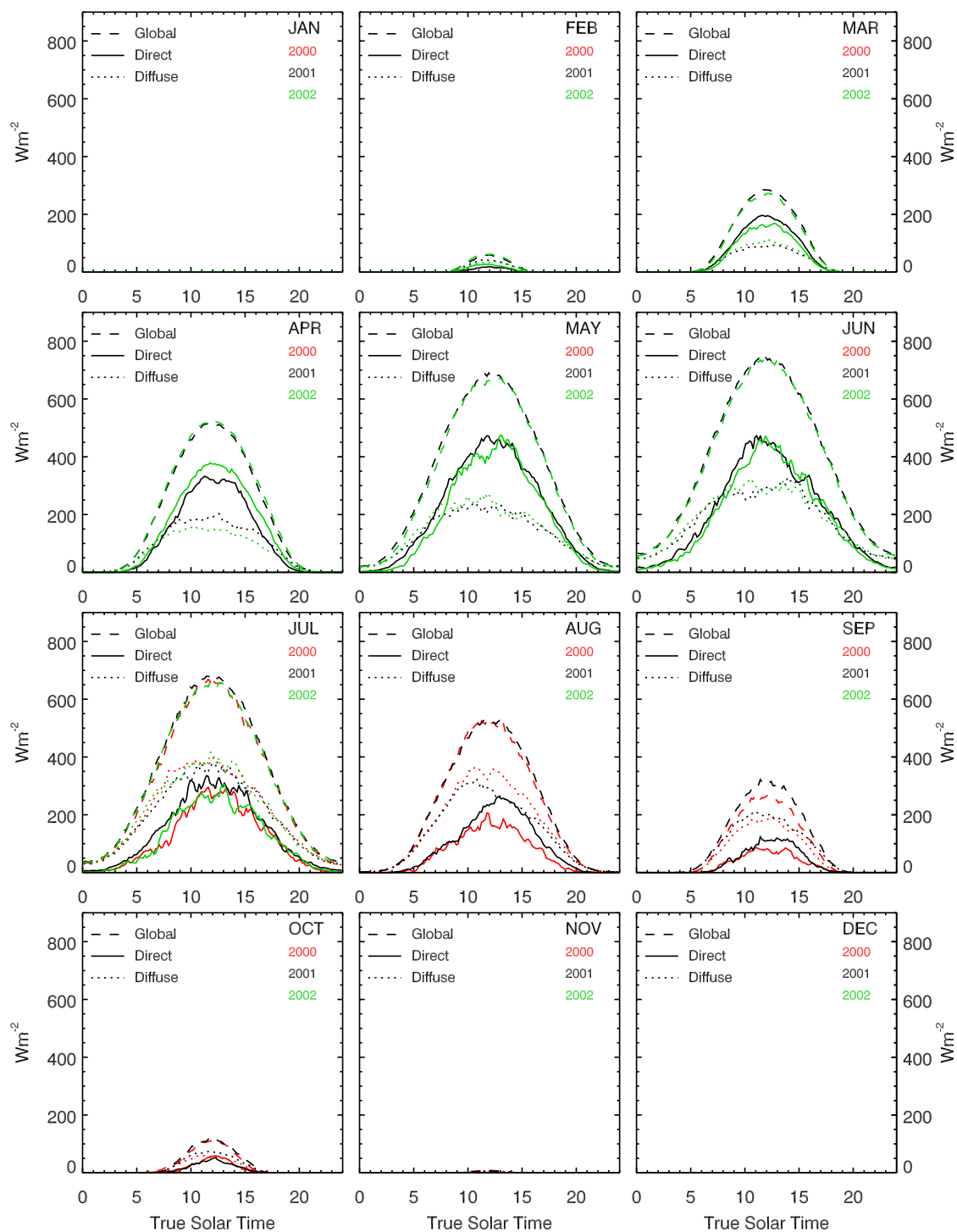


Figure 2.3: Monthly diurnal cycles of global (dashed), direct solar (solid) and diffuse irradiances (dotted) at Summit, Greenland, 2000-2002.

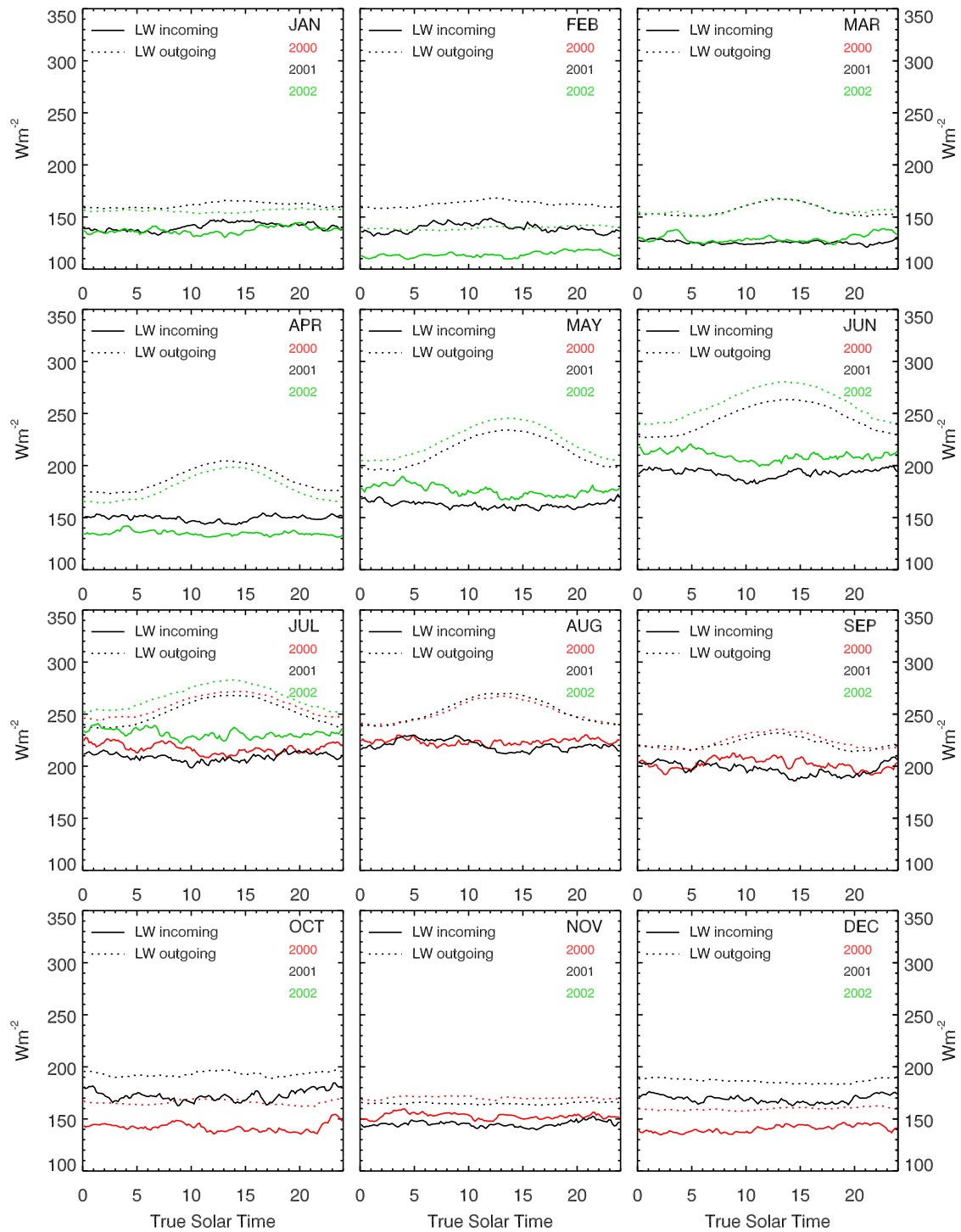


Figure 2.4: Monthly diurnal cycles of longwave incoming (solid) and longwave outgoing irradiances (dotted) at Summit, Greenland, 2000-2002.

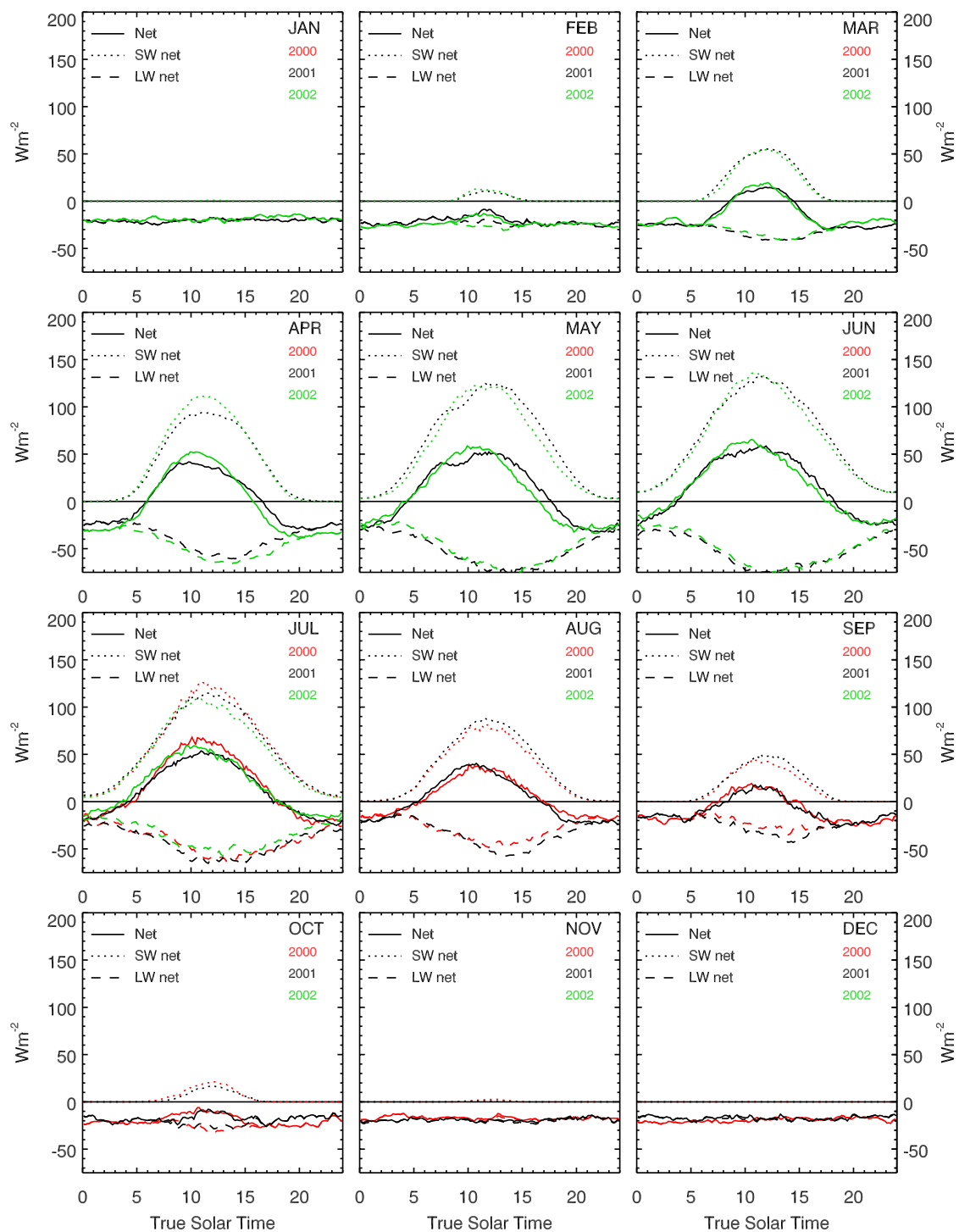


Figure 2.5: Monthly diurnal cycles of shortwave net (dotted), longwave net (dashed) and net irradiances (solid) at Summit, Greenland, 2000-2002.

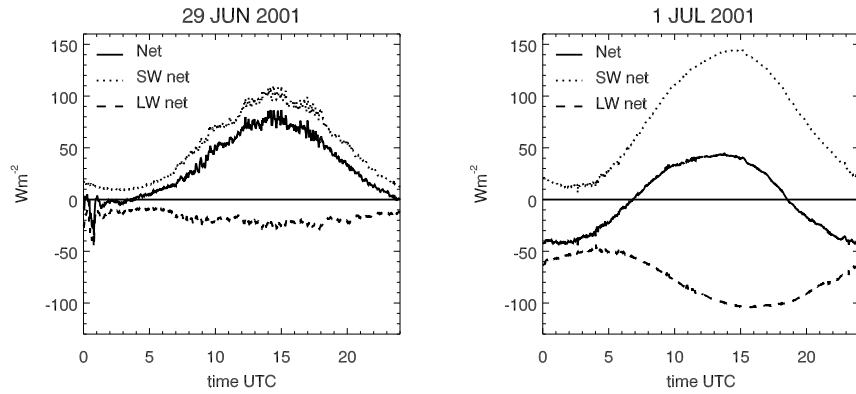


Figure 2.6: Daily cycle of the shortwave net (dotted), longwave net (dashed) and net radiation (solid) on an overcast day (left panel, June 29th, 2001) and a clear sky day (right panel, July 1st, 2001) at Summit, Greenland.

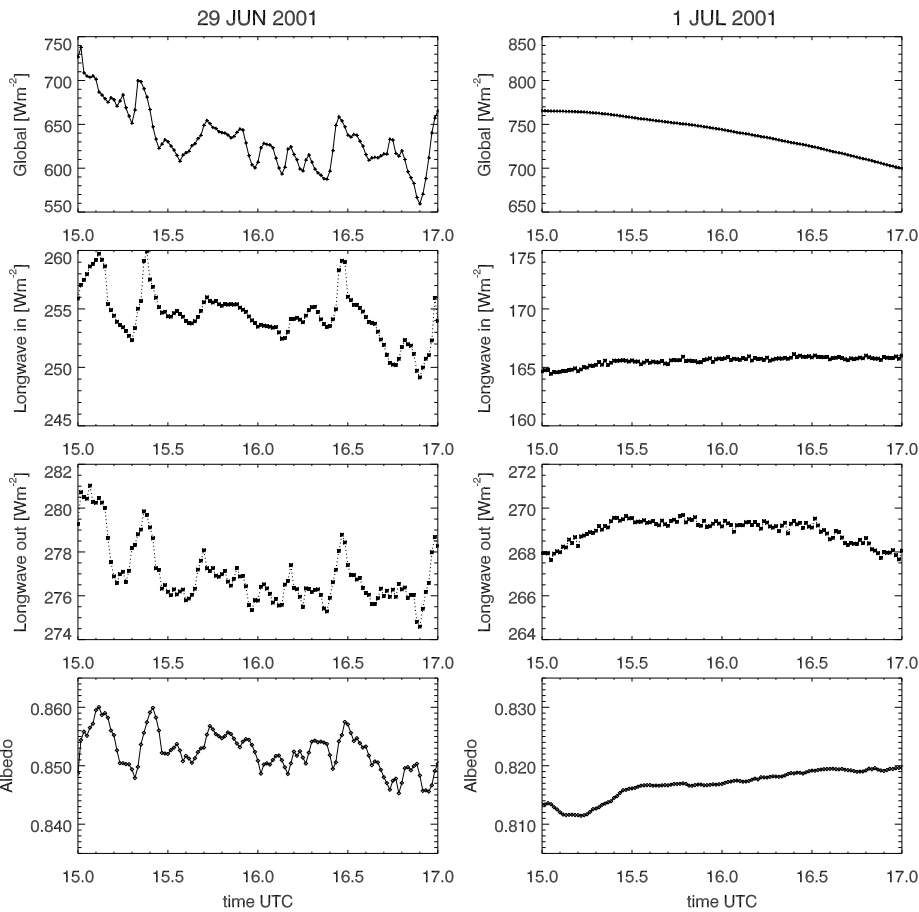


Figure 2.7: Minute to minute variability of chosen radiative quantities for clear sky and overcast situations: Global irradiance (top panels), longwave incoming irradiance (second panel from top), longwave outgoing irradiance (second panel from bottom) and albedo (bottom panels) are shown for a selected 2-hour period between 15 UTC and 17 UTC during an overcast day (June 29th, 2001, left panels) and a clear sky day (July 1st, 2001, right panels) at Summit, Greenland. Plotted ranges are equal, but minimum and maximum values vary.

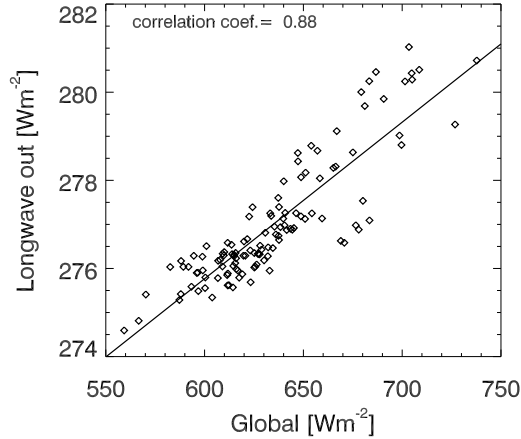


Figure 2.8: Scatter plot of global irradiance versus longwave outgoing irradiance for the selected 2-hour period between 15 UTC and 17 UTC during an overcast day (June 29th, 2001) at Summit, Greenland.

a maximum minute to minute variability of 0.005, whereas it is very smooth on the clear sky day of July 1st 2001.

A higher albedo is observed under overcast conditions. This is due to the spectral variation of the albedo of snow, with higher values at shorter wavelengths. Cloud extinction shows a spectral variation as well. Light with longer wavelength is reduced to a greater extent, which leads to a different spectral composition of the global radiation under clear and cloudy skies. Shorter wavelengths dominate the spectral composition of global radiation under cloudy skies, which reflects in a higher broadband albedo.

The high temporal resolution of our data allows to detect a correlation between the global irradiance and the longwave outgoing irradiance. The snow surface reacts very fast to changes in global irradiance. A certain part of the shortwave net energy must be absorbed by the very top layer of the snow surface as suggested by Ohmura (1980). The warming of this topmost layer causes an instantaneous increase in longwave emission according to the Stefan-Boltzmann law. A scatter plot showing the relationship between global radiation and outgoing longwave irradiance for the selected overcast day is shown in Figure 2.8. The correlation coefficient is as high as 0.88.

2.4.5 Cloud forcing

The effect of clouds on the surface climate system can be expressed as cloud radiative forcing (CF_s). This term has been introduced by Charlock and Ramanathan (1985) and Ramanathan (1987). On one side, clouds have a cooling effect as they reflect incoming shortwave radiation before it reaches the surface. On the other side, clouds have a warming effect for the surface, as they reduce the absolute magnitude of the negative net longwave balance, blocking the escape of longwave radiation to space. Surface cloud forcing CF_s can therefore be expressed as the sum of the shortwave cloud forcing ($CF_{s,SW}$) and longwave cloud forcing ($CF_{s,LW}$). Surface cloud forcings

are defined as the differences between surface fluxes under all-sky and clear-sky (superscript *cs*) conditions (Gupta et al., 1993):

$$CF_{s,SW} = SW_{net} - SW_{net}^{cs}, \text{ and} \quad (2.2)$$

$$CF_{s,LW} = LW_{net} - LW_{net}^{cs}. \quad (2.3)$$

The total cloud forcing at the surface is simply the sum of the shortwave and longwave components,

$$CF_s = CF_{s,SW} + CF_{s,LW}. \quad (2.4)$$

Cloud forcings were calculated from the monthly mean diurnal cycles and monthly mean clear sky diurnal cycles of the radiative variables for the months between June 2001 and July 2002. Two criteria were used to separate clear sky and cloudy scenes. The minimum diffuse radiation was calculated as $d_{min} = a \cdot \cos(z)^b$ for zenith angles z less than a critical value z_{krit} . The factors a and b were determined from selected clear sky situations for each month. This minimum diffuse criteria has been introduced by Long and Ackerman (2000) to separate clear sky values during daytime. As second criteria was chosen to separate clear sky situations during nighttime, a minimum LW_{net} radiation threshold value. This value was again determined from manually selected situations during each month.

Monthly mean longwave, shortwave and net cloud forcing are shown in Figure 2.9. The shortwave cloud forcing is largest in summer. Clouds lead to a reduction of the shortwave net flux of more than 20 Wm^{-2} . From September to April, the shortwave influence of clouds is negligible, as the shortwave energy supply is either zero or very small. The warming influence of clouds in the longwave is greatest in summer, reaching 40 Wm^{-2} in July. The combination of both effects, the cloud radiative forcing is positive throughout the year and reaches an annual mean of 14 Wm^{-2} . Cloud radiative forcing peaks in fall, when the absolute value of the shortwave forcing is already small, and the longwave forcing is still large. Cloud forcing, as defined above, depends on the cloud amount and cloud type observed during the individual months. If cloud forcing is normalized with the total cloud amount, the peak of the longwave forcing observed in fall is reduced (Figure 2.9), as the maximum of cloud cover is observed during this time.

The influence of cloud cover has been demonstrated earlier in the comparison of the two example summer days (Figure 2.6). Under overcast conditions, net radiation was barely negative at night, while it dropped to -45 Wm^{-2} under clear conditions. The reduced shortwave input is more than compensated by the reduction of energy loss through longwave emission. Daily mean net radiation was 33 Wm^{-2} higher during the overcast day.

2.5 Summary

For two years, all components of the radiation balance were collected with a temporal resolution of one minute at Summit, Greenland. The dataset draws a detailed picture of the radiation regime of the dry snow zone of the Greenland ice sheet. The annual

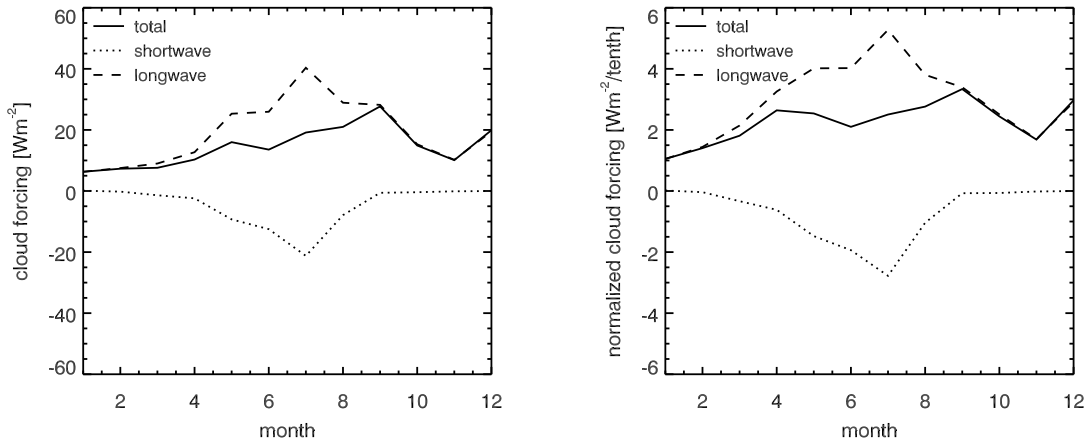


Figure 2.9: Monthly mean surface cloud forcing at Summit, Greenland. The right panel shows the cloud forcing normalized with the total cloud amount.

mean net radiation is negative with -6 Wm^{-2} , the surface is characterized by a high albedo of 0.82. The cloud radiative forcing at a high elevation arctic site as Summit is positive throughout the year.

The effect of cloud cover on the distribution of diffuse sky radiation and direct radiations as components of the global shortwave radiation can be seen in the monthly means as well as in the monthly mean diurnal cycles.

Net radiation is positive throughout the three summer months. A maximum net radiation of 17 Wm^{-2} was observed in July 2002. This high value observed at the top of the ice sheet suggests that net radiation is possibly positive across the entire Greenland ice sheet. Net radiation is close to zero in April and August and lowest in the winter months between November and February (-20 Wm^{-2}).

The comparison of clear sky and overcast days demonstrate the effect of cloud cover on the components of the net radiation and on snow albedo. The high temporal resolution of the dataset collected at Summit allows the study of the interplay of the radiative fluxes. The correlation of global irradiance and longwave outgoing radiation emphasizes the importance the topmost firn layer for the absorption of shortwave energy.

3 The energy balance at Summit, Greenland

The main energy source for the global climate system is the shortwave energy input from the sun. In Chapter 2 however, it was shown that at Summit, Greenland, the energy gain from shortwave radiation is smaller than the energy loss through longwave emission. The annual net radiation is negative. In this Chapter, the remaining terms of the surface energy balance are discussed: the subsurface heat flux, the sensible heat flux and the latent heat flux. All of these terms were calculated from measured meteorological variables for the time period between June 2001 and July 2002.

3.1 Subsurface heat flux

Subsurface heat flux was determined using temperature measurements from within the firn. Two vertical arrays of temperature measurements were used. One consist of eight thermistors (Campbell Scientific, T107), initially installed in May 2001, at depths of -0.3 m, -0.5 m, -1 m, -2 m, -5 m, -10 m, and -15 m. The depths increased with accumulation. By the end of December 2001, 60 cm of snow had been accumulated, positioning the first thermistor of this thermistor array to a depth of -0.9 m. To monitor the temperatures within the topmost meter of the snowpack at high vertical resolution, a second array of temperature measurements was installed. It consists five thermocouples (Meteolabor). One thermocouple was put directly onto the snow surface, the others were installed at depths of 0.05, 0.1, 0.3 and 0.5 m. The thermocouples were reinstalled at these depths sporadically (August 30th 2001, December 19th 2001, April 28th 2002, July 27th 2002), to allow for an accurate determination of the subsurface heat flux.

The subsurface heat flux is calculated from the rate of change of thermal energy storage in each layer. This method of calculating the subsurface heat flux is possible, as the temperature variation in the maximum measurement depth (15 m) can be neglected. The advantage over the calculation using thermal conductivity is that not only the thermal transport through conduction but also all other processes that lead to a warming or cooling within the firn are included. These processes include the heating of the snow due to the absorption of penetrating shortwave radiation, sensible heat transport within the snow by wind pumping, and sublimation and re-sublimation (latent heat transport) within the snow.

The subsurface heat flux (G) is defined positive if directed towards the surface. It is calculated as

$$G = -c_{ice} \cdot \sum_{i=1}^n \frac{\Delta T(z_i)/\Delta t + \Delta T(z_{i+1})/\Delta t}{2} \cdot \rho_i \cdot (z_i - z_{i+1}). \quad (3.1)$$

Here c_{ice} is the specific heat capacity of ice, $2100 \text{ J kg}^{-1}\text{K}^{-1}$, ρ_i is the mean density of the i th snow layer, z_i the i th height of the temperature measurement ($z_1=0 \text{ m}$, $z_n=-15 \text{ m}$).

The density profile used for the calculations was determined as an approximation to a series of profiles that were observed in the vicinity of the installation site of the temperature profile. The density profile is approximated by two linear sections. To a depth z of -1.5 m density is well represented in units of kg m^{-3} as

$$\rho = 275 - \frac{280}{3}z, \quad (3.2)$$

and below -1.5 m as

$$\rho = 400 - 10z. \quad (3.3)$$

The observed density profiles from several snow pits and from a shallow core, and the approximation for the calculation of subsurface heat flux is shown in Figure 3.1.

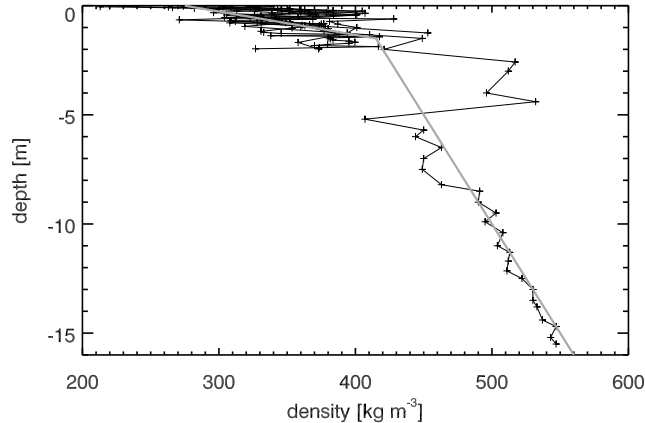


Figure 3.1: Density profiles from measurements in snow pits and from shallow drilling. The thick curve indicates the approximation used for the calculation of the subsurface heat flux.

3.2 Sensible and latent heat flux

Between June 2001 and July 2002, turbulent fluxes of sensible heat H and of latent heat $L_v E$ were measured directly with sonic anemometers (Gill R2) and fast sampling hygrometers (Krypton). In addition to these direct observations, profiles of temperature, humidity and wind speed are available for calculations of the sensible and latent heat fluxes with the profile method: Temperature, humidity and

wind speed were measured at eight levels of a 50 m meteorological tower (0.5, 1, 2, 5, 10, 19, 35 and 49 m). The direct observation of the turbulent fluxes will be the subject of the Ph.D. thesis by Peter Schelander. The sensible and latent heat fluxes presented in this work were derived by the profile method, and may be treated as a first estimate.

Turbulent fluxes of sensible heat H and latent heat $L_v E$ are determined following the parameterization used in the ECHAM4 general circulation model (Roeckner et al., 1996):

$$H = \rho c_p \frac{k^2}{\ln\left(\frac{z}{z_0}\right)^2} f_H \cdot \bar{u} \cdot (\bar{\theta} - \bar{\theta}_s) \quad (3.4)$$

and

$$L_v E = \rho L_v \frac{k^2}{\ln\left(\frac{z}{z_0}\right)^2} f_Q \cdot \bar{u} \cdot (\bar{q} - \bar{q}_s). \quad (3.5)$$

Here, ρ is the air density, c_p specific heat of air at constant pressure, k the von Kármán constant, u the wind speed at height z , θ and θ_s potential temperature at height z and at the surface, q and q_s the specific humidity at height z and the surface, L_v the specific heat of sublimation, g the acceleration of gravity and z_0 the roughness length. The stability functions for heat and water vapor, f_H and f_Q , are expressed as functions of the bulk Richardson number, Ri_b , defined as

$$Ri_b = \frac{gz \cdot (\bar{\theta} - \bar{\theta}_s)}{\bar{\theta} \cdot |\bar{u}|^2}. \quad (3.6)$$

For $Ri_b < 0$, and with z_0 the roughness length for heat,

$$f_{H,Q} = 1 - \frac{10 Ri_b}{1 + 75 C_N \sqrt{-Ri_b \cdot \left(\frac{z}{z_0} + 1\right)}}. \quad (3.7)$$

The neutral transfer coefficient, C_N , is calculated as

$$C_N = \frac{k^2}{\ln\left(\frac{z}{z_0}\right)^2}. \quad (3.8)$$

For stable conditions with $Ri_b \geq 0$, the stability functions for heat and water vapor f_H and f_Q are given as

$$f_{H,Q} = \frac{1}{1 + 15 Ri_b \sqrt{1 + 5 \cdot Ri_b}}. \quad (3.9)$$

For the analysis of the sensible and latent heat fluxes, z is chosen to be 2 m. A value of 0.001 m is used for the roughness length z_0 . For the air at the surface, a relative humidity of 100% is assumed.

3.3 Mean diurnal cycles of the energy balance at Summit, Greenland

Monthly mean diurnal cycles of the energy balance components for the months June to December 2001 are shown in Figure 3.2, the months January to July 2002

in Figure 3.3. The monthly means of the components of the energy balance are summarized in Table 3.1. A seasonal energy balance is given in Table 3.2.

Table 3.1: Monthly energy balance for Summit, Greenland, from measurements between June 2001 and July 2002. All values in Wm^{-2} .

year	month	net radiation	sensible heat flux	latent heat flux	subsurface heat flux	residual
2001	Jun	16	-1	-7	-7	1
2001	Jul	12	-1	-10	-6	-5
2001	Aug	2	1	-3	-4	-4
2001	Sep	-9	6	-3	2	-5
2001	Oct	-18	9	-2	5	-6
2001	Nov	-20	21	0	5	7
2001	Dec	-18	10	1	4	-4
2002	Jan	-18	3	0	9	-6
2002	Feb	-24	20	1	5	2
2002	Mar	-13	18	-1	3	6
2002	Apr	-3	17	-4	-1	9
2002	May	7	4	-7	-7	-2
2002	Jun	16	-1	-11	-9	-5
2002	Jul	18	2	-9	-7	4

Net radiation is positive in the summer months May, June and July. This is the result of a positive net radiation during the larger part of the day, while negative values are observed during the night despite the day-round insolation. The positive net radiation is balanced in equal parts by a negative subsurface heat flux and by a cooling due to sublimation (negative latent heat flux). The subsurface heat flux reaches its minimum around 10 TST and its maximum in the early night (21-22 TST). Latent heat flux is negative throughout the monthly mean diurnal cycle. The energy loss of the surface due to sublimation is greatest at 13 TST. Nevertheless, positive latent heat fluxes are frequently observed during clear summer nights, when rime is deposited at the surface. The monthly means of the sensible heat flux are close to zero in summer, but a strong diurnal variation is observed. While the sensible heat flux is directed towards the surface at night, upward sensible heat fluxes are observed during a great part of the mean summer day, indicating unstable conditions. In July 2001, for example, sensible heat flux was negative for 11 hours (6.30 TST to 17.30 TST). Negative values of sensible heat flux, indicating unstable conditions, are observed as early as in April. An upward mean sensible heat flux was recorded from 10.30 TST to 13.30 TST in April 2002.

In fall, the diurnal cycle of the energy balance quickly decays. In September, net radiation is still positive between 8.30 TST and 14 TST, but the strong cooling at night (negative longwave net radiation) leads to a negative radiation balance. Corresponding to the net radiation, the subsurface heat flux is reduced in amplitude. Starting in October, the terms of the balance show no significant diurnal cycle. The negative net radiation is balanced by a positive sensible and a positive subsurface heat flux. The snowpack releases the heat stored from the summer months back into the atmosphere.

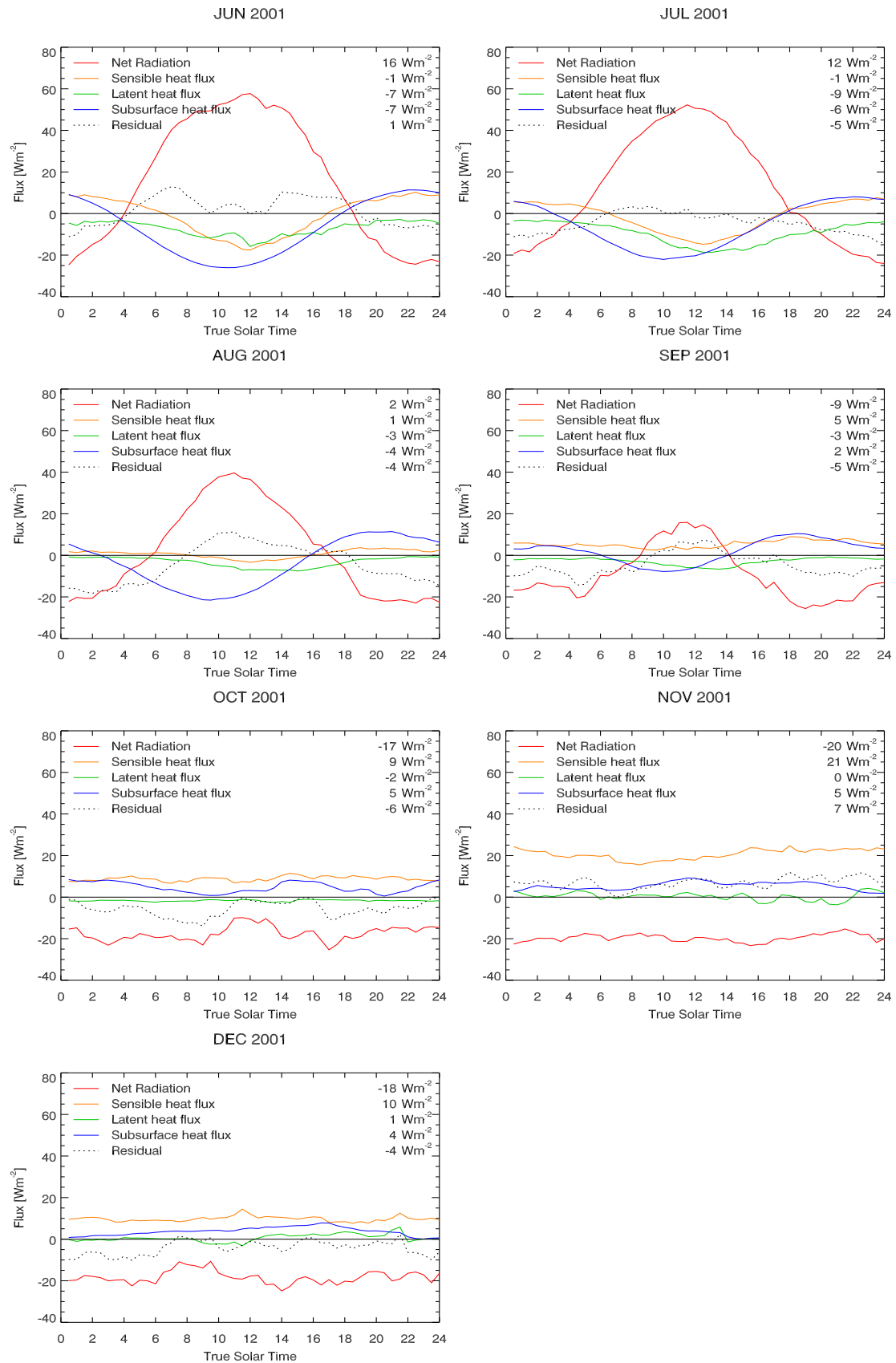


Figure 3.2: Monthly mean diurnal cycles of the energy balance for June to December 2001 at Summit, Greenland. Monthly means of the energy fluxes are given at the right edge of each panel.

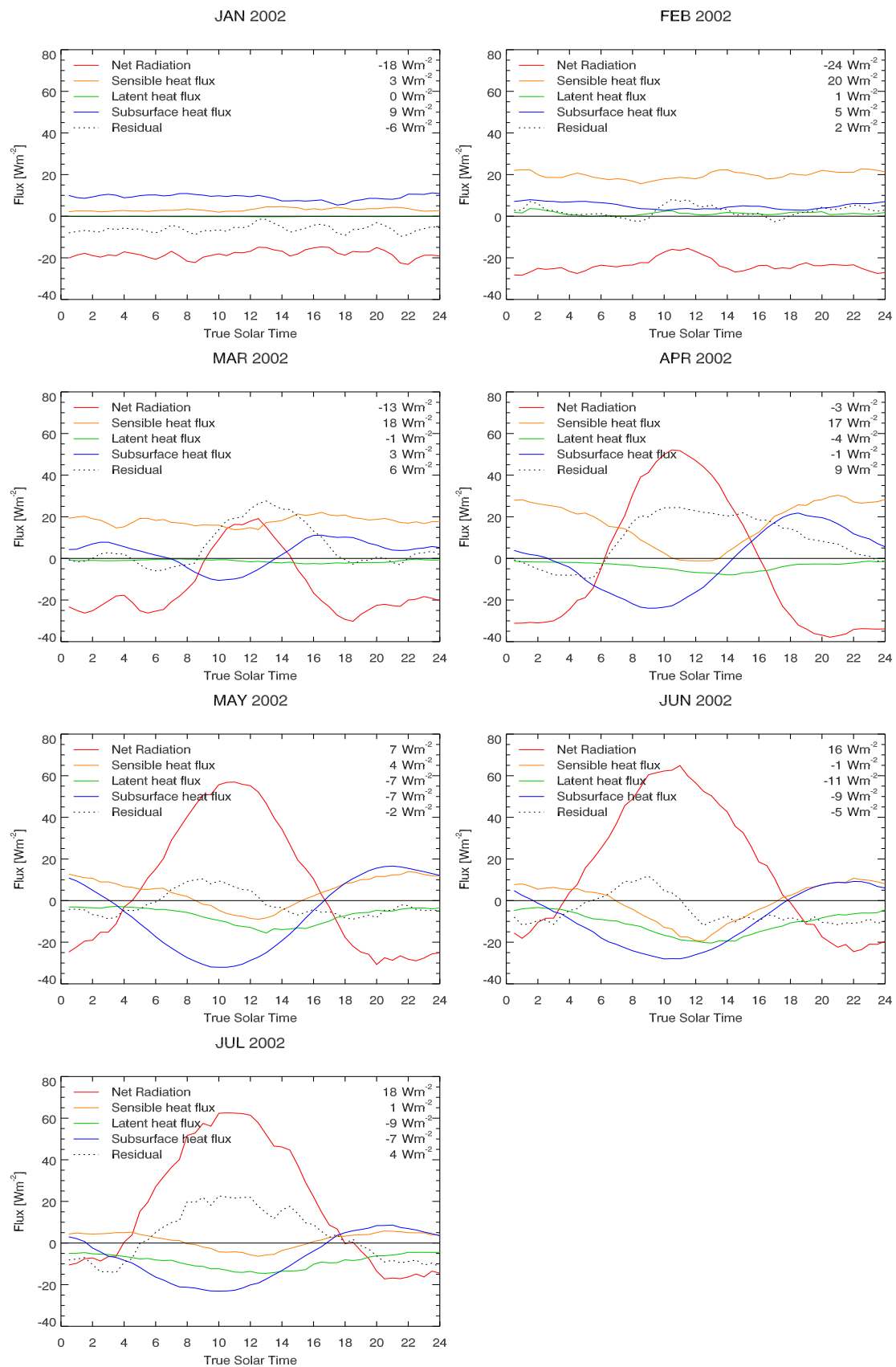


Figure 3.3: Monthly mean diurnal cycles of the energy balance for January to July 2002 at Summit, Greenland. Monthly means of the energy fluxes are given at the right edge of each panel.

Table 3.2: Seasonal energy balance for Summit, Greenland, from measurements between June 2001 and July 2002. All values in Wm^{-2} .

season	net radiation	sensible heat flux	latent heat flux	subsurface heat flux	residual
DJF	-20	12	1	6	-2
MAM	-3	12	-3	-2	4
JJA	11	1	-6	-6	-1
SON	-15	8	-2	4	-6
year	-7	8	-3	1	-1

During the winter months (DJF), no diurnal variation is observed in the energy fluxes. The snow surface is cooled by a negative longwave radiation balance. This cooling is counteracted by a positive sensible and subsurface heat flux. In the winter mean, one third of the negative net radiation is balanced by the subsurface flux, two thirds by sensible heat flux. Latent heat flux is small in winter, but positive monthly mean values (Dec. 2001, Feb. 2002) indicate a deposition of water on the surface.

In spring, the transition from uniform fluxes to fluxes with a strong diurnal cycle occurs. In March, net radiation reaches positive values during 5.5 hours. This variation in the net radiation and the still uniform positive sensible heat flux leads to a warming of the surface in the morning hours, which reflects in a negative subsurface heat flux. In April, a diurnal variation of the sensible heat develops, with a negative sensible heat flux observed around noon.

The residual in the monthly mean energy balance, and its monthly mean diurnal variation, is rather large. A residual as large as 9 Wm^{-2} results in April. In October and January, residuals of -6 Wm^{-2} result. In the annual mean, however, the residual of the energy balance is only -1 Wm^{-2} .

3.4 Energy and mass balance

The seasonal mass balance for Summit, representing the conditions of the dry snow zone of the Greenland ice sheet, is presented in Table 3.3. Melt and mass changes due to snow drift are neglected. The mass balance is measured as the accumulation at the field site. The mass loss due to sublimation is calculated from latent heat flux. In the annual mean 12 % of the mass gain through precipitation is sublimated.

In the summer months, the positive net radiation supplies enough energy to lead to a loss of nearly 30 % of the precipitation. Only due to the fact that the subsurface heat flux acts as a strong sink, an even greater mass loss through sublimation is avoided.

In spring, net radiation is still negative and accumulation is small. Nevertheless, 25 % of the mass gained is lost through sublimation. The necessary energy is provided by a positive sensible heat flux. Early in the year the subsurface flux is still a rather small heat sink. It therefore can not compensate the high energy input from the sensible heat flux.

In fall, almost 40 % of the annual precipitation is observed. Then, the percentage of mass loss due to sublimation is small, as net radiation is negative and acts as a strong heat sink for the energy supplied by the positive sensible and subsurface heat fluxes.

During the winter months, the negative radiation balance is mainly compensated by a positive sensible and subsurface heat flux. But even the latent heat flux contributes to this compensation. In the winter mean, it is directed towards the surface, and a small mass gain through resublimation results.

Table 3.3: Seasonal mass balance for Summit, Greenland, from measurements between June 2001 and July 2002.

season 2001/02	precipitation (P) [mmWE]	sublimation (E) [mmWE]	mass balance (M) [mmWE]
DJF	62	-1	63
MAM	41	11	30
JJA	69	20	50
SON	103	4	99
year	275	34	242

Part III

Radiative flux divergence

4 Introduction

The surface boundary layer reacts much faster to changes in the surface energy balance than the ground. While the subsurface temperatures are mainly influenced by conduction, air temperature is controlled by several processes. To understand these processes that lead to a temporal evolution of the temperature profile and to its vertical structure is one of the key goals in meteorology. The rate of change of temperature can be expressed as:

$$\frac{\partial T}{\partial t} + v_j \frac{\partial T}{\partial x_j} = \nu_T \frac{\partial^2 T}{\partial x_j^2} - \frac{1}{\rho c_p} \left(\frac{\partial Q_j}{\partial x_j} \right). \quad (4.1)$$

Here, T is the temperature, t the time, v_j the wind in the j th direction x_j , ρ the air density, c_p specific heat of air at constant pressure and ν_T the thermal diffusivity. Q_j is the sum of the energy fluxes of shortwave radiation, longwave radiation, sensible and latent heat.

If the net fluxes of the quantities contained in Q_i are known relative to the horizontal surface, and neglecting thermal diffusion, temperature change can be expressed in terms of the vertical divergence of these net fluxes,

$$\frac{\partial T}{\partial t} + \vec{v} \nabla T = -\frac{1}{\rho c_p} \left(\frac{\partial NR}{\partial z} + \frac{\partial H}{\partial z} + \frac{\partial L_v E}{\partial z} \right). \quad (4.2)$$

Here, NR is the net radiation, H the sensible heat flux and $L_v E$ the latent heat flux.

Neglecting horizontal advection, convection and phase changes, two divergence terms remain that control the evolution of temperature: radiative flux divergence and sensible heat flux divergence. Both processes depend upon and influence the vertical distribution of temperature. Therefore, they can not readily be separated (Kondratyev, 1969). One of the unsolved problems in micrometeorology is the determination of the relative influence of radiative flux divergence and sensible heat flux divergence. The questions raised are: How do, under different conditions, radiative flux divergence and sensible heat flux divergence influence the temporal evolution of the air temperature? How does their influence vary with height? What is the diurnal cycle of heating due to the two components? When and where are they important?

Investigations of the role of radiative flux divergence started with theoretical approaches, before instruments had been developed to measure radiative fluxes with sufficient accuracy. The influence of the divergence of sensible heat flux was mostly determined by calculations or by limited measurements combined with turbulent

heat transfer theory. In many studies, radiative fluxes were calculated and the divergence of the sensible heat flux was determined as the difference to the observed temperature tendency, neglecting other processes such as advection.

The different studies summarized in the following paragraphs all deal with radiative flux divergence in the surface layer or the atmospheric boundary layer. Investigations range from model studies of persistent Antarctic wintertime inversions (Cerni and Parish, 1984) to observations under unstable conditions over dry-steppe during daytime in summer (Eliseev et al., 2002).

Measurements of radiative flux divergence became possible with the development of the first radiometers with sufficient sensitivity. The first observations of radiative flux divergence were performed with polythene-shielded net radiometers by Funk (1960). His measurements were taken over grass at heights between 1 m and 11 m at night and reached values of typically 120 Kd^{-1} (Funk, 1960; Funk, 1962). Stronger cooling was observed at higher levels (2-4 m) than at lower ones (1-2 m). Gaevskaya et al. (1963) reported on measurements using net radiometers in an air layer between 1 m and 8 m over steppe. Tremendous daytime radiative heating rates (1000 Kd^{-1}) and nighttime radiative cooling rates (-400 Kd^{-1}) were recorded. Disagreement between measured radiative flux divergence and calculations with radiation charts were reported by both authors, Funk and Gaevskaya. The first measurements of radiative flux divergence over a snow surface were carried out by Lieske and Stroschein (1967) at Barrow, Alaska. They found experimental evidence for radiative heating close to the surface during stable clear nights. Heating rates of up to 120 Kd^{-1} were observed at a height of 1.5 m. These observations contradicted their calculations with radiation charts, but are in line with the theoretical considerations of Fleagle (1953). Timanovskaya and Faraponova (1967) were the first to measure the vertical gradients of all four components of the radiation balance (shortwave and longwave radiation, incoming and outgoing components). Their measurements at 1 m and 8 m above dry steppe cover the entire diurnal cycle. The relative importance of the divergence of the outgoing longwave flux is seen in their analysis, as well as its cooling effect at nighttime and heating effect during the day. Fuggle and Oke (1976) and Nunez and Oke (1976) conducted measurements of radiative flux divergence in an urban environment. They reported a correlation between wind gradient and radiative cooling. Nkemdirim (1978) measured longwave radiative flux divergence between 1 m and 3 m over both grass and snow surfaces. Over snow, radiative cooling between 15 LT (local time) and 23 LT was found to be about twice as large (-100 Kd^{-1}) as over grass (-60 Kd^{-1}). Over both surfaces, radiative cooling exceeded the observed temperature tendency. Eliseev et al. (2002) presented observations of longwave radiative flux divergence from flux measurements with an optoacoustic receiver. Some of the measurements, taken in 1981 over dry steppe, resolve longwave fluxes very close to the surface (0.1 m, 0.5 m, 2 and 6 m). Between 0.5 m and 2 m, daytime longwave radiative heating rates of 240 Kd^{-1} were observed. Closer to the ground (0.02 m-0.1 m), heating due to a convergence of the outgoing longwave flux of 1500 Kd^{-1} were measured. During the 1999 Cooperative Atmosphere-Surface Exchange Study experiment (CASES-99), Sun et al. (2003) measured longwave divergence between 2 m and 48 m. They reported cooling in this bulk layer due to divergence of outgoing flux and slight heating due to convergence of incoming longwave flux. This is

in qualitative agreement with the measurements of Timanovskaya and Faraponova (1967). Maximum cooling in this bulk layer between 2 m and 48 m was found in the early evenings, and amounted to typically 24 Kd^{-1} .

Due to the difficulty of measurements, radiative fluxes and their divergence were often calculated. These calculations range from rather theoretical considerations such as the work by Fleagle (1953) to calculations with narrow band radiative transfer models like those presented by Tjemkes and Duynkerke (1989). In the following paragraph, a short overview is given over selected studies that have focused on the calculation of longwave radiative flux divergence.

In an investigation on fog formation, Fleagle (1953) presented a calculation of longwave radiative heating rates in the lowest 10 m of the atmosphere. He showed that a negative radiative flux divergence above a cold black-body surface leads to a heating of the air just above the surface (lowest 1 m). If the surface is warmer than the atmosphere, a cooling results. Above this shallow near-surface layer, the sign changes, and a clear air radiative cooling (warming) is predicted above the cold (warm) surface. Numerous researchers calculated radiative divergence from radiation charts (Funk, 1960; Gaevskaya et al., 1963; Elliott, 1964; Lieske and Stroschein, 1967; Faraponova, 1969; Kondo, 1971) or used the formulation presented by Funk (1961). In many of these studies, divergence of the sensible heat flux ('turbulent cooling') was calculated from the observed temperature change and the calculated radiative heating rates. Kondo (1971) illustrated the diurnal cycle of radiative heating rates in the lowest 100 m of the boundary layer. Coantic and Seguin (1971) used an emissivity model to calculate radiative divergence over water. Garratt and Brost (1981) calculated the radiative flux divergence over the entire height of the nocturnal boundary layer using an emissivity approach in their radiative transfer calculations. They stressed the importance of the radiative processes and pointed out that many boundary layer models still neglect radiative cooling effects. In their analysis, a 3-layer structure was identified. Radiative cooling was shown to dominate in the lowest tenth and the topmost two tenths of the stable nocturnal boundary layer. In the layer in between, radiative cooling was reported to be small, while cooling was dominated by turbulence. André and Mahrt (1982) analyzed data from the Wangara and Voves experiments. Radiation fluxes were modeled using the emissivity approach. They identified two layers of the nocturnal boundary layer. The lower layer is strongly stratified but turbulent. In the upper and thicker layer, cooling is generated mainly by the divergence of the longwave radiative flux. As in the calculations by Kondo (1971) and Coantic and Seguin (1971), a shallow layer of radiative heating results near the surface under stable conditions. The most important effect of longwave radiative flux divergence was found to be a reduction of the temperature gradient over the nocturnal boundary layer. This effect leads to less stable but thicker inversions. Cerni and Parish (1984) developed a gray-body radiative model for the stable nocturnal boundary layer. With this model, they were able to simulate the formation of the strong surface inversions observed in Antarctica. Estournel and Guedalia (1985) investigated nocturnal cooling during the ECLATS experiment in the African Sahel. They calculated radiative fluxes with a high spectral resolution model. Neglecting the lowest 10 m, they concluded that cooling in the inversion layer is essentially due to turbulent cooling. Carlson and Stull (1986)

attributed the cooling in the lowest third of the nocturnal boundary layer mainly to turbulence. In the top third, they estimated the contribution of radiative, turbulent and subsidence cooling to be of equal magnitude. Gopalakrishnan et al. (1998) used a boundary layer model and an emissivity approach for the calculation of radiative cooling rates. They modeled the stable boundary layer under weak and strong wind conditions. The same 3-layer structure as reported by Garratt and Brost (1981) could be observed. Räisänen (1996) compared two radiation schemes that are used in numerical weather forecast models. His model experiments showed the high importance of vertical resolution on radiative heating rate calculations. Tjemkes and Duynkerke (1989) used a narrow band model with 178 spectral bands to model the longwave fluxes and radiative heating rates in the nocturnal boundary layer. Maximum cooling in near surface layers of -100 Kd^{-1} resulted. They concluded that sensible heat fluxes must thus converge in this surface near layer, and must have a maximum just above the surface. In the lowest 10% of the boundary layer they judged the radiative cooling to be at least as important as the turbulent cooling. Above the lowest 10% and below 80% of the boundary layer height, they found that radiative cooling is of minor importance (less than 20% of cooling). This is in good agreement with the findings of Garratt and Brost (1981). Ha and Mahrt (2003) used the column radiation model of the Community Climate Model (emissivity approach in the longwave spectral region) to calculate radiative cooling during the CASES-99 experiment. They concluded that radiative flux divergence is the primary contributor to the initial formation of the nocturnal surface inversion.

Although there are agreements between some of the different studies summarized above, differences become obvious as well. Theoretical considerations and some model calculations showed a sign change of the radiative heating rate above cold or warm surfaces. A cooling above warm, and a heating over cold surfaces is indicated. This was confirmed by measurements above snow (Lieske and Stroschein, 1967). On the other hand, this pattern was not supported by the measurements of Eliseev et al. (2002), who was able to measure radiative fluxes very close to the surface, nor by the high spectral resolution calculations of Tjemkes and Duynkerke (1989).

The relative importance of the two cooling components, radiative and turbulent, for the formation of inversions is also still under discussion. Estournel and Guedalia (1985) attribute inversion formation to turbulent cooling, Tjemkes and Duynkerke (1989) judge the radiative influence to be equally large as the turbulent, and Ha and Mahrt (2003) identify radiative flux divergence to be the primary contributor to inversion formation.

Clean data are necessary to resolve the open questions. Aim of the present work was to collect longwave fluxes with the highest accuracy possible to obtain longwave radiative flux divergence in the lowest atmospheric layers. The site for the field experiment was chosen to allow highly accurate measurements of sensible heat flux divergence. The dry snow zone of the Greenland ice sheet, with its smooth surface, has a practically unlimited fetch. The frequent occurrence of strong stratifications at night and of neutral to slightly unstable conditions during the midday hours in summer allows a fundamental analysis of flux divergence under all stratifications.

Radiative flux divergence between 2 m and approximately 50 m was measured for an entire year, covering all seasons and meteorological conditions that can be met at

a high arctic site. In addition, a more detailed profile of longwave radiative flux divergence was obtained in the summer 2002 field season, with two additional levels of flux measurements. Longwave radiative flux divergence was observed in three layers, in a variety of conditions of cloud cover, wind field and temperature stratification. During intensive observational phases, a mobile boom on the tower allowed flux measurements at two additional levels. Heating rates at up to five layers between the surface and 50 m could be determined. The detailed profiles of longwave radiative heating offers a unique dataset and the possibility to investigate the influence of longwave radiative flux divergence on the evolution of the temperature profile.

4.1 Fluxes, divergence and heating: Definitions

In order to assign positive numbers to fluxes directed *towards* the surface the z -axis of our coordinate system is pointing towards the surface. Incoming or down-welling fluxes are always positive numbers, outgoing or up-welling fluxes are always negative. Net flux is positive when directed towards the surface and is calculated as the sum of the incoming and outgoing fluxes.

$$F_{net} = F_{in} + F_{out}. \quad (4.3)$$

A positive divergence of a heat flux results in a cooling. When, for example, more radiation leaves an air parcel than is entering it, the air cools. With the sign convention above, and F only depending on z , divergence of the net flux becomes

$$\nabla \cdot F_{net} = \frac{\partial F_{net}}{\partial z} = \frac{\partial F_{in}}{\partial z} + \frac{\partial F_{out}}{\partial z}. \quad (4.4)$$

Flux divergence is usually expressed in units of Wm^{-3} . However, divergence can also be expressed as a heating rate in units of K s^{-1} or K d^{-1} . With LW the net longwave flux, the longwave radiative flux divergence is

$$\left(\frac{\partial T}{\partial t} \right)_{rad,LW} = -\frac{1}{\rho c_p} \frac{\partial LW}{\partial z}, \quad (4.5)$$

with ρ the density and c_p the specific heat of air at constant pressure.

In the following, the terms 'radiative flux divergence' and 'radiative heating rate' are used for the same phenomenon. The change of the radiative flux with height leads to a change in the temperature profile. The first term expresses the physical process in a comprehensive way, while the second is more applicable when the discussion is focused on the evolution of the temperature in the atmosphere.

4.2 Shortwave and longwave radiative flux divergence

The radiative flux divergence term in Equation 4.2 can be separated into a longwave and a shortwave component,

$$\frac{\partial NR}{\partial z} = \frac{\partial SW_{net}}{\partial z} + \frac{\partial LW_{net}}{\partial z}. \quad (4.6)$$

The change of the net shortwave radiative flux with height does not vary much in the surface boundary layer, as the transmissivity of the air shows little change in the shortwave spectrum. The shortwave radiative flux divergence is therefore rather constant with height, and the shortwave radiative heating is vertically equally distributed. To roughly evaluate the shortwave contribution to radiative flux divergence, radiative heating due to the absorption of shortwave radiation in the lower part of the boundary layer was estimated using a simple parameterization based on model calculation results. This analysis in the shortwave spectral region is presented in Appendix A. Values for shortwave radiative flux divergence on a clear sky summer day at Summit in Greenland range between zero and -0.04 Wm^{-3} (4 K d^{-1}).

The longwave radiative flux, however, strongly depends on the vertical temperature profile and shows a strong variation with height. It is capable to influence the structure of the temperature profile.

For these reasons, the longwave component of radiative flux divergence is of primary interest and lies in the focus of this work.

4.3 Infrared radiative transfer

In this section the basic equations of infrared radiative transfer are introduced, following closely Liou (1987), Liou (1992) and Stephens (1984). The sign convention of the authors (all fluxes positive) is kept.

Radiation traversing a medium is weakened by its interaction with matter. Intensity I_ν becomes $I_\nu + dI_\nu$ after traveling through a thickness ds in the direction of its propagation. With the density of the attenuating material ρ , and k_ν the mass extinction cross section and J_ν the source function in units of radiant intensity

$$\frac{dI_\nu}{k_\nu \rho ds} = -I_\nu + J_\nu. \quad (4.7)$$

In a non-scattering medium, a beam of intensity I_ν will be attenuated due to absorption and will increase due to emission from the medium. The source function is then given by the Planck function $B_\nu(T)$. The equation of transfer is then:

$$\frac{dI_\nu}{k_\nu \rho ds} = -I_\nu + B_\nu(T). \quad (4.8)$$

This equation is also called Schwarzschild's equation. We define the monochromatic optical thickness of the medium between two points s and s_1 as

$$\tau_\nu(s, s_1) = \int_s^{s_1} k_\nu \rho ds. \quad (4.9)$$

As

$$d\tau_\nu = -k_\nu \rho ds, \quad (4.10)$$

we can now write

$$-\frac{dI_\nu(s)}{d\tau_\nu} = -I_\nu(s) + B_\nu(T(s)). \quad (4.11)$$

Multiplying both sides with $e^{-\tau_\nu(s_1, s)}$ and integrating ds from 0 to s_1 , we get after rearrangement,

$$I_\nu(s_1) = I_\nu(0)e^{-\tau_\nu(s_1, 0)} + \int_0^{s_1} B_\nu[T(s)]e^{-\tau_\nu(s_1, s)}k_\nu\rho ds. \quad (4.12)$$

The first term on the right hand side represents the absorption attenuation, the second term the emission contribution along the path from 0 to s_1 .

Plane-parallel atmospheres

In plane-parallel atmospheres, with z the linear distance normal to the plane of stratification, θ the inclination to the upward normal (zenith angle) and ϕ the azimuth, the general equation of transfer is

$$\cos\theta\frac{dI(z; \theta, \phi)}{k\rho dz} = -I(z; \theta, \phi) + J(z; \theta, \phi). \quad (4.13)$$

Omitting the subscript ν and with the normal optical thickness

$$\tau = \int_z^\infty k\rho dz', \quad d\tau = -k\rho dz, \quad (4.14)$$

measured from the outer boundary downward, and with $\mu = \cos\theta$,

$$\mu\frac{dI(\tau; \mu, \phi)}{d\tau} = I(\tau; \mu, \phi) - J(\tau; \mu, \phi). \quad (4.15)$$

This equation can be solved to yield upward and downward intensities for a finite atmosphere bounded on two sides at $\tau = 0$ and $\tau = \tau_1$. The upward intensity ($\mu > 0$) at level τ is obtained multiplying by the factor $e^{-\tau/\mu}$ and integrating from τ to $\tau = \tau_1$:

$$I(\tau; \mu, \phi) = I(\tau_1; \mu, \phi)e^{-(\tau_1-\tau)/\mu} + \int_\tau^{\tau_1} J(\tau'; \mu, \phi)e^{-(\tau'-\tau)/\mu}\frac{d\tau'}{\mu}. \quad (1 \geq \mu > 0) \quad (4.16)$$

To get the downward intensity ($\mu < 0$) at level τ , a factor $e^{\tau/\mu}$ is used and μ is replaced with $-\mu$. Integrating from $\tau = 0$ to τ , we get

$$I(\tau; -\mu, \phi) = I(0; -\mu, \phi)e^{-\tau/\mu} + \int_0^\tau J(\tau'; -\mu, \phi)e^{-(\tau-\tau')/\mu}\frac{d\tau'}{\mu}. \quad (1 \geq \mu > 0) \quad (4.17)$$

A non-scattering plane-parallel atmosphere at local thermodynamic equilibrium is considered, and the assumption is made that thermal infrared radiation from the atmosphere is independent of the azimuthal angle ϕ . The source function being given as the Planck function, we get the solutions for the upward and downward intensities as

$$I_\nu(\tau, \mu) = I_\nu(\tau_1, \mu)e^{-(\tau_1-\tau)/\mu} + \int_\tau^{\tau_1} B_\nu[T(\tau')]e^{-(\tau'-\tau)/\mu}\frac{d\tau'}{\mu}, \quad (4.18)$$

$$I_\nu(\tau, -\mu) = I_\nu(0, -\mu)e^{-\tau/\mu} + \int_0^\tau B_\nu[T(\tau')]e^{-(\tau-\tau')/\mu}\frac{d\tau'}{\mu}. \quad (4.19)$$

At the base of the atmosphere, upward radiation arises from the emission of the surface, only. The surface is approximated as a black body, $I_\nu(\tau_1, \mu) = B_\nu(T_s)$ where T_s is the surface temperature. At the top of the cloud-free atmosphere ($\tau = 0$), there is no down-welling radiation and we have $I_\nu(0, -\mu) = B_\nu(TOA) = 0$. Now, the upward and downward monochromatic irradiances can be given as

$$F_\nu^\uparrow(\tau) = 2\pi B_\nu(T_s) \int_0^1 e^{-(\tau_1-\tau)/\mu} \mu d\mu + 2\pi \int_0^1 \int_\tau^{\tau_1} B_\nu[T(\tau')] e^{-(\tau'-\tau)/\mu} d\tau' d\mu, \quad (4.20)$$

$$F_\nu^\downarrow(\tau) = 2\pi \int_0^1 \int_0^\tau B_\nu[T(\tau')] e^{-(\tau-\tau')/\mu} d\tau' d\mu. \quad (4.21)$$

Transmission functions

Now, we want to express the flux as function of z instead of τ . With $k_\nu(p, T)$ the absorption coefficient (function of temperature T and pressure p), u the concentration of the attenuating gas defined along a path from z to z' and $\mu = \cos\theta$ the cosine of the zenith angle, the transmittance function \mathcal{T}_ν can be defined in order to express exponential attenuation as (Stephens, 1984)

$$\mathcal{T}_\nu(z, z', \mu) = \exp\left[-\frac{1}{\mu} \int_{u(z)}^{u(z')} k_\nu(p, T) du\right]. \quad (4.22)$$

We are interested in heating rate calculations, and need the upward and downward fluxes, that are the sums of the upward and downward intensities from the two hemispheres. The parameter *slab transmission* or *diffuse transmission* is defined, in order to obtain the fluxes, as

$$\mathcal{T}_\nu^f(z, z') = 2 \int_0^1 \mathcal{T}_\nu(z, z', \mu) \mu d\mu. \quad (4.23)$$

The total flux is then

$$F^\uparrow(z) = \int_0^\infty \pi B_\nu(z=0) \mathcal{T}_\nu^f(z, 0) d\nu + \int_0^\infty \int_0^z \pi B_\nu(z') \frac{d\mathcal{T}_\nu^f}{dz'}(z, z') dz' d\nu, \quad (4.24)$$

$$F^\downarrow(z) = \int_0^\infty \int_z^\infty \pi B_\nu(z') \frac{d\mathcal{T}_\nu^f}{dz'}(z, z') dz' d\nu. \quad (4.25)$$

These equations can also be written as

$$F^\uparrow(z) = \pi \int_0^\infty B_\nu(z=0) \mathcal{T}_\nu^f(z, 0) d\nu + \pi \int_0^\infty \int_{\mathcal{T}_\nu^f(z,0)}^{\mathcal{T}_\nu^f(z,z)} B_\nu(z) d\mathcal{T}_\nu^f(z, z') d\nu, \quad (4.26)$$

$$F^\downarrow(z) = \pi \int_0^\infty \int_{\mathcal{T}_\nu^f(z,z)}^{\mathcal{T}_\nu^f(z,\infty)} B_\nu(z) d\mathcal{T}_\nu^f(z, z') d\nu. \quad (4.27)$$

Four integrals are nested within the equations for longwave radiative transfer. One refers to the integration over all zenith angles and is included in the definition

of the slab transmission function, Equation 4.23. The second integral refers to the summation of the contributions of all the layers dz' to the flux at layer z . The third integration is over the spectral interval $d\nu$. The fourth integration is over the absorption path u in Equation 4.22 (Stephens, 1984).

The first integral is adequately solved by introducing the slab transmission. The approximation is made that the transmission of a flux can be represented by the transmission of a beam along the direction defined by a representative zenith angle. The problem of the parameterizations of infrared radiation are the approximations for the integration over the path and over the wavelength.

Integrations of absorption over the optical path is complicated by the fact that k_ν depends on pressure and temperature and that the path through the atmosphere is not homogeneous. Different approximations try to describe the absorption along an inhomogeneous path as an absorption along a homogeneous path with adjusted pressures and temperatures. Such approximations include the scaling approximation and the two parameter approximations (e.g. Curtis-Godson approximation).

The integration of absorption over frequency is complicated, as there are different frequency scales contained within the integral in Equations 4.24 and 4.25. One scale is the slow variation of the Planck curve, one the unresolved contour of the absorption band. For most gases, the Planck function can be treated as a constant with frequency for each band. For water vapor, the absorption lines need to be subdivided into smaller intervals, however. The next smaller scale is associated with the separation of individual absorption lines. On the smallest scale, Lambert's law of absorption applies. On this smallest scale, the exponential transmission functions and hence Equations 4.24 and 4.25 are valid.

Band models

To calculate broadband fluxes, two methods can be used. One is to resolve the variation of the Planck function into discrete intervals and to define a mean absorption for each interval. Band models such as the "random model" of Goody (1952) are an example for this approach. Rodgers and Walshaw (1966) apply this model with 21 frequency bands. Their calculation of fluxes and radiative cooling rates are often used as benchmarks for cooling rate calculations with simpler radiation schemes (Stephens, 1984; Savijärvi, 1990).

Wu (1980) used a similar model to calculate spectral heating rates in 3 km thick layers of a tropical model atmosphere. With these calculations, he showed that the true energy exchange between layers does not happen in the strong regions of the absorption bands, but rather in the wings of strong lines, in the center regions of moderately weak lines, and in the water vapor continuum.

The k distribution method

A newer approach to solve the problem of frequency integration is the *k distribution method*. It is based on an idea of Ambartsumian (1936) and was introduced by

Arking and Grossman (1972). Chou and Arking (1980) used this method for computations of infrared cooling in the water vapor bands. The method is summarized below following Stephens (1984). For a homogeneous atmosphere, the transmission within a quite wide spectral interval is independent of the ordering of k with respect to ν . Transmission depends more on the fraction of the interval which is associated with a particular value of k . This fraction is a probability density function defined that $f(k)dk$ is the fraction of the frequency interval for which the absorption coefficient lies between k and $k + dk$. The integration of the absorption coefficient k_ν over ν can be replaced by the integration of $f(k)$ over k . The calculations of Chou and Arking (1980) using this approach proved to be better than the band model approach by Rodgers and Walshaw (1966). Compared to line-by-line calculations, the error was reduced by a factor of two, and computations were an order of magnitude faster (Chou and Arking, 1980; Stephens, 1984).

The broadband flux emissivity method

In the broadband emissivity methods, the integration over the frequency domain is done once and for all. An emissivity function is derived by integrating the absorption over frequency and weighting it with the Planck function. This reduces computational time, but introduces certain errors (Stephens, 1984).

If we define an absorptivity of the gas as $\mathcal{A}_\nu = 1 - \mathcal{T}_\nu^f$ we can write the flux equations as

$$F^\uparrow(z) = \int_0^\infty B_\nu(z=0)[1 - \mathcal{A}_\nu(z, z=0)]d\nu + \int_0^\infty \int_0^z \pi B_\nu(z') \frac{d\mathcal{A}_\nu}{dz'}(z, z') dz' d\nu \quad (4.28)$$

and

$$F^\downarrow(z) = \int_0^\infty \int_z^\infty \pi B_\nu(z') \frac{d\mathcal{A}_\nu}{dz'}(z, z') dz' d\nu. \quad (4.29)$$

Defining the flux emissivity ϵ along the path from z to z' as

$$\epsilon(z, z') = \frac{1}{\sigma T^4} \int_0^\infty \mathcal{A}_\nu(z, z') \pi B_\nu(T) d\nu, \quad (4.30)$$

with σ the Stefan-Boltzmann constant, T_g the ground temperature, and neglecting longwave reflectivity of the ground, the flux equations become

$$F^\uparrow(z) = \sigma T_g^4(1 - \epsilon(z, 0)) + \int_0^z \sigma T^4(z') \frac{d\epsilon}{dz'}(z, z') dz' \quad (4.31)$$

and

$$F^\downarrow(z) = \int_z^\infty \sigma T^4(z') \frac{d\epsilon}{dz'}(z, z') dz'. \quad (4.32)$$

Savijärvi (1990) gives an overview over the broadband emissivity methods. A general problem of longwave broadband radiation schemes is that $d\epsilon/dz$ is not very well known. Some values are based on band model calculations for water vapor e.g. Elsasser (1942) and Yamamoto (1952). Often, the values compiled by Staley and Jurica (1970) are used. Differences in the ϵ values of different authors arise,

as some correct for the spectral overlap of the absorption of H₂O and CO₂, and others do not. Usually, the absorption in the continuum region, and the contribution of other absorbers as methane and ozone, is not included. The absorption in the continuum region however, has been proven to be especially important for cooling rate calculations close to the surface (Wu, 1980). When the down-welling radiation is calculated with the broadband methods, the fluxes obtained are much smaller than those observed in measurements. The reason for the low values lies mainly in the missing representation of the water vapor continuum, and of other gases and aerosols. Differences between the model calculations and observations are large, especially close to the surface (Luther et al., 1988).

The broadband methods do have the advantage of good computational performance. Therefore, the effects of longwave radiative heating on the temperature evolution were often evaluated with such simplified models (Coantic and Seguin, 1971; Garratt and Brost, 1981; André and Mahrt, 1982; Cerni and Parish, 1984). However, the drawbacks of the use of these models are the reductions in accuracy of the modeled fluxes and heating rates. Even the state-of-the-art climate models such as ECHAM and HadAM, and in the radiative transfer calculations included in the ERA Reanalysis reveal problems in the calculation of longwave fluxes when compared to measured fluxes (Wild et al., 2001).

In this work, computational time is not a limiting factor, as the model is only used to calculate fluxes and heating rates for particular situations for which detailed measurements of the necessary input variables as temperature and humidity are available. Here, the aim is to compare the measurements of fluxes, and the radiative heating inferred from those, to model calculations that are as accurate as possible. Therefore, the radiative transfer model MODTRAN was chosen for the calculations of longwave fluxes and heating rates at our field site. A brief introduction on this model is given in Section 6.1, after presenting the observational results.

5 Measurements of longwave radiative flux divergence

5.1 Experimental setup

The experimental setup is designed to allow measurements of longwave fluxes with high accuracy at different heights above the surface. The divergence of the longwave fluxes is then determined for the layers between the measurement heights.

The core installation for the measurements is the 50 m meteorological tower. It forms the stable platform for the measurements of longwave fluxes and of other meteorological variables such as temperature, humidity and wind speed. The setup for the pyrgeometers is identical for all instruments involved in the measurement campaign. All instruments are mounted in a distance of 1.25 m from the main tower structure and are ventilated with slightly heated air. The number of instruments and their deployment heights on the tower, however, were varied over the 14-month period of the experiment.

In the following sections, the deployments patterns of the instruments are presented. The pattern varied from a simple bulk measurement between 2 m and 50 m to a detailed monitoring of the longwave flux profile. An introduction is given to the pyrgeometer type used for our observations, and the relative calibration of the instruments is thoroughly discussed. After presenting a method to correct the influence of the tower structure on the measurements, the data reduction and analysis is described.

5.1.1 Deployments patterns

Bulk measurement between 2 m and 50 m

Measurements of the longwave flux profile started in June 2001. In the first period which lasted until May 2002, two levels of the 50 m meteorological tower were equipped with pairs of pyrgeometers. During this time, the bulk longwave radiative flux divergence between 2 m and the 50 m level was measured. As these measurements cover all seasons and the full range of meteorological conditions, an annual climatology of longwave flux divergence can be compiled from these measurements. Results and analysis of this dataset are presented in Section 5.2.7.

Three-layer profile

In May 2002, two additional horizontal booms equipped with pairs of pyrgeometers were installed at the tower. They were fixed at the heights of 0.5 m and 10 m above the snow surface. For the summer season 2002, the divergence of the longwave radiative fluxes is available for the three layers 0.5 m-2 m, 2 m-10 m and 10 m-50 m at all times.

Intensive Observation Periods (IOPs)

During intensive observation periods (IOP) in the 2002 summer field season, a mobile boom equipped with a pair of pyrgeometers was used to sample longwave fluxes at two additional levels (20 m and 35 m). During these periods, divergence of the longwave radiative flux was recorded additionally in the layers 10 m-20 m, 20 m-35 m and 35 m-50 m. During an IOP, divergence could therefore be determined for a total of five layers. However, IOP measurements were limited to selected time intervals and could not cover all meteorological conditions. Especially situations with strong winds could not be probed, to avoid damage of the power and data cables to the instruments of the mobile instruments.

5.1.2 Instrument setup

The pyrgeometer is mounted on a round steel plate, which has an opening with the diameter of the ventilator. The pyrgeometer can be leveled relative to the steel plate. A dome shaped radiation shield covers the instrument. Only a thin gap between the pyrgeometer dome and the radiation shield remains, through which the ventilation air is forced over the dome of the instrument. A heating coil in the upper part of the radiation shield, or a heating element glued to the base plate, heats the ventilation air slightly above ambient temperature. This helps to keep the dome of the instrument free of rime. The axial ventilator under the steel plate is then mounted on an rectangular aluminum tube. The two openings of the rectangular tube form the intake for the ventilation air. A filter material is used in the intakes to avoid rime deposition in the inside of the tube, ventilator or instrument cover. The rectangular tube with the connected instrument is then attached to a horizontal boom on the meteorological tower. The distance of the instrument from the tower is 1.25 m. Two instruments are attached to each boom, one facing down to measure the up-welling or outgoing longwave flux, the other facing up to monitor the down-welling or incoming longwave flux. Pyrgeometers were not shaded from the direct beam of solar radiation. A correction for the 'shortwave leaking' needs to be applied (c.f. Section 5.1.3).

5.1.3 Instrumentation: Pyrgeometers and their calibration

The pyrgeometer

One of the most commonly used pyrgeometers for measuring longwave incoming and outgoing radiation is the Eppley Precision Infrared Radiometer (PIR). It was developed from the Eppley Precision Spectral Pyranometer (PSP), replacing the glass domes with a dome transparent only to the longwave range: at first, a dome of KRS-5 glass and since 1976, a silicon dome with a vapor deposited low-pass interference filter is used (Drummond et al., 1970; Weiss, 1981). This dome transmits about 20-40 % in the frequency range between 3.5-50 μm (Miscolczi and Guzzi, 1995). The thermopile signal results from the temperature difference between the black thermopile sensor exposed to the transmitted radiation and the reference junction which is in contact with the instrument's body. It is proportional to the net radiation loss of the sensor surface. Performance of the instrument was improved by several modifications. One of them is to disable the thermistor-battery-resistance circuit correcting for the instruments emission, which led to systematic errors (Albrecht and Cox, 1977). Instead, the temperature measured at the cold junction is used to calculate the instruments emission. As transmission of the dome is rather small and a large part of the radiation passing through the dome is absorbed, the dome can heat up significantly. This introduces an extra longwave irradiance on the sensor. To correct for this so-called dome effect, the temperature of the pyrgeometer dome is monitored with a thermistor close to the dome's rim. It was shown, however, that one thermistor does not suffice to accurately monitor the temperature of the dome, as the dome can heat up inhomogeneously (Philipona et al., 1995). Applying three additional thermistors at an elevation angle of 45 degrees and in azimuthal distance of 120 degrees inside the dome helps to better correct for the dome effect. Ventilation systems have been developed to further reduce excessive heating of the dome.

Thermal flux balance of the PIR

Different pyrgeometer formulas have been stated in literature for calculating longwave irradiance from raw data measured by the Eppley PIR (Albrecht and Cox, 1977; Philipona et al., 1995; Fairall et al., 1998). A closer look is taken at the thermal flux balance of the Eppley PIR pyrgeometer, which will lead to the pyrgeometer formula of Philipona et al. (1995). While all authors cited above agree that the radiation balance at the sensor surface can be written as

$$F_{net} = F_{in} - F_{out}, \quad (5.1)$$

differences start when they formulate the individual incoming and outgoing fluxes. Albrecht et al. (1974) and Fairall et al. (1998) specify the fluxes F_{in} and F_{out} just above the thermopile, while Philipona et al. (1995) specify the fluxes absorbed by and emitted from the sensor, those fluxes that directly change the temperature of the sensor surface.

Following the approach of Philipona et al. (1995), the absorbed incoming flux is made up of three components: the irradiance transmitted through the dome, the

emission from the dome and the radiation emitted by the sensor surface and reflected by the dome. With LW_{IN} the incoming longwave irradiance, the absorptance of the sensor surface a_S , the emissivities of sensor surface ϵ_S and dome ϵ_D , the transmittance of the dome τ_D , the reflectivity of the dome ρ_D , the dome's temperature T_D and the Stefan-Boltzmann constant σ and neglecting multiple reflections,

$$F_{in} = LW_{IN} \cdot \tau_D a_S + \epsilon_D \sigma T_D^4 a_S + \rho_D \epsilon_S \sigma T_S^4 a_S. \quad (5.2)$$

The outgoing flux from the sensor is

$$F_{out} = \epsilon_S \sigma T_S^4 \quad (5.3)$$

With Kirchhoff's law $\epsilon_S = a_S$, the net flux at the sensor surface can be expressed as

$$F_{net} = LW_{IN} \cdot \tau_D \epsilon_S + \epsilon_D \sigma T_D^4 \epsilon_S + \rho_D \epsilon_S^2 \sigma T_S^4 - \epsilon_S \sigma T_S^4. \quad (5.4)$$

The net thermal flux at the sensor surface produces a temperature difference between sensor and the cold junction of the thermopile, the instrument's body. With the sensitivity c (in $K(Wm^{-2})^{-1}$),

$$F_{net} = \frac{T_S - T_B}{c}. \quad (5.5)$$

The voltage signal of the thermopile U_{emf} is result of, and proportional to, the temperature difference $T_S - T_B$ between sensor surface and instrument body. Here the sensitivity factor is γ (in $K(mV)^{-1}$):

$$U_{emf} = \frac{T_S - T_B}{\gamma}. \quad (5.6)$$

The temperature of the sensor surface can thus be expressed as

$$T_S = T_B + \gamma \cdot U_{emf}, \quad (5.7)$$

and provided that $\gamma U_{emf} = T_S - T_B \ll T_B$,

$$T_S^4 \simeq T_B^4 + 4T_B^3 \gamma U_{emf}. \quad (5.8)$$

The net flux can now be written as

$$F_{net} = \frac{U_{emf} \gamma}{c}. \quad (5.9)$$

Dividing by $\tau_D \epsilon_S$ we get

$$\frac{U_{emf} \gamma}{c \tau_D \epsilon_S} = LW_{IN} + \frac{\epsilon_D}{\tau_D} \sigma T_D^4 + \frac{\epsilon_S \rho_D}{\tau_D} \sigma T_B^4 - \frac{1}{\tau_D} \sigma T_B^4 + \frac{\epsilon_S \rho_D - 1}{\tau_D} \cdot 4T_B^3 \gamma U_{emf}. \quad (5.10)$$

The longwave incoming irradiance becomes

$$\begin{aligned} LW_{IN} = & \frac{U_{emf}}{\left(\frac{c \tau_D \epsilon_S}{\gamma}\right)} + \left(4c \epsilon_S (1 - \epsilon_S \rho_D)\right) \frac{U_{emf}}{\left(\frac{c \tau_D \epsilon_S}{\gamma}\right)} \sigma T_B^3 \\ & - \left(\frac{1 - \epsilon_S \rho_D - \epsilon_D}{\tau_D}\right) \sigma T_B^4 - \left(\frac{\epsilon_D}{\tau_D}\right) \sigma (T_D^4 - T_B^4). \end{aligned} \quad (5.11)$$

With the following definitions of coefficients,

$$C = \frac{c\tau_D\epsilon_S}{\gamma}, \quad (5.12)$$

$$k_1 = 4c\epsilon_S(1 - \epsilon_S\rho_D), \quad (5.13)$$

$$k_2 = \frac{1 - \epsilon_S\rho_D - \epsilon_D}{\tau_D} \quad (5.14)$$

and

$$k_3 = \frac{\epsilon_D}{\tau_D} \quad (5.15)$$

we obtain

$$LW_{IN} = \frac{U_{emf}}{C} + k_1 \cdot \frac{U_{emf}}{C} \sigma T_B^3 + k_2 \sigma T_B^4 - k_3 \sigma (T_D^4 - T_B^4). \quad (5.16)$$

and the pyrgeometer formula of Philipona et al. (1995):

$$LW_{IN} = \frac{U_{emf}}{C} \cdot (1 + k_1 \sigma T_B^3) + k_2 \sigma T_B^4 - k_3 \sigma (T_D^4 - T_B^4). \quad (5.17)$$

Using the energy conservation law $1 = \epsilon + \rho + \tau$, and distinguishing between dome transmission for incoming ($\tau_{D\downarrow}$) and outgoing ($\tau_{D\uparrow}$) fluxes, k_2 can be written as

$$k_2 = \frac{\tau_{D\uparrow}}{\tau_{D\downarrow}} + \frac{\rho_D}{\tau_{D\downarrow}} \cdot (1 - \epsilon_S). \quad (5.18)$$

Assuming $\tau_{D\uparrow} = \tau_{D\downarrow}$, k_2 should be equal to or greater than 1.0. When, in addition, assuming $\epsilon_S = 1$, k_2 becomes unity. Neglecting the small k_1 and writing $k_3 = K$ we obtain the Albrecht and Cox (1977) pyrgeometer formula:

$$LW_{IN} = \frac{U_{emf}}{C} + \sigma T_B^4 - K \sigma (T_D^4 - T_B^4). \quad (5.19)$$

Problems with pyrgeometers

The cut-on of the pyrgeometer dome usually lies between 3 and 4 μm . Therefore some of the solar radiation is included in the pyrgeometer measurement. Especially the contribution of the shortwave direct radiation can not be ignored, as it extends to wavelengths above 3.5 μm , depending on atmospheric water vapor content and air mass (Enz et al., 1975). Unfortunately the cut-on can differ from instrument to instrument, and errors greater than 10 Wm^{-2} can occur. Therefore, shading of the dome with a shading disk is proposed. If shading is not possible, the influence of the direct solar radiation needs to be corrected for, taking the behavior of the individual PIR dome into account. An additional term is included into the pyrgeometer formula:

$$LW_{IN} = \frac{U_{emf}}{C} \cdot (1 + k_1 \sigma T_B^3) + k_2 \sigma T_B^4 - k_3 \sigma (T_D^4 - T_B^4) - f \cdot D/1000, \quad (5.20)$$

with D the direct horizontal solar radiation. The f -factor needs to be determined for all individual PIRs during shading experiments. This correction for the 'shortwave leaking' using direct solar radiation was proposed by Marty (2000).

Laboratory calibration

At present, no standardized calibration technique has been proposed for the calibration of pyrgeometers, but a Round Robin experiment showed good agreement between six participating laboratories using different calibration apparatus (Philipona et al., 1998). The responsivity C of the pyrgeometers proved to be stable over the 3 year duration of the experiment. The absolute deviation of the difference between the individual C values and the median of the respective instrument is less than 1%. At PMOD/WRC a recently developed black body cavity is used as calibration apparatus. This cavity allows calibrations of the instruments at conditions close to those met at the deployment site. The cavity can be cooled down to -30°C and the instruments body temperature and the dome temperature can be varied.

All pyrgeometers used in our field campaign at Summit, Greenland, were calibrated prior to the deployment at PMOD/WRC. The pyrgeometers used at the radiation tower were re-calibrated against the traveling standard instrument of PMOD/WRC in spring 2002 at the field site (Section 2.2). Instruments used for measurements of the longwave radiative flux divergence at the 50 m meteorological tower were calibrated relative to each other, as described in the next section.

Relative calibration for flux profile measurements

Dataset for relative calibration All pyrgeometers used at the 50 m meteorological tower for measurements of the longwave flux profile were calibrated relative to each other prior and past every summer field season, to improve the accuracy of the difference measurement. In the beginning of each field season, the instruments were mounted at the tower base, facing upwards. As instruments could not be shaded during measurements of the longwave flux profile, shading experiments were performed. At different times during clear sky days, the individual instrument domes were shaded with a long bamboo pole for approximately 5 minutes. From the apparent reduction in longwave radiation measured during the shade period and the simultaneously sampled direct horizontal solar radiation, a first guess of the f -factor was determined. Instruments showing smallest f -factors were chosen to measure the downward longwave fluxes. Then, instruments were mounted at the tower base, pointing in their designated direction, to collect additional calibration data. This setup was also chosen for the relative calibration at the end of each summer field season. During the campaign, the use of the mobile boom on the tower allowed a direct comparison of flux measurements at the different levels from time to time. The elevator boom was then parked from several hours to several days at the same height as a fixed boom. This data could also partially be used for relative calibration. The pyrgeometers used were numbered PIR 1 to PIR 4 in 2001 and PIR 1 to PIR 8 in 2002. Table 5.1 lists the instruments used on the meteorological tower with serial numbers, measured component and height of deployment. Relative calibration will be discussed separately for the instruments measuring the incoming and outgoing longwave fluxes.

The reference for the relative calibration is formed by the mean of the fluxes from all instruments involved. The individual fluxes were calculated with the cali-

Table 5.1: Pyrgeometers used at the meteorological tower during the 2001-2002 over-winter and the 2002 summer field campaign, whereby PIRs are numbered PIR 1 to PIR 4 and PIR 1 to PIR 8, respectively. Serial number, measured component, deployment height and the name of the level, indicating the approximate height of the instrument, are given. In Summer 2002, the mobile boom was equipped with PIR 3 and PIR 4. The values in brackets refer to the use during intensive observation periods.

	serial number	measured component	deployment height	level name
2001-2002				
PIR 1	31465F3	LW out	1.8 m	2 m
PIR 2	29435F3	LW in	1.8 m	2 m
PIR 3	32553F3	LW in	48-47 m	50 m
PIR 4	32554F3	LW out	48-47 m	50 m
summer 2002				
PIR 1	31465F3	LW out	2 m	2 m
PIR 2	29434F3	LW in	2 m	2 m
PIR 3	32553F3	LW in	47 m (19 m, 34 m)	50 m (20 m, 35 m)
PIR 4	32554F3	LW out	47 m (19 m, 34 m)	50 m (20 m, 35 m)
PIR 5	31464F3	LW in	10 m	10 m
PIR 6	29435F3	LW out	10 m	10 m
PIR 7	31964F3	LW in	0.5 m	0.5 m
PIR 8	26802F3	LW out	0.5 m	0.5 m

bration constants determined at PMOD/WRC and using the preliminary f -factor values from shading experiments. Sometimes, one instrument was excluded from the calculation of the mean value, as it showed a strongly varying behavior. As the importance of the different terms in the pyrgeometer formula (Equation 5.16) varies, relative calibration is performed slightly different for instruments measuring incoming and outgoing fluxes.

Incoming fluxes For incoming fluxes, two relative calibrations were performed. The first was done including calibration and direct comparison data collected between June 1st, 2001, and May 5th, 2002. The heating system was changed after May 5th, 2002 from a heating element on the base plate to a heating coil just below the outlet of ventilation air. The second relative calibration included all calibration data collected after this modification, in May 2002 and in July 2002.

When measuring the incoming longwave irradiance the third term in the pyrgeometer formula (Equation 5.16), describing the instrument's own emission, is usually the largest. The second largest is normally the first term, the response of the thermopile. The second term, involving coefficient k_1 and C describes the thermal nonlinearity of the pyrgeometer. It can amount to up to 10 Wm^{-2} . The fourth term, often referred to as the 'dome factor' is controlled by coefficient k_3 . During the calibration period, this term ranged between 0 Wm^{-2} and 30 Wm^{-2} .

A robust least-squares minimization is used to optimize the calibration coefficients C , k_1 , k_2 , k_3 and f for the individual pyrgeometers. Different calibration approaches,

keeping some coefficients fixed to the values determined during the lab calibrations at PMOD/WRC in Davos have been tested. The best fit to the reference can be achieved when all coefficients are varied, within a certain range ($C=[0,5]$, $k_1=[0,0.5]$, $k_2=[0.95,1.05]$, $k_3=[0,5]$). To reach a reasonably good fit and a small standard deviation C and k_3 , and to a lesser extent k_2 , should be varied. It is suggested to include k_1 in the relative calibration as well, as the available calibration data represents the temperature range met in the field environment, varying between -40°C and -5°C . The fit between instruments can be clearly improved. Including k_1 in the relative calibration routine reduces the standard deviation for PIR 2 from 0.44 Wm^{-2} to 0.34 Wm^{-2} for example.

In Table 5.2, the calibration results are presented for the instruments used for measurement of the down-welling longwave fluxes in the 2001-2002 over-winter season, in Table 5.3 the results for the 2002 summer season.

Table 5.2: Overview of relative calibration results of the two PIRs used for incoming longwave measurements (PIRs 2 and 3) in the 2001-2002 winter-over campaign (June 1st, 2001 to May 5th, 2002). All available 16690 calibration data points collected between June 1st and April 4th are used. Reference is the mean of the irradiances calculated with PMOD/WRC coefficients. Calibration constants are C , k_1 , k_2 , k_3 and f . Lab coefficients from calibration at PMOD/WRC and fitted coefficients determined during relative calibration are listed. f -factors in brackets are determined through shading experiments at the field site. Standard deviations (std) of differences to reference are given in Wm^{-2} for lab (PMOD/WRC) and fitted coefficients.

PIR/Calibration	C	k_1	k_2	k_3	f	n	std	std
								lab
PIR 2: 29435: $LW_{IN}(2\text{ m})$								
PMOD/WRC	4.050	0.1500	1.0010	3.680	(9.30)			
FIT	4.153	0.1890	1.0056	3.800	6.66	16690	0.47	0.60
PIR 3: 32553: $LW_{IN}(50\text{ m})$								
PMOD/WRC	3.770	0.1343	1.0068	3.560	(9.53)			
FIT	3.540	0.0591	0.9997	3.757	10.05	16690	0.44	0.60

Figure 5.1 shows an example of the relative calibration results. The distribution of differences between the calibrated PIR 5 and the reference is shown. The standard deviation is only 0.32 Wm^{-2} . The use of the original PMOD/WRC coefficients would have led to a standard deviation of 0.67 Wm^{-2} .

As we are interested in the flux differences, the differences between to calibrated instruments is of interest. Figure 5.2 shows the differences between the PIR 2 and PIR 7 and between PIR 3 and PIR 5 after relative calibration. Standard deviations vary from 0.36 to 0.60 Wm^{-2} and represent the uncertainty of the flux difference measurement. The use of PMOD/WRC coefficients would lead to offsets of up to 1.9 Wm^{-2} and standard deviations of up to 1.02 Wm^{-2} .

Outgoing fluxes Relative calibration of the down-facing instruments for measurement of the outgoing longwave flux proved more difficult than the relative calibration of the up-facing instruments. This was due to PIR 4 (32554F3), which showed

Table 5.3: Overview of relative calibration results of the four PIRs used for incoming longwave measurements (PIRs 2, 3, 5, 7) during the 2002 summer campaign. All available 7468 calibration data points collected prior (May) and after (July) the field campaign measurements are used. Reference is mean of irradiances of PIR 2, PIR 3 and PIR 8 calculated with PMOD/WRC coefficients. Calibration constants are C , k_1 , k_2 , k_3 and f . Lab coefficients from calibration at PMOD/WRC and fitted coefficients determined during relative calibration are given. f -factors in brackets are determined through shading experiments at the field site. Standard deviations (std) of differences to reference are given in Wm^{-2} for lab (PMOD/WRC) and fitted coefficients.

PIR/Calibration	C	k_1	k_2	k_3	f	n	std	std
								lab
PIR 2: 29434: $LW_{IN}(2 \text{ m})$								
PMOD/WRC	4.210	0.1305	1.0070	3.550	(9.30)			
FIT	4.657	0.2475	1.0069	3.471	10.07	7468	0.34	0.44
PIR 3: 32553: $LW_{IN}(50 \text{ m})$								
PMOD/WRC	3.770	0.1343	1.0068	3.560	(9.53)			
FIT	3.524	0.0728	1.0069	3.778	8.42	7468	0.20	0.39
PIR 5: 31464: $LW_{IN}(10 \text{ m})$								
PMOD/WRC	4.060	0.0599	0.9964	2.870	(10.10)			
FIT	4.307	0.1471	0.9964	3.031	8.69	7468	0.32	0.67
PIR 7: 31964: $LW_{IN}(0.5 \text{ m})$								
PMOD/WRC	4.100	0.0708	1.0015	3.130	(8.29)			
FIT	3.997	0.0356	1.0026	3.089	8.32	7468	0.30	0.44

changing behavior during the 2002 summer season as well as during the winter-over campaign.

A relative calibration of the two down-facing pyrgeometers (PIR 1 and PIR 4) in the 2001-2002 winter-over campaign fails. When all available comparison data is used, including comparison data from August and September 2001 and April 2002, and calibrating them relative to their mean, a bimodal distribution of differences between the two instruments results (Figure 5.3). The time series of differences between the two instruments shows a sudden change from calibration data collected in June 2001 to data in August and later on. As PIR 4 showed sudden changes in characteristics during the summer 2002 season as well, strong indication is given that PIR 4 caused this distribution.

To improve the performance of pyrgeometer PIR 1, a set of calibration constants for PIR 1 is determined from calibration data collected in June 2001, during the time when all four available instruments were mounted pointing down. The reference of this relative calibration is formed by the mean of all four fluxes calculated with PMOD/WRC coefficients.

PIR 4 is then calibrated relative to PIR 1, once using calibration data from before the sudden change in its behavior, once for the time thereafter. The time of transition was determined by analyzing flux differences for times when this difference was assumed to be small: when the temperature difference between the 2 m and 50 m air temperature was near neutral. The first set of coefficients for PIR 4, 'Summer 2001',

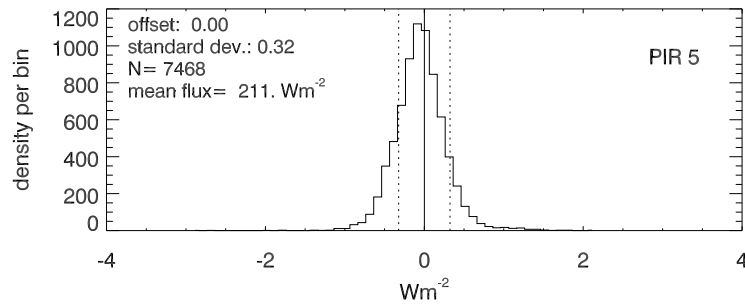


Figure 5.1: Relative calibration of up-facing PIRs. Histogram of differences between reference (mean of PIR 2, PIR 3 and PIR 5 with PMOD/WRC constants) and PIR 5 after relative calibration. N is number of minute values. Bin size is 0.1 Wm^{-2} .

is then used for all data collected before June 19th, the second set ('Fall-Spring') for measurements after June 21st, 2001. For the time in between a weighted mean is used between fluxes calculated with both sets of coefficients. Table 5.4 presents the results for the relative calibration of instruments used for measurements of the outgoing flux in the over-winter season 2001-2002.

Table 5.4: Relative calibration results for the two PIRs used for outgoing longwave measurements in the over-winter field campaign 2001-2002. PIR 1 Was relatively calibrated to the mean of four down-facing instruments in Summer 2001. As PIR 4 showed a strong change in behavior, it was directly compared to PIR 1 using data from August 2001, September 2001 and April 2002 (8410 data points). Calibration constants are C , k_1 , k_2 and k_3 . Lab coefficients from calibration at PMOD/WRC and fitted coefficients determined during relative calibration are listed. Coefficient k_1 is not changed as fitting k_1 does not significantly improve the fit. Standard deviations (std) of differences to reference are given in Wm^{-2} for lab (PMOD/WRC) and fitted coefficients.

PIR/Calibration	C	k_1	k_2	k_3	n	std	std lab
PIR 1: 31465: $LW_{OUT}(2 \text{ m})$							
PMOD/WRC:	3.860	0.0539	0.9986	2.840			
FIT	4.039	0.0539	0.9931	2.923	5580	0.33	0.50
PIR 4: 32554: $LW_{OUT}(50 \text{ m})$							
PMOD/WRC:	3.620	0.0434	0.9986	2.990			
FIT 'Summer 2001'	3.381	0.0434	1.0017	3.849	5580	0.36	1.01
FIT 'Fall-Spring'	2.978	0.0434	0.9991	4.875	8410	0.63	1.64

For the relative calibration of the down-facing instruments during the summer campaign 2002, all calibration data collected prior the campaign in June 2002 and after the campaign in July, 2002 is used. The reference was formed by the means of two instruments (PIR 1 and PIR 8) that were chosen for their homogeneous behavior. Relative calibration gives good results for PIR 1, PIR 6 and PIR 8. The deviation from the reference of PIR 4, however, shows a bimodal distribution, indicating a change of the instrument characteristics. As for the 2001-2002 over-winter campaign,

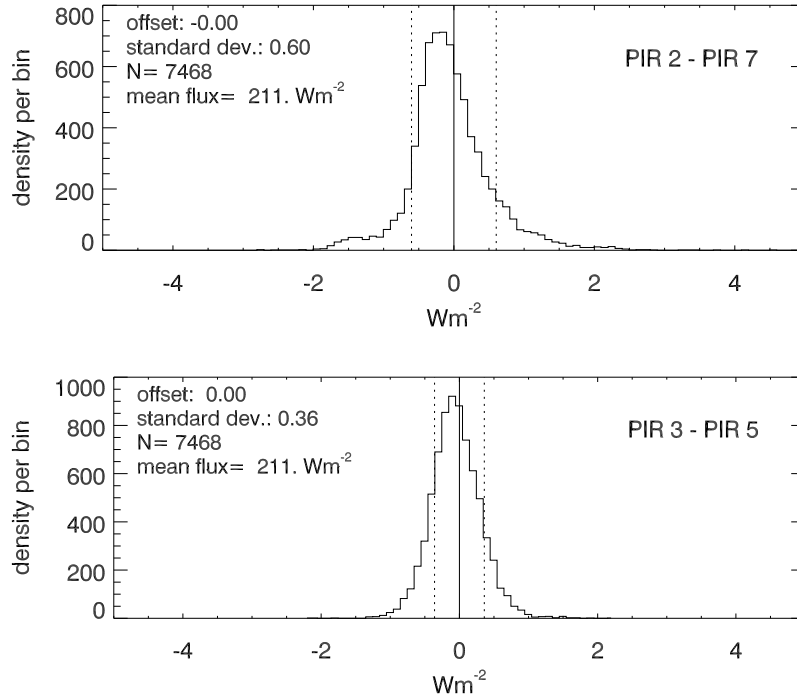


Figure 5.2: Relative calibration of up-facing PIRs. Histogram of differences between irradiances measured by different pyrgeometers, after relative calibration. N is number of minute values. Bin size is 0.1 Wm^{-2} . Upper panel: Difference between PIR 2 and PIR 7. This marks the worst case. Lower panel: Difference between PIR 3 and PIR 5.

the time of shift in behavior is located from analysis of observational data. Two sets of coefficients are then determined for PIR 4. The first set ('May'), derived from June 2002 calibration data is used for data collected before June 25th, 2002, the second set ('July'), based on calibration data collected in July 2002, is used after June 29th. Again, for the days in between, a weighted mean is calculated from fluxes determined using both sets of coefficients. Table 5.5 presents the coefficients determined with relative calibration for the four down-facing pyrgeometers.

When the Eppley PIR is used for the investigation of the outgoing longwave irradiance, the weight of the different terms in formula 5.16 is different from the situation when incoming longwave radiation is measured. The radiative temperature difference between the instrument and the target (the ground) is not as large as the difference between an up-facing instrument and a cold clear sky. Therefore the first two terms lose their dominance, ranging between $0\text{-}10 \text{ Wm}^{-2}$ (first term) and $0\text{-}2 \text{ Wm}^{-2}$ (second term). The third term describing the instruments emission stays the dominating term and the term involving the dome factor (fourth term) becomes the second largest. A variation of k_1 will therefore not change the quality of the fit. The standard deviation does not decrease, so k_1 can be kept at the value determined at PMOD/WRC.

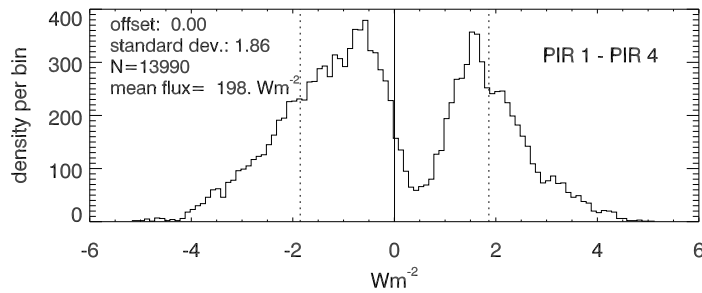


Figure 5.3: Histogram of differences between PIR 1 and PIR 4 measurements after relative calibration of down-facing PIR 4 against PIR 1 using all available calibration data. Standard deviation in Wm^{-2} . N is number of data points used for calibration. Bin size is 0.1 Wm^{-2} . The bimodal distribution is caused by a shift in behavior of PIR 4.

Relative accuracy and uncertainty

For the investigation of longwave radiative flux divergence, we need to improve the relative accuracy of the pyrgeometer measurements. Improved relative accuracy helps to detect small differences between pyrgeometers in a group of pyrgeometers. The relative differences are more important than the absolute accuracy of the flux measurement.

The standard deviation of the distribution of differences between the relatively calibrated pyrgeometers reflects the uncertainty in the measured flux differences which are used for the investigation of flux divergence. Tables 5.6 and 5.7 list these values for measurements of incoming and outgoing fluxes. The uncertainty in flux differences of the incoming flux is 0.84 Wm^{-2} for the winter-over campaign and ranges between 0.36 and 0.60 Wm^{-2} in the summer 2002 campaign. Differences of outgoing flux show an uncertainty between of 0.65 Wm^{-2} for the winter-over campaign and an uncertainty less than 0.45 Wm^{-2} in the summer 2002 campaign.

The improvement to the use of coefficients from the calibration at PMOD/WRC is remarkable. The distribution of incoming flux differences, using the coefficients determined at PMOD/WRC, would show offsets of up to 2.37 Wm^{-2} (incoming fluxes) and 3.42 Wm^{-2} (outgoing fluxes) and standard deviations of up to 1.20 Wm^{-2} . These numbers reflect the absolute accuracy of the instruments, as they were compared to standard instruments at PMOD/WRC before the field deployment.

Uncertainties in calculated heating rates

Uncertainties in heating rates arise from the uncertainties in the flux measurements. In the previous section, it was shown that relative calibration of the pyrgeometers improves the quality of data. However, a level of uncertainty, reflected in the standard deviation of flux differences, remains. For the summer 2002 field campaign, the maximum uncertainty in the measurement of the difference in incoming and outgoing fluxes is 0.60 Wm^{-2} and 0.45 Wm^{-2} , respectively. The uncertainty is expressed here

Table 5.5: Overview of relative calibration results of the four PIRs used for outgoing longwave measurements in the 2002 summer season. All available 6718 calibration data points collected prior and after the field campaign measurements are used for relative calibration of instruments PIR 1, PIR 6 and PIR 8. Reference is mean of PIR 1 and PIR 8. Two sets of new coefficients are calculated for PIR 4, as it showed a shift in behavior. The first set ('May') is used for data collected before June 25th, 2002, the second set ('July') for data after June 29th, 2002. A weighted mean is calculated for the days in between. For the two relative calibrations, PIR 1 using new coefficients was used as reference. Lab coefficients from calibration at PMOD/WRC and the fitted coefficients determined during relative calibration are listed. Calibration constants are C , k_1 , k_2 and k_3 . Coefficient k_1 is not changed as it does not significantly improve the fit. Standard deviations (std) of differences to reference are given in Wm^{-2} for lab (PMOD/WRC) and fitted coefficients.

PIR/Calibration	C	k_1	k_2	k_3	n	std	std lab
PIR 1: 31465: $LW_{OUT}(2 \text{ m})$							
PMOD/WRC	3.860	0.0539	0.9986	2.840			
FIT	3.919	0.0539	1.0005	2.888	6718	0.18	0.24
PIR 4: 32554: $LW_{OUT}(50 \text{ m})$							
PMOD/WRC	3.620	0.0434	0.9986	2.990			
FIT 'May'	2.924	0.0434	1.0031	3.723	835	0.39	0.77
FIT 'July'	2.951	0.0434	1.0003	4.415	6388	0.29	1.41
PIR 6: 29435: $LW_{OUT}(10 \text{ m})$							
PMOD/WRC	4.050	0.1500	1.0010	3.680			
FIT	4.034	0.1500	1.0055	3.251	6718	0.34	0.99
PIR 8: 26802: $LW_{OUT}(0.5 \text{ m})$							
PMOD/WRC	3.950	0.1054	1.0024	3.510			
FIT	3.936	0.1054	1.0003	3.458	6718	0.22	0.24

as one standard deviation of the distribution of flux differences.

Flux difference measurements are averaged in 15-minute means as described in Section 5.1.5. Averaging reduces the uncertainty of the flux difference measurement, and therefore of the heating rate. For example, the standard deviation of the difference between PIR 6 and PIR 8 during the summer season 2002 is reduced from 0.45 Wm^{-2} to 0.41 Wm^{-2} , the standard deviation of differences between PIR 3 and PIR 5 from 0.36 Wm^{-2} to 0.29 Wm^{-2} .

The uncertainty in the heating rate calculated from the flux differences strongly depends of the thickness of the layer under investigation. The thinner the layer, the larger is the uncertainty in calculated longwave radiative heating rate due to the uncertainties in the measured longwave flux differences.

As an example, the uncertainty of the longwave radiative heating rate due to the uncertainty in flux difference of incoming, outgoing and net longwave radiation between the 2 m and 10 m level is calculated: Assuming an air density of 0.90 kg m^{-3} and with $c_p=1005 \text{ J kg}^{-1} \text{ K}^{-1}$, the uncertainty of a 15-minute value of heating rate due to divergence of incoming and outgoing longwave fluxes becomes $\pm 4.8 \text{ Kd}^{-1}$ and $\pm 3.6 \text{ Kd}^{-1}$, for the heating rate due to the net divergence $\pm 6.1 \text{ Kd}^{-1}$. Table 5.8

Table 5.6: Standard deviations of flux differences in Wm^{-2} between up-facing instruments after relative calibration for instruments used in the winter-over campaign (2001-2002) and the summer campaign 2002. Offsets are 0 Wm^{-2} .

winter-over 2001-2002	PIR 3			
PIR 2	0.84			
summer 2002	PIR 2	PIR 3	PIR 5	PIR 7
PIR 2	-	0.47	0.46	0.60
PIR 3	0.47	-	0.36	0.39
PIR 5	0.46	0.36	-	0.47
PIR 7	0.60	0.39	0.47	-

Table 5.7: Standard deviations of flux differences in Wm^{-2} between down-facing instruments for the winter-over campaign (2001-2002) and for the summer 2002 campaign. Two values are given for the winter-over campaign, as PIR 4 underwent a shift, and was calibrated for two time intervals. Values for summer 2002 are for relative calibration using all calibration data collected in May and July 2002. Values marked with a (*) are from the 'July'-calibration using only data collected in July 2002, when PIR 4 was optimized to fit PIR 1. Offsets between instruments are less than 0.03 Wm^{-2} .

winter-over 2001-2002	PIR 4			
PIR 1	0.65			
summer 2002	PIR 1	PIR 4	PIR 6	PIR 8
PIR 1	-	0.29*	0.33	0.39
PIR 4	0.29*	-	0.42*	0.38*
PIR 6	0.33	0.42*	-	0.45
PIR 8	0.39	0.38*	0.45	-

lists the introduced uncertainties for the different air layers under investigation.

In the following sections, mean profiles of longwave radiative heating rates are presented, averages of n (of the order of 100 to 1000) measured 15-minute profiles. Due to the large amount of profiles contained within the means, the uncertainty is expected to reduce drastically. Theoretically, assuming the measurements to be independent identically distributed random variables, the uncertainty reduces by a factor of $\frac{1}{\sqrt{n-1}}$. This assumption is rather optimistic, as the measurements slightly depend on each other. Error bars, however, become very small and are omitted from the graphs.

5.1.4 Tower influence correction

The pyrgeometers are suspended on horizontal booms of a tower structure. Inevitably the tower is in the field of view of the instruments. An up-facing instrument,

Table 5.8: Uncertainties of a single 15-minute value of measured longwave flux differences in Wm^{-2} and the corresponding uncertainty in heating rate in Kd^{-1} during the summer 2002 field campaign. Values in brackets are for the 2001-2002 winter over season. Air density ρ of 0.90 is used in calculation of heating rates.

layer		uncertainty flux difference			uncertainty heating rate		
base	top	in	out	net	in	out	net
0.5 m	2.0 m	0.57	0.35	0.67	36.1	22.2	42.5
2.0 m	10 m	0.41	0.30	0.51	4.8	3.6	6.1
10 m	50 m	0.29	0.37	0.47	0.8	1.0	1.2
2 m	50 m	0.40 (0.84)	0.23 (0.63)	0.47 (1.05)	0.9 (1.8)	0.5 (1.3)	1.0 (2.2)

for example, will receive radiation emitted by the tower, while a part of the sky radiation is blocked by the tower structure. As the tower structure usually has a higher radiative temperature than the sky, the measured flux is larger than the flux from the sky. A correction for the tower's influence is thus needed.

Tower geometry

The tower is a 48 m high (summer 2002) aluminum structure with a triangular base and a side length of 1.30 m. The two instrument pairs are mounted on horizontal booms in a distance of 1.25 m from the main tower structure. A sketch of the side view and top view of the tower is provided in Figure 5.4. Seen from an instrument, the azimuthal range a_t between the tower edges is 53° . Within 30% of this azimuthal range, however, the sky is seen through the tower structure. This can be described by a structural density, td of 0.7, which has been determined by photographic means. The tower structure is made of aluminum, but is often covered by rime under normal weather conditions at Summit. This makes it more difficult to calculate the correction for the radiation emitted by the tower, as an emissivity ϵ_{tower} representing an aluminum structure partially covered with rime needs to be assumed.

Direct measurements of the tower structure have shown that the temperature of the tower can vary with height. The tower is therefore split up into seven segments, and the emission of each section is calculated. The tower segments are separated by the levels of temperature measurements, the snow surface and the tower top (Figure 5.4). The first and lowest segment is between 0 m and 0.5 m, the second between 0.5 m to 2.0 m, and so forth. The last segment is the part of the tower above the highest radiation measurement level, between 47 m and 48 m. Table 5.9 gives an overview of the tower segments.

As the first step, a solid tower covering the azimuthal range from $a = 0$ to a_t is considered. The tower is assumed to be a Lambertian source of radiation emitting the radiance L_t . With z_t and z_b the zenith angles of the top and bottom points of the tower segment of interest as seen from the instrument, the irradiance from the

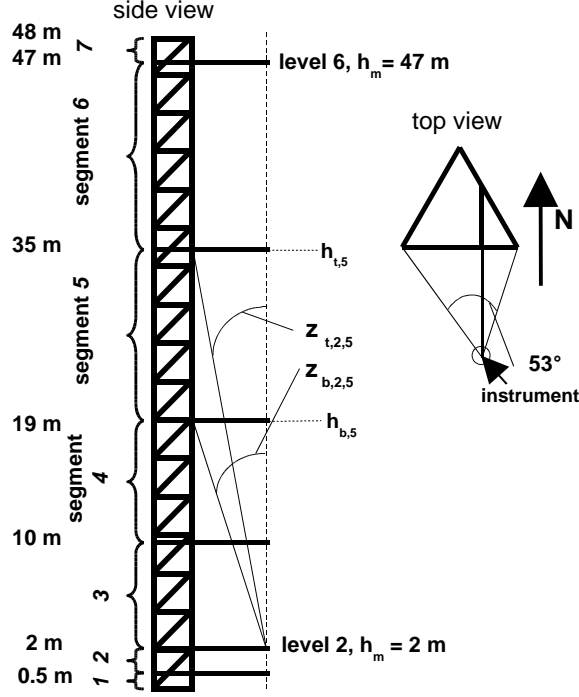


Figure 5.4: Schematic diagrams (side and top views) of the tower structure and viewing geometry for the correction of the tower's influence on the pyrgeometer measurements. As example, the zenith angles of tower section 5 seen by an up-facing instrument at level 2 are illustrated.

tower segments $I_{segment}$ measured by the instrument can be expressed as:

$$I_{segment}(a_t, z_b, z_t) = \int_0^{a_t} \int_{z_t}^{z_b} L_t \sin z \cos z \, dz \, da. \quad (5.21)$$

With E_t the emitted exitance of the tower structure ($E_t = \pi L_t$) we obtain

$$I_{segment}(a_t, z_b, z_t) = \frac{E_t a_t}{\pi} \frac{1}{2} [\sin^2 z]_{z_t}^{z_b}. \quad (5.22)$$

The zenith angles of the top and the base of the j th tower segment seen from the instrument at the i th measurement level at height $h_{m,i}$ are calculated as

$$z_{t,i,j} = \arctan\left(\frac{l}{h_{t,j} - h_{m,i}}\right), \quad z_{b,i,j} = \arctan\left(\frac{l}{h_{b,j} - h_{m,i}}\right), \quad (5.23)$$

with l the distance of the instrument from the tower (1.25 m). When $h_{t,j} = h_{m,i}$ or $h_{b,j} = h_{m,i}$, $z_{t,i,j}$ and $z_{b,i,j}$ are set to 90° , respectively. For measurements at the i th level, let $\alpha_{i,j}$ describe the weight given to the emitted flux of the j th tower segment arising from the zenith distance of this segment. For example, the longwave incoming measurement at the height of 2 m (second measurement level $i = 2$), the flux emitted from the segment between 10 m and 19 m (segment 4, $j=4$) has a weight of

$$\alpha_{2,4} = [\sin^2 z]_{z_{t,2,4}}^{z_{b,2,4}} = 0.018 \quad (5.24)$$

Table 5.9: Tower segments and PIR deployment or main measurement levels. For all of these levels, a tower correction is calculated. Heights refer to measurements during summer campaign 2002.

	segment base height h_b [m]	segment top height h_t [m]		measurement height h_m [m]
segment 1	0.0	0.5	level 1	0.5
segment 2	0.5	2.0	level 2	2.0
segment 3	2.0	10.0	level 3	10.0
segment 4	10.0	19.0	level 4	19.0
segment 5	19.0	34.0	level 5	34.0
segment 6	34.0	47.0	level 6	47.0
segment 7	47.0	48.0		

The emitted flux from the entire tower measured by an up-facing instrument at 1.8 m (level 2) can now be calculated as

$$I_{tower,2} = \epsilon_{tower} \cdot \frac{d}{2\pi} \cdot \left(\begin{aligned} &\alpha_{2,3} \cdot \sigma(T_{t,3})^4 \\ &+ \alpha_{2,4} \cdot \sigma(T_{t,4})^4 \\ &+ \alpha_{2,5} \cdot \sigma(T_{t,5})^4 \\ &+ \alpha_{2,6} \cdot \sigma(T_{t,6})^4 \\ &+ \alpha_{2,7} \cdot \sigma(T_{t,7})^4. \end{aligned} \right)$$

Here, ϵ_{tower} is the emissivity of the tower structure, $T_{t,j}$ the mean temperature of the j th tower section, d the effective azimuth (the product of the density of tower structure td and the azimuth range of the tower a_t). The flux from the entire tower measured by an up-facing pyrgeometer at the i th measurement level becomes

$$I_{tower,i} = \epsilon_{tower} \cdot \frac{d}{2\pi} \cdot \sum_{j=i+1}^n \alpha_{i,j} \cdot \sigma(T_{t,j})^4. \quad (5.25)$$

Let $\alpha_{tot,i}$ be sum of the weights $\alpha_{i,j}$ of the emissions of the tower segments above the measurement level,

$$\alpha_{tot,i} = \sum_{j=i+1}^n \alpha_{i,j}. \quad (5.26)$$

The radiative flux measured at the i th level can be written as the sum of four terms:

$$I_{measured,i} = \left(1 - \frac{d}{2\pi}\right) \cdot I_{sky,i} \quad (5.27)$$

$$+ \frac{d}{2\pi} \cdot (1 - \alpha_{tot,i}) \cdot I_{sky,i}$$

$$+ \frac{d}{2\pi} \cdot \alpha_{tot,i} \cdot (1 - \epsilon_{tower}) \cdot I_{sky,i}$$

$$+ I_{tower,i}.$$

The first two terms on the right describe the flux received from the unobstructed part of the sky, in respect to the azimuthal range not covered by the tower, and

the unobstructed zenith angle range in the azimuthal range covered by the tower structure. The last two terms describe the radiation from the tower structure. The third term describes the radiation (assumed to be coming from the sky) reflected by the tower structure, the fourth term the flux emitted by the aluminum tower. The longwave sky radiation can now be calculated as:

$$I_{sky,i} = \frac{I_{measured,i} - I_{tower,i}}{\left(1 - \frac{d}{2\pi}\right) + \frac{d}{2\pi} \cdot (1 - \alpha_{tot,i}) + \frac{d}{2\pi} \cdot \alpha_{tot,i}(1 - \epsilon_{tower})}. \quad (5.28)$$

In the same way, outgoing fluxes at the measurement heights can be calculated accounting for the tower structure.

Tower emissivity

The emissivity of the tower structure is estimated to be 0.2. Aluminum has a very low emissivity if the surface is polished. The aluminum tower elements are lightly oxidized, some more than others, as parts of the tower had been in use in earlier field experiments. Often, rime forms on the structure, which then has a high emissivity. A mixture of blank aluminum of different oxidation strength and rime covered aluminum is estimated to result in an emissivity of 0.2, which corresponds to the emissivity of very oxidized aluminum (Sala, 1986).

Tower temperature

The temperature of the tower structure was measured at the 2 m and 35 m levels with thermistors during the second summer field season, from May 13th to July 18th, 2002. It was observed that the temperature of the tower structure varied with height. When winds were below a threshold level of 9.3 m s^{-1} , the tower structure was warmer than the air. For these conditions, an empiric relationship was found for the difference between the temperature of the tower structure and the air temperature, involving wind speed u and global radiation Gl :

$$T_{tower} = T_{air} + (c_1 + c_2 \cdot u) \cdot Gl. \quad (5.29)$$

Figure 5.5 illustrates the empiric relationship. Coefficients c_1 and c_2 were determined minimizing the difference between tower and air temperatures from all concurrent measurements at the 2 m and 35 m levels. This relationship is used to calculate the temperature of the tower structure at all eight levels where air temperature was measured. The temperatures of the tower segments $T_{t,i}$ were obtained by averaging the tower structure temperatures laying within each segment (Table 5.10).

Correction magnitude

Generally, with predominating stable conditions, the radiative temperature of the tower is greater than that of the sky. Up-facing instruments mounted on the tower therefore measure a flux that is larger than the flux from the sky. The correction varies depending roughly on the difference of radiative temperature of the tower and

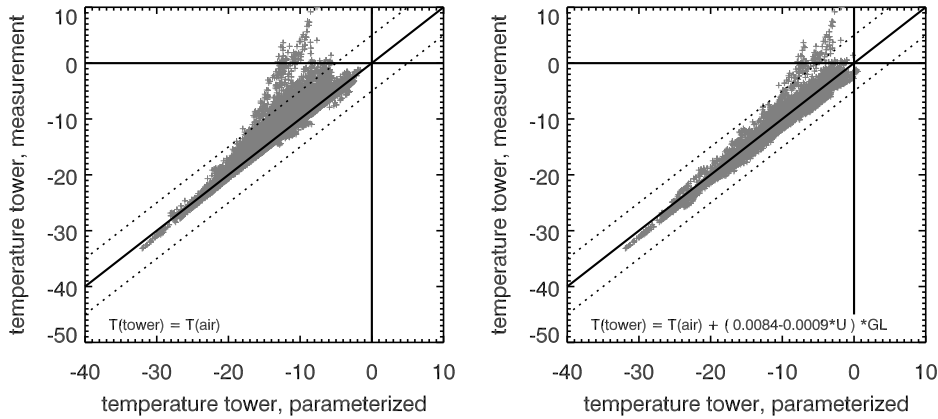


Figure 5.5: Temperature of the tower structure measured and parameterized. Left: Tower structure temperature assumed to equal ambient air temperature. Right: Tower structure temperature is parameterized involving air temperature, wind speed and global radiation. All measurements involved are 10-minute means at the 2 m and 35 m levels between May 13th and July 18th, 2002.

the sky. Under overcast situations, this difference is small, as the cloud base is much warmer than a clear sky. The correction applied to the incoming fluxes under overcast conditions is in the order of -1 Wm^{-2} . The difference of radiative temperature between the tower structure and the snow surface is smaller than between the tower structure and the sky. Therefore the correction of the fluxes measured by the down-facing instruments is generally smaller. During overcast situations the correction ranges between 0.0 and 0.2 Wm^{-2} . The tower structure is normally slightly warmer than the snow surface, due to stable conditions. With the down-welling fluxes having a negative sign, the correction is positive. During clear sky situations, the correction for the tower influence on the up-facing instruments can reach -2.5 Wm^{-2} . Corrections for the down-facing instruments under clear conditions usually do not exceed 1 Wm^{-2} .

For heating rate calculations the differences between the fluxes is of importance. If the influence of the tower is similar for two levels, for example for the two up-facing instruments at 2 m and 10 m, then the effect of the correction on the heating rate due to the divergence of incoming longwave radiation is negligible. The tower correction has the greatest impact when the flux difference or heating rate between two levels are investigated of which one is affected by the tower influence, and one is not. This is the case for the heating rate between 2 m and 50 m and between 10 m and 50 m. The effect of the correction of the tower's influence can amount to a significant percentage of the heating. The correction expressed as a heating rate amounts to typically 3 Kd^{-1} under clear sky summer conditions. Under average summer conditions, neglecting the tower's influence on the measurements would lead to an underestimation of the net longwave radiative heating at noon by 30% and to an overestimation of the peak longwave radiative cooling around midnight by 10%.

Table 5.10: Tower segment temperatures $T_{s,i}$ calculated from tower structure temperatures T_{ts} . T_{ts} are available for all levels with air temperature measurements.

	segment base height $h_b[m]$	segment top height $h_t[m]$	calculation of tower segment temperature $T_{s,i}$
segment 1	0.0	0.5	$T_{t,1} = T_{ts}(0.5 m)$
segment 2	0.5	2.0	$T_{t,2} = (T_{ts}(0.5 m) + T_{ts}(1.0 m) + T_{ts}(2.0 m))/3$
segment 3	2.0	10.0	$T_{t,3} = (T_{ts}(2.0 m) + T_{ts}(5.0 m) + T_{ts}(10.0 m))/3$
segment 4	10.0	20.0	$T_{t,4} = (T_{ts}(10.0 m) + T_{ts}(20.0 m))/2$
segment 5	20.0	35.0	$T_{t,5} = (T_{ts}(20.0 m) + T_{ts}(35.0 m))/2$
segment 6	35.0	48.0	$T_{t,6} = (T_{ts}(35.0 m) + T_{ts}(49.0 m))/2$
segment 7	48.0	49.5	$T_{t,7} = T_{ts}(49.0 m)$

5.1.5 Data analysis

Data was analyzed using 15-minute averages. This was chosen due to the extended measurements during intensive observational periods (IOP). During an IOP, the mobile boom was usually parked at 50 m, 35 m and 20 m for 20 minutes during every hour. Measurements were conducted using a special measurement pattern. Usually, an IOP was started on a full hour. The mobile boom was then moved to the 35 m level at 20 minutes past the hour, and to the 20 m level at 40 minutes past the hour, before being returned to the 50 m level at the next full hour. The first 5 minutes of measurements at a new level were discarded. All other minute values are corrected for the tower influence as described in Section 5.1.4, and averaged for every level. This is also done for the levels with fix instrumentation. The measurement pattern is summarized in Figure 5.6.

A temporal interpolation is used to obtain values for the longwave fluxes at the two levels without measurement. Two of the three 15-minute averages for every hour need to be calculated, using the two available bordering averages of the same level. As longwave fluxes can vary very fast due to changing cloud cover, information on the temporal change from the highest fix measurement level (10 m level) is included in the interpolation. This is done by linearly interpolating the ratio between the flux at the height of the mobile measurement and the flux from the 10 m level. Let $f_{35}(t_1)$ and $f_{35}(t_4)$ represent the means of the fluxes at the 35 m level sampled at times t_1 and t_4 by the mobile instruments. The fluxes $f_{35}(t_2)$ and $f_{35}(t_3)$ are obtained by interpolation. At the 10 m level, all measurements are available and the four average values $f_{10}(t_1)$, $f_{10}(t_2)$, $f_{10}(t_3)$ and $f_{10}(t_4)$ can be calculated. The assumption is made that the ratio between $f_{35}(t_i)$ and $f_{10}(t_i)$ changes linearly. The values between the known $f_{35}(t_1)/f_{10}(t_1)$ and $f_{35}(t_4)/f_{10}(t_4)$ are interpolated. From the obtained ratios the unknown $f_{35}(t_2)$ and $f_{35}(t_3)$ are calculated.

5.2 Observational Results

In this section, the most important results from the measurements of longwave radiative flux divergence are presented. First, the focus lies on the measurements

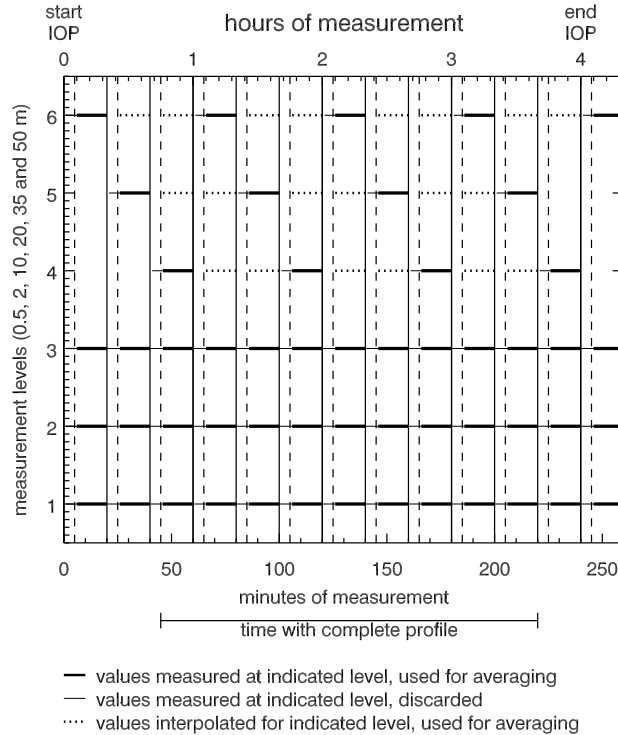


Figure 5.6: Measurement pattern used during intensive observational periods (IOP).

of the summer field campaign in 2002 when incoming and outgoing fluxes were recorded at four levels. The diurnal cycle and mean daytime and nighttime profiles of longwave radiative flux divergence are shown.

In a second step, the vertical and temporal distribution of longwave radiative flux divergence is shown for different meteorological conditions, such as clear-sky, overcast, windy and calm situations. The influence of fog formation on the longwave radiative flux divergence is investigated by comparing measurements from two intensive observational periods. Two nights are compared, one with and one without fog formation in the surface layer.

Furthermore, the relationship between longwave radiative flux divergence, temperature gradient and humidity is addressed. While temperature gradients are shown to play an important role, the influence of humidity is rather small.

In the last part of this section, results of the year-round measurements of the longwave flux divergence between 2 and 50 m are presented

The uncertainties of the measurements were discussed in Section 5.1.3. It was shown that uncertainties are larger for thin layers than for the thicker layers. As the number of measurements contained within each profile is large, the uncertainty is expected to reduce drastically, and error bars are omitted from the graphs.

The results of longwave radiative flux divergence measurements are discussed as heating rates in units of Kd^{-1} . The flux divergence in units of Wm^{-3} is obtained simply by a multiplication with the factor -0.0105 , with the assumption that the density of air is 0.9 kg m^{-3} .

5.2.1 Summer conditions

Mean summer longwave radiative heating Mean profiles of net longwave radiative flux divergence are shown in Figure 5.7. The solid profile is the average over all available measurements, while the dashed profile is the mean of all available daytime observations between 9 and 17 TST. The dotted profile is the mean of the nighttime measurements between 21 and 5 TST. In addition, the mean diurnal cycle of longwave radiative heating is illustrated in Figures 5.8 to 5.11, for each of the three layers and the bulk layer between 2 m and 50 m.

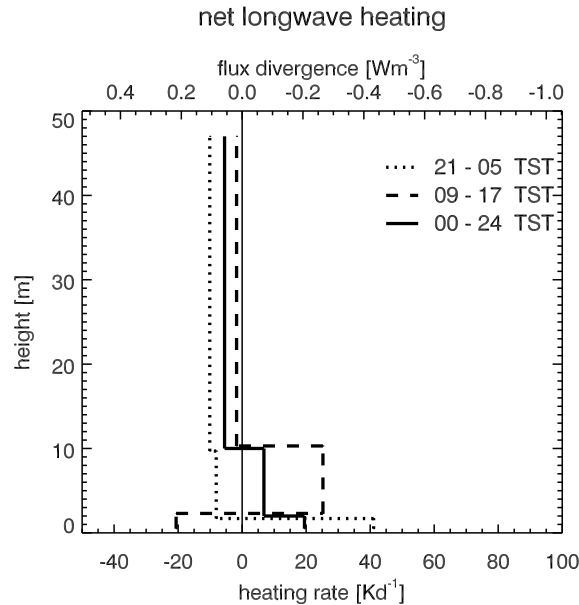


Figure 5.7: Mean profile of the divergence of net longwave flux under mean summer conditions. Solid profile is the daily mean (of $n=3849$ 15-minute values), dotted profile represents nighttime (21-5 TST, $n=1409$), dashed profile daytime (9-17 TST, $n=1256$) conditions.

On average in summer, in the thick layer between 10 m and 50 m a light divergence of -5 Kd^{-1} is observed. Below, in the layer between 2 m and 10 m a mean heating of 7 Kd^{-1} results. Between 0.5 m and 2 m, a mean heating of 20 Kd^{-1} is indicated. Nighttime and daytime profiles of longwave radiative heating differ from the mean profile.

During the day, only a very weak cooling (-2 Kd^{-1}) is observed in the layer between 10 m and 50 m. In the layer below (2-10 m), the sign changes, and a heating of 26 Kd^{-1} is caused by a convergence of the net flux. In the next layer between 0.5 m and 2 m, the sign changes again. Here, a mean cooling of -19 Kd^{-1} results.

The relative importance of the components of net longwave radiative heating is visible in the diurnal cycles. In the layer between 0.5 m and 2 m, both, daytime heating due to convergence of outgoing flux and daytime cooling due to divergence of the incoming flux are very large (Figure 5.8). Absolute values of about 200 Kd^{-1} are reached. The resulting mean daytime heating is very small compared to the two

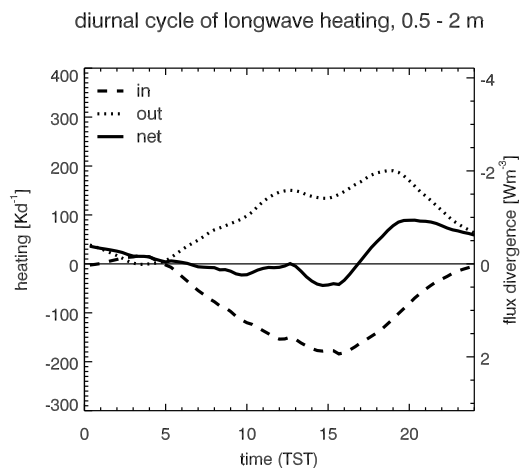


Figure 5.8: Mean diurnal cycle of longwave radiative heating in the layer between 0.5 m and 2 m. Solid curve: net longwave heating; Dashed: incoming; Dotted: outgoing longwave heating. All data collected between May 19th and July 18th, 2002.

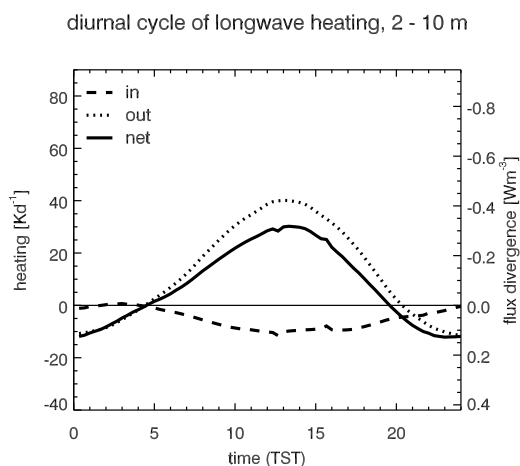


Figure 5.9: As Figure 5.8, for layer between 2 m and 10 m.

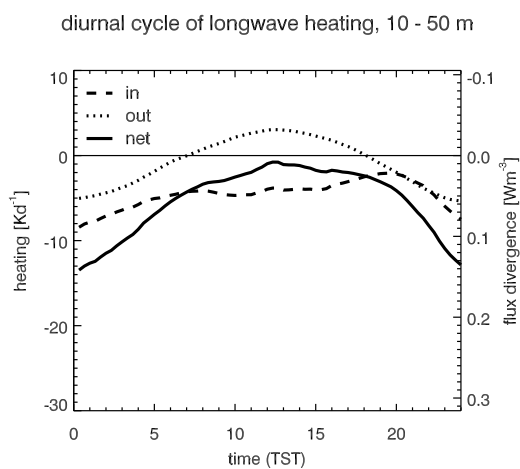


Figure 5.10: As Figure 5.8, for layer between 10 m and 50 m.

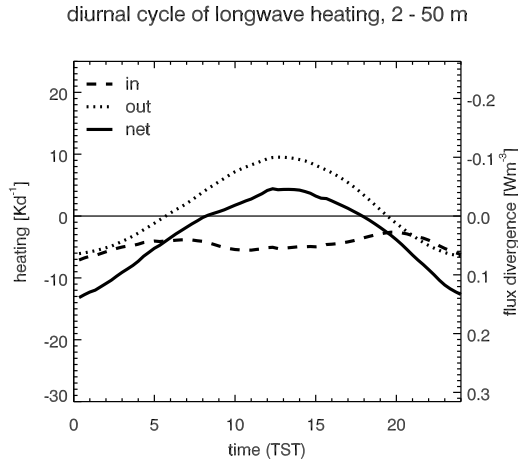


Figure 5.11: As Figure 5.8, for bulk layer between 2 m and 50 m.

counteracting incoming and outgoing components. Between 2 m and 10 m, the heating from outgoing flux convergence dominates over the cooling from the divergence of the incoming flux (Figure 5.9). Maximum net heating of 35 Kd^{-1} is observed at noon. In the layer between 10 m and 50 m, the slight cooling is the result of the divergence of the incoming flux which is slightly larger than the convergence of the outgoing flux (Figure 5.10). Absolute values of heating rates of 5 Kd^{-1} are two orders of magnitude lower than the heating rates observed in the 0.5-2 m layer.

The nocturnal heating rate profile shows a cooling in both, the 10-50 m and 2-10 m layers of -10 Kd^{-1} and -8 Kd^{-1} , respectively. In the shallow layer below, between 0.5 m and 2 m, a heating of 41 Kd^{-1} is indicated. The diurnal cycle reveals the relative importance of the incoming and outgoing components. In the 0.5-2 m layer, a heating due to a converging outgoing flux dominates over a very light cooling due to the divergence of the incoming flux. In the 2-10 m layer, divergence of the outgoing flux controls the net cooling effect. In the thicker layer above, between 10 m and 50 m, the divergence of the incoming flux is stronger than the effect of the outgoing flux, which shows a divergence as well.

5.2.2 Longwave radiative heating under clear and overcast conditions

In the previous section, the diurnal cycle and the vertical structure of longwave radiative heating was presented. The question arises, how the features of longwave heating may look under different meteorological conditions. Therefore subsets of data collected in the summer field season between May 19th and July 18th, 2002, were analyzed, representing different conditions. In the first comparison, longwave radiative heating under clear sky conditions and under overcast skies are compared. The criteria for clear skies are an opacity of less or equal to three tenths, a low and middle cloud amount of one tenth or less, and a high cloud amount less or equal to five tenths. These criteria are not very strict. They were chosen to include cases with high and optically thin cirrus clouds. The criterion for overcast situations was more

straightforward: a low cloud amount of nine tenths or more. Synoptic conditions may vary between observations, and the interpolation of cloud amounts and opacity in between the observation hours may lead to errors.

In Figure 5.12, profiles of longwave radiative heating rates are presented for clear sky (left panel) and overcast conditions (right panel). Average profiles are shown as solid line, daytime (9-17 TST) and nighttime (21-5 TST) profiles as dashed and dotted lines, respectively. Qualitatively, the profiles are very similar.

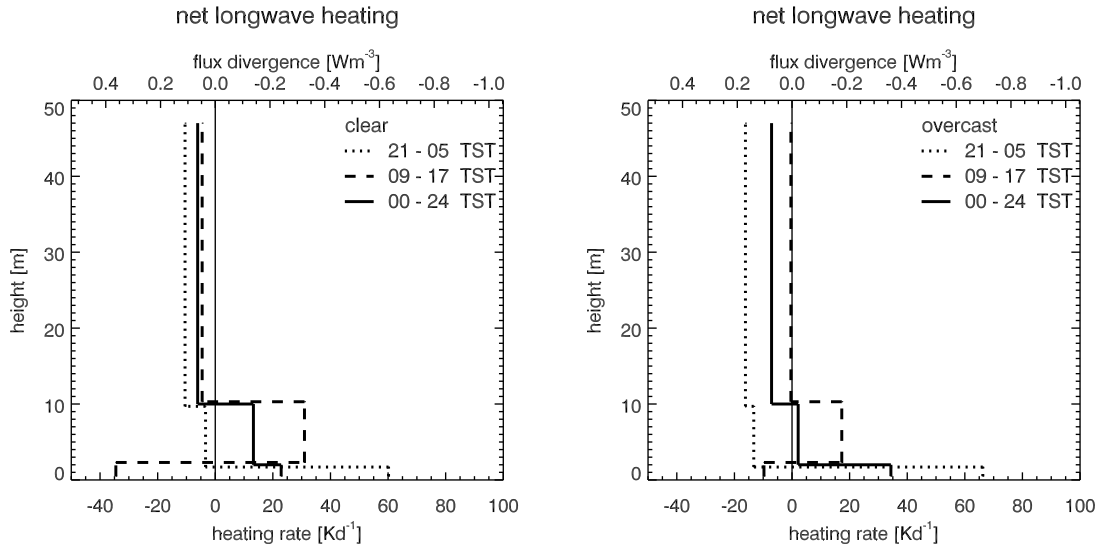


Figure 5.12: Mean profile of the divergence of net longwave flux under clear sky (left panel) and overcast (right panel) conditions. Solid profile is the daily mean (of $n=507$ and $n=611$ 15-minute values for clear sky and overcast, respectively), dotted profile represents nighttime (21-5 TST, $n=134$ and $n=235$, respectively), dashed profile daytime conditions (9-17 TST, $n=187$ and $n=199$, respectively).

For the daily average, a light cooling is observed in the 10-50 m layer, in the layer below (2-10 m) a light heating results. In the layer between 0.5 m and 2 m a stronger heating is seen. Cooling in the upper part of the profile (10 m to 50 m) is the same for clear sky and overcast conditions (-6 Kd^{-1} and -7 Kd^{-1}). Below, between 2 m and 10 m a stronger heating is seen under clear sky conditions (13 Kd^{-1}) than under overcast conditions (2 Kd^{-1}). In the lowest layer investigated (0.5-2 m), daily mean longwave heating is lower under clear skies than under overcast skies (22 Kd^{-1} and 36 Kd^{-1}).

The daytime profiles for clear and overcast situations agree qualitatively as well. Zero heating or a light cooling is found in the layer between 10 m and 50 m, a heating in the 2 m to 10 m layer. Below 2 m a cooling is seen. Clear sky values of longwave radiative heating are larger in absolute values, however. Daytime heating in the 2-10 m layer is, with 30 Kd^{-1} , twice as strong as under overcast conditions. Cooling in the 0.5 m-2 m layer is much stronger under clear skies as well: -36 Kd^{-1} compared to -7 Kd^{-1} under overcast skies.

The nighttime profiles for clear and overcast skies are qualitatively similar as well. A cooling is seen between 10 m and 50 m and between 2 m and 10 m, a heating

in the 0.5-2 m layer below. Cooling in the two upper layers, between 2 m and 10 m and between 10 m and 50 m is about twice as strong under overcast skies than under clear conditions, but all values range between -10 and -20 Kd^{-1} . Heating in the 0.5 m to 2 m layer is the same for both conditions ($60\text{-}65 \text{ Kd}^{-1}$).

The diurnal cycles of incoming, outgoing and net longwave radiative heating are presented for the three layers and for overcast and clear sky situations in Figures 5.13 to 5.15. The diurnal cycles within the bulk layer (2 m to 50 m) is illustrated in Figure 5.16. The relative importance of the divergence of the incoming and outgoing fluxes becomes visible.

For the 0.5 m to 2 m layer, the differences between the diurnal cycles of longwave radiative heating during overcast and clear conditions is not very strong (Figure 5.13). A nighttime net heating and a net cooling around the noon hours is observed for both conditions. The outgoing flux converges at all times, which results in strong heating rates of 100 to 200 Kd^{-1} under both, clear and overcast conditions. Maximum values are reached in the late afternoon, a minimum of zero heating is observed between 3 and 5 TST. This heating effect is counteracted by the divergence of the longwave incoming flux. Maximum cooling of -200 Kd^{-1} under clear sky conditions and of -150 Kd^{-1} are reached, lower cooling (and even heating) is observed in the nighttime hours. In the 0.5 m to 2 m layer, a strong divergence of the incoming flux is balanced by a strong convergence of the outgoing flux. From the analysis of model results, the strong effect of the outgoing flux convergence surprises. As will be shown in Section 6.2, calculations suggest a reduction of the cooling or heating effect caused by the divergence or convergence of the outgoing flux component in the vicinity of the snow surface.

The differences in the diurnal cycles of longwave cooling in the 2 m to 10 m layer are more obvious than in the layer below (Figure 5.14). The difference lies in the magnitudes of heating and cooling. Net heating at noon reaches 50 Kd^{-1} during clear, and only 20 Kd^{-1} during overcast conditions. Nighttime cooling of -20 Kd^{-1} is observed for overcast, cooling of only -5 Kd^{-1} for clear situations. Qualitatively, however, the two diurnal cycles still agree well: a net heating effect between 6 TST and 20 TST, a net cooling at night. The influence of the outgoing flux component dominates over the counteracting influence of the incoming component.

In the 10 m to 50 m layer, the diurnal variation is larger during overcast conditions. Net heating rates range between -20 and 0 Kd^{-1} under overcast skies. Clear conditions lead to a rather constant cooling of about -10 Kd^{-1} in this layer. This stronger diurnal variation which is also seen in Figure 5.12, is caused by the stronger variation of the incoming flux divergence under overcast conditions. It varies between -5 Kd^{-1} during the day and -15 Kd^{-1} at night. Under clear skies, divergence of the incoming flux is rather constant with slightly higher cooling caused at noon (-5 to -10 Kd^{-1}) than during nighttime (0 to -5 Kd^{-1}). For both conditions, outgoing flux shows a divergence during the night. Daytime convergence of the outgoing flux is negligible under clear skies, but leads to a heating of about 5 Kd^{-1} under overcast conditions.

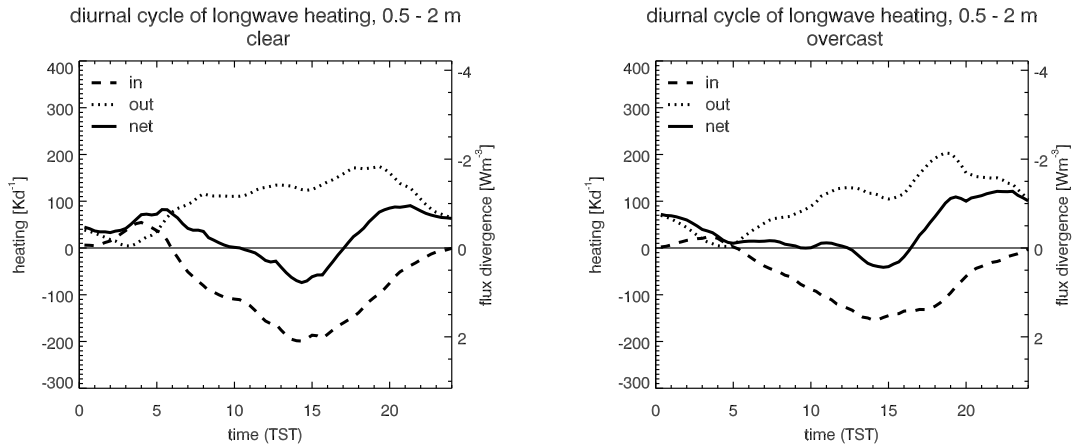


Figure 5.13: Mean diurnal cycle of longwave radiative heating in the layer between 0.5 m and 2 m, for clear sky situations (left panel) and overcast conditions (right). Solid curve: net longwave heating; Dashed: incoming longwave heating; Dotted: outgoing longwave heating. All data collected between May 19th and July 18th, 2002.

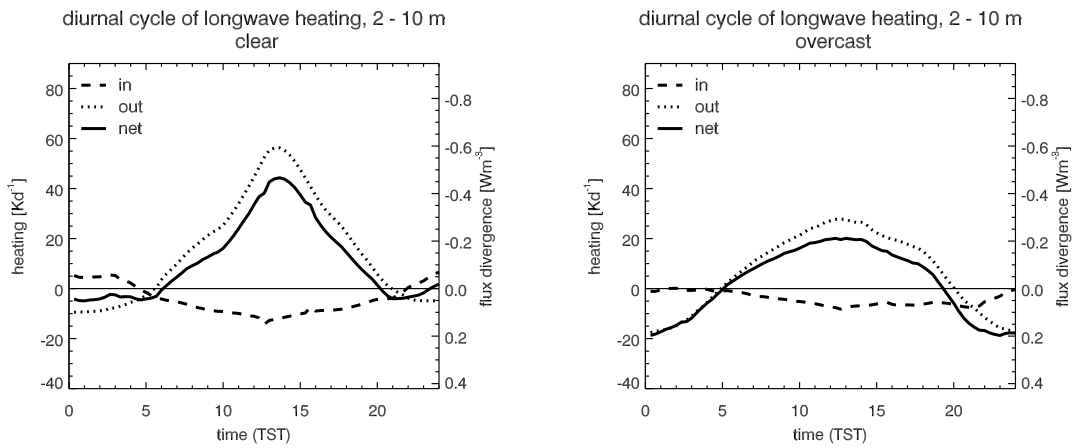


Figure 5.14: As Figure 5.13, for layer between 2 m and 10 m.

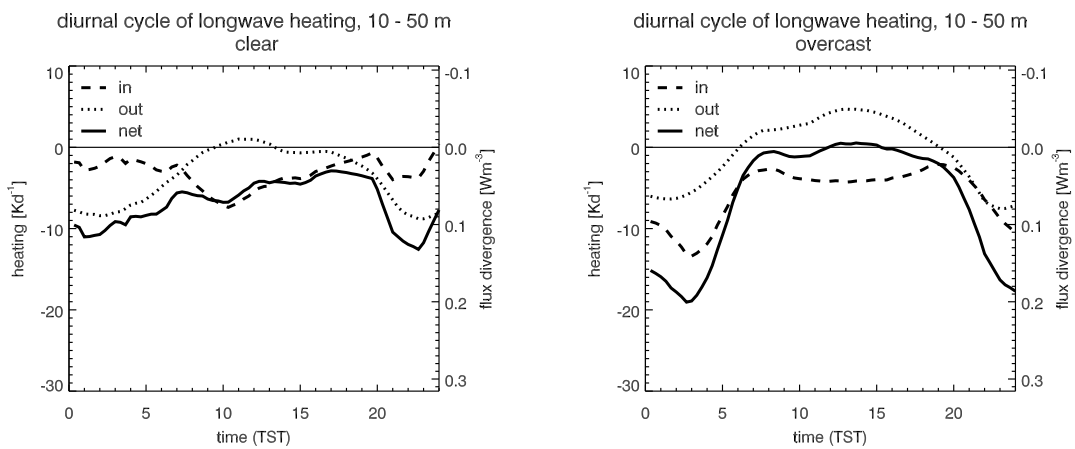


Figure 5.15: As Figure 5.13, for layer between 10 m and 50 m.

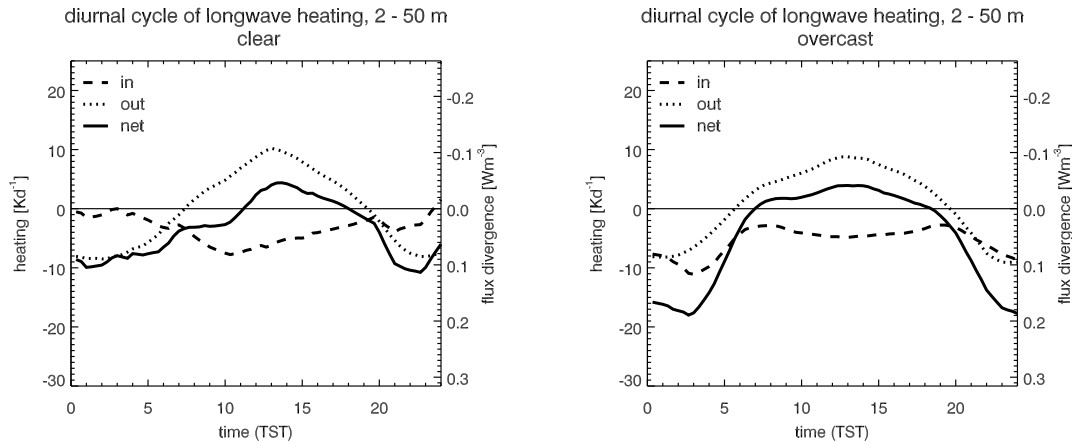


Figure 5.16: As Figure 5.13, for bulk layer between 2 m and 50 m.

5.2.3 Longwave radiative heating under calm and windy conditions

In a second step, differences in the spatial and temporal patterns of longwave radiative heating between calm and windy conditions are presented. Stronger wind leads to a better mixing of the air layers, and the temperature gradients must reduce. As temperature gradients are of prime importance for longwave clear air cooling, a comparison of situations with reduced and enhanced mixing are of interest. Two subsets of data collected in the summer field season between May 19th and July 18th, 2002, were analyzed: One subset contains data which was collected under calm conditions. Calm conditions were defined as situations when the wind speed at the 2 m level was less or equal 2 ms^{-1} . Data collected when the wind speed was greater or equal to 5.5 ms^{-1} is selected as the second subset, representing windy conditions.

In Figure 5.17, profiles of longwave radiative heating rates are presented for calm (left panel) and windy conditions (right panel). Average profiles are shown as solid line, daytime (9-17 TST) and nighttime (21-5 TST) profiles as dashed and dotted lines, respectively.

The mean daily profiles are qualitatively the same in the upper part of the profile. Between 10 m and 50 m a cooling is observed, between 2 m and 10 m a heating. Under calm conditions, the cooling between 10 m and 50 m (-9 Kd^{-1}) and the heating in the 2-10 m layer (8 Kd^{-1}) are about twice as strong as the corresponding cooling and heating under windy conditions. Qualitative differences emerge in the layer between 0.5 m to 2 m. Under calm conditions, a strong heating of 69 Kd^{-1} is observed, while a mean cooling of -13 Kd^{-1} results for the windy case.

Daytime profiles show a minor heating (2 Kd^{-1}) in the 10-50 m layer under calm, and a small cooling (-4 Kd^{-1}) under windy conditions. In the layer between 2 m and 10 m, a stronger daytime heating is reached under calm conditions (56 Kd^{-1}) than under windy conditions (12 Kd^{-1}). For both conditions, a daytime cooling is observed in the shallow 0.5-2 m layer.

The nighttime profiles show the strongest differences between calm and windy

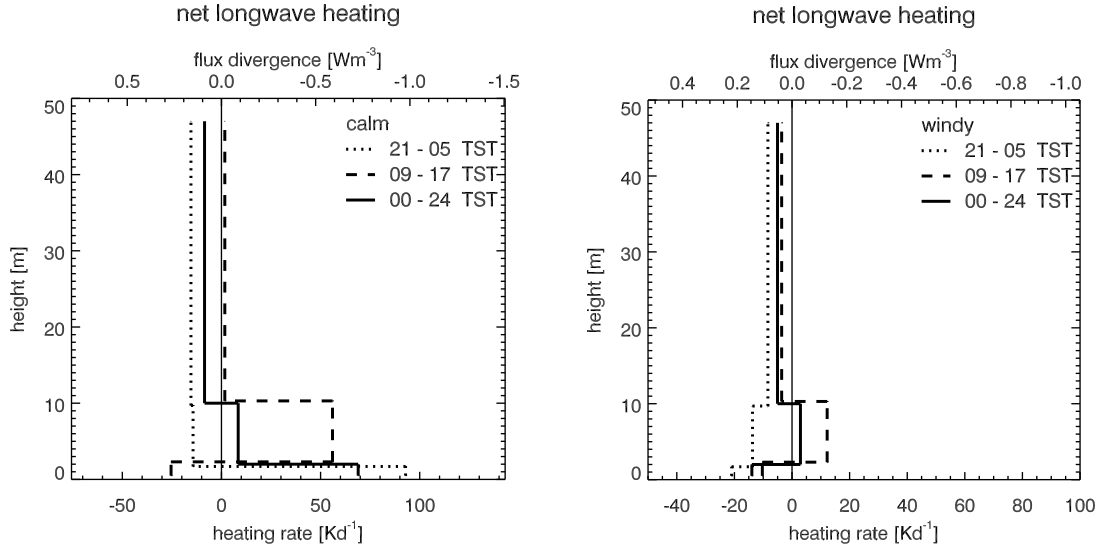


Figure 5.17: Mean profile of the divergence of net longwave flux under calm (left panel) and windy (right panel) conditions. Solid profile is the daily mean (of $n=507$ and $n=611$ 15-minute values for calm and windy conditions, respectively), dotted profile represents nighttime (21-5 TST, $n=423$ and $n=174$, respectively), dashed profile daytime conditions (9-17 TST, $n=180$ and $n=444$, respectively).

situations. Under calm conditions, a cooling is observed above 2 m, and a very strong heating (93 Kd^{-1}) in the layer between 0.5 m and 2 m. Under windy conditions, an increasing cooling towards the surface is suggested.

The diurnal cycles of net, incoming and outgoing longwave radiative cooling are presented for the three layers and for calm and windy situations in Figures 5.18 to 5.20. Diurnal cycles for the bulk layer between 2 m and 50 m can be seen in Figure 5.21. The relative importance of the divergence of the incoming and outgoing fluxes is seen.

In Figure 5.18, the differences in magnitude of the incoming and outgoing components of longwave radiative heating in the 0.5 m to 2 m layer become obvious. Tremendous heating rates of 400 Kd^{-1} and -300 Kd^{-1} are observed under calm conditions. To a great extent, the two components counteract each other. However, in the early evening, a maximum net heating of 200 Kd^{-1} results. In the windy case, the diurnal variations of outgoing flux convergence and of incoming flux divergence are in phase.

The diurnal cycles of longwave flux divergence in the 2 m to 10 m layer (Figure 5.19), shows the dominating effect of the outgoing flux convergence during the day, which counteracts a relatively small cooling due to incoming flux divergence. The magnitudes differ largely between calm and windy conditions. During the noon hours, a net heating of 70 Kd^{-1} is measured during calm, and only 15 Kd^{-1} under windy conditions.

Strong differences can be seen in the diurnal cycles in the 10-50 m layer. Under windy conditions, the diurnal variation is very small. Outgoing flux divergence is rather constant, the heating rate varies around zero. Incoming flux divergence leads

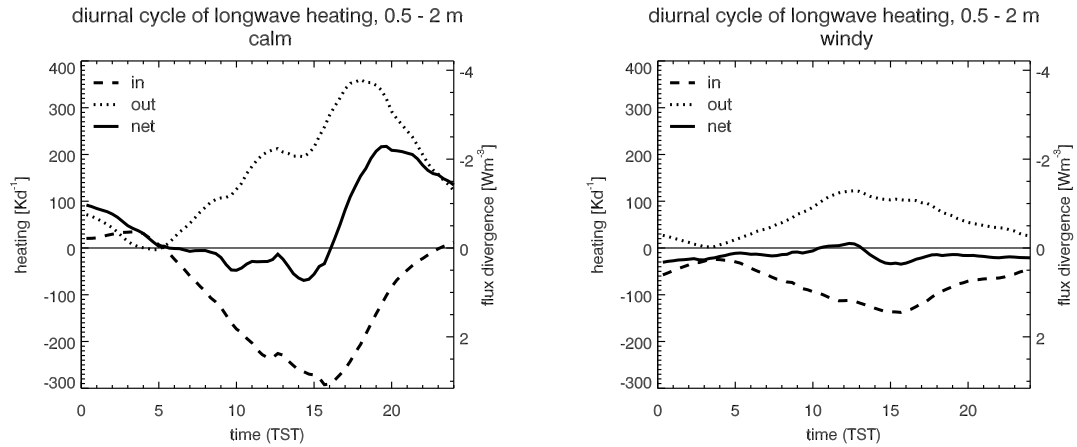


Figure 5.18: Mean diurnal cycle of longwave radiative heating in the layer between 0.5 m and 2 m, for calm situations (left panel) and windy conditions (right). Solid curve: net longwave heating; Dashed: incoming longwave heating; Dotted: outgoing longwave heating. All data collected between May 19th and July 18th, 2002.

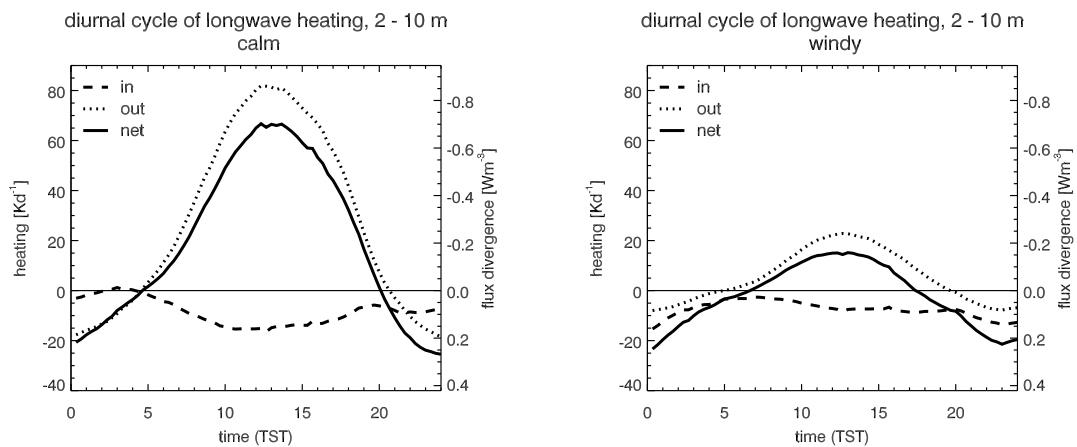


Figure 5.19: As Figure 5.18, for layer between 2 m and 10 m.

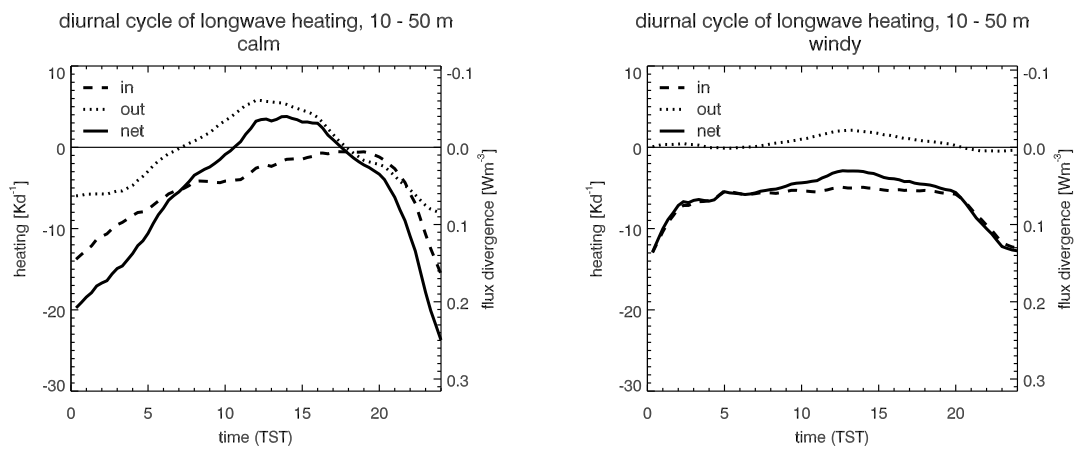


Figure 5.20: As Figure 5.18, for layer between 10 m and 50 m.

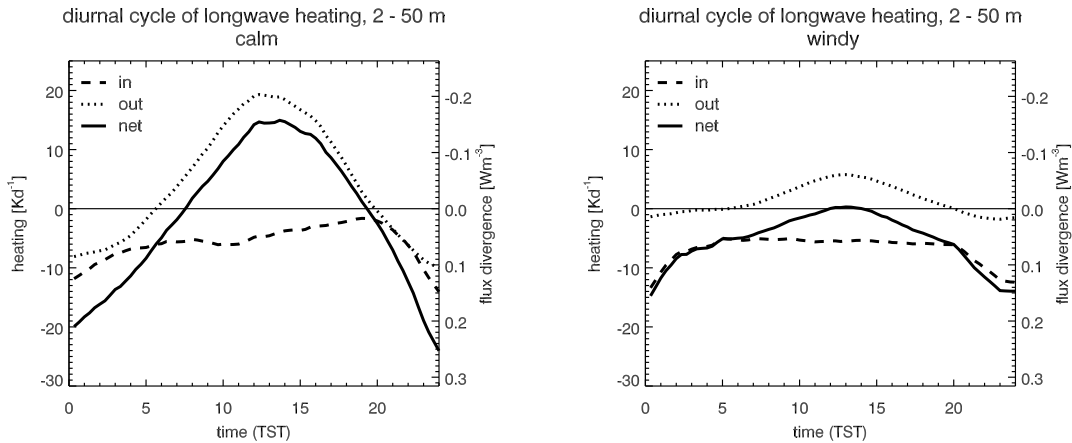


Figure 5.21: As Figure 5.18, for bulk layer between 2 m and 50 m.

to a quite constant cooling which is slightly larger around midnight. This contrasts to the observations under calm conditions, when a pronounced diurnal variation is observed. Incoming flux divergence is strongest at night, and approximately zero in the early afternoon. Outgoing flux induces a cooling during the night and a heating during the day.

5.2.4 Heating rates at night with and without fog formation

To demonstrate the differences in longwave radiative cooling between clear nights and nights with fog development, measurements from two nights in July 2002 are presented.

In the night from 8th to 10th of July, 2002, fog formed in the surface layer, reaching a thickness of about 50 m, but with an increasing density towards the ground. The second night presented here, from July 10th to 11th, 2002, stayed fog free. However, in this summer night, some stratocumulus invaded the sky. During both nights, intensive observation measurements covered longwave fluxes at six levels: 0.5 m, 2 m, 10 m, 20 m, 35 m and 50 m. In Figure 5.22, the incoming and outgoing longwave fluxes measured at 2 m, 10 m and 50 m are shown. Outgoing fluxes are plotted here as positive values. Temperature and humidity profiles for the two nights are presented in Figure 5.23.

In the night with fog formation (July 8th), a divergence of the up-welling flux is observed. The up-welling flux at 50 m is higher than that at 10 m. A slight divergence between 2 m and 10 m is also observed. The incoming longwave flux shows a divergence as well, which is even larger than that of the outgoing flux: the incoming flux at 50 m is smaller than the flux at 10 m, which again is smaller than the incoming flux at 2 m.

During the clear night from July 10th to 11th, a divergence of the outgoing flux is observed in both layers, between 50 m and 10 m as well as between 10 m and 2 m. However, the incoming longwave flux shows a convergence. Incoming flux at 2 m is lower than the incoming flux at 10 m. A slight convergence of the incoming flux

between 10 m and 50 m is indicated as well. The increase of the incoming longwave fluxes at all levels after 22:40 TST can be attributed to invading stratocumulus clouds.

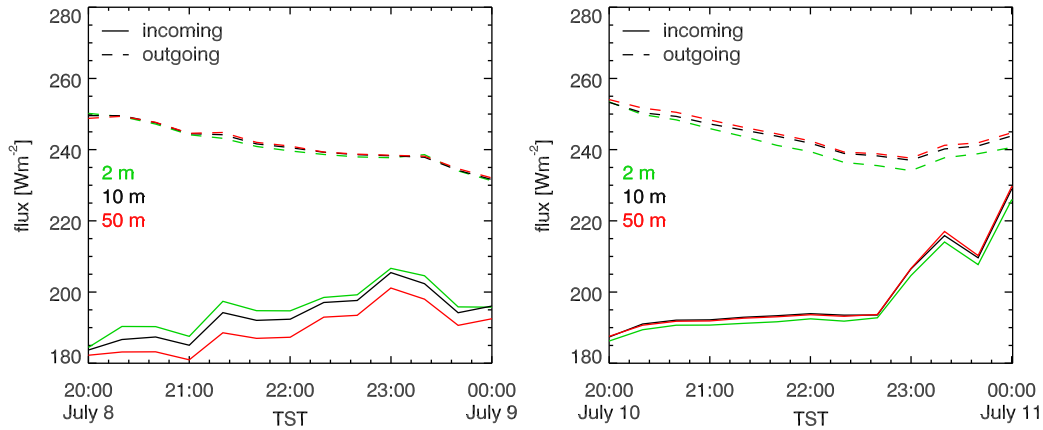


Figure 5.22: Longwave incoming and outgoing fluxes at three levels for two nights, for 20 TST to 24 TST. Left: July 8th-9th, fog formation observed. Right: July 10th-11th, 2002, fog-free, but the influence of invading stratocumulus became visible starting about 23 TST.

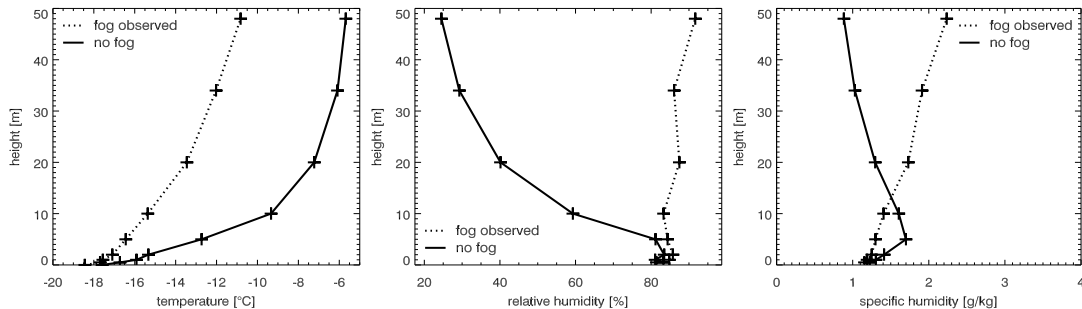


Figure 5.23: Profiles of temperature (left), relative humidity (middle), and specific humidity for two nights between 22 TST and 24 TST. Solid: July 8th-9th, 2002, fog formation observed. Dotted: July 10th-11th, 2002, a night without fog.

The resulting heating rates from the divergence of the incoming, outgoing and net longwave flux for the bulk air layer between 2 m and 50 m for the two nights is shown in the top panels of Figure 5.24. The main difference between the two example nights is the enhanced cooling due to a divergence of the incoming longwave flux when fog has formed. When no fog is present, the incoming longwave flux shows a convergence, dampening the dominating cooling caused by divergence of the outgoing flux. Remarkable strengths of cooling are reached: Cooling under fog conditions amounts to -50 Kd^{-1} , the clear sky cooling to -10 Kd^{-1} .

In the middle and bottom panels of Figure 5.24, heating rates for the same days and time spans are shown, split up in two air layers: the shallow layer between 2 m and 10 m and the thicker layer between 10 m and 50 m.

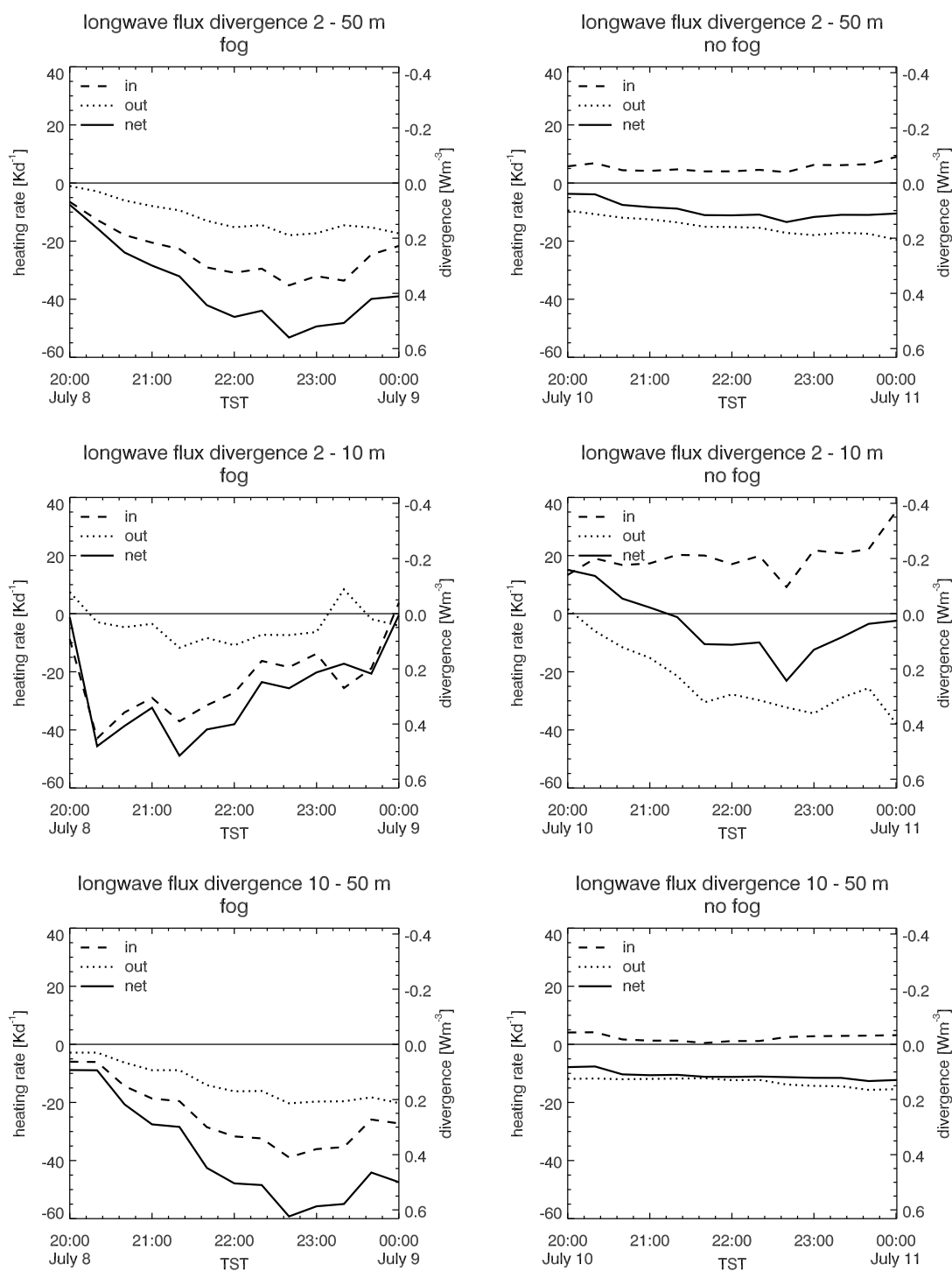


Figure 5.24: Heating rates from incoming, outgoing and net longwave fluxes between 20 TST to 24 TST for the night of July 8th-9th, 2002, under fog conditions (left panels) and for the fog-free night of July 10th-11th, 2002 (right panels). Top panels: Layer between 2 m and 50 m. Middle panels: Layer 2 m to 10 m. Bottom panels: Layer 10 m to 50 m.

In the case without fog forming in the surface layer, cooling rates of the outgoing and incoming flux reach larger values in the layer closer the surface than in the layer above 10 m. In this lower layer (2-10 m), divergence of the outgoing flux reaches -30 Kd^{-1} . However, the convergence of the incoming flux compensates this cooling to a large extent. In the beginning of the night, when any effect of the later invading stratocumulus clouds can be ruled out, a net longwave cooling of more than -10 Kd^{-1} results. In the thicker layer above (10-50 m), longwave radiative heating shows less variation. The slight heating due to the convergence of incoming longwave radiation amounts to less than 5 Kd^{-1} . The stronger divergence of the longwave outgoing leads to a net cooling rate of about -10 Kd^{-1} .

During the night with fog, the divergence of the outgoing longwave flux plays a minor role in the layer between 2 m and 10 m. The divergence of the incoming flux leads to a very strong cooling in the early night. Cooling reaches peak values of -40 Kd^{-1} . With time, however, a reduction of the cooling is observed. In the layer between 10 m and 50 m, the divergence of the incoming longwave flux dominates the strong cooling as well. The cooling is enhanced by the cooling effect associated with a growing divergence of the outgoing flux. Net longwave heating rates of -60 Kd^{-1} are observed.

Longwave radiative heating rates inferred from flux measurements can now be compared to observed temperature changes. In Figure 5.25, the observed temperature tendency in the 2 m to 10 m layer as well as the net longwave heating rate for the same layer are illustrated for the evening with fog formation. The two curves agree remarkably well. One may conclude, that the cooling observed could be attributed to longwave radiative cooling alone.

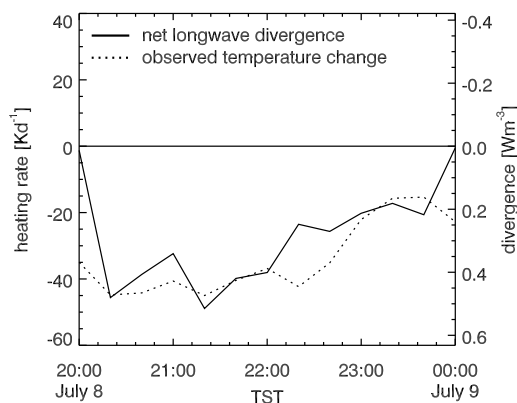


Figure 5.25: Heating rates from net longwave flux divergence and the observed temperature tendency for the night of July 8th-9th, 2002, for the layer between 2 m and 10 m, 20 TST to 24 TST.

More detailed flux and heating rate profiles can be composed using all available data from the intensive observational periods, including the flux measurements at 20 m and 35 m. Mean profiles are compiled for the time between 22 TST and 24 TST. Figure 5.23 shows the mean temperature and relative humidity profiles from tower

profile measurements, the corresponding profiles of net longwave radiative heating are shown in the left panel of Figure 5.26. Observed heating rates for the same time span are shown in the right panel. The temperature gradients above 10 m are remarkably similar for both nights, although the temperatures in the clear night are about 5°C higher. In the fog free night, a stronger stratification develops in the layers below 10 m. While stability smoothly increases towards the surface in the fog case, the temperature profile in the clear sky case shows a very strong temperature gradient below 10 m. This causes a stronger overall stability (0-50 m temperature difference) during the fog-free night. During the night with fog, the air must be at saturation. Thus, the uncertainties in the measurements of relative humidity become clearly visible. During the clear night, saturation is reached at the surface, but relative humidity drops very fast with increasing height.

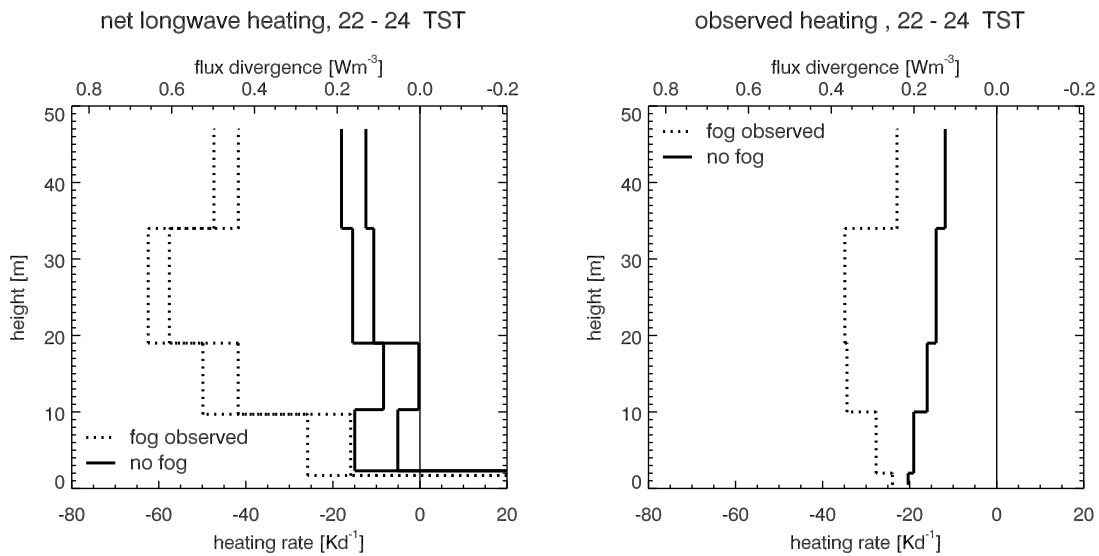


Figure 5.26: Mean longwave net radiative heating rates determined from longwave flux measurements (left) where double lines mark the range of uncertainty and observed temperature tendency (right), 22 TST to 24 TST, for two nights. Dotted: July 8th-9th, 2002, fog formation observed. Solid: July 10th-11th, 2002, a clear night without fog.

During the clear, fog-free night, longwave radiative divergence leads to a cooling of about -10 Kd^{-1} , which is rather constant or slightly increasing with height. The observed temperature tendency shows a cooling in the same range. However, a decrease of cooling with height from -20 to -12 Kd^{-1} is seen. In the case with fog formation, longwave radiative flux divergence leads to a increasing cooling up to the 20-35 m layer. Cooling is about -20 Kd^{-1} in the 2-10 m layer, and reaches -60 Kd^{-1} in the 20-35 m layer. Further above, longwave radiative cooling is reduced. The shape of the profile of observed temperature change is quite similar. An increasing cooling from the lower layers to the layer between 20 and 35 m, and a rapid reduction of cooling above is observed. Measured longwave cooling is larger than the observed temperature tendency. Observed cooling amounts to only about half of the longwave radiative cooling.

Longwave radiative heating and fog: diurnal cycle A subset of data from the observations in the summer field season 2002 between May 19th and July 18th was analyzed for the times when the synoptic observations indicate fog. A mean diurnal cycle of longwave radiative flux divergence under fog conditions is composed. There are times during the day, however, when fog was never observed. This leads to gaps in the diurnal dataset. Figure 5.27 shows the diurnal cycles for incoming, outgoing and net longwave radiative heating for the two layers between 2 and 10 m, and between 10 m and 50 m. The main difference between fog-free cases and situations with fog are revealed when comparing these figures with Figure 5.9 and Figure 5.10. When fog has formed, the influence of the incoming heating rate component becomes more important. A strong cooling effect due to the divergence of the incoming flux is introduced, which is even larger than the cooling due to the outgoing component under clear conditions.

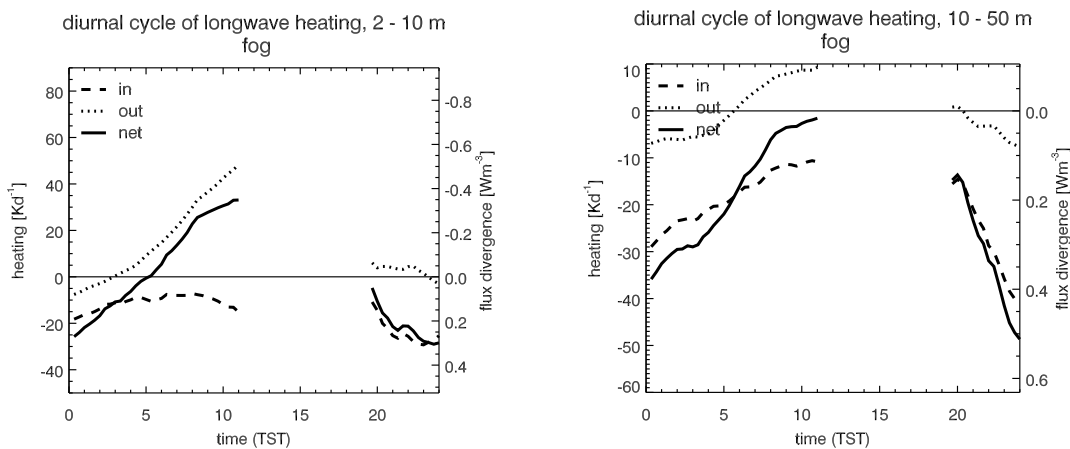


Figure 5.27: Mean diurnal cycle of longwave radiative heating in the layers between 2 m and 10 m (left panel) and 10 m to 50 m (right) under fog conditions. Solid curve: net longwave heating; Dashed: incoming longwave heating; Dotted: outgoing longwave heating. All data collected between May 19th and July 18th, 2002.

5.2.5 Longwave radiative heating and temperature gradient

A correlation of heating rate with the temperature gradient becomes apparent when longwave radiative flux divergence data is analyzed. In earlier studies on longwave radiative flux divergence, the link between flux divergence and temperature gradient has already been emphasized (Eliseev et al., 2002; Sun et al., 2003; Ha and Mahrt, 2003).

In this section, the relationship between measured longwave radiative heating rate and temperature gradient is presented. It will be shown that a dependence of longwave flux divergence on the temperature gradient exists, but that this dependence changes with height. The data used in this analysis was collected during the summer 2002 field season (May 19th to July 18th, 2002). It comprises more than 3700 15-minute means. Divergence measurements for the three layers 0.5-2 m, 2-10 m and 10-50 m, and corresponding means of temperature difference across these layers are

available. For the calculation of temperature gradients, the z -coordinate is defined positive upward, so a positive gradient represents stable conditions.

At the beginning, however, the relationship between longwave radiative heating and temperature gradient is presented for the bulk layer between 2 m and 50 m. For the same layer, under mid latitude summer conditions, the relationship between the outgoing flux difference and the temperature difference has been presented by Sun et al. (2003).

Bulk Layer, 2 m to 50 m The relationship between the bulk longwave radiative heating between 2 m and 50 m and the temperature gradient across this layer is shown in Figure 5.28. In the upper panels, the relationship is shown for the incoming longwave flux divergence, in the middle panels for the outgoing, and in the bottom panels for the net longwave flux divergence. The panels on the left show all the data points collected between May 19th and July 18th, 2002. In the panels on the right, the heating rate data is binned into equal width bins of temperature gradients. Plotted is the mean temperature gradient and the mean heating rate of all the points included in each bin. The error bars indicate one standard deviation of the data points.

Visually, a slight increase of incoming heating rate is suggested with increasing stability. However, a large number of outliers is seen, which indicate the occurrence of strong cooling over the whole range of stabilities. The vertical spread of these outliers is much larger than the slight increase with growing stability which is suggested by the dense cloud of data under stable conditions. As shown in Section 5.2.4, the incoming flux shows a strong divergence under conditions when fog is present. As will be shown later, the outliers can be attributed to such fog situations. A better correlation is found between the outgoing longwave heating and temperature gradient. A r^2 of 0.56 is reached for a linear regression. For the relationship of the net longwave heating rate with temperature gradient, the large spread of cooling rate introduced by the fog situations reduces the goodness of the linear fit to a r^2 of 0.23. It can be shown that the outliers in the regime of very strong cooling under stable conditions are originating from fog situations: In Figure 5.29, which correspond exactly to the top and bottom left panels of Figure 5.28, we highlight the data points collected between 22 and 24 TST during the two nights discussed in Section 5.2.4. The data plotted as diamonds was collected under clear conditions (July 10th, 22-24 TST), the crosses represent the data collected under fog conditions (July 8th, 22-24 TST).

Near surface layer, 0.5 m to 2 m For the 0.5 m to 2 m layer, a correlation between heating rate and temperature gradient is not as obvious as for the bulk layer between 2 m and 50 m (Figure 5.30). Incoming flux tends to diverge in this layer, under stable as well as under unstable conditions. Situations with stable conditions and resulting heating are found in the data as well. A maximum cooling of up to -400 Kd^{-1} is observed. Strongest cooling occurs under rather moderate temperature gradients. Maximum heating rates of up to 200 Kd^{-1} are observed, large heating rates tend to occur under stronger stabilities. The outgoing flux in the 0.5 m to 2 m

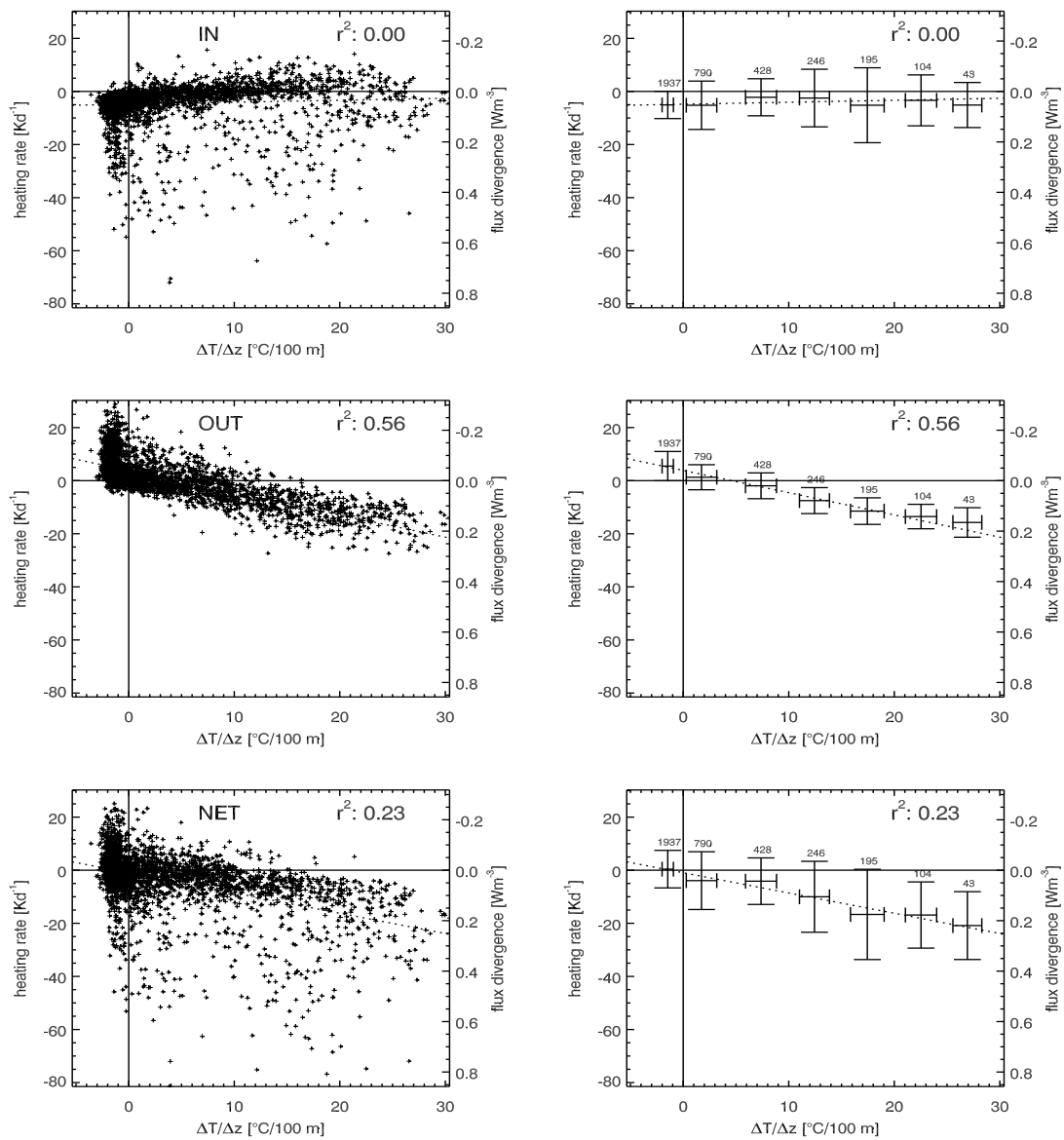


Figure 5.28: Incoming (top), outgoing (middle) and net (bottom) longwave radiative heating rate versus layer mean temperature gradient for the layer between 2 m and 50 m. Left panels: Each data point represents a 15-minute average ($n=3700$), collected between May 19th and July 18th, 2002. A linear fit is indicated by a dashed line. The r^2 value for the fit is given in the top right. In the right hand panels, heating rate data is binned into equal width bins of temperature gradients. Plotted is the mean temperature gradient and the mean heating rate of all the points included in each bin. Error bars indicate one standard deviation of the data points. The number of data points in each bin is printed above the plotting symbol. The dotted line indicates the linear fit through all data points.

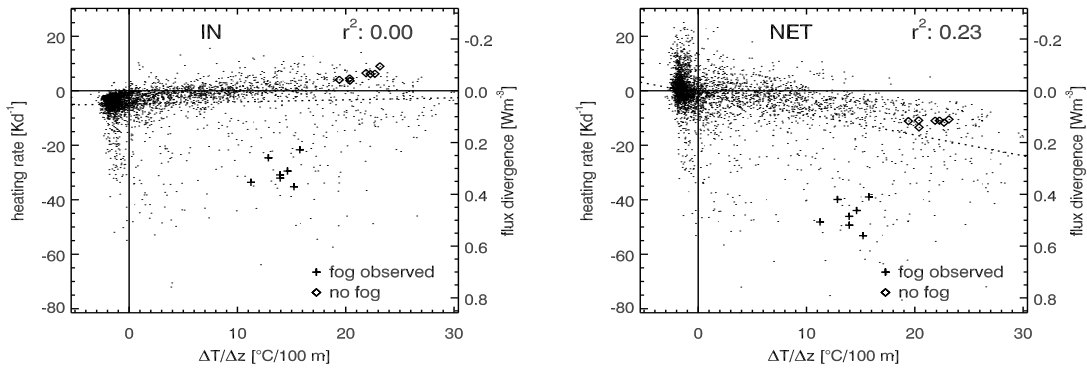


Figure 5.29: Incoming (left panel) and net (right panel) longwave radiative heating rate versus layer mean temperature gradient for the layer between 2 m and 50 m. Each data point represents a 15-minute average ($n=3700$), collected between May 19th and July 18th, 2002. A linear fit is indicated by a dashed line. The r^2 value for the fit is given in the top left. Data plotted with diamonds was collected during clear sky conditions on July 10th (22-24 TST), data in crosses under fog conditions on July 8th (22-24 TST). Under fog conditions, the incoming flux shows a strong divergence.

layer tends to converge under stable conditions, and heating rates of 400 Kd^{-1} and more result. Under unstable conditions, heating is also the predominant resulting effect. However, under near neutral conditions, a cooling of up to -200 Kd^{-1} can be observed. The relationship between temperature gradient and net longwave radiative cooling in the 0.5-2 m near-surface layer can be seen in the third panel of Figure 5.30. Under near neutral conditions, the observed net longwave heating rate ranges between -300 Kd^{-1} and 300 Kd^{-1} . Towards more stable conditions, a trend to stronger heating rates is seen. Unstable conditions lead to a net heating in this layer as well. In the lower right panel of Figure 5.30, the data is binned into equal width bins of temperature difference across the air layer. The points plotted represent the mean heating rate of all values in each temperature difference bin, at the mean temperature difference. The vertical and horizontal error bars represent one standard deviation of all heating rate values and temperature differences in each bin. In this figure, the trend to stronger heating under increasingly stable conditions is well visible.

Eliseev et al. (2002) report very similar results. Their measurements with an optoacoustic receiver were carried out over dry-steppe. They measured cooling rates between 0.1 m and 2 m of up to -240 Kd^{-1} , and heating of up to 450 Kd^{-1} . Maximum cooling is reported for isothermal conditions. Eliseev et al. (2002) see the same trend to heating under increasingly unstable conditions, as suggested in Figure 5.30. Due to a lack of data for stable conditions, however, they could not resolve the increasing heating rate with higher stabilities.

2 m to 10 m layer The relationship between temperature gradient and the longwave radiative heating rates for the layer between 2 m and 10 m is shown in Fig-

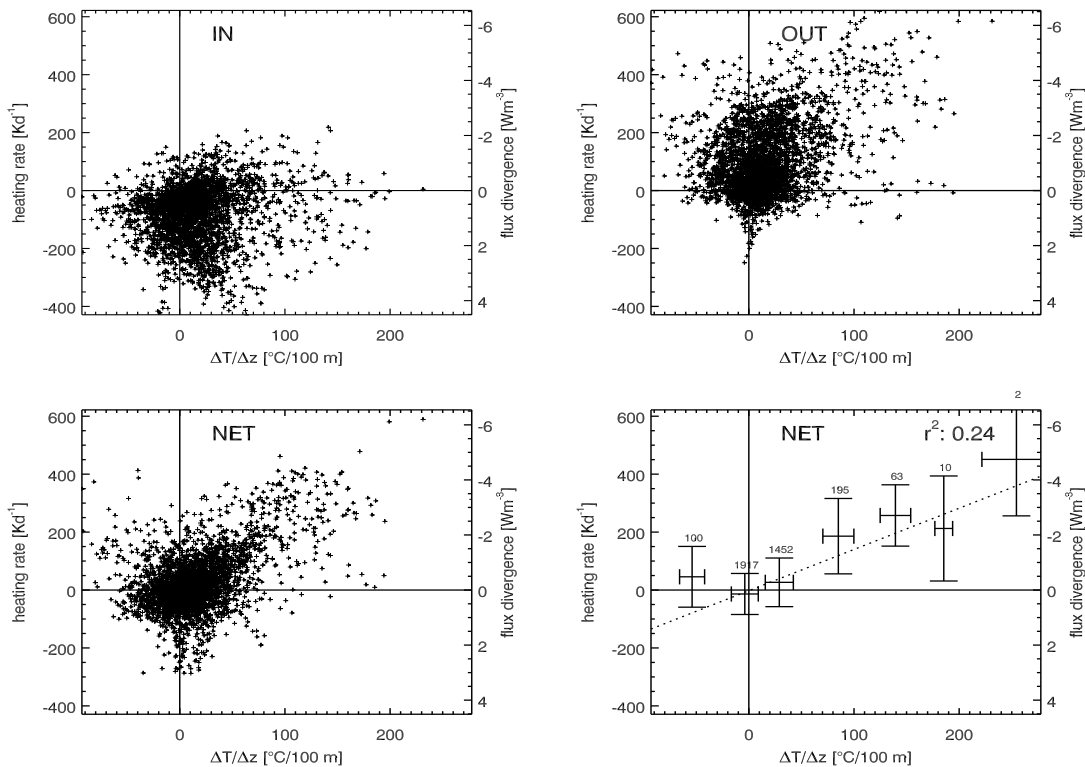


Figure 5.30: Incoming (top left), outgoing (top right) and net (bottom left) longwave radiative heating rate versus layer mean temperature gradient for the layer between 0.5 m and 2 m. Each data point represents a 15-minute average ($n=3700$) collected between May 19th and July 18th, 2002. In the bottom right, net longwave heating rate data is binned into equal width bins of temperature gradients. Plotted is the mean temperature gradient and the mean heating rate of all the points included in each bin. The number of data points in each bin is printed above the plotting symbol. Error bars indicate one standard deviation of the data points. A linear fit through the data is indicated by the dashed line, the r^2 value for the fit is given in the top right.

ure 5.31. The incoming component shows an increasing heating with increased stability, but there are several data points showing a cooling of up to -50 Kd^{-1} . These outliers represent data collected under fog conditions (c.f. Section 5.2.4). The divergence of the outgoing longwave flux increases with stability, producing strong cooling (-50 Kd^{-1} at temperature differences of 1 Km^{-1}). Under near-neutral conditions, a large variation of the heating rate is observed (-20 to 100 Kd^{-1}). The relationship between the two heating rate components and temperature gradient are of opposite sign: Increased stability leads to a increased heating caused by the convergence of the incoming flux, and to a increased cooling due to stronger divergence of the outgoing flux. When the net longwave heating data is binned into several subsets representing different ranges of temperature gradients, the relationship between net longwave radiative heating rate and temperature gradient becomes more apparent (Figure 5.31, bottom left panel). Growing stability leads to a stronger net cooling. A temperature difference in the 2 m to 10 m layer of 1 Km^{-1} corresponds to a cooling

rate of about -50 Kd^{-1} or a divergence of about 0.5 Wm^{-3} .

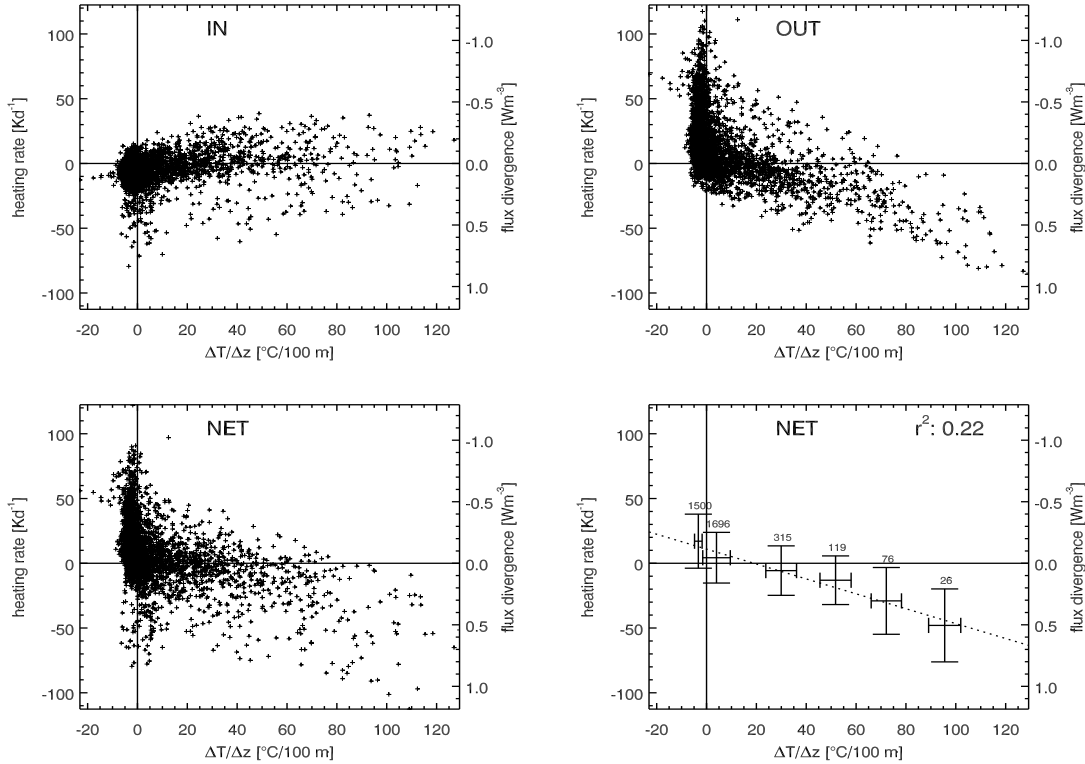


Figure 5.31: Incoming (top left), outgoing (top right) and net (bottom left) long-wave radiative heating rate versus layer mean temperature gradient for the layer between 2 m and 10 m. Each data point represents a 15-minute average ($n=3700$) collected between May 19th and July 18th, 2002. In the bottom right, net longwave heating rate data is binned into equal width bins of temperature gradients. Plotted is the mean temperature gradient and the mean heating rate of all the points included in each bin. Error bars indicate one standard deviation of the data points. The number of data points in each bin is printed above the plotting symbol. A linear fit through the data is indicated by the dashed line, the r^2 value for the fit is given in the top right.

10 m to 50 m layer In the thicker layer between 10 m and 50 m, temperature differences across the layer depth are an order of magnitude lower than for the layers below. Neglecting the data collected under fog conditions, the heating rate due to incoming flux convergence shows a slight increase with growing stability. On the other hand, an increased cooling with stronger stabilities is observed for the outgoing component. The dependence of the outgoing flux divergence on temperature gradient is stronger. It dominates over the heating effect due to the incoming component. The net longwave heating rate thus shows an increasing cooling with increasing stability (Figure 5.32).

Longwave radiative flux divergence exhibits a dependence on the temperature gradient (temperature difference across the air layer). However, the relationship is

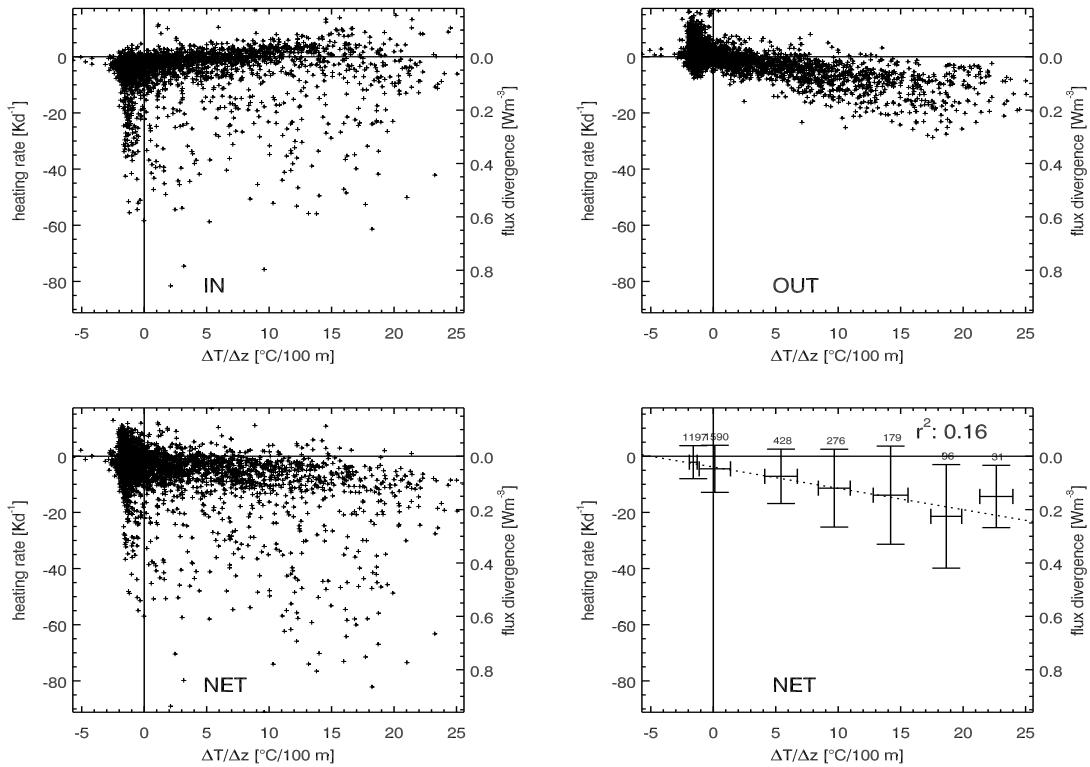


Figure 5.32: Incoming (top left), outgoing (top right) and net (bottom left) longwave radiative heating rate versus layer mean temperature gradient for the layer between 10 m and 50 m. Each data point represents a 15-minute average ($n=3700$) collected between May 19th and July 18th, 2002. In the bottom right, net longwave heating rate data is binned into equal width bins of temperature gradients. Plotted is the mean temperature gradient and the mean heating rate of all the points included in each bin. Error bars indicate one standard deviation of the data points. The number of data points in each bin is printed above the plotting symbol. A linear fit through the data is indicated by the dashed line, the r^2 value for the fit is given in the top right.

not the same for all layers investigated. In the air layers above 2 m, net longwave flux shows a growing divergence with higher stabilities. In the air layer between 0.5 m and 2 m, the opposite is the case. Under fog-free conditions, the increased cooling with growing stability above 2 m is caused by the dependence of the divergence of the outgoing flux on temperature gradient. Incoming flux shows the opposite behavior, an increasing convergence with growing stability. Under conditions with fog, strong cooling is induced by a strong divergence of the incoming longwave flux.

Diurnal variation of longwave flux divergence and temperature gradient

Yet another way to analyze the relationship between temperature gradient and longwave radiative heating rate is offered by the investigation of the diurnal cycles. The mean diurnal cycles of temperature gradients across the four layers under investigation (the bulk layer between 2 m and 50 m, 0.5-2 m, 2-10 m and 10-50 m) are

presented as solid lines in Figure 5.33. The range of one standard deviation is plotted as dotted lines, to visualize the variability in the diurnal cycle. The mean diurnal cycles of longwave radiative heating rates were presented in Figures 5.8 to 5.10.

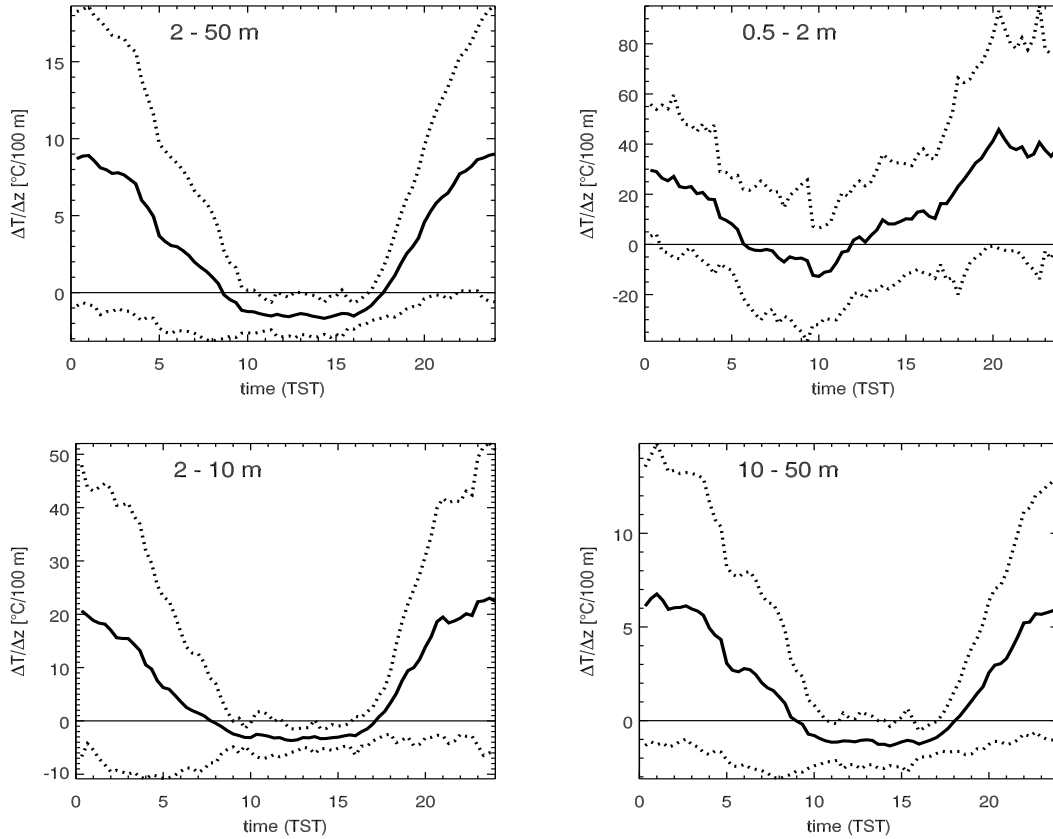


Figure 5.33: Mean diurnal cycle of temperature difference across the air layers between: 2 m to 50 m (top left), 0.5 and 2 m (top right), 2 m and 10 m (bottom left), and 10 m and 50 m (bottom right). Data represents summer conditions (May 19th to July 18th, 2002). Dotted lines mark plus and minus one standard deviation for each 15-minute average.

When the values of temperature difference across the bulk layer between 2 m and 50 m from a diurnal cycle analysis are plotted against the heating rate values, a rather smooth relationship results (Figure 5.34, top left panel). Incoming longwave divergence leads to a cooling of about -5 Kd^{-1} for the entire range of temperature differences. A clear dependence of the outgoing longwave flux divergence on temperature gradient is found: a temperature difference of $9 \text{ K}/100 \text{ m}$ corresponds to a cooling of -5 Kd^{-1} , zero heating results for a temperature gradient of $3 \text{ K}/100 \text{ m}$. Under slightly unstable conditions, with $-1 \text{ K}/100 \text{ m}$, a heating between 7 and 10 Kd^{-1} is induced. The resulting dependence of net longwave heating on temperature gradient can be approximated by a linear fit (dotted line). The goodness of the fit, r^2 , reaches 0.96 . At a temperature difference of $1 \text{ K}/100 \text{ m}$ the sign of the heating rate changes. Under isothermal and unstable conditions, a heating results, under stable conditions, a cooling is observed.

For the 0.5 m to 2 m layer, a form of a hysteresis is observed for the relationship

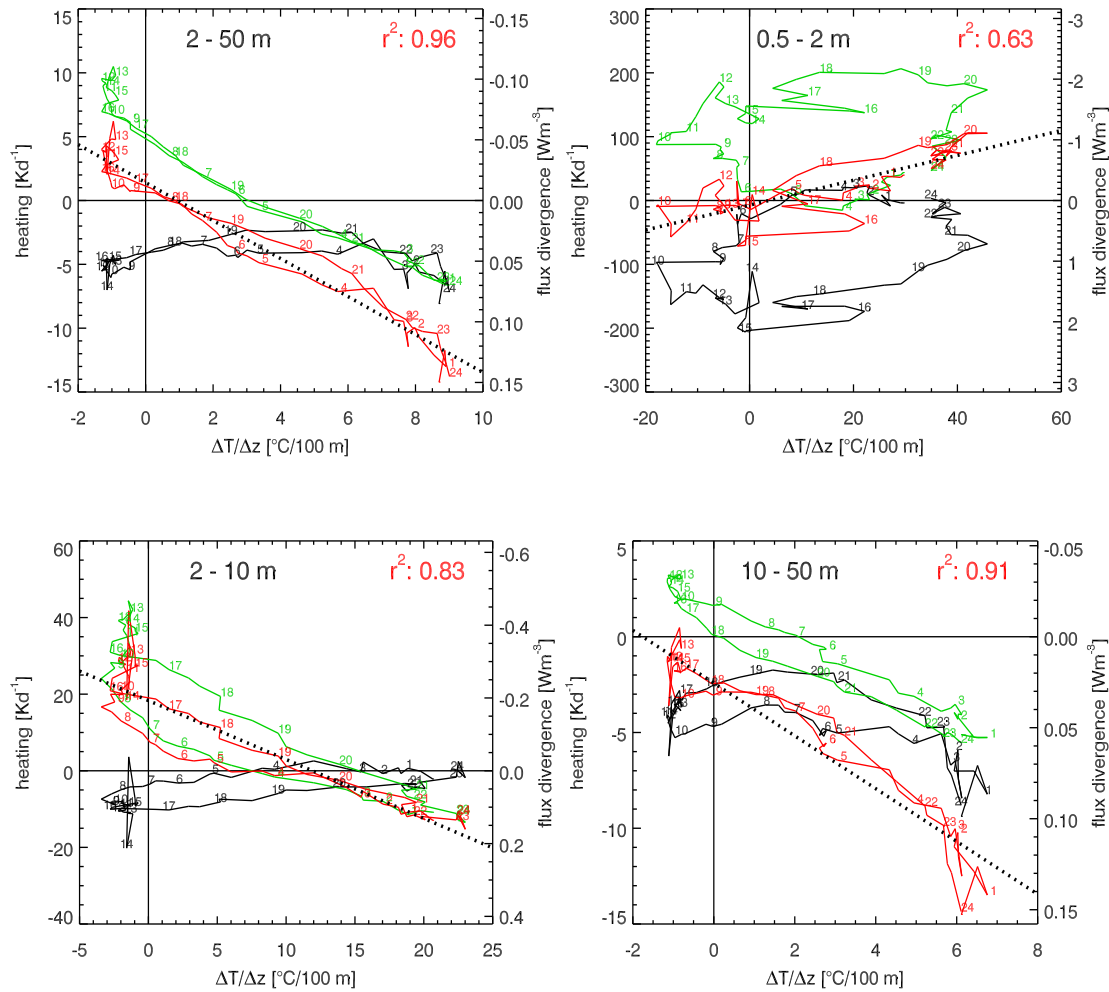


Figure 5.34: Relationship between mean diurnal temperature gradient across air layer and longwave radiative heating rates, for layer between between 2 m and 50 m (top left), 0.5 and 2 m (top right), 2 m and 10 m (bottom left), and 10 m and 50 m (bottom right). Data represents mean summer conditions (May 19th to July 18th, 2002). Heating rates due to divergence of incoming (black), outgoing (green) and net longwave flux (red). Numbers refer to the time represented by the data point in TST. A linear fit approximates the relationship between net longwave heating and layer temperature difference. The goodness of the fit r^2 is given in the upper right of each panel.

between temperature gradient and incoming and outgoing flux divergence. Nevertheless, the relationship for the net longwave flux divergence can be approximated linearly with an r^2 of 0.63. In contrast to the bulk 2-50 m layer, an increase of heating with stability can be seen. Numbers in the plots indicate the time of day (TST) corresponding to the measurements. During the transition from early evening into the night, stability increases. While the heating due to a negative outgoing flux divergence stays at maximum values (200 Kd^{-1}), the cooling due to the incoming flux reduces. After the maximum stability of $45 \text{ K}/100 \text{ m}$ is reached, cooling due to incoming flux divergence reduces to zero, and stays close to zero until 6 TST. With decreasing stability, the outgoing flux convergence reduces as well, and zero heating

results between 3 and 6 TST. After 6 TST, stratification becomes unstable in this near-surface layer. Heating due to outgoing flux convergence and cooling due to divergence of the incoming flux both increase to values of $\pm 100 \text{ Kd}^{-1}$. As they tend to compensate each other, the net radiative heating rate is small. The outgoing heating and incoming cooling further increase to magnitudes of $\pm 200 \text{ Kd}^{-1}$ towards the evening hours, while the stratification changes from unstable to stable conditions.

A similar but much smaller hysteresis can be seen in the interplay between mean diurnal changes of longwave radiative heating rates and temperature stratification in the layers between 2 m and 10 m, and 10 m and 50 m (Figure 5.33, bottom panels). While the net longwave heating rate in the layer between 0.5 m and 2 m shows a trend to increased heating under more stable conditions, the opposite is seen for the layers above. A stronger stability leads to weaker heating or stronger cooling. In the 2-10 m layer, the transition from a net longwave radiative heating to a cooling is observed at stabilities of about $12 \text{ K}/100 \text{ m}$. At stronger stratifications, a cooling results. In the layer from 10 m to 50 m, a light cooling results even for slightly unstable conditions. Linear fits reach an r^2 of 0.83 and 0.91 for the 2-10 m and 10-50 m layer, respectively.

5.2.6 Longwave radiative heating and humidity

The relationship between humidity and longwave radiative heating rate is investigated based on the data collected in the summer season 2002 (May 19th and July 18th, 2002). As shown in previous section, longwave heating rates shows a dependence on temperature gradient. Humidity strongly depends on temperature. As strong stabilities are usually associated with low temperatures, a link between humidity and temperature gradient exists. To analyze the relationship between longwave radiative heating rates and humidity, data therefore needs to be grouped into classes that represent only a certain limited range of temperature gradients.

2 m to 50 m bulk layer The top left panel of Figure 5.35 shows the relationship between humidity at 2 m and temperature difference across the 2 m to 50 m bulk layer. The dataset is divided into subsets, including only a certain range of temperature differences. The dashed lines mark the borders of these temperature difference bins. The dependence of the net longwave heating rate on humidity is shown for the data contained in three selected bins (temperature difference ranges are $-5-0 \text{ K}/100 \text{ m}$ (top right panel), $5-10 \text{ K}/100 \text{ m}$ (bottom left), and $20-25 \text{ K}/100 \text{ m}$ (bottom right)). A linear fit is plotted through the data, and the r^2 value is given in the upper right of each panel. From this analysis, there are no indications for a dependence of the heating rate on humidity.

0.5 m to 2 m layer A similar picture arises from the analysis for the 0.5 m to 2 m layer. Figure 5.36 shows the relationship between the humidity at 2 m and the temperature differences across this layer. Dashed horizontal lines indicate the borders of the temperature difference bins. For three of these bins, the relationship between humidity and net longwave radiative heating is shown ($-50-0 \text{ K}/100 \text{ m}$ (top right panel), $50-100 \text{ K}/100 \text{ m}$ (bottom left), and $100-150 \text{ K}/100 \text{ m}$ (bottom right)). In

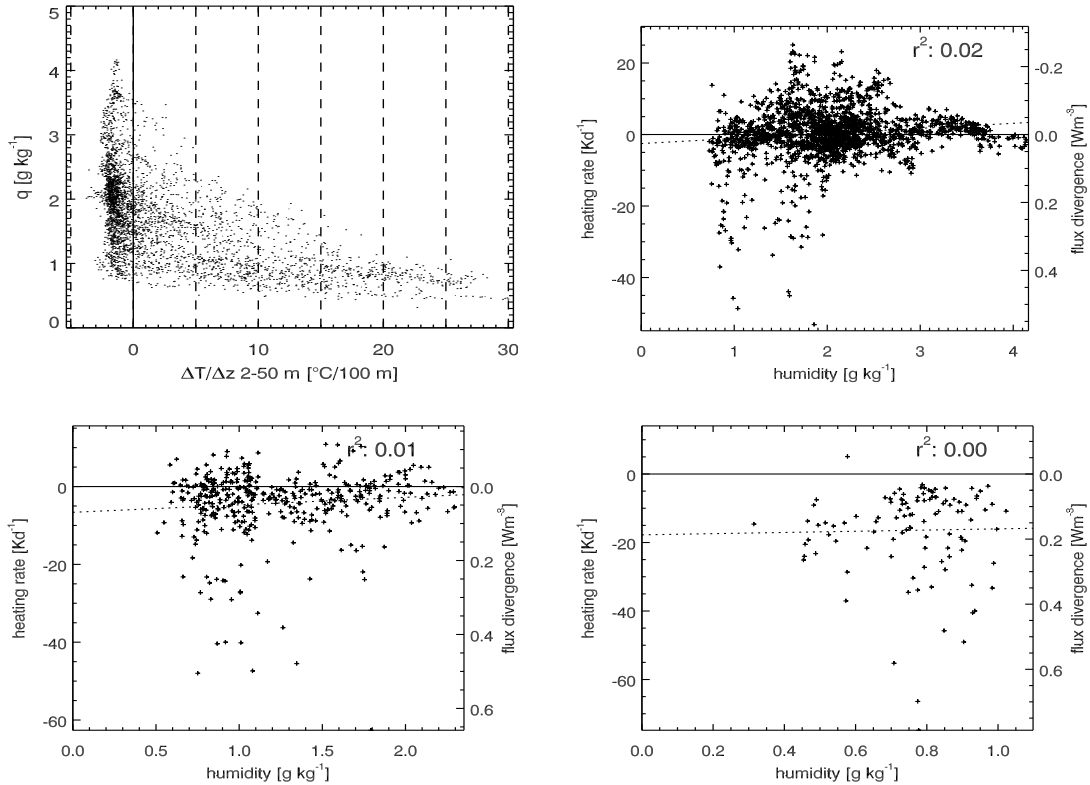


Figure 5.35: Net longwave radiative heating rate in the bulk layer between 2 m and 50 m versus specific humidity (2 m). Top left panel shows the relationship between specific humidity and the temperature differences between 50 m and 2 m. The data is separated into classes of temperature difference, marked by the dashed lines. These subsets of data are used to investigate the dependence of net longwave heating rate on specific humidity. Results for three subsets are shown: -5-0 K/100 m (top right), 5-10 K/100 m (bottom left), and 20-25 K/100 m (bottom right). A linear fit is plotted through the data, and the goodness of the fit, r^2 is given in the top right.

two of the subsets, a decrease of heating rate with increasing humidity is suggested by a linear fit, while one subset suggests an increase. For all analyzed subsets, the r^2 of the linear fit is below 0.25.

2 m to 10 m layer Figure 5.37 reveals the relationship between humidity (2 m) and temperature difference across the 2 m to 10 m layer. Again, dashed lines mark the borders of the bins chosen for further analysis. The analysis for three subsets is presented. They contain data collected under conditions when the temperature differences across the layer ranged between -10 and 0 K/100 m (top right panel), 10 and 20 K/100 m (bottom left), and 30 and 40 K/100 m (bottom right). Again, no significant linear relationship is found between humidity and net longwave radiative heating.

An influence of humidity on longwave radiative flux divergence can not be inferred from our observations. The quality of the linear fits between net longwave heating rates and humidity expressed as r^2 is below 0.25 for all analyzed cases in the 0.5-2 m,

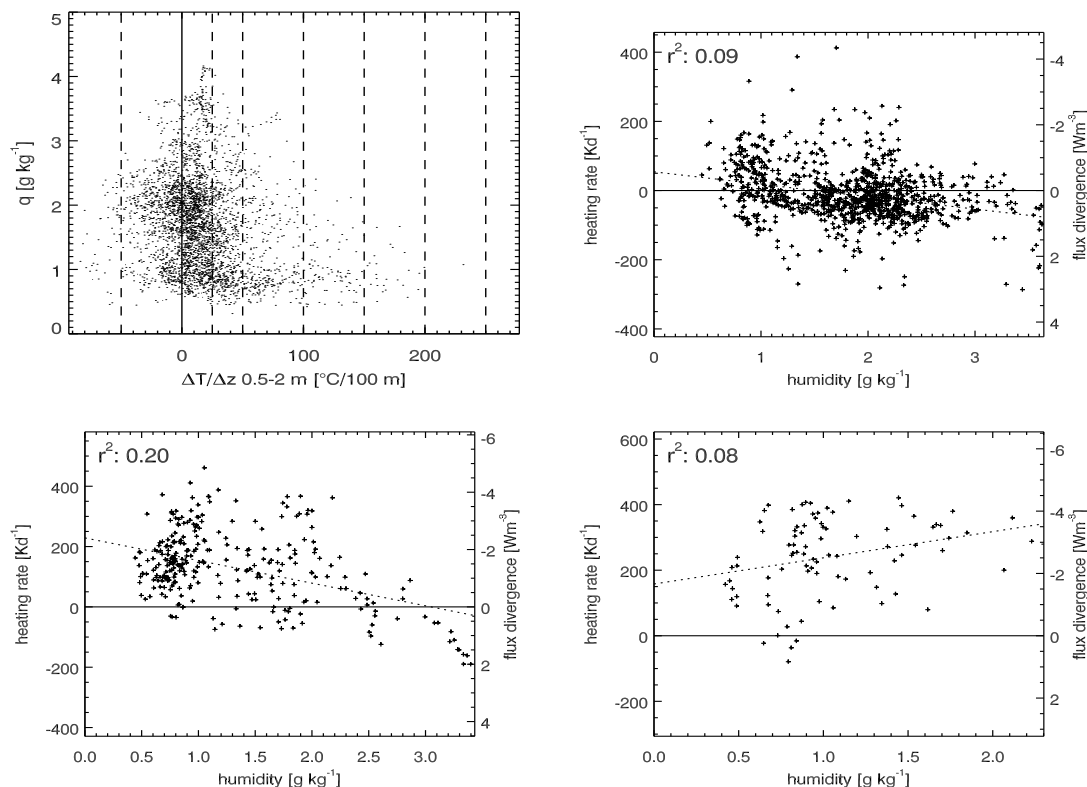


Figure 5.36: Net longwave radiative heating rate in the layer between 0.5 m and 2 m versus specific humidity (2 m). Top left panel shows the relationship between specific humidity and the temperature differences between 2 m and 0.5 m. The data is separated into classes of temperature difference, marked by the dashed lines. These subsets of data are used to investigate the dependence of net longwave heating rate on specific humidity. Results for three subsets are shown: -50-0 K/100 m (top right), 50-100 K/100 m (bottom left), and 100-150 K/100 m (bottom right). A linear fit is plotted through the data, and the goodness of the fit, r^2 is given in the top left.

2-10 m and 2-50 m layers.

5.2.7 Year-round measurements of bulk divergence between 2 m to 50 m

The divergence of longwave radiative flux between the 2 m and 50 m level has been measured continuously over the 14-month period between June 2001 and July 2002. Monthly means of the divergence of the incoming, outgoing and net longwave flux are presented as heating rates in Figure 5.38. Remarkable strengths of cooling are reached in the cold season. In January 2002, a monthly mean longwave radiative cooling of -19 Kd^{-1} is observed. During the summer months, the net cooling amounts to -1 to -5 Kd^{-1} . The relative importance of the incoming and outgoing contribution to the net divergence changes over the year. From August to May, a cooling due to the divergence of the outgoing flux dominates over a small effect of the divergence of the incoming flux. In the summer months, however, the divergence of the incoming

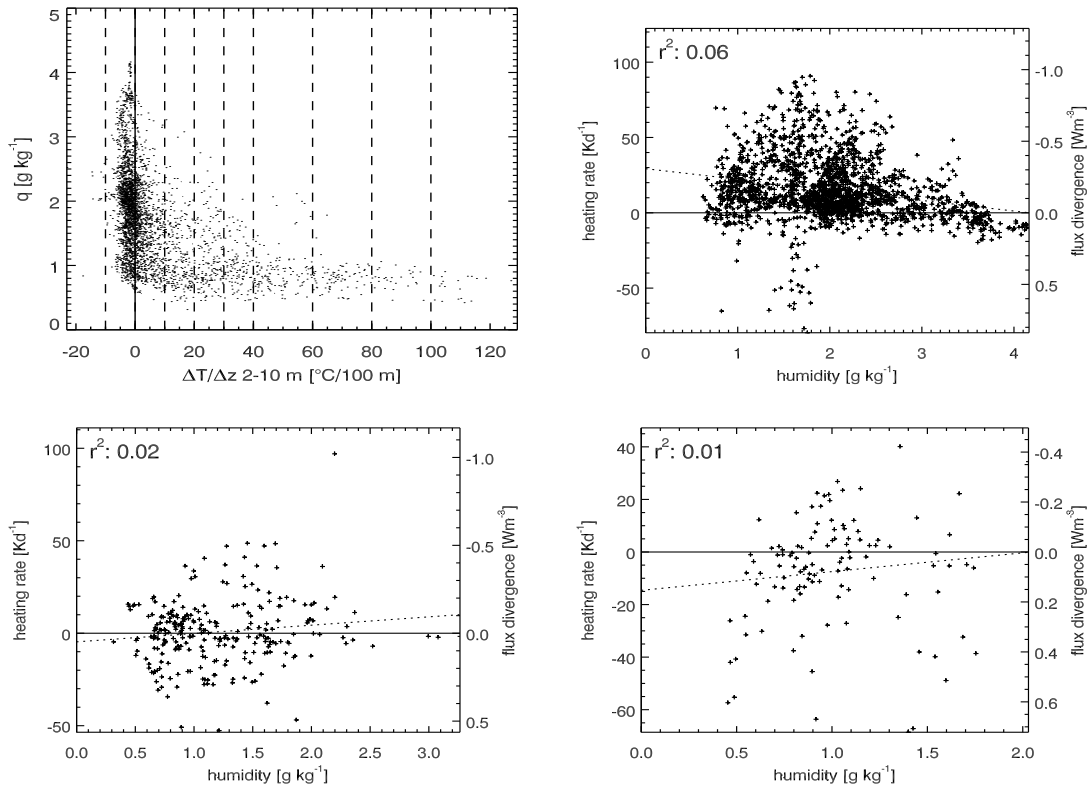


Figure 5.37: Net longwave radiative heating rate in the layer between 2 m and 10 m versus specific humidity (2 m). Top left panel shows the relationship between specific humidity and the temperature differences between 10 m and 2 m. The data is binned into bins of temperature difference, marked by the dashed lines. These subsets of data are used to investigate the dependence of net longwave heating rate on specific humidity. Results for three subsets are shown: -10 to 0 K/100 m (top right), 10-20 K/100 m (bottom left), and 30-40 K/100 m (bottom right). A linear fit is plotted through the data, and the goodness of the fit, r^2 is given in the top left.

flux dominates the net longwave radiative cooling. From May to July, monthly mean values of the outgoing flux show a slight convergence.

A strong correlation between monthly mean longwave radiative heating rates and the monthly mean temperature gradient between 2 m and 50 m is found. In Figure 5.39, the relationship between temperature gradient and heating rate is approximated by linear fits. Incoming flux shows a trend to cause heating under higher stabilities, while outgoing flux shows a increasing cooling with higher stabilities. The cooling due to the outgoing flux divergence is stronger than the heating due to incoming flux convergence. With higher stabilities, a stronger cooling results due to the divergence of the net longwave flux.

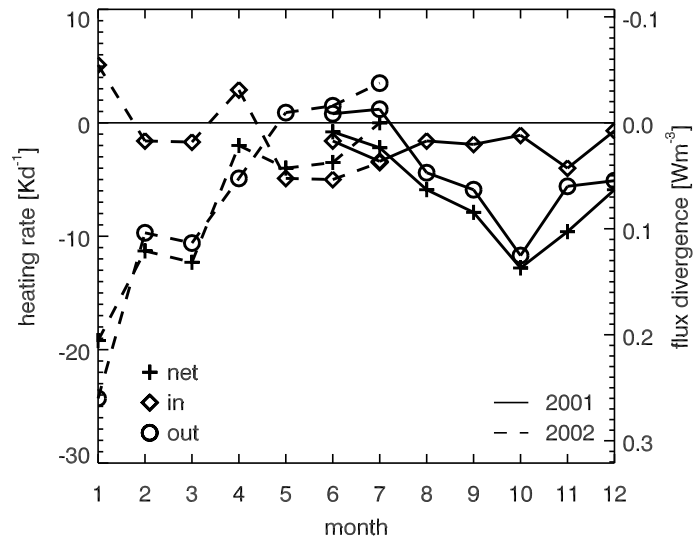


Figure 5.38: Annual cycle of monthly mean longwave radiative flux divergence composed from measurements in year 2001 (solid line) and 2002 (dashed). Divergence of the incoming longwave flux (diamonds) plays a minor role. Net longwave radiative flux divergence (crosses) is mainly controlled by the divergence of the outgoing longwave flux (circles).

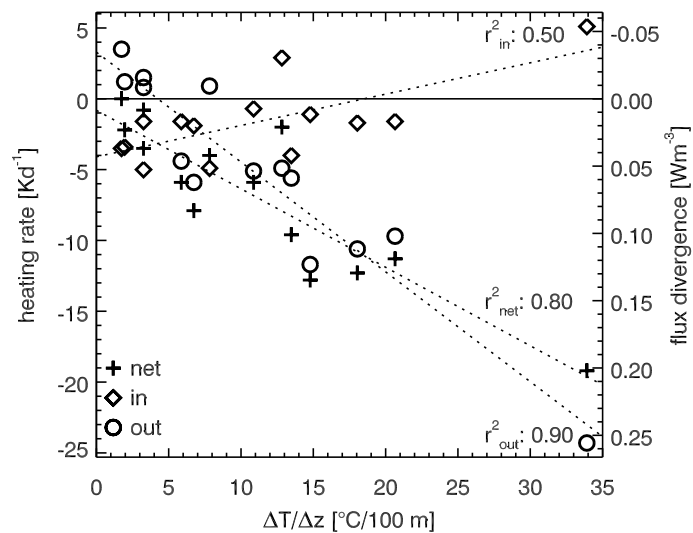


Figure 5.39: Monthly mean longwave radiative flux divergence versus monthly mean temperature difference between 2 m and 50 m. Divergence of the incoming longwave flux (diamonds) shows a trend to increased heating with higher stability. Net longwave radiative flux divergence (crosses) is mainly controlled by the divergence of the outgoing longwave flux (circles), which shows a stronger divergence with higher stability.

6 Model calculations

A radiative transfer model is used to simulate the measurements of radiative flux divergence taken in the field. The use of the model is not primarily to reproduce observed fluxes or heating rates. The model is used to understand the processes that influence the spectral composition of the longwave radiative flux divergence that can not be resolved by the broadband measurements. Also, the effects of parameters such as humidity, temperature gradients and surface temperature are studied in sensitivity experiments.

6.1 MODTRAN Radiative transfer model

The MODerate Resolution TRANsmittance (MODTRAN) code calculates atmospheric transmittance and radiance for wavenumbers from 0 to 50000 cm^{-1} . The spectral resolution is primarily 2 cm^{-1} (Berk et al., 1999). It was developed in the Air Force Research Laboratory / Geophysics Directorate from the LOWTRAN model, and has adopted all its capabilities as spherical refractive geometry, solar source functions, scattering (Rayleigh, Mie, single and multiple), and default profiles of gases, aerosols, clouds, fog and rain (Kneizys et al., 1996). The model employs a large pre-stored spectral dataset: Band model parameters for molecular line absorption are based on the HITRAN96 database (Rothman et al., 1998). Extinction coefficients for continuous molecular absorption, such as the H_2O continuum (Clough et al., 1989) and for heavy molecules (e.g. CFCs), and for water particulates (rain, clouds, fog) are included. The correlated- k (CK) approach is used, which is a adaptation of the k -distribution method for inhomogeneous paths. This method significantly improves the accuracy of radiance calculations (Berk et al., 1998; Berk et al., 1999). All calculations are done using 33k values in the correlated- k method, and the DISORT algorithm (Stamnes et al., 1988) is used with eight streams for the calculation of the scattered thermal radiances. MODTRAN was tested as a model to calculate heating rates. Comparisons of calculated heating rates with results of line-by-line models show a very good agreement (Anderson et al., 1995; Bernstein et al., 1996).

6.1.1 Model input

For the present application, MODTRAN input was assembled from atmospheric profiles of temperature and humidity, containing ninety atmospheric levels. The lowest

levels were constructed from measurements at the meteorological tower. Above the tower height, the profile measured by the radio sounding was used, which had been launched at the closest designated time. A standard atmosphere data set (sub-arctic summer) was used for the levels above the maximum sounding height (approximately 17 km). The height distribution of the ninety input layer heights plays an important role, especially when strong surface inversions are observed (Räisänen, 1996). Therefore, the lowest 10 m were covered by 14 levels and the lowest kilometer contained 42 levels. Model calculations were performed for wave-numbers between 20 and 2500 cm^{-1} , with a spectral resolution of 1 cm^{-1} . Radiance calculations were done for equivalent zenith angles of 51.8° for down-welling and 125° for up-welling radiances. The equivalent zenith angles were determined from multiple radiance calculations resolving the zenith angle range as fine as 5° . Fluxes were inferred from the radiances calculated for the equivalent zenith angles.

6.1.2 Model output

The model output of MODTRAN is organized in several output files, called 'tapes'. The main output, 'tape6' repeats the input parameters and lists the spectral radiances. At the end of this file, the integrated fluxes at each of the model input levels are given. These can be used to calculate the longwave radiative flux divergence (longwave radiative heating rates).

When the model is run in the longwave spectral region, several radiance components are listed in a spectral table ('tape7'): the path thermal down-welling radiation, the up-welling path thermal radiation, the surface emitted and the ground reflected radiation. These radiance components can be integrated spectrally, separated in the down-welling and up-welling flux components, if they are calculated for the equivalent zenith angles. The effect of Gaussian quadrature on the accuracy of fluxes obtained from radiances is thoroughly discussed by Clough et al. (1992)

Yet another file lists spectral fluxes (irradiances) at all input levels of the model. Incoming and outgoing fluxes and the flux from the solar disc (direct solar, which is very small in the longwave) are tabulated. From this output file, spectral radiative flux divergence (spectral heating rates) can be inferred.

6.2 Results from model calculations

In this section, model calculations using the radiative transfer model MODTRAN are presented. In the first subsection, two model calculations with MODTRAN are presented that represent typical nighttime and daytime conditions. It is shown that the model qualitatively represents the observed profiles of longwave radiative flux divergence. This shows that the model is suited to perform sensitivity studies to investigate the influences of different factors on the longwave radiative heating rate profile, such as the shape of the temperature profile, temperature gradient and humidity.

In the second subsection the importance of the shape of the temperature profile is demonstrated. A linear representation of a surface inversion and a curved profile are shown to lead to very different profiles of radiative heating rates.

The third subsection demonstrates the height dependency of the relationship between longwave radiative flux divergence and temperature gradient. Close to the surface, increasing stability leads to an increase of radiative heating. Above 10 m, however, increasing stability enhances radiative cooling. This subsection also deals with the relationship of humidity and longwave flux divergence. While measurements suggest no significant relationship between humidity and longwave radiative heating, the model calculations indicate the opposite. Higher humidity enhances to cooling (heating) due to longwave radiative flux divergence (convergence).

The influence of the surface emissivity on the profile of longwave radiative heating is investigated in a simple model experiment. Results of this experiment are presented in the fourth subsection. It is demonstrated that over cold gray bodies, a heating due to the convergence of the outgoing flux may result.

The fifth subsection presents radiative flux divergence from a spectral viewpoint. Model calculations reveal the relevant spectral regions where the cooling and heating takes place.

The sixth subsection deals with the causes for heating and cooling. The different contributions to the divergence of the outgoing flux by the three outgoing flux components (path thermal, surface emitted, ground reflected) are resolved by the model calculations with MODTRAN.

Subsection seven focuses on the spectral differences of radiative flux divergence under clear sky and fog conditions.

6.2.1 Stable nighttime and unstable daytime conditions

Two observed cloud free situations were modeled using MODTRAN. The first situation represents stable nighttime conditions (July 10th, 21.40 LT), the second a daytime situation with unstable stratification close to the surface (July 9th, 12.40 LT). The temperature profile for the model input was constructed from measurements on the meteorological tower and from radiosonde data. Temperatures in the lowest 50 m were smoothed by fitting a function through the temperatures measured on the tower. Above 50 m, the temperatures from the radiosonde ascends were used. The temperature profiles for both situations are illustrated in Figure 6.1. Relative humidity was linearly interpolated between the 2 m measurement with a dew point mirror hygrometer and the measurement of the radiosonde at 80 m.

The modeled flux profiles are shown in Figure 6.2. The upper, middle and bottom panels shows the incoming, outgoing and net flux profiles, respectively. The left hand panels show the flux profiles emerging from the stable case, the profiles on the right hand side the fluxes determined for the unstable case.

Under stable conditions, the incoming flux shows a decrease towards the surface in the lowest 50 m. The profile of the downward flux closely resembles the temperature profile. Air layers must be heated due this convergence of the incoming flux. The

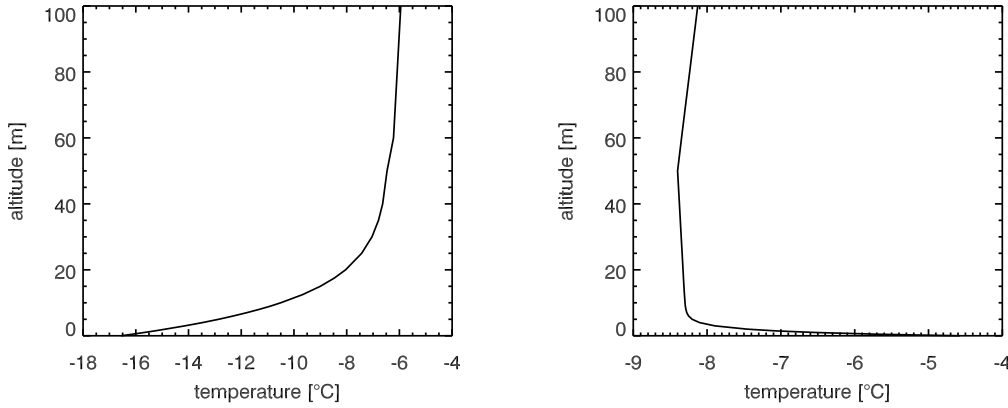


Figure 6.1: Temperature profile from two observations: Left: July 10th, 21:40 LT representing stable conditions and a strong surface inversion; Right: July 9th, 12:40 LT, representing strong instabilities close to the surface. Profiles were smoothed.

upward flux shows an increase towards the surface. The increase is strongest between 20 m and 10 m. Closer to the surface, the increase is greatly reduced. The divergence of the outgoing flux must lead to a cooling of the air layers. The profile of the net longwave flux shows an increase towards the surface in the upper part of the profile, and a decrease in the lowest few meters above the surface. The slope of the net flux profile in the upper part is dominated by the outgoing flux profile, while the strong decrease of the incoming flux in the lowest few meters dominates the net flux profile close to the surface, where the slope in the outgoing flux profile is reduced. A change from a divergence of the net longwave flux in the upper part of the profile to a convergence close to the surface results.

Under unstable conditions the opposite is seen. Incoming flux shows an increase towards the surface, resulting in a cooling. Again, the flux profile closely resembles the temperature profile. The outgoing flux decreases towards the surface. This convergence must lead to a heating of the air layers. A reduction of the flux gradient can be seen just above the surface, where the resulting heating effect must be reduced. The shape of the net longwave flux profile is dominated by the profile of the outgoing flux. Close to the surface, however, the strong gradient of the incoming flux together with the reduced gradient of the outgoing flux leads to a change from a heating to a cooling just above the surface.

The profiles of the modeled longwave radiative heating rates are shown in Figure 6.3. In the stable case, a cooling takes place above about 7 m, reaching a maximum cooling of -15 Kd^{-1} at 20 m. Below 7 m, a heating results which reaches 40 Kd^{-1} in the lowest 1 m. Above 40 m the outgoing longwave radiative heating dominates the net longwave radiative heating profile, as the effect of the incoming flux divergence is zero. Incoming longwave radiative heating rate becomes the dominating component of the net longwave radiative heating below 10 m, where the divergence of the outgoing flux shows a decrease.

In the unstable case, longwave radiative heating is close to zero above 30 m, where a light cooling due to the divergence of the incoming flux is compensated by

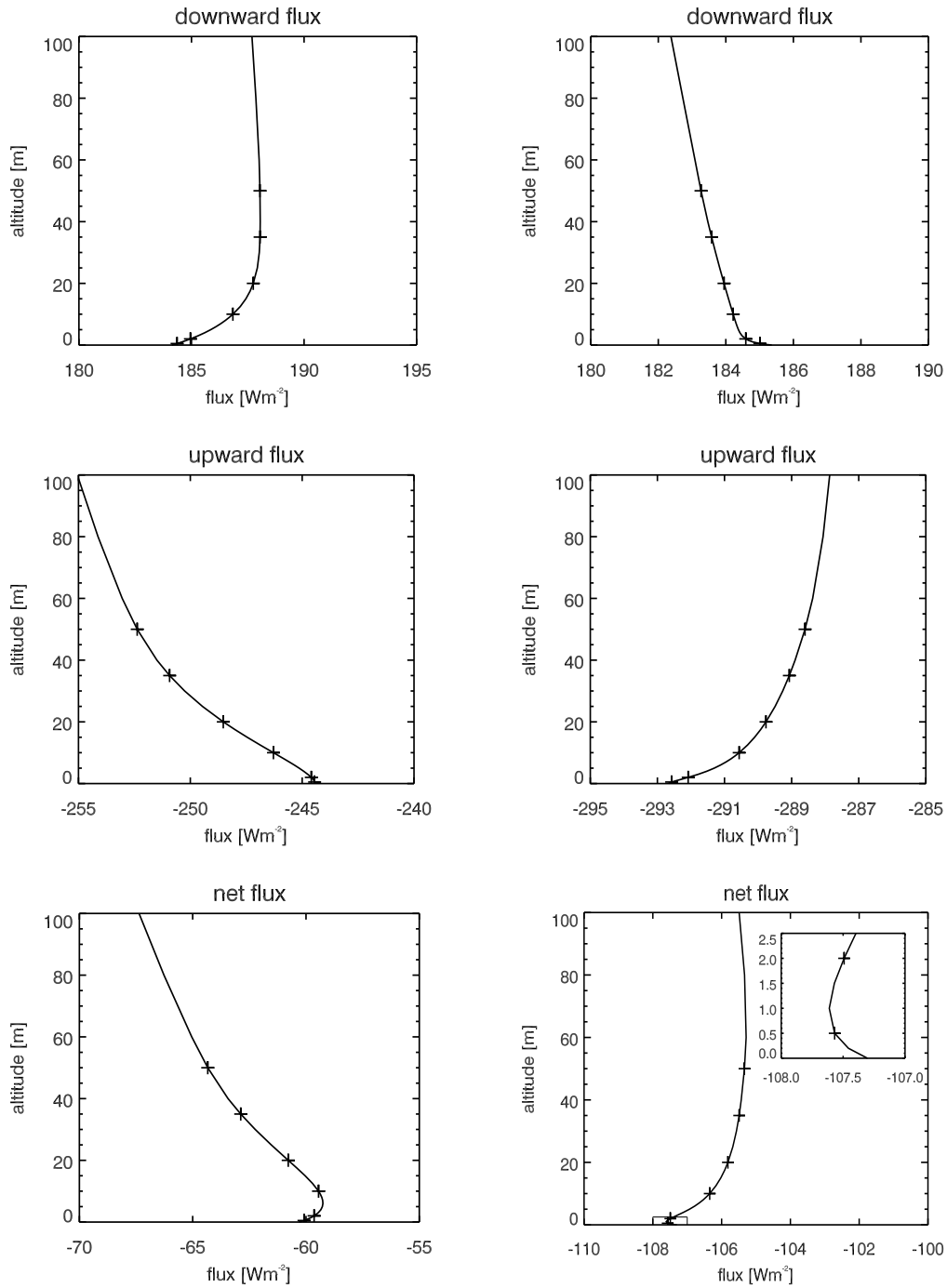


Figure 6.2: Modeled profiles of incoming, outgoing and net longwave flux, for two observations: Left: July 10th, 21:40 LT representing stable conditions and a strong surface inversion. Right: July 9th, 12:40 LT, representing a strong instability close to the surface. The plotted symbols refer to the levels at which flux measurements were taken during intensive observational periods.

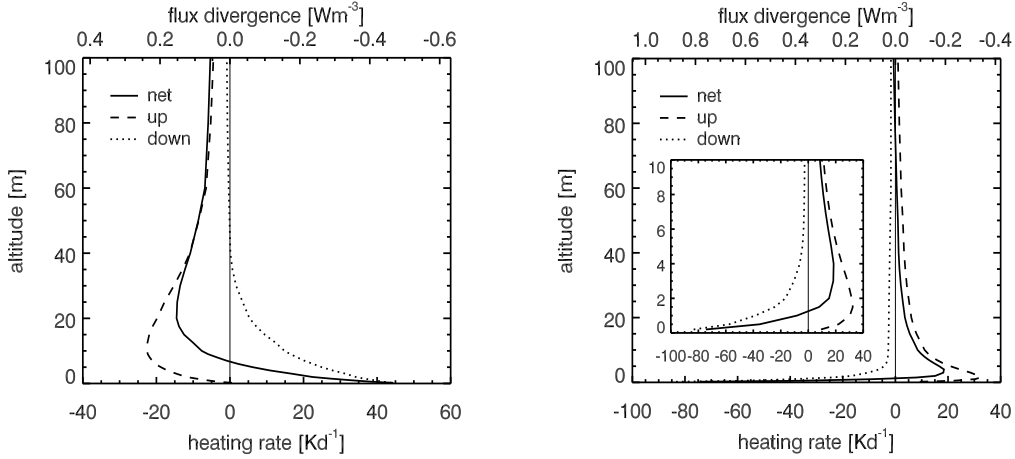


Figure 6.3: Modeled profile of longwave radiative heating rates (incoming, outgoing and net) for two observations: Left: July 10th, 21:40 LT representing stable conditions and a strong surface inversion. Right: July 9th, 12:40 LT, representing a strong instability close to the surface.

the convergence of the outgoing flux. Below 30 m, the convergence of the outgoing flux increases, reaching a maximum of more than 30 Kd^{-1} at about 1.5 m above ground. A net longwave radiative heating of close to 20 Kd^{-1} is seen between 2 m and 6 m. Below 2 m, the outgoing longwave radiative heating quickly reduces. The influence of the divergence of the incoming flux becomes important below 5 m, where the cooling effect increases quickly towards the surface. A net cooling effect results below 1 m, exceeding -40 Kd^{-1} in the lowest 50 cm.

The modeled longwave radiative heating rates can be compared to observed heating rates for clear sky conditions presented in Section 5.2.2. A detailed comparison of measured and modeled heating rates follows in Section 7. The shape of the heating rate profile for the stable case agrees qualitatively well with the mean nighttime (21-5 TST) heating rate profile for clear conditions shown in Figure 5.12. The change from a cooling to a heating close to the surface is seen in both, measurement and model. The results of the modeled unstable case agrees well with the observed mean daytime (9-17 TST) profile presented in Figure 5.12. Although the measurements indicate stronger heating rates between 2 m and 10 m, the overall shape of the heating rate profile, including the transition from heating to cooling close to the surface is very well represented by the model. The good agreement between observations and model results of typical daytime and nighttime situations indicates that the MODTRAN radiative transfer model can be used to investigate sensitivities of the longwave radiative heating profiles.

6.2.2 Shape of temperature profile

It is important to reproduce the *shape* of the temperature profile realistically, in order to model representative heating rates. This is demonstrated by modeling longwave radiative heating rates using two different representations for a stably stratified layer

in the lowest 50 m. In one case, a linear temperature profile is used ('linear-T' case). A more realistically curved profile ('curved-T' case) represents the second case. The strength of the inversion is the same for both cases, 5°C . The two temperature profiles are shown in Figure 6.4.

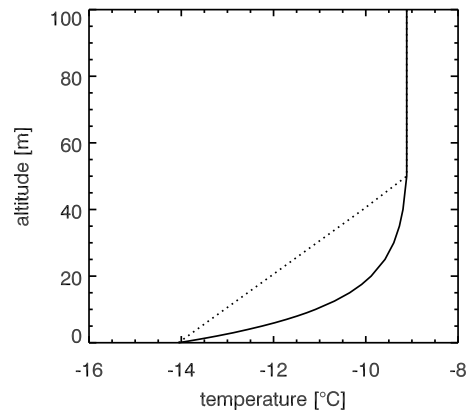


Figure 6.4: Temperature profiles used for two model calculations with an inversion strength of 5°C over the lowest 50 m. Once, a linear temperature profile (dotted line) and once a curved profile (solid line) is used.

Figure 6.5 shows the modeled fluxes and Figure 6.6 the modeled heating rates. Quite different pictures evolve for the linear and the curved temperature profiles. The downward fluxes start to deviate as soon as the temperature profiles differ (below 50 m). In the linear-T case the incoming flux start to decrease at 45 m, while it continues to increase down to 20 m in the curved-T case. This has a strong effect on the incoming longwave radiative heating, as this transition leads to a change from a cooling to a heating (Figure 6.6). The outgoing longwave flux is identical at the surface for both temperature profiles. Above the surface, the decrease of the outgoing flux with increasing height is stronger for the curved-T case than for the linear-T case. The maximum cooling due to the divergence of the outgoing flux thus lies at different levels for the two temperature profiles. The net flux profile clearly differs for the two representations. Especially the height of the change from an increasing to a decreasing net flux differs. In the more realistic curved-T case, the transition from heating close to the surface to cooling above happens at about 5 m, in the linear-T case at about 20 m. In the curved representation, heating directly above the surface is stronger. The magnitude of maximum cooling is the same for both cases, but the height of maximum cooling lies at 50 m for the linear-T case, and below 20 m for the curved-T case.

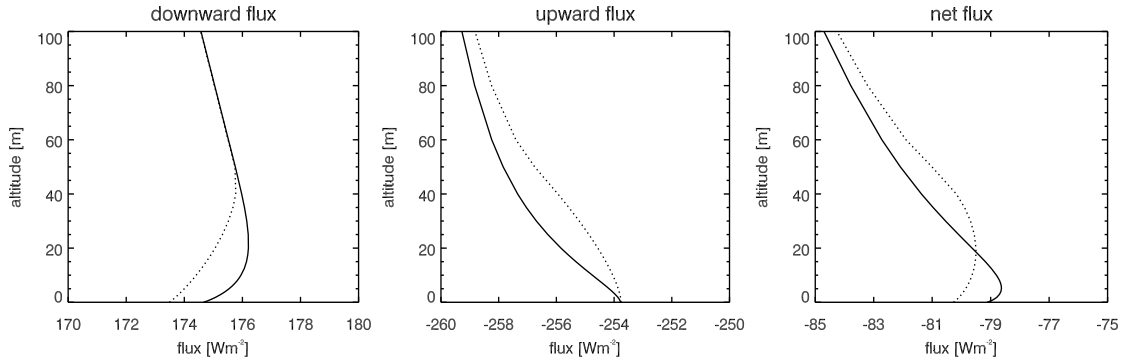


Figure 6.5: Profiles of incoming (left), outgoing (middle) and net (right) longwave flux profiles for two model calculations of a stable stratification in the lowest 50 m above the surface with an inversion strength of 5°C . Once, a linear temperature profile (dotted line), and once a curved profile (solid line) were used as model input.

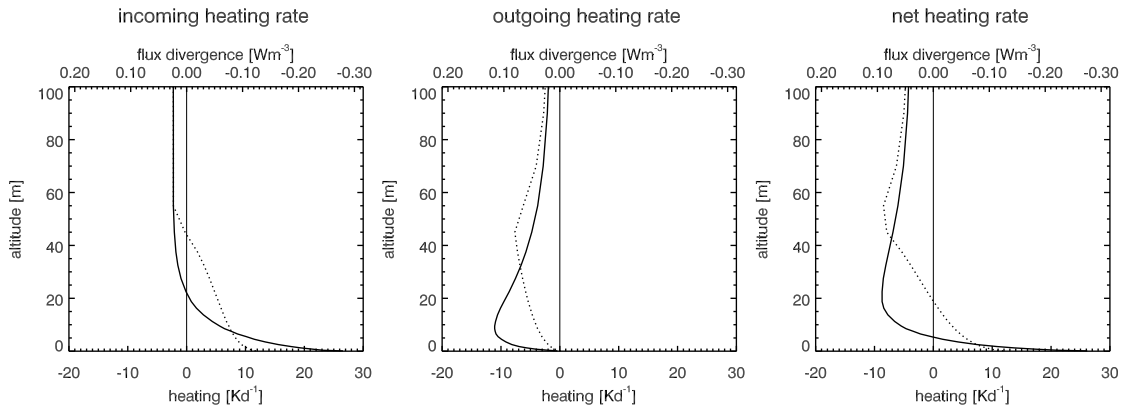


Figure 6.6: Profiles of incoming (left), outgoing (middle) and net (right) longwave radiative heating rate profiles for two model calculations of a stable stratification in the lowest 50 m above the surface with an inversion strength of 5°C . Once, a linear temperature profile (dotted line), and once a curved profile (solid line) were used as model input.

6.2.3 Longwave radiative heating, temperature gradient and humidity

MODTRAN is used to model the longwave radiative heating rates for different inversion strengths and humidities, to determine the influence of these variables on the model results. Measurements have indicated a strong relationship between temperature gradient and longwave radiative heating rate (Section 5.2.5), while no significant role of humidity could be identified (Section 5.2.6).

A series of idealized model atmospheres is composed, based on the radiosonde ascent of July 8th, 2002, 20:39 UTC, and the sub-arctic summer atmosphere above 23 km (supplied with MODTRAN). Temperature profiles and the corresponding

profiles of temperature gradient are shown in Figure 6.7. The temperature difference between the surface and the 50 m level is varied between 15°C and -3°C and the profile is expressed as

$$T = T_0 + (T_{50} - T_0)(1 - e^{-\gamma z}), \quad (6.1)$$

where T_0 and T_{50} represent the temperature at the surface and a 50 m. respectively, z is the height above the surface, and γ is a constant (0.09). This function was suggested by Fleagle (1953) to represent the temperature profile close to the surface. Temperature is kept constant between 50 m and 500 m. Above, the temperature from the sounding and the model atmosphere is used. Humidity is kept at a constant value up to a height of 400 m. Above 400 m it is interpolated linearly to the value of the sounding at a height of 700 m. To evaluate the influence of specific humidity, it is varied in the lowest 400 m between 0.5 g kg^{-1} and 3 g kg^{-1} . Whenever the combinations of the temperature and humidity profiles lead to saturation, relative humidity is reset to 100%.

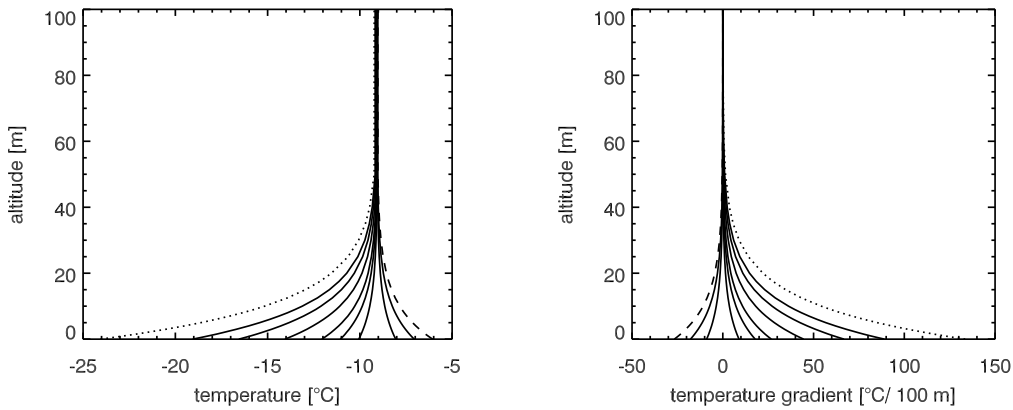


Figure 6.7: Profiles of temperature and temperature gradient used to model longwave radiative heating rate. The temperature difference across the lowest 50 m was varied between 15°C (dotted curve) and -3°C (dashed curve).

Longwave radiative heating rate and temperature gradient

The modeled incoming, outgoing and net longwave radiative heating rates resulting from the different temperature profiles and a constant humidity of 0.5 g kg^{-1} below 400 m are presented in Figure 6.8. The profiles of incoming heating rate closely resemble the profile of the temperature gradient. Under stable conditions a heating results which increases towards the surface. Under unstable conditions the opposite is seen, an increasing cooling towards the surface. Outgoing heating rates show a maximum cooling for stable and a maximum heating for unstable temperature stratifications at a level well above the surface (approximately 10 m). Below this level, the cooling (stable cases) or heating (unstable cases) due to the change of the outgoing flux reduces, and zero heating results at the surface. The profile of the net longwave radiative heating rate can be separated into two sections. In the upper section, the influence of the outgoing flux divergence dominates. Under stable

conditions, the cooling increases from higher levels down to a height where a maximum cooling is reached. Below this height, cooling decreases quickly to a value close to zero. Below the level of zero heating, in the bottom section of the profile, the influence of the incoming heating component becomes dominating. The incoming heating under stable conditions (cooling in the unstable case), which increases towards the surface, causes a sign change of the net longwave radiative heating rate. Strong heating rates result just above the surface under stable conditions, and strong cooling in unstable situations.

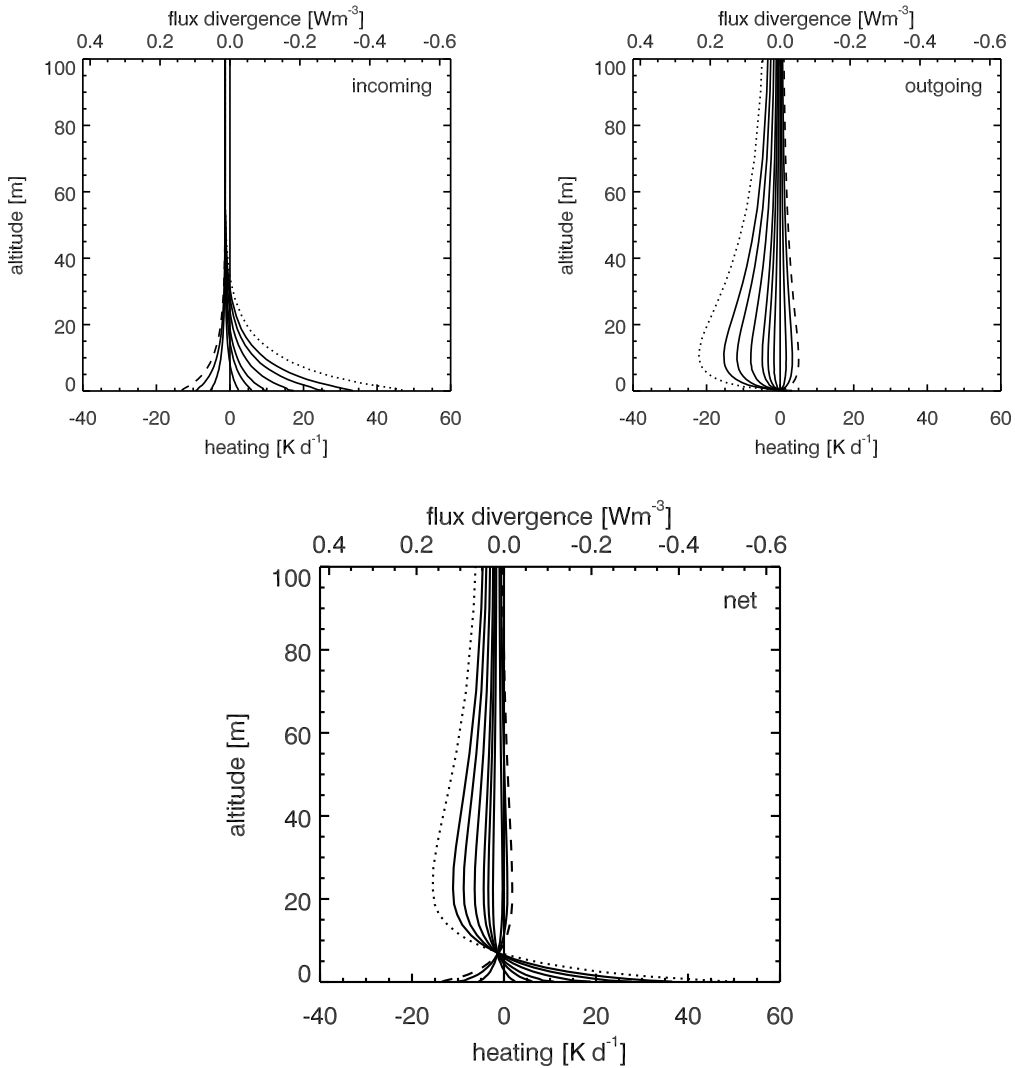


Figure 6.8: Profile of incoming, outgoing and net longwave radiative heating rates. Temperature difference between surface and 50 m was varied between -15°C (dotted curve) and 3°C (dashed curve), specific humidity is kept constant at 0.5 g kg^{-1} . All curves of the net heating rate meet at one point.

The relationship between longwave radiative heating rate and temperature gradient changes with height. This relationship seems to be caused by the relationship between outgoing flux divergence and temperature gradient as function of height. The relationship between the heating rate due to divergence of the incoming flux

and temperature gradient seems not to depend on the height above the surface. Longwave radiative heating rates measured at different level above the surface were presented in Section 5.2.5. In Figure 6.9 modeled longwave heating rates and their relationship with temperature gradient are shown for different heights, 0.35 m, 7.5 m, 11.25 m and 27.5 m.

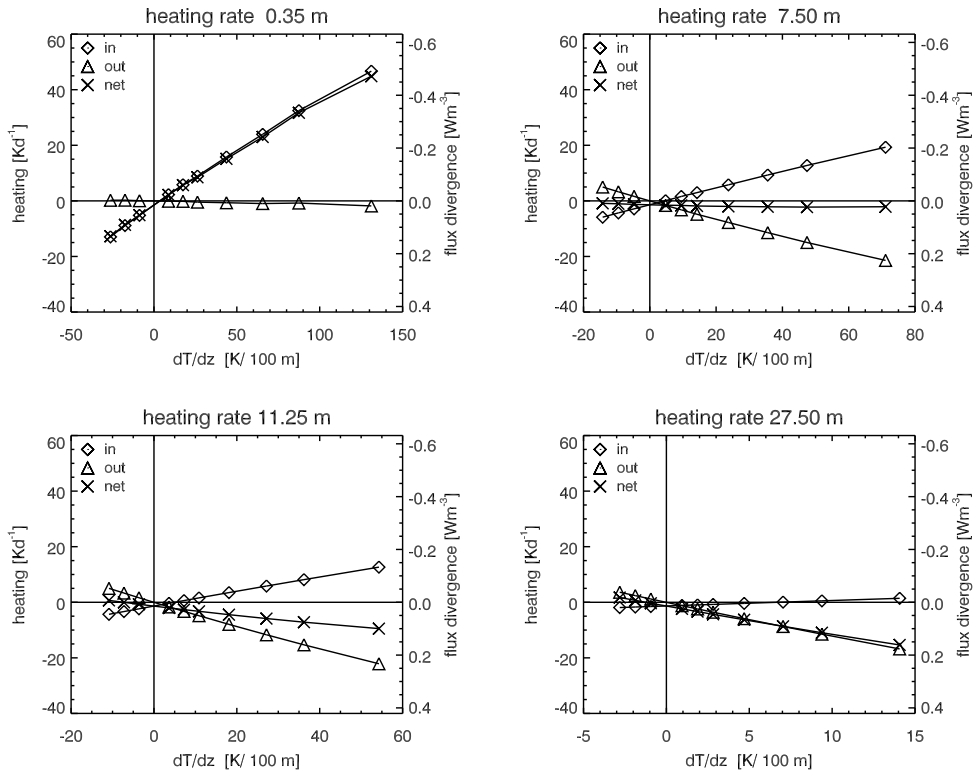


Figure 6.9: Relationship of incoming (diamonds), outgoing (triangles) and net (crosses) longwave radiative heating rate with temperature gradient at different heights: Very close to the surface, at 0.35 m (between the 2nd and 3rd model layer, 0.2 m and 0.5 m), at 7.5 m, 11.25 m and 27.5 m. Results are from model calculations with constant specific humidity of 0.5 g kg^{-1} .

Close to the surface, no dependence of the outgoing component of the net heating rate on temperature gradient can be seen. An increased net heating is seen with growing stabilities, which arises from the relationship between the incoming heating component. At the height of 7.5 m, there is no relation between net heating rate and temperature gradient. This is the level at which the net heating is the same for all modeled temperature profiles. While we see no relationship for the net heating, an increase of incoming heating rate with growing stability and a decrease (increasing cooling) of outgoing heating rate is observed. These two effects cancel each other at this height. At higher levels, the relationship between outgoing longwave heating and temperature gradient becomes stronger than the relationship between incoming heating and temperature gradient. At a height of 27.5 m, the relationship between temperature gradient and net heating is mainly due to the outgoing component.

Figure 6.10 shows the relationship between incoming (upper left panel) outgo-

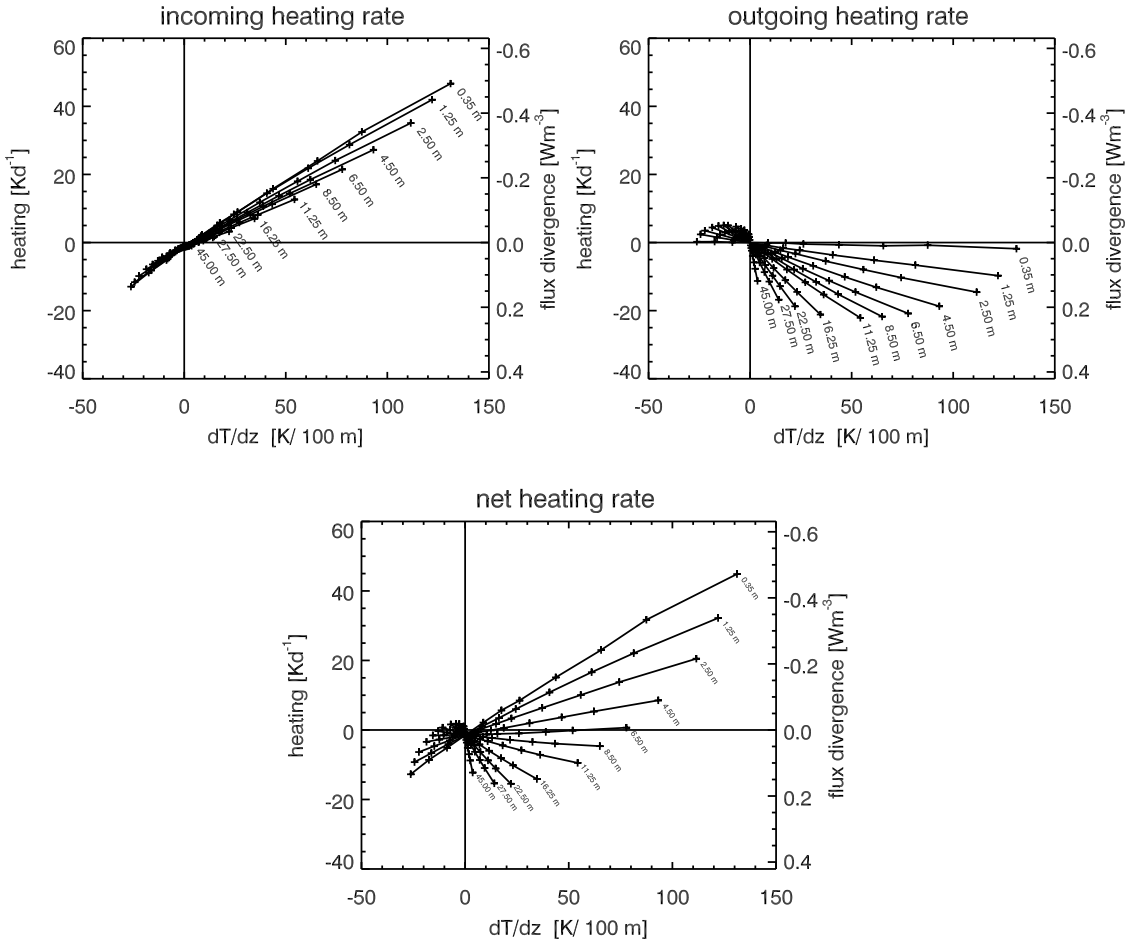


Figure 6.10: Relationship between incoming (upper left panel), outgoing (upper right) and net (lower panel) longwave radiative heating rate, temperature gradient, and height.

ing (upper right panel) and net (lower panel) longwave radiative heating rate and temperature gradient at different levels. Incoming flux convergence leads to an increased heating with growing stability. This relationship shows no strong dependence on height. A slightly stronger increase of heating is seen for air layers closer to the ground. Outgoing flux divergence shows an increase with a growing stable temperature gradient, which again depends on height above ground. The higher the level above the surface, the stronger is the increase of the cooling rate with growing stability. The net longwave radiative flux divergence shows two regimes for its relationship with temperature gradient: Close to the surface, the role of incoming flux divergence dominates. Therefore, an increased heating is seen with stronger stabilities. With increasing height, the outgoing component gains importance. The increase of heating with higher stability becomes weaker. At a height of about 7 m, no relationship between heating rate and temperature gradient is seen, as the incoming and outgoing components cancel each other. Further up, in the second regime, the outgoing component dominates. The higher the level above the surface, the stronger is the increase of cooling seen under growing stabilities.

In a next step, the shape of the inversion or superadiabatic layer is varied. The previous analysis focused on various temperature profiles described by Equation 6.1 with the factor γ of 0.09. Temperature profiles calculated with this value of γ well represent an average summer nighttime inversion. If a larger value is used for γ , the inversion layer (or superadiabatic layer) is compressed closer to the surface (Figure 6.11, left panel). This leads to stronger temperature gradients close to the surface. The effects on the radiative heating rate profile are presented in the right panel of Figure 6.11. A reduction of the height at which the sign of the heating rate changes is observed, as well as lowering of the level of maximum cooling. In addition, the strength of the cooling increases due to the stronger gradients. In all modeled cases, the height of maximum cooling, however, falls within a height range where the temperature difference between layer and surface reaches 85-90% of the overall inversion strength.

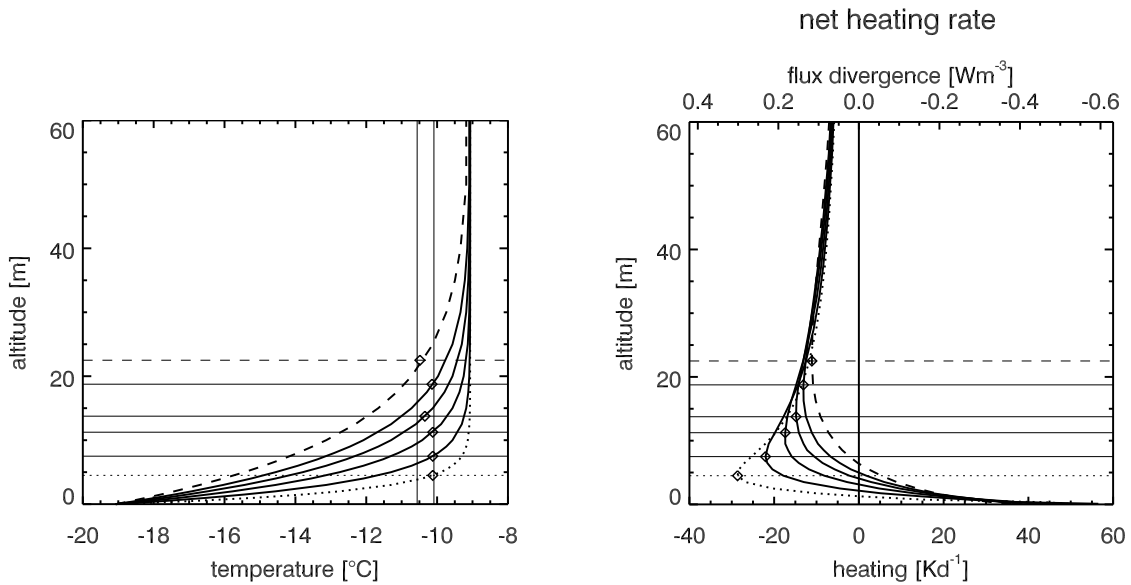


Figure 6.11: Temperature profiles and resulting modeled net longwave heating rate profiles. Temperature profiles were calculated using different γ between 0.09 (dashed) and 0.5 (dotted) in Equation 6.1. Horizontal lines indicate the height where maximum cooling results. This height corresponds well to the height where temperature reaches 85-90% of the inversion temperature difference.

The relationship between longwave radiative heating rate and temperature gradient is influenced by the shape of the inversion which is varied by changing factor γ . This is illustrated in Figure 6.12. The height of the layer changes, at which a zero heating rate is observed, as the cooling due to the outgoing flux divergence is compensated by the heating due to the convergence of the incoming flux (under stable conditions). When γ is 0.09 the level of zero heating is found at 6.5 m, while a γ of 0.5 lowers this level to 1.25 m. Furthermore, a smaller increase in temperature gradient is needed in the lower layers (below 2 m) to reach a higher value of heating if γ is greater. In the layers where a net cooling results, a larger γ leads to a larger cooling under the same stability.

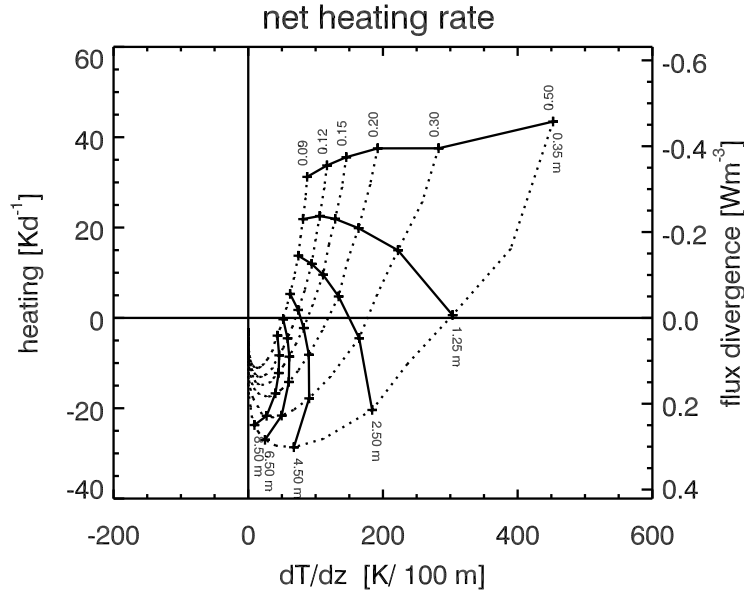


Figure 6.12: Relationship between net longwave radiative heating rate, temperature gradient and height under different inversion shapes: Temperature profiles are realizations of Equation 6.1 using different γ between 0.09 and 0.5. Solid lines indicate isolines of height, dotted lines are isolines of γ . A compressed inversion (a larger gamma) leads to a change of the height above which an increase of stability leads to stronger cooling.

Longwave radiative heating rate and humidity

A relationship of longwave radiative heating rate with humidity could not be inferred from measurement results (Section 5.2.6). Model calculations, however, indicate a relationship between longwave radiative heating and humidity. This relationship is illustrated in Figure 6.13 for the net longwave radiative heating rate and for two different heights. Very close to the surface, at 0.35 m (left panels) and at 27.5 m (right panels). The different plotting symbols refer to different classes of temperature gradients. Under unstable conditions, with a temperature gradient between -40 Kd^{-1} and -20 Kd^{-1} , an increasing net longwave radiative cooling is seen with rising humidity. Under stable conditions, for example with a temperature gradient between 60 Kd^{-1} and 80 Kd^{-1} , an increased net longwave radiative heating results from a higher humidity. At a height of 27.5 m, increasing cooling with growing humidity is observed under stable conditions. Increasing humidity enhances the cooling or heating induced by longwave radiative flux divergence. The sign and strength of the cooling or heating, however, depends much stronger on the temperature gradient and on the distance of the air layer from the surface.

6.2.4 Longwave radiative heating and surface emissivity

André and Mahrt (1982) report a weak dependence of their heating rate results on surface emissivity. The effect of the change of the emissivity from 0.965 to 1.0 is visible in their calculation to a height of 300 m above the surface. Nkemdirim (1978)

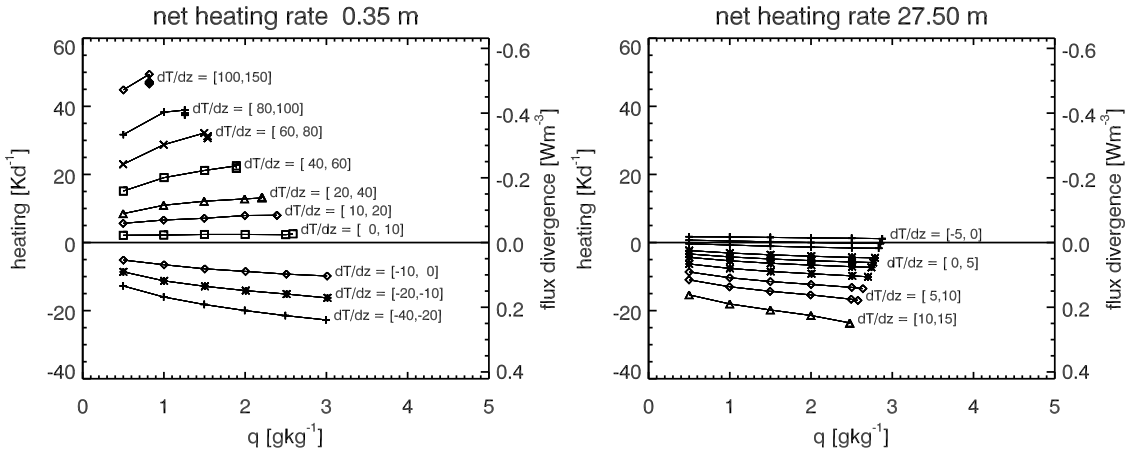


Figure 6.13: Relationship of net longwave radiative heating rate with humidity at two different heights: Very close to the surface, at 0.35 m (left panels), and at 27.5 m (right panels). Different plotting symbols mark classes of temperature gradient, given to the right. Under stable conditions, some calculations with higher humidities were not possible, due to over-saturation.

attributes differences in radiative cooling to the different emissivities of snow and grass, with stronger cooling above snow cover. Measurements in Greenland are all taken above snow, which has a high emissivity. To evaluate the effect of a changing surface emissivity, model calculation were performed. A stable situation with an inversion of 5°C within the lowest 50 m is modeled. The surface emissivity is varied between zero and 1.0. The resulting profiles of longwave radiative heating rates are shown in Figure 6.14. The variation of the surface emissivity has no impact on the incoming flux and its vertical variation. The incoming heating rate profile is identical for all emissivities. The variation of the emissivity, however, is reflected in the outgoing heating rate. Under black body surface conditions the maximum cooling is stronger and located at a lower level than for surfaces with lower emissivities. While zero heating results at the surface in the black body case, a heating is observed close to the surface in the grey body case. This has an effect for the net heating rate profile. The lower the emissivity, the stronger is the enhancement of the heating close to the surface, which, in the black body case, is only due to the convergence of the down-welling flux. In Figure 6.14, the results for a black body surface and for a surface with a realistic spectral emissivity of snow lie so close together that the individual curves can not be separated. This shows that a black body assumption for a snow surface is valid. The model calculations presented here show a smaller effect of emissivity on longwave radiative heating rate than reported by André and Mahrt (1982). The effects of a change of emissivity from 0.9 to 1.0 becomes negligible above about 40 m. The effect reported by André and Mahrt (1982) due to an emissivity variation of only 0.035 was stronger.

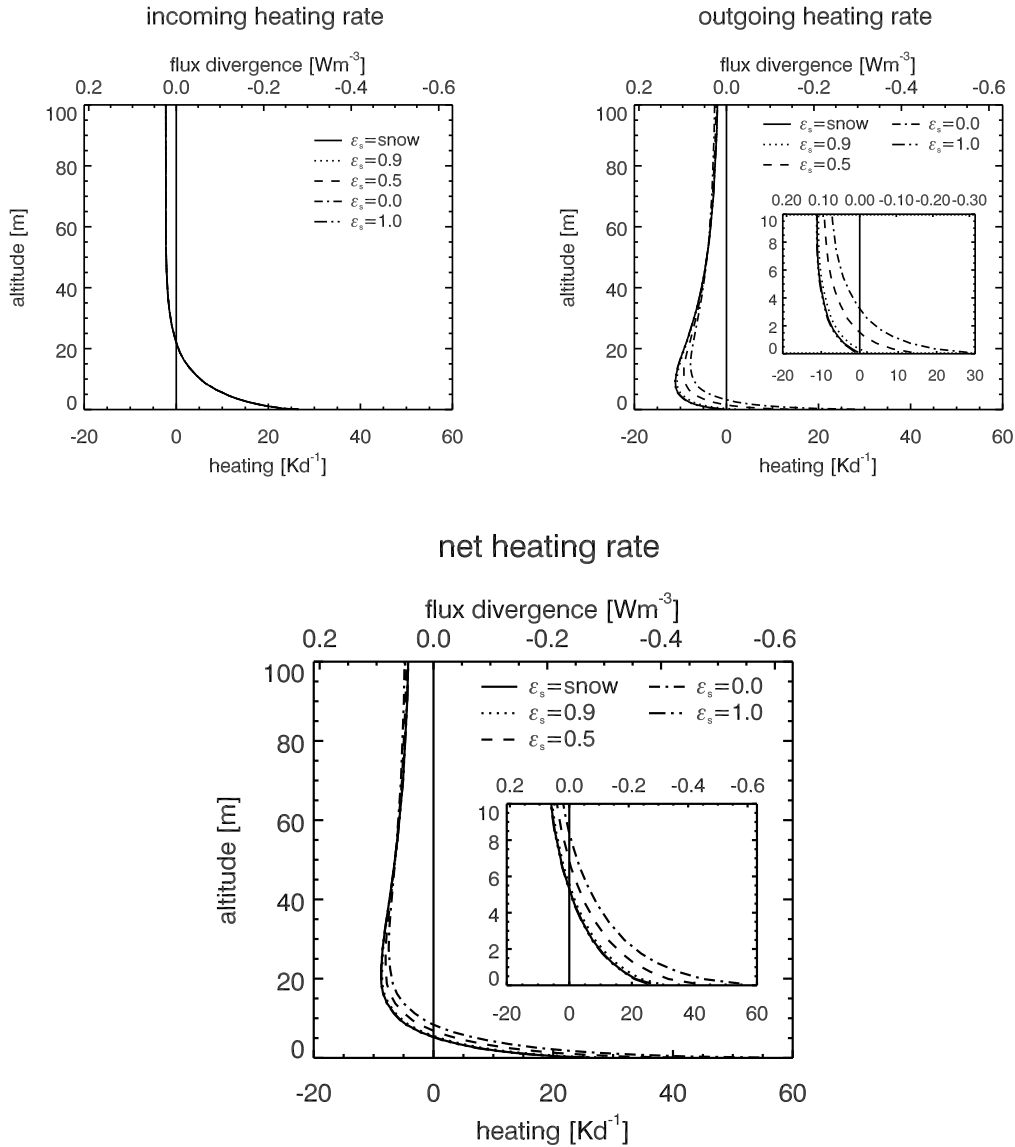


Figure 6.14: Profile of longwave incoming (top left), outgoing (top right) and net (bottom) radiative heating rates for model calculations with an inversion strength of 5°C in 50 m. Solid line: spectral emissivity model used for snow surface, surface emissivity ϵ_s of 0.9 (dotted), 0.5 (dashed), 0.0 (dash-dot), 1.0 (dash-dot-dot). Lines for snow and $\epsilon_s=1$ overlap.

6.2.5 A spectral viewpoint

The results of the MODTRAN calculations offer a spectral viewpoint on longwave radiative flux divergence. Results for one of the idealized cases from Section 6.2.3, the inversion of 10 K in the lowest 50 m, are presented in Figure 6.15. On the left hand side, contour plots of the vertical distribution of the spectral radiative heating rate are shown for the incoming (top), outgoing (middle) and net (bottom) components. On the right hand side, the profiles of the three spectrally integrated radiative heating rate components are shown.

The importance of the strong absorption band of carbon dioxide at $15\ \mu\text{m}$ and of water vapor at $6.7\ \mu\text{m}$ becomes visible. Most of the heating due to a converging incoming flux originates in these strong absorption bands. In the same bands, most of the cooling due to a diverging outgoing longwave flux is induced. The elevated maximum of the cooling at 10 m is well visible. The sum of both components is seen in the lowest panels. The heating close to the ground and the elevated cooling maximum at 20 m result. The strongest spectral cooling is seen in the strong absorption bands. From calculation with either water vapor or carbon dioxide removed from the model atmosphere, the relative importance of these two strongest absorbers was assessed. Roughly 70% of the radiative cooling occurs in the water vapor absorption bands, 30% in the carbon dioxide absorption bands.

The effects of the temperature inversion on the longwave radiative heating profile becomes visible in the contour plots of spectral radiative flux divergence. The effect of the inversion on the down-welling flux is confined to levels below the inversion top at 50 m. The maximum of the induced heating is seen at the surface, where temperature gradients are strongest. An effect of the temperature inversion on the outgoing longwave flux is seen even above the inversion top, where radiative cooling is induced. Close to the surface, where the highest temperature gradients occur, the effect of the outgoing longwave flux divergence is reduced, and the heating due to the converging incoming flux dominates. The cause for the sign change of longwave radiative flux divergence close to the surface is addressed in the following section.

6.2.6 The causes for heating and cooling

In this section, the question for the causes for longwave radiative flux divergence is addressed. Over both, colder and warmer surfaces, we see a sign change in the radiative heating rate close to the surface (Figure 6.3). This change is due to a change of the relative importance of the flux divergence components (incoming and outgoing). A reduction in the gradient of the outgoing flux, which contributes the dominating part to the net flux divergence over the major part of the inversion layer, is observed below an altitude of about 10 m. On the other hand, the gradient in the incoming flux strongly increases towards the surface and therefore becomes the dominating factor.

The question arises, why the outgoing flux gradient reduces close to the surface, even though the temperature gradient still increases. When the emissivity of the surface is greatly reduced in model calculations, even a heating due to a convergence of the outgoing flux is seen close to the surface under stable conditions. This then enhances the heating effect which is mainly induced by the converging incoming flux (Figure 6.14).

To understand the cause for the gradients in the heating rate profile, the components of the incoming and outgoing fluxes are analyzed. They are available from the model calculations.

The incoming flux has only one component, the *path thermal*. The path thermal radiation is the radiation emitted by the radiatively active atmospheric constituents of all air layers above the observing point, attenuated by the corresponding optical

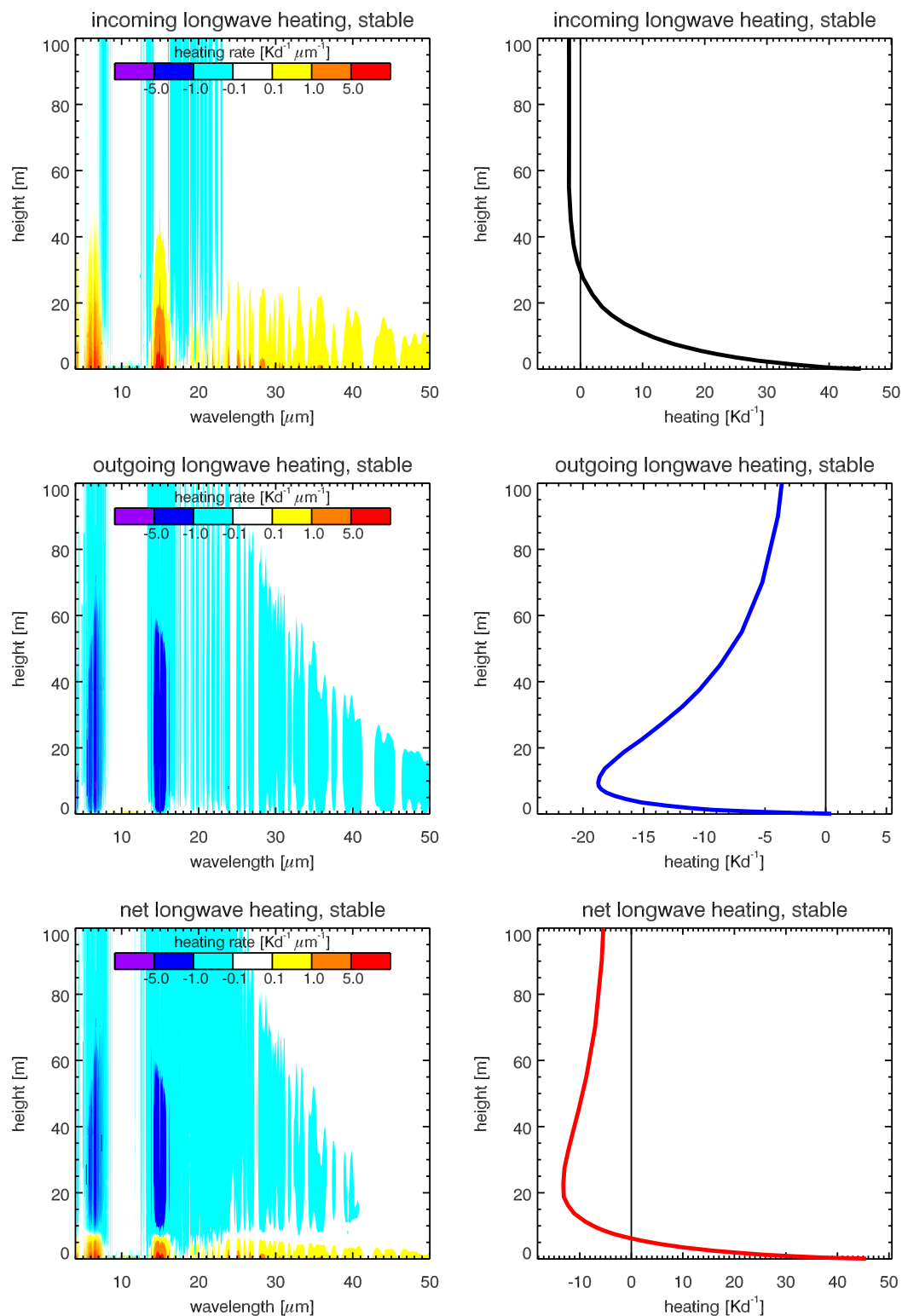


Figure 6.15: Contour plots of the vertical and spectral distribution of longwave radiative heating rate (left) and the spectrally integrated profiles (right) in the lowest 100 m of a stable stratified boundary layer. Top panels show the incoming, middle panels the outgoing, and bottom panels the net longwave radiative heating component. The temperature profile of the model input is an inversion of 10 K across the lowest 50 m, and an isothermal layer between 50 m and 500 m.

paths. Path thermal incoming radiation is sensitive to change in stratification, as the emission of the radiatively active atmospheric constituents is a function of temperature. The stronger the gradient in temperature, the greater the increase or decrease of the incoming longwave flux, and the greater is the absolute value of the resulting incoming flux divergence. This was illustrated in Figure 6.10. Stable conditions lead to a convergence of the incoming flux, unstable conditions to a divergence. When temperature gradients increase towards the ground, the heating (stable) and cooling (unstable) due to the incoming flux divergence increases towards the surface as well.

Outgoing longwave radiation can be split into three components. The first component is the *outgoing path thermal radiation*. It is the radiation emitted by the radiatively active atmospheric constituents of all air layers below the observer which are then transmitted to the observing point. The second component is the *surface emitted radiation*, which is attenuated in the air layers underlying the observing point. At the surface, it corresponds to a Planck emission curve convolved with the surface emissivity. The third component is the *ground reflected radiation*. It is the part of initially downward directed radiation that is reflected by the ground surface and is then attenuated through the air layers below the observing point. The relative magnitude of surface emitted and ground reflected components, and therefore the spectral composition of the outgoing flux, depends on the emissivity of the surface.

Outgoing path thermal radiation is, just as incoming path thermal flux, controlled by the temperature of the air layers and by the concentration of absorbers. Outgoing path thermal radiation does not change when different emissivities are introduced for the surface. We see an increase of the outgoing path thermal flux towards the surface, regardless whether we have a stable or unstable surface layer. At the surface, path thermal outgoing radiation is zero, as there is no air layer to emit radiation. Close to the surface, the decrease of the path thermal radiation with height is mainly a function of increasing path length or growing distance from the surface, and the ambient temperature gradient plays only a secondary role.

As noted above, surface emissivity decides on the relative importance of the surface emission and ground reflected components. In Figure 6.14, the effect of different emissivities on the profile of outgoing longwave radiative heating was presented. Differences in the profile of outgoing heating rate arise. For simplicity, let us first consider the two extreme cases: a black body surface when the ground reflected component becomes zero, and a surface with an emissivity of zero, which leads to zero emission and total reflection.

In the case of a black body surface, a cooling due to the outgoing flux results throughout the inversion layer. Outgoing path thermal flux divergence (cooling) is stronger than convergence (heating) of the surface emission. Outgoing path thermal cooling is due to the increasing distance from the surface and the changing emission temperatures. Surface emission shows a stronger convergence nearer to the surface (Beer's law). However, the differences in the gradients in path thermal and surface emission vary with height. Close to the surface, the gradient in surface emission is stronger than above, which leads to a reduction of the cooling close to the surface, and a maximum of the outgoing cooling at a height of approximately 10 m. Close to the surface, in the surface emitted radiation, there is more energy available to be absorbed in the air which increases the gradient in surface emission. This explains the

stronger reduction of the outgoing flux divergence close to the surface. At a short distance away from the surface, radiation contained within the strong absorption bands is removed, and the weaker absorption bands gain importance. However, the decrease of the flux is now less strong, and the gradient in heating rate is controlled by the outgoing path thermal heating rate.

In the case of zero emissivity, the emitted component disappears. The outgoing path thermal flux divergence (cooling) is stronger than convergence (heating) of the surface reflected flux above 5 m. Below 5 m, a heating results due to the domination of the convergence of the ground reflected flux. Outgoing path thermal flux divergence (cooling) is due to the increasing distance from the surface and the changing emission temperatures. The ground reflected radiation shows a convergence, similar to the emission in the black body case. The stronger heating close to the surface is due to the fast removal of radiation in the strong absorption bands, while further up, the attenuation takes place in the weaker bands. As it stems from the incoming longwave flux, the ground reflected radiation mainly consists of radiation in the absorption bands of the radiatively active gases. In an inversion case, due to warmer air layers above, the ground reflected radiation in the absorbing bands may even be larger than the radiation of black body emission at the colder surface temperature. Then, there is more radiation available in the spectral regions of the strong bands and the heating rate in the shallow layer above the surface due to the converging reflected flux can be larger than the convergence of the surface emitted flux in the black body case. Convergence of the ground reflected flux can then be even larger than the divergence of the path thermal flux, and a net heating rate due to the outgoing flux divergence becomes possible.

The above mentioned effects can be illustrated using the spectral results of model calculations. A nighttime surface inversion of a strength of 10°C over 50 m was modeled under varying surface emissivities. Figure 6.16 presents contour plots of the outgoing heating rate components modeled for several air layers under these stable nighttime conditions for black body surface conditions (left) and conditions with a surface with a zero emissivity (right). The top panels show the spectral heating rate due to the outgoing path thermal flux, which is identical for both situations. The middle panels show the spectral heating rate due to the divergence of surface emitted flux under black body surface conditions, and the spectral heating rate due to the diverging ground reflected flux for surface with zero emissivity. A stronger heating is indicated for the case with zero emissivity. The total outgoing longwave radiative heating rates are shown in the bottom panes of Figure 6.16, where the differences between the two surface conditions now become very well visible. While an overall cooling effect results in the black body surface situation, a heating results in the lower layers when the reflectivity is unity and emissivity zero.

Figure 6.17 shows spectral radiances of the three outgoing flux components at a height of 0.2 m (top left) and at 35 m (bottom left). Comparing these two graphs, the fast decrease of the outgoing path thermal (red) is visible. The strong increase of the surface emitted (orange) under black body surface conditions and of the ground reflected (black) under conditions with ϵ_S of zero, is clearly visible as well. The spectral composition of the ground reflected and surface emitted is very different. However, the attenuation of these outgoing components takes place in the regions of

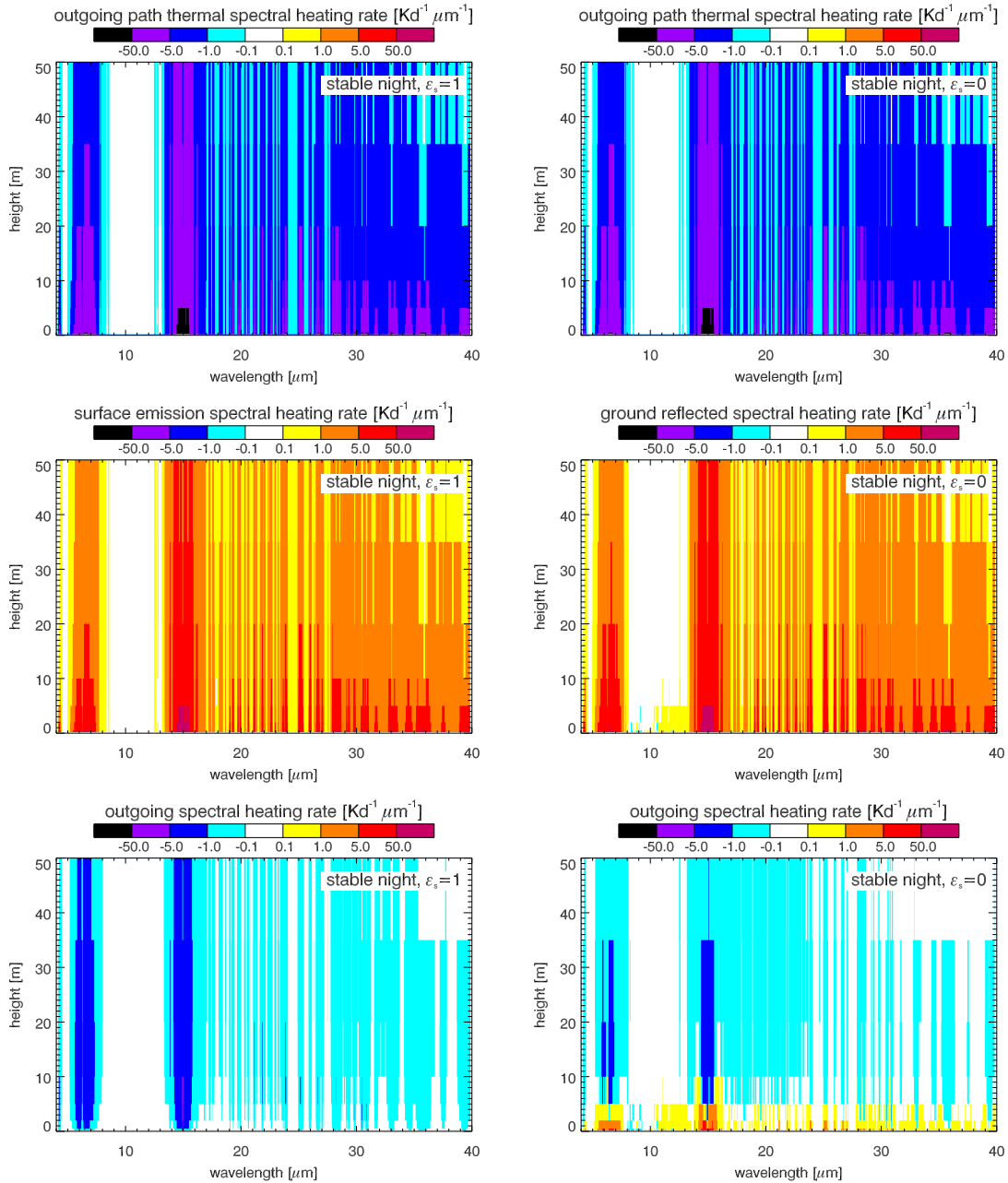


Figure 6.16: Spectral outgoing longwave radiative heating rate components at various levels above the surface for different surface emissivities. A black body surface (left), and a surface with zero emissivity (right).

the strong absorbing bands. In the case of a lower emissivity, there is more radiation contained in these spectral regions, and a stronger heating is possible. This is visible in the right hand panels of Figure 6.17. They show the spectral heating rates of the outgoing flux components in a layer close to the surface (0.2-0.5 m) and at the top of the inversion (35-50 m). In both layers, the heating due to the converging surface emission is lower than the heating due to the converging ground reflected. In the near-surface layer, the heating under low emissivity surface conditions even exceeds the path thermal cooling, and a outgoing heating results. Under black body

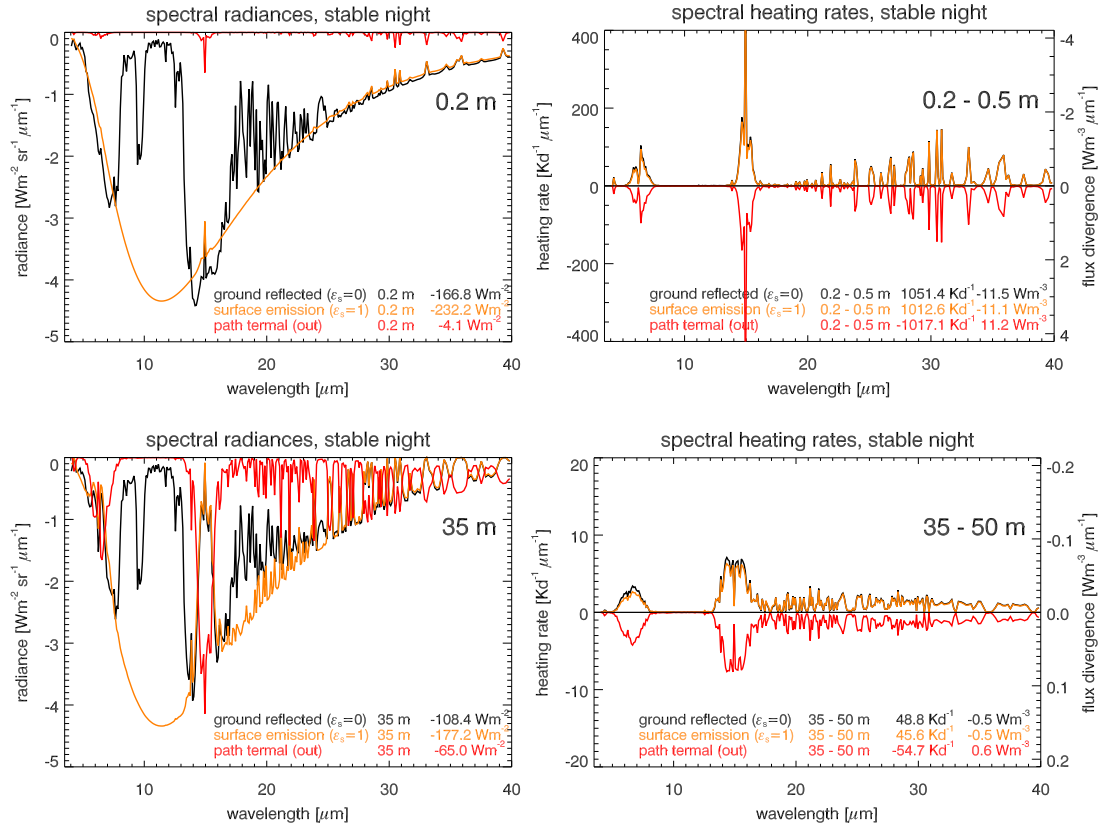


Figure 6.17: Spectral radiances (left panels) and spectral radiative heating rates of outgoing flux components at different levels. Close to the surface (top panels) and close to the top of the inversion (lower panels). Ground reflected components are for a surface emissivity of zero, surface emitted components for an emissivity of one. Inversion strength is 10 K over the lowest 50 m.

surface conditions, the strong absorption of the surface emitted component close to the ground at least compensates the outgoing path thermal cooling. This leads to the strong reduction of the outgoing flux divergence towards the ground.

6.2.7 Spectral radiative flux divergence under clear sky and fog conditions

The observations presented in Section 5.2.4 have shown that fog has a strong impact on longwave radiative flux divergence. Under condition with fog, the incoming flux shows a divergence which may exceed the divergence of the outgoing flux. This effect was modeled using MODTRAN by introducing a radiation fog in the lowest 60 m of a stable nighttime model atmosphere. Figure 6.18 shows the spectral radiative heating rates for the four flux components of the MODTRAN model output for clear sky conditions and a fog case: incoming and outgoing path thermal heating rates, surface emitted heating rate and ground reflected heating rate. The spectral radiative heating rates of the incoming, the sum of the outgoing components, and the net longwave radiative heating rate are shown in Figure 6.19, together with

profiles of the corresponding spectrally integrated heating rates.

As the water droplets in the fog layer radiate with a near-Planck emission, the path thermal heating rate components do not only show a strong convergence (incoming path thermal) and divergence (outgoing path thermal) in the strong absorption bands of CO_2 and H_2O , but also a strong divergence in the window regions of the spectrum. The fog layer introduced into the atmosphere leads to a rapid increase of the emissivity of the air in the window region. The resulting emissivity gradient causes a cooling. This effect increases from the 35-50 m layer down to the 10-20 m layer. Below 10 m, a decrease of the cooling in the window region is seen towards the surface. The effect of the rapidly decreasing temperatures which reduce the emission of the fog droplets is now larger. The difference in the outgoing path thermal heating between the clear and fog free case lies in the spectral window region as well. The cooling is enhanced, but this effect is compensated by the increased heating due to the surface emission and ground reflected heating rate components. The comparison of spectral net longwave cooling under fog and clear conditions shows that the main difference arises in the atmospheric window region. Under fog conditions, additional cooling in this region is mainly caused by the divergence of the incoming path thermal component. The profiles of the spectrally integrated longwave radiative heating rates under fog and clear skies conditions (lowest panels of Figure 6.19) show that the enhanced cooling under fog conditions peaks between 10 and 20 m.

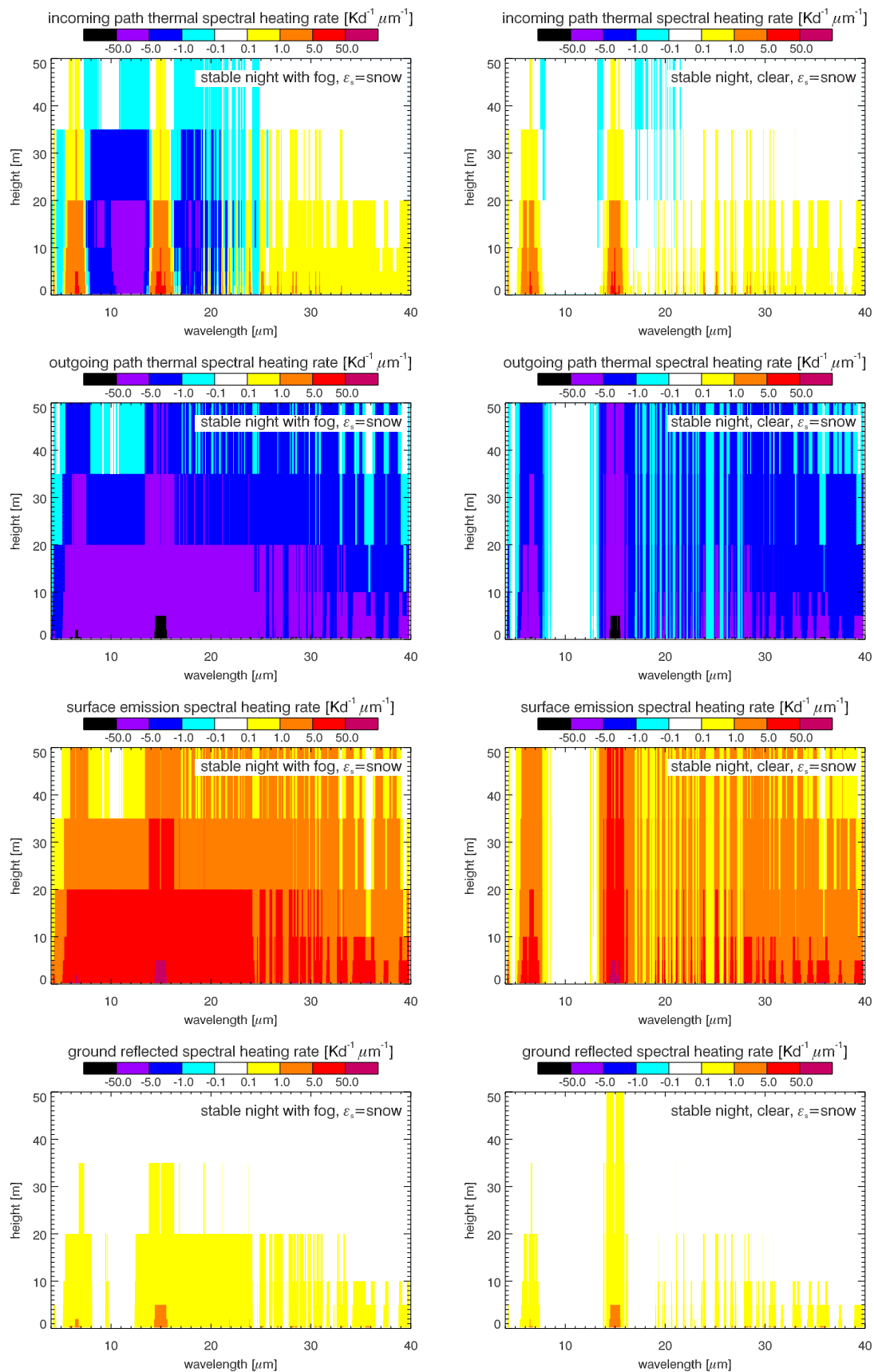


Figure 6.18: Spectral radiative heating rates for stable nighttime conditions under fog (left) and clear (right) conditions. Heating rate components shown are incoming path thermal (top), outgoing path thermal (second row), surface emission (third row) and ground reflected (bottom).

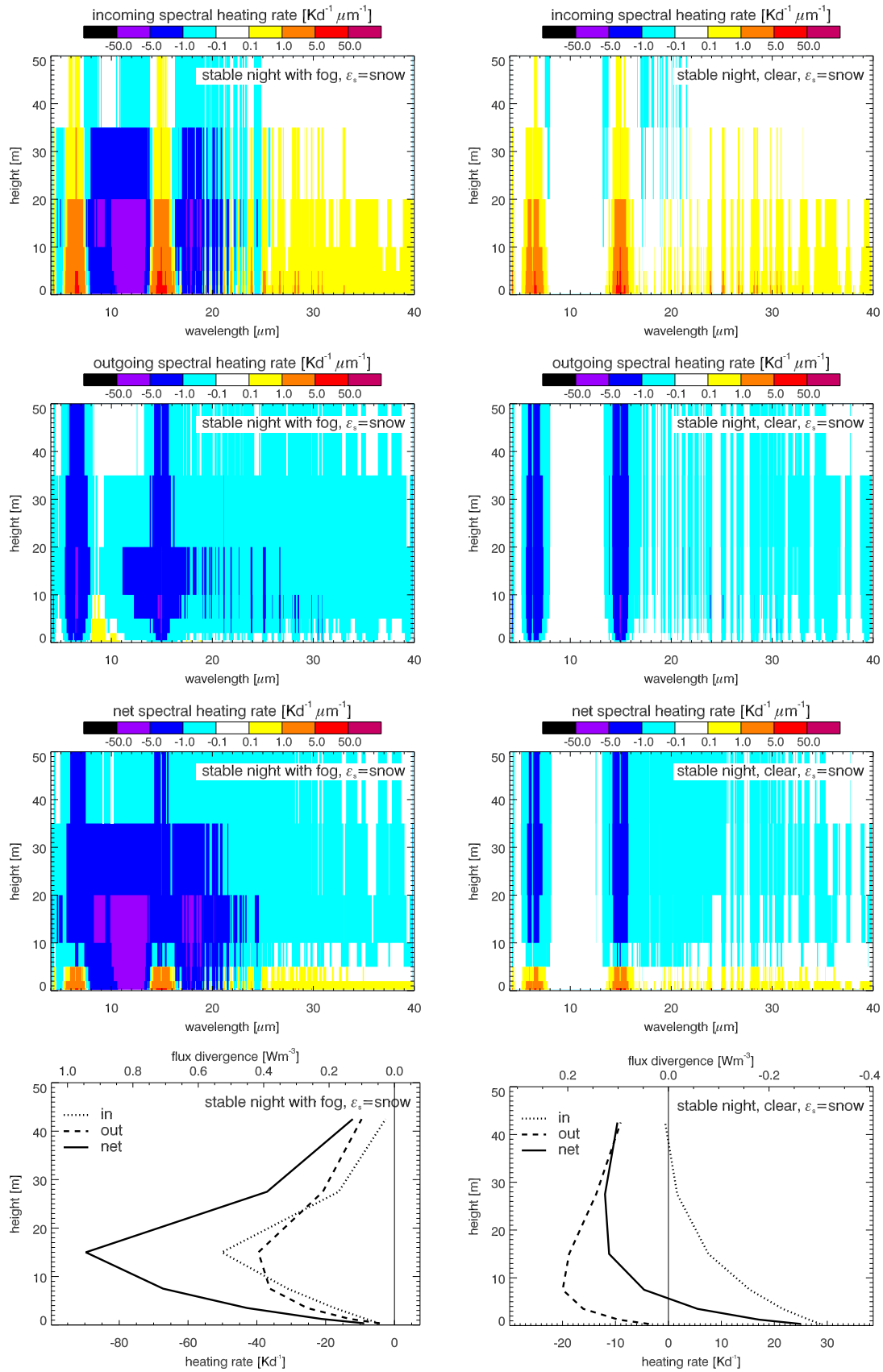


Figure 6.19: Spectral radiative heating rates for stable nighttime conditions under fog (left) and clear (right) conditions. Heating rate shown are incoming (top), outgoing (second row) and net longwave (third row). Profiles of net longwave radiative heating and the in- and outgoing component for the lowest 50 m are shown in the bottom panels.

7 Comparison of detailed measurements with model calculations

Three situations are selected to compare detailed measurements during intensive observational periods with model calculations. The first situation represents a daytime condition with a very thin cirrusstratus cloud layer. The second comparison focuses on a clear nighttime case, the third on a night with fog. Model input is composed from the temperature and humidity profiles measured on the tower and by a radiosonde. Surface temperatures are obtained from a thermocouple measurement on the snow-air interface. The temperature profile is smoothed by fitting a function (Equation 6.1) through the lowest 50 m of the profile. The humidity profile is constructed by linearly interpolating between the measurement of the radiosonde at 80 m and the observation at 2 m with a dew-point mirror (THYGAN, Meteolabor). In the fog situation, relative humidity is set to 100 %.

7.1 Unstable day

The unstable daytime case centers on the radio sounding of July 9th, 12:40 LT. The temperature and humidity profiles used as model input are shown in Figure 7.1. Measured and modeled fluxes and the corresponding heating rates are presented in Figure 7.2.

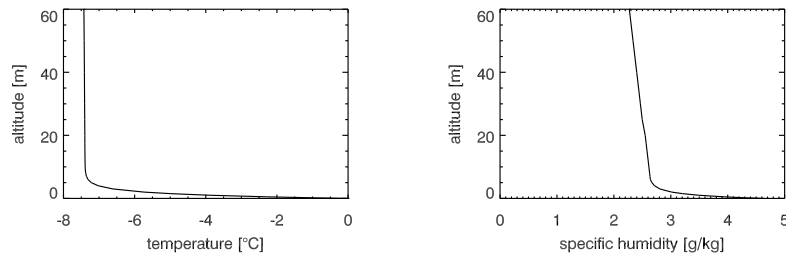


Figure 7.1: Profiles of temperature and humidity for July 9th, 12:40 LT.

A thin cirrusstratus cloud layer of 9/10 was observed at the closest synoptic observation, 13 LT. Thus, a standard cirrus model is included in MODTRAN (Berk et al., 1999) to account for this high cloud cover. If the cirrus cloud cover is not taken

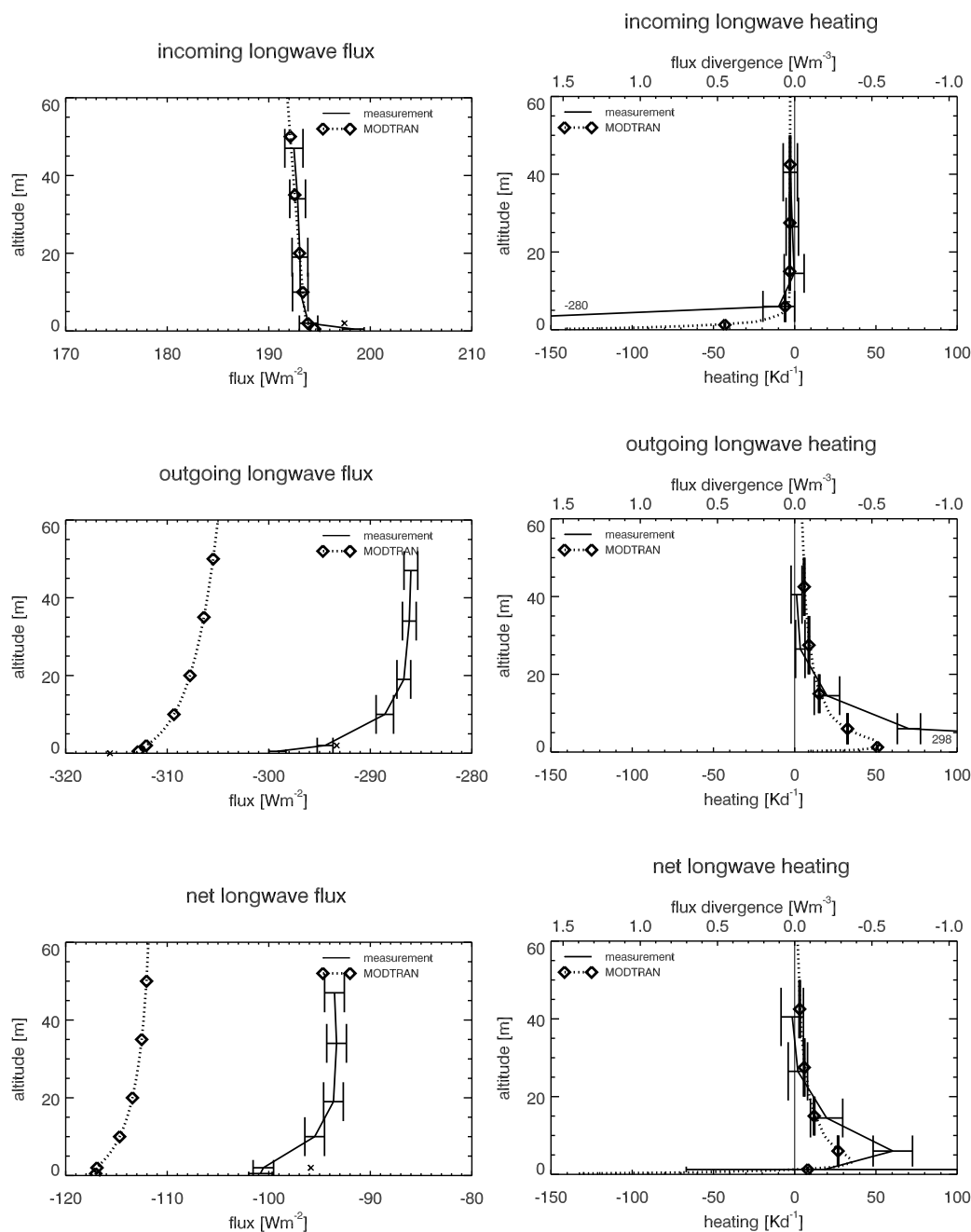


Figure 7.2: Profiles of incoming, outgoing and net longwave fluxes (left panels) and the corresponding heating rates (right panels) for July 9th, 12:40 LT. Dotted line: modeled profiles; Solid line: measured profiles. Crosses at a height of 2 m indicate measurements at a site 200 m away. Crosses at 0 m indicate the value of black body surface emission. Extreme heating rate values not fitting on the graph are given as numbers in Kd^{-1} .

into account in the model, an offset of about 10 Wm^{-2} is seen between modeled and observed incoming longwave flux. The raw surface thermocouple data showed positive temperatures during the time of interest, which is a clear sign for a strong radiation error. All thermocouple measurements are therefore corrected with the offset value between two overlapping measurements of a thermocouple and a ventilated Vaisala HMP35A temperature probe at 0.5 m above the surface (see Appendix B). After applying this correction, the surface temperature still showed a positive value of 1.1°C . This indicates that the correction of the radiation error was not sufficient. The reason for the too small correction is that the thermocouple at 0.5 m is cooled by the wind, which leads to a smaller radiation error. As the snow surface temperature can not exceed melting temperature it was reset to 0.0°C .

Modeled flux profiles agree qualitatively well with the measured fluxes. The profiles of the incoming longwave flux both show a slight increase towards the surface. The increase of the down-welling flux from the 2 m to the 0.5 m level is, however, much larger for the measurements, although the enhanced increase is also seen in the model calculations. The corresponding profiles of incoming longwave radiative heating rates show a very good agreement in the upper parts of the profile. An exception is the lowest layer. The cooling due to the measured longwave radiative flux divergence in the 0.5 m to 2 m layer is much larger than the modeled cooling.

Outgoing flux profiles agree qualitatively well. However, modeled fluxes shows a smaller variation with height. Throughout most of the flux profiles, a rather large offset in the order of 20 Wm^{-2} is found. The same offset is seen between the modeled flux at 2 m and the measurement of the longwave outgoing flux at the radiation tower about 200 m away from the flux tower. This additional measurement is indicated in Figure 7.2 by a cross symbol at 2 m height. Below 10 m, the decrease of the measured outgoing flux towards the surface is much stronger than the decrease of the modeled flux. In Figure 7.2, the cross symbol at the surface level marks the Planck emission of the snow surface (under black body assumption) calculated from the surface temperature measurement. Adding this surface value into our consideration, the outgoing fluxes show a further increase towards the surface. The corresponding outgoing longwave radiative heating rates agree very well, although a deviation is seen below 10 m. There, the measured longwave radiative heating rate increases much faster, while the model results indicate a reduction of the outgoing longwave heating rate very close to the surface. The vertical resolution of the measurements, however, is not high enough to resolve this change.

The modeled and measured net longwave flux profile show an excellent qualitative agreement. However, the constant offset of about 20 Wm^{-2} is seen. A decrease of the net flux is observed towards the surface, which is reduced in the direct vicinity of the snow surface. The corresponding heating rate profile shows the characteristic shape for unstable conditions: a zero heating rate in the upper profile, an increasing heating to a maximum in the 2-10 m layer. Below 2 m, a reduction of the heating is suggested by both, measurement and model. Mean daytime measurements indicated this shape of heating rate profile as well. They were presented in Figure 5.7.

7.2 Stable night

The stable nighttime situation is centered on the radio sounding of July 10th, 21:40 LT. Temperature and humidity profiles used as model input are shown in Figure 7.3. Measured and modeled fluxes and the corresponding heating rates are shown in Figure 7.4.

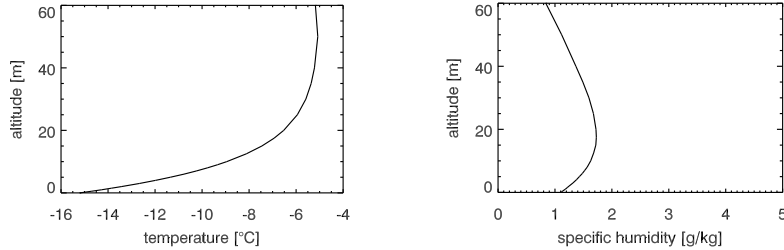


Figure 7.3: Profiles of temperature and humidity for July 10th, 21:30 LT.

Nighttime observations of the longwave fluxes and model results are in rather good agreement if we exclude the measurement at 0.5 m. A constant offset between the profiles of incoming longwave flux of about 4 Wm^{-2} is avoided by introducing cirrus clouds into the model. The incoming longwave flux profiles show little change above 10 m. Below 10 m, they increase towards the ground. The lowest measurement at 0.5 m, however, is somewhat larger than the flux at 2 m, which leads to an incoming longwave cooling. This contrasts to the heating modeled for the 0.5-2 m layer. Outgoing flux profiles differ by an offset of about 5 Wm^{-2} . The increase of the outgoing fluxes towards the ground matches very well throughout most of the profile. At 0.5 m, however, the outgoing flux shows a sudden decrease, which leads to an extremely large heating rate. The model shows a reduction of the slope of the flux, which leads to the characteristic reduction of the outgoing cooling under stable conditions. This characteristic shape that was seen in previous model studies is not seen in the measured heating rate profile.

Modeled and measured net flux profiles agree very well. The observed reduction of the net flux across the lowest air layer is larger, however. This leads to a strong heating which is only qualitatively represented in the model result. The offset between the profile is about 5 Wm^{-2} . The shape of the resulting net longwave cooling profiles match very well. Maximum cooling takes place between 10 m and 20 m, a sign change occurs close to the surface. This shape is seen as well in the mean nighttime net longwave heating rate profile (Figure 5.7).

7.3 Fog situation

An intensive observational period took place in the night from July 8th to 9th, 2002. During this night, strong fog formation was observed. This situation was modeled with MODTRAN to compare observations with the model results. The temperature and humidity profiles used as model input are based on the radiosonde launched at 1 LT (Figure 7.5). A fog layer of 100 m thickness was introduced into the model

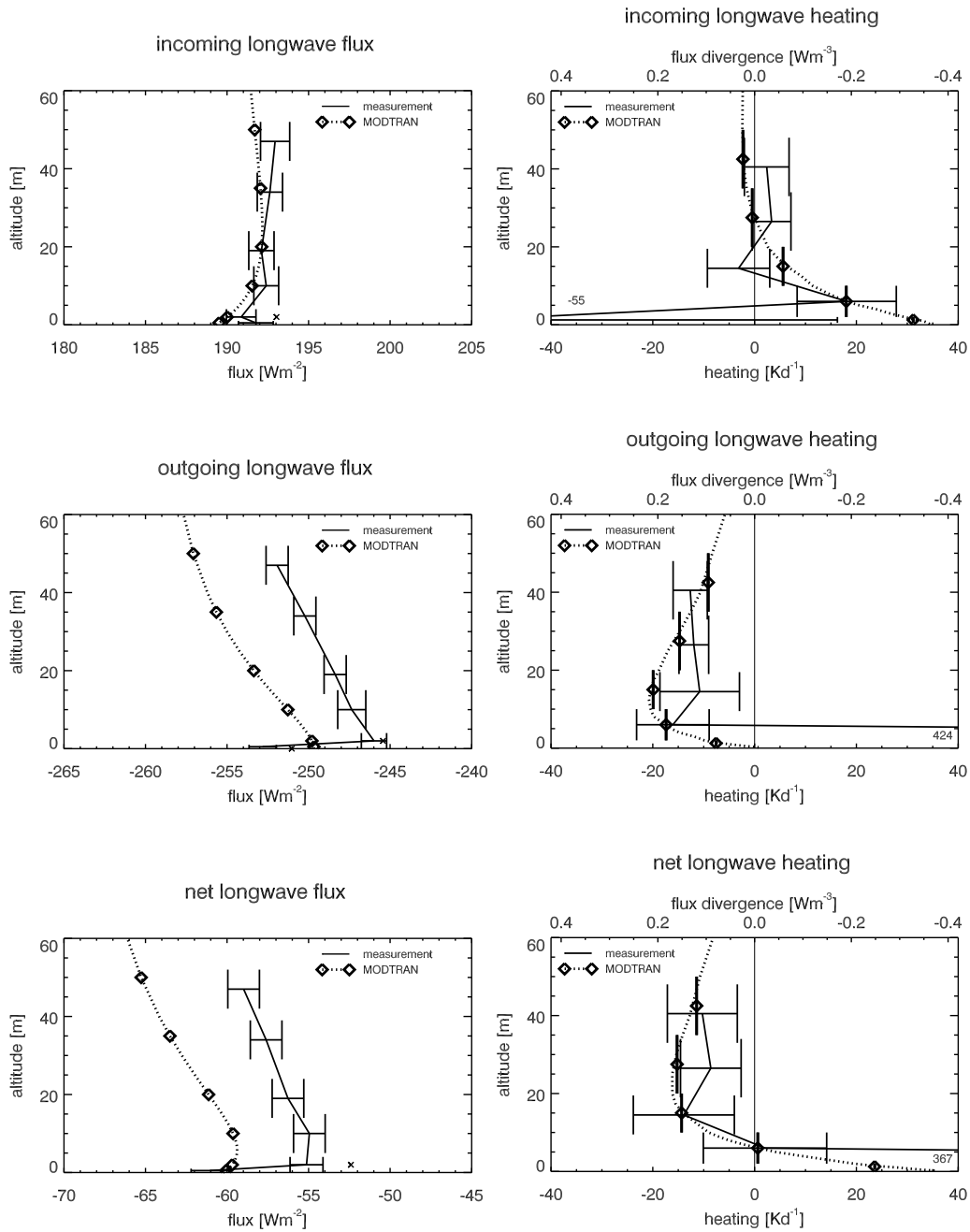


Figure 7.4: Profiles of incoming, outgoing and net longwave fluxes (left panels) and the corresponding heating rates (right panels) for July 10th, 21:30 LT. Dotted line: modeled profiles; Solid line: measured profiles. Crosses at a height of 2 m indicate measurements at a site 200 m away. Crosses at 0 m indicate the value of black body surface emission. Extreme heating rate values not fitting on the graph are given as numbers in Kd⁻¹.

calculation. A cirrus cloud cover of 5/10 and of 3/10 had been observed three hours prior and three hours past the launch of the radiosonde, respectively. Cloud observations had not been possible at 1 LT, as the fog obscured the sky. It was assumed that the cirrus cover persisted during the fog situation, and it was included into the model calculations. Without the introduction of a cloud layer, an offset between modeled and observed down-welling flux of 5 Wm^{-2} would result. As strong rime formation had been observed on the tower structure, the emissivity of the tower structure used in the correction of the measurements was raised to an average value of 0.5.

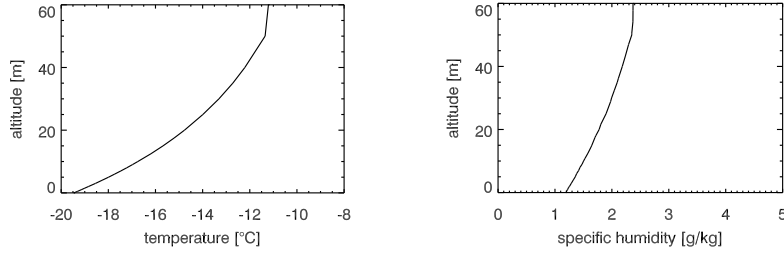


Figure 7.5: Profiles of temperature and humidity for July 9th, 1:00 LT.

The modeled and measured fluxes and the corresponding heating rates are presented in Figure 7.6. Incoming flux profiles show an excellent agreement. The slope of the increase of the down-welling flux is largest in the layer between 20 m and 35 m. Thus maximum cooling rates result in this layer. A reduction of the slope towards the surface leads to a smaller cooling close to the ground. The cooling due to the divergence of the incoming flux has already been shown to be the main difference to fog free situations (Section 5.2.4 and 6.2.7).

Outgoing fluxes are in good agreement in the upper profile, apart from an offset of 5 Wm^{-2} . Measurements show a somewhat larger increase in the slope which leads to a larger measured cooling above 20 m. In the lower part of the profile, the decrease of the outgoing flux towards the surface is smaller for both model and observation. This leads to a reduction in the cooling closer to the ground. In the lowest layer (0.5 to 2 m) the differences between observation and model are greatest. A reduction in the down-welling flux between 2 m and 0.5 m, and a resulting heating, is seen in the measurements. Contrary, the model shows a reduced gradient with a resulting zero heating rate.

Net longwave flux profiles agree very well if the offset of 5 Wm^{-2} , which is introduced by differences in the outgoing fluxes, is ignored. The curvature of the measured heating rate profile is well reproduced by the model. The only difference arises in the lowest layer. Between 2 m and 0.5 m the measurements indicate a heating, while the model calculations show zero heating.

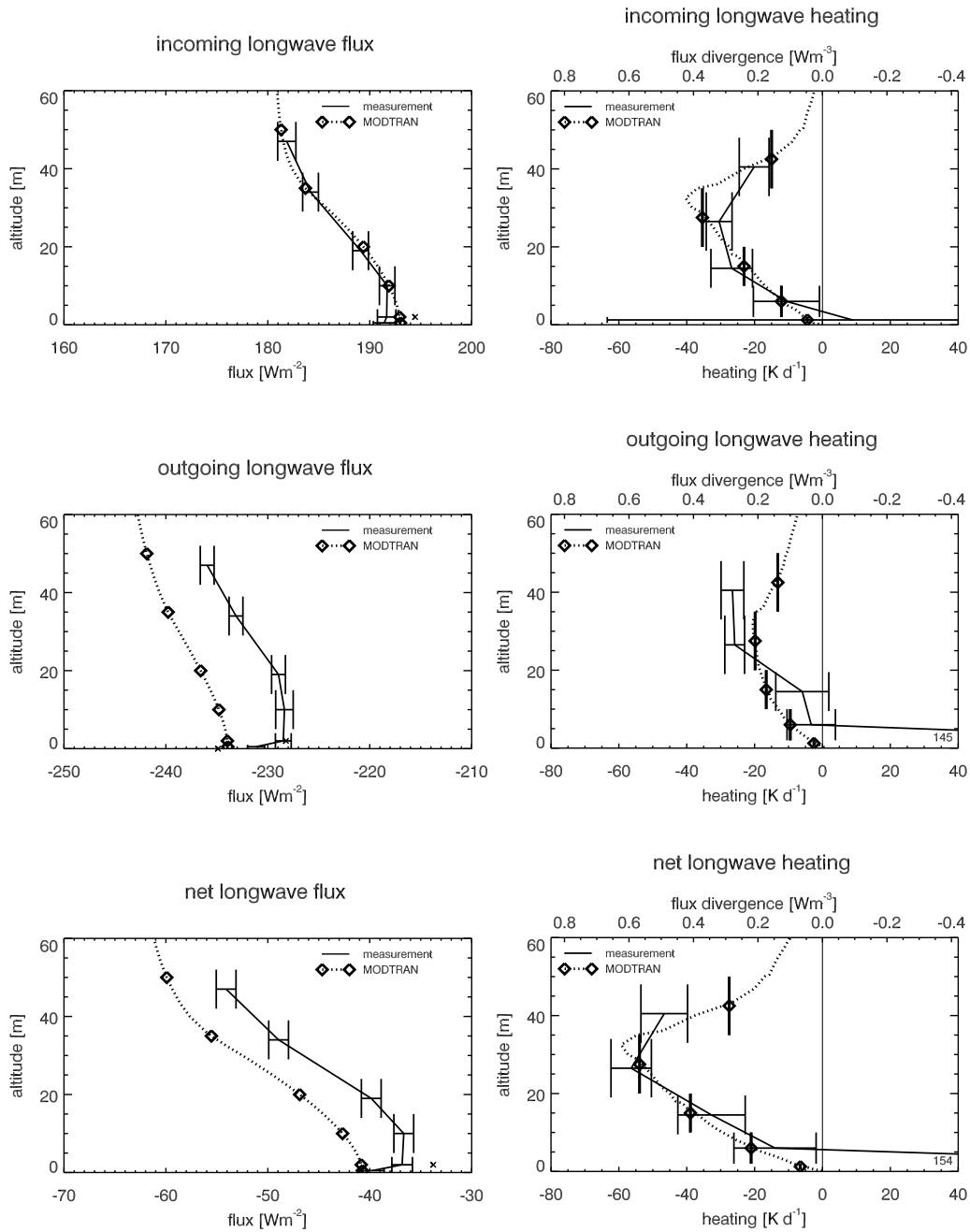


Figure 7.6: Profiles of incoming, outgoing and net longwave fluxes (left panels) and the corresponding heating rates (right panels) for July 9th, 1:00 LT. Dotted line: modeled profiles; Solid line: measured profiles. Crosses at a height of 2 m indicate measurements at a site 200 m away. Crosses at 0 m indicate the value of black body surface emission. Extreme heating rate values not fitting on the graph are given as numbers in Kd^{-1} .

8 Discussion

8.1 Divergence of the incoming and outgoing flux

Longwave radiative flux divergence can be separated into the incoming and outgoing components. In the following, the relative importance of the two components is discussed.

Under stably stratified, fog free conditions, the divergence of the outgoing flux is generally larger than the divergence of the incoming flux. The outgoing component is responsible for the strong cooling which is observed in the vicinity of the inversion top. Likewise, it causes the strong radiative heating of the air at heights between about 2 m and 10 m above surfaces that are warmer than the overlaying air (unstable stratification).

This relative importance of incoming and outgoing components has previously been observed experimentally. Timanovskaya and Faraponova (1967) observed the pattern of dominating outgoing flux divergence (cooling) at night and of dominating negative outgoing flux divergence (heating) during the day in the air between 1 m and 8 m above steppe. The minor role of the divergence of the incoming flux, with light heating at night and a light cooling during daytime, was also visible in their measurements. Sun et al. (2003) similarly observe outgoing longwave radiative cooling and light incoming longwave radiative heating between 2 m and 48 m during the early night.

The measurements presented in this work clearly support the above findings. The bulk measurements between 2 m and 50 m as well as the measurements between 2 m and 10 m show the same pattern. However, new information can be extracted from the measurements, as a full 3-layer profile of the divergence is available. For example, in the layer between 10 m and 50 m, the dominance of the outgoing flux divergence is greatly reduced compared to the situation in lower layers (Figure 5.10). Nevertheless, the outgoing component in the 10-50 m layer is still the main driver of the diurnal cycle, as it causes the variation from cooling at night to zero heating during daytime, whereas the incoming component remains rather constant over the entire day. In the lowest layer represented in our observations (0.5 m to 2 m), the outgoing and incoming components of the radiative flux divergence are of the same magnitude but of opposite sign.

In the presence of fog, the relative importance of the incoming and outgoing component of radiative flux divergence changes. A cooling due to a diverging incoming flux, which is larger than the cooling due to the diverging outgoing flux is observed.

The cause for this effect lies in the spectral distribution of the longwave radiative cooling. The cooling is now no longer limited to the strong absorption bands of water vapor and carbon dioxide but extends into the window regions of the spectrum. These features are discussed in Section 8.3.

8.2 Vertical structure of longwave flux divergence

The detailed measurements of the longwave radiative flux profile have allowed for the first time to examine the full vertical structure of the longwave radiative flux divergence based on observations. The shape of the profile has been under debate (Stull, 1988). Now, a comprehensive picture evolves from the available longwave radiative flux divergence data within three adjacent layers. Below the strong cooling close to the inversion top, a sign change of the longwave flux divergence is seen. Heating in the layer close to the surface has previously been observed by Lieske and Stroschein (1967) under conditions of strong and thick inversions over snow in the Arctic. Their measurements were too shallow however, to resolve the strong divergence that must have occurred at higher levels close to the inversion top.

The measurements presented in Section 5.2.1 show the transition from cooling in upper layers to heating close to the surface at about 2-5 m above ground during nighttime. During the day, a transition occurs from a cooling in upper layers (10-50 m) to a heating between 2 m and 10 m and back to a cooling close to the surface (0.5-2 m). These features of the radiative heating rate profile under stable and unstable conditions are also represented by the model calculations with MODTRAN (Section 6.2.1). This shows that MODTRAN is capable to resolve the fine structure of the radiation profile, and that it therefore is a suitable tool for further investigating longwave radiative flux divergence.

The comparison of the different findings on longwave radiative cooling and heating clearly shows the importance of vertical resolution. Some theoretical approaches such as Fleagle (1953) and calculations with very high vertical resolution on the order of 10 cm (Räisänen, 1996) clearly resolve the transition from cooling in the upper layers to heating close to the surface under stable conditions. On the other hand, other model approaches using a coarser resolution like those of Tjemkes and Duykerke (1989) and Ha and Mahrt (2003) miss this feature.

A consistent longwave radiative heating above the surface under stable conditions was suggested by Räisänen (1996). He compared two radiation schemes used in numerical weather forecasts. Both, the ECMWF and DWD schemes are broadband models. When Räisänen (1996) introduced a step function or temperature discontinuity close to the surface ($T_s - T_{0+} = -3$ K, with T_s the surface temperature and T_{0+} the temperature of the air just above the surface) the picture changed. An enhanced cooling resulted close to the surface. When he kept the temperature profile isothermal in the lowest 2 m, his results again changed remarkably. A positive heating rate resulted in the lowest layers. Unfortunately, his results were presented graphically with a vertical resolution of 1 mb (8 m), which might hide additional interesting features within the fine structure of the cooling profile.

Contrary to the findings of Räsänen (1996), an intense near-surface cooling was found by Ha and Mahrt (2003), when the surface temperature is specified to be 1.5 K cooler than the theoretical air temperature extrapolated to the surface. Although they refer to the work of Räsänen (1996), they use a coarse 1 m resolution and are therefore not able to resolve the sign change of the heating rate profile close to the ground. When Ha and Mahrt (2003) discuss the vertical resolution, they criticize the fact that coarse resolution will miss the stabilizing effect of radiative cooling near the surface. This is true for resolutions of the order of 10 m, which lead to a loss of information in the layer between about 5-15 m, where maximum cooling occurs under stable conditions. As Räsänen (1996) showed, however, an even higher resolution (below 1 m) is necessary to illustrate the heating just above the surface that was reported already by Fleagle (1953). In general, the presented observations and model calculations support the conclusions of Räsänen (1996) and set question marks on the findings of Ha and Mahrt (2003) and Tjemkes and Duynkerke (1989) which do not resolve the sign change of longwave radiative heating close to the ground, as they are based on calculations with a too coarse resolution in the vicinity of the surface.

The measurements and calculations in this work clearly show that longwave radiative heating occurs in air layers just above a cold surface, and cooling is induced above a warmer surface. Above this near-surface layer, which is represented by the 0.5 m-2 m layer in our measurements, the sign of the heating rate changes. In the 2 m to 10 m layer, cooling results under stable conditions (layer is warmer than the surface) and heating results under unstable conditions (layer is colder than the surface). This is shown in Figure 8.1 and the corresponding model results are seen in Figure 6.8 of Section 6.2.3. The height at which the transition between cooling and heating occurs depends on the temperature profile. From the model experiment with artificial temperature profiles described by Equation 6.1, the height of maximum cooling under stable conditions stays constant when the temperature difference across the inversion layer is varied. It is suggested that the height of maximum cooling does therefore not depend on the temperature gradient but on the height of the inversion. However, as was clearly demonstrated, the strength of cooling within a layer strongly depends on the temperature gradient across this layer and on the height of the layer above the surface (Figure 6.10). When the parameter γ is varied in Equation 6.1, the shape of the temperature profile varies. A growing γ leads to a compression of the inversion layer and to stronger temperature gradients close to the surface. The height where the sign of the heating rate changes moves closer to the surface, and a lowering of the level of maximum cooling is observed. In addition, the strength of cooling increases due to the stronger gradients. In all modeled cases, the height of maximum cooling, however, falls within a height range where the temperature difference between layer and surface reaches 85-90 % of the overall inversion strength (Figure 6.11).

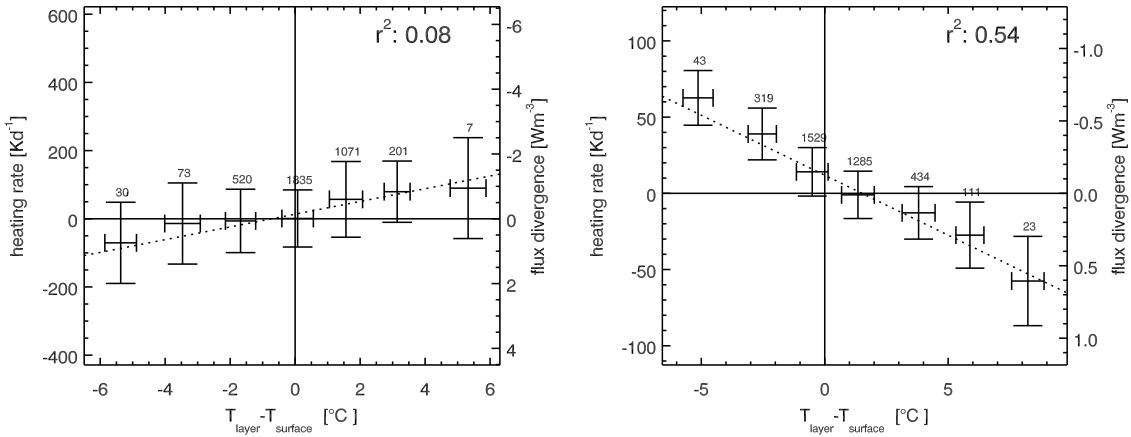


Figure 8.1: Net longwave radiative heating rate versus temperature difference between mean layer temperature and surface temperature. For 0.5 m to 2 m (left) and for 2 m to 10 m layer. Data was binned into seven classes representing temperature differences. Plotted is the mean temperature difference and the mean heating rate of data included in each bin. Error bars indicate the standard deviation of the data points.

8.3 Longwave radiative flux divergence and fog

When fog is present in the lower boundary layer, the relative importance of the incoming and outgoing components of radiative flux divergence changes. The case study presented in Section 5.2.4 clearly indicates this change. The incoming flux now shows a stronger divergence than the outgoing flux, in both layers between 2 m and 10 m and between 10 m and 50 m. Under these conditions, the strongest rates of cooling in elevated air layers are observed, reaching values of -60 Kd^{-1} (Figure 5.26).

Under fog conditions, radiative cooling is equal to or stronger than the observed cooling rate. This agrees with the findings of Roach et al. (1976). The sudden onset of radiative cooling in the 2 m to 10 m layer and the subsequent development from strong cooling in this layer to even stronger cooling in higher layers (10–50 m) are also confirmed.

The spectral model calculations with MODTRAN of clear conditions and situations with fog illustrate the cause for the changing effect of incoming component. The strong cooling due to the diverging incoming flux under fog conditions is caused by the radiative exchange between the fog droplets in the window region of the spectrum (Figure 6.19). This cooling dominates over the heating which results from the radiative flux convergence in the strong absorption bands of water vapor and carbon dioxide.

8.4 Detailed comparisons between observation and model

The net longwave radiative heating rate profiles modeled with MODTRAN show a good agreement with the profiles measured during intensive observational periods under varying meteorological conditions. The incorporation of a cirrus layer into the model calculation was sufficient to remove offsets in the order of $5\text{--}10\text{ Wm}^{-2}$ in the down-welling fluxes. Under unstable daytime conditions, an excellent agreement of the modeled and observed longwave radiative heating rate profile is seen. Nevertheless, an underestimation of the magnitude of the radiative flux divergence components by the model is suggested. Measurements show a much larger cooling due to the divergence of incoming flux in the lowest layer (0.5–2 m), as well as a larger heating due to the converging outgoing flux. Much better agreement is obtained for the divergence of the net longwave flux. The shape of the modeled and observed heating rate profile well represents the observations. Under strong inversion conditions as typically observed during nighttime, the largest discrepancy between observations and model results was found in the layer between 0.5 m and 2 m. While observations indicate a large reduction in the outgoing flux towards the ground, the simulations suggest a slight increase. In this case we could not rule out the possibility that this difference was caused by problems in the acquisition of the field data. All radiation instruments are ventilated with heated air to prevent rime formation on the instrument domes. It is thinkable that this may have induced a warming of the surface by the down-facing instrument at 0.5 m. The flux difference between the measured value and the value at 2 m (assuming zero flux change between 2 m and 0.5 m) corresponds to a radiative temperature change of 1.8°C . It is doubted that the warmed ventilation air can have an effect this large on the snow surface. As shown in Appendix C, a possible shortwave leaking of the down-facing pyrgeometers can also be excluded as the cause of this discrepancy. The measured incoming flux, on the other hand, shows an increase between 2 m to 0.5 m. This again does not fit the picture suggested by the model, and a coherent explanation is not at hand. These uncertainties regarding the lowest measurements level must be emphasized, as they do not show up in the resulting net longwave radiative heating rates. Here, the overall shape of the measured and the modeled profile is again in agreement. In the nighttime situation with fog, it is again the outgoing flux at 0.5 m which causes the largest difference between measured and modeled profile. A large heating contribution is added into the lowest layer.

8.5 Causes for longwave radiative flux divergence

The causes for longwave radiative flux divergence are not directly obvious when only the net longwave flux profile and the temperature profile are on hand. A decrease of the incoming flux under stable conditions is plausible, but the reason for a sign change of radiative flux divergence close to the surface is not entirely obvious. The causes for radiative flux divergence are often, as in Kondo (1971), attributed to 'the nature of radiative transfer'.

In Section 6.2.6, the causes for longwave radiative flux divergence were addressed in detail. Model calculations with MODTRAN proved very helpful, as the different flux components are resolved spectrally.

Measurements had already indicated that the largest part of the stable surface boundary layer (from the 2-10 m layer upward) is mainly influenced by the divergence of the outgoing longwave flux. Model calculations show the same domination of the outgoing component and demonstrate the importance of the strong absorption bands of water vapor and carbon dioxide. They also show the increasing influence of the divergence of the incoming flux below 10 m.

The various components of the outgoing flux (path thermal, surface emission and ground reflected) show marked differences in their divergence profiles. In the surface boundary layer, the outgoing path thermal component always diverges (regardless of stability), while the surface emitted always exhibits a convergence. Above a snow surface, the ground reflected component plays a minor role, as its emissivity is close to unity. A positive divergence of the outgoing flux results under stable conditions as the increase of the path thermal flux with increasing distance from the surface is larger than the decrease of the surface emitted flux. The dominance of the cooling effect of the path thermal component is not equally strong at all heights. This leads to a maximum of the outgoing flux divergence at a height of about 7-10 m.

On the other hand, an increase of the down-welling longwave flux towards the surface is seen under unstable conditions, and a decrease under stable conditions. This is caused by the weaker (stronger) emission in the strong absorbing bands during stable (unstable) situations.

With these results in mind, the cause of the change of sign in the net longwave flux divergence profile near the surface becomes clear. It is the result of the increasing divergence of the incoming flux while the magnitude of the divergence of the outgoing flux is greatly reduced.

This explanation is based on the model calculations with idealized temperature profiles. It is in good correspondence with the results of the measurement of the net longwave radiative heating. However, there is one discrepancy. While the outgoing flux divergence in the model calculations shows a reduction in absolute magnitude in the vicinity of the surface, measurements indicate an increasing magnitude in the 0.5 m to 2 m layer. For a very shallow superadiabatic layer near the surface this discrepancy may be explained. The layer is so shallow that the height where the divergence of the outgoing flux reduces falls below the 0.5-2 m measurement layer, and is therefore not resolved. For the nighttime case, when the outgoing flux divergence even dominates the net cooling in the 0.5-2 m layer, at this time, there is no explanation at hand.

The partitioning of the outgoing longwave flux between surface emission and ground reflected radiation depends on the surface emissivity. Model calculation could demonstrate that under hypothetical conditions of very small surface emissivity, a heating just above the surface may be caused by the negative divergence of the outgoing flux. But with the snow surface being so close to a black body, this does not happen in nature.

8.6 Flux divergence, temperature gradient and humidity

The relationship between longwave radiative flux divergence and temperature profile was addressed in Section 5.2.5 and Section 6.2.3. The relationship was analyzed from both, measurements, and model results.

Measurements indicated an increasing divergence (or cooling) with higher stability in the layers between 2 m and 10 m, between 10 m and 50 m, and in the bulk layer between 2 m and 50 m (Figures 5.28 to 5.32). It was shown that the relationship is mainly due to the strong relationship of the outgoing component of radiative flux divergence with stability. When the relationship for the incoming component is investigated, the majority of data suggests an increased heating with growing stability. There is, however, a rather large scatter, as cases of very strong cooling due to the divergence of the incoming flux are indicated. This scatter could be qualitatively explained and attributed to situations with fog. Assuming a linear relationship between net longwave radiative heating rate and temperature gradient the linear correlation coefficient r^2 is small. Nevertheless, there is an increase of cooling of roughly 6 Kd^{-1} , 7.5 Kd^{-1} and 7.5 Kd^{-1} with an increase of stability of 0.1 Km^{-1} across the 2-10 m, 10-50 m and 2-50 m layers, respectively. Measurements in the layer between 0.5 m and 2 m show the opposite. An increased heating is seen under increasingly stable conditions. The linear fit indicates an increase of heating by 14 Kd^{-1} when the temperature gradient increases by 0.1 Km^{-1} .

When mean diurnal cycles of longwave radiative heating rates and of temperature differences across the corresponding air layers are analyzed, similar patterns are observed (Figure 5.34). With increasing stability, an increase in heating rate results in the 0.5-2 m layer, and a decreasing heating rate in the layers above 2 m. The rates of increase and decrease are different, however. The changes in heating rate for an increase in the temperature difference by 0.1 Km^{-1} are now 19.5 Kd^{-1} , -15.5 Kd^{-1} , -14 Kd^{-1} and -15 Kd^{-1} across the 0.5-2 m, 2-10 m, 10-50 m and 2-50 m layers, respectively. These differences are due to the different weighting of the data, when either single data points or temporal means are used when deriving the linear fit.

The analysis of the relationship between longwave radiative heating rate and temperature gradient from model results was summarized in Figure 6.10. While the incoming component of longwave radiative heating shows an increase with growing stability, which is rather constant at all levels, a decrease of heating (increased cooling) with growing stability is seen in the outgoing component. The relationship between the outgoing component of heating rate and temperature gradient, however, strongly depends on the height of the layer above the surface. Close to the surface, outgoing longwave radiative heating changes very little, while large changes are seen in higher layers.

The relationship of the net longwave radiative heating rate with temperature gradient therefore depends on the distance of the individual layer from the surface. For idealized temperature profiles described by Equation 6.1 with γ of 0.09 the following relationship is visible: layers below 5 m show a clear increase in heating rate with increasing stability, whereas layers above 7 m show a decrease in heating

rate. Between 5 m and 7 m the cooling induced by the divergence of the outgoing flux and the heating from the convergence of the incoming flux compensate each other, regardless of stability.

The level where the relationship between temperature gradient and longwave radiative heating rate disappears depends on the detailed shape of the temperature inversion. If the parameter γ is varied, the height of this level changes. This is illustrated in Figure 6.12. A lower inversion layer (lower inversion top, stronger temperature gradients) leads to a reduction of the height of zero heating. This explains the large scatter when longwave radiative heating within near-surface layers is plotted against the temperature difference across this layer (Figure 5.30).

Information on temperature gradient alone does not suffice to evaluate the longwave radiative heating within a layer. The shape of the inversion, as well as the height of the layer above the surface, plays an important role. This explains the hysteresis-type pattern that is observed in the analysis of the diurnal cycles of longwave radiative heating and temperature gradients (Figure 5.34). Differences between the heating rates that are observed for the same temperature gradients are greatest in the times of transition between the noon and mid-night periods of steady state temperature profiles. As shown in Figure 8.2, the shapes of growing and decaying inversion are different, and can therefore be approximated best using different γ . This leads to different longwave radiative heating rates, although the temperature gradient across the individual layer is the same.

Under unstable conditions like those observed during daytime close to the ground, convection will erode the warm pool at the surface from above. The warm pool will remain shallow. The temperature profile will therefore be best described by a large γ (Figure 8.2). With a larger γ , the height of the sign change of radiative flux divergence is lowered to a height very close to the surface. The layer between 0.5 m and 2 m which, under stable conditions, usually falls within the layers below the sign change of radiative flux divergence, may now lie above this level. Therefore, the 0.5-2 m layer falls within the height range of strong radiative heating. This explains why the measurements in this layer show an increasing heating under increasingly unstable conditions (Figure 5.30).

Model calculations suggest an influence of humidity on the strength of longwave radiative cooling. This is also expected, as water vapor is the strongest absorber in the longwave spectrum. The sign of the heating rate was shown to be related to the temperature gradient, the height of the layer above surface and to the inversion shape and overall height. An increase in specific humidity simply enhances the integrated effect of all these factors. Both, cooling and heating trends are intensified. When humidity is raised from 0.5 to 1 g kg⁻¹ the heating rate increases by roughly 15-20 %. A change from 1 to 1.5 g kg⁻¹ already has a smaller effect of about 10-15 %. Although subsets of observed longwave radiative heating rates were analyzed, representing classes of observed temperature gradients to eliminate a dominating influence of a varying temperature gradient, the enhancing effect of higher humidities could not be inferred from the measurements.

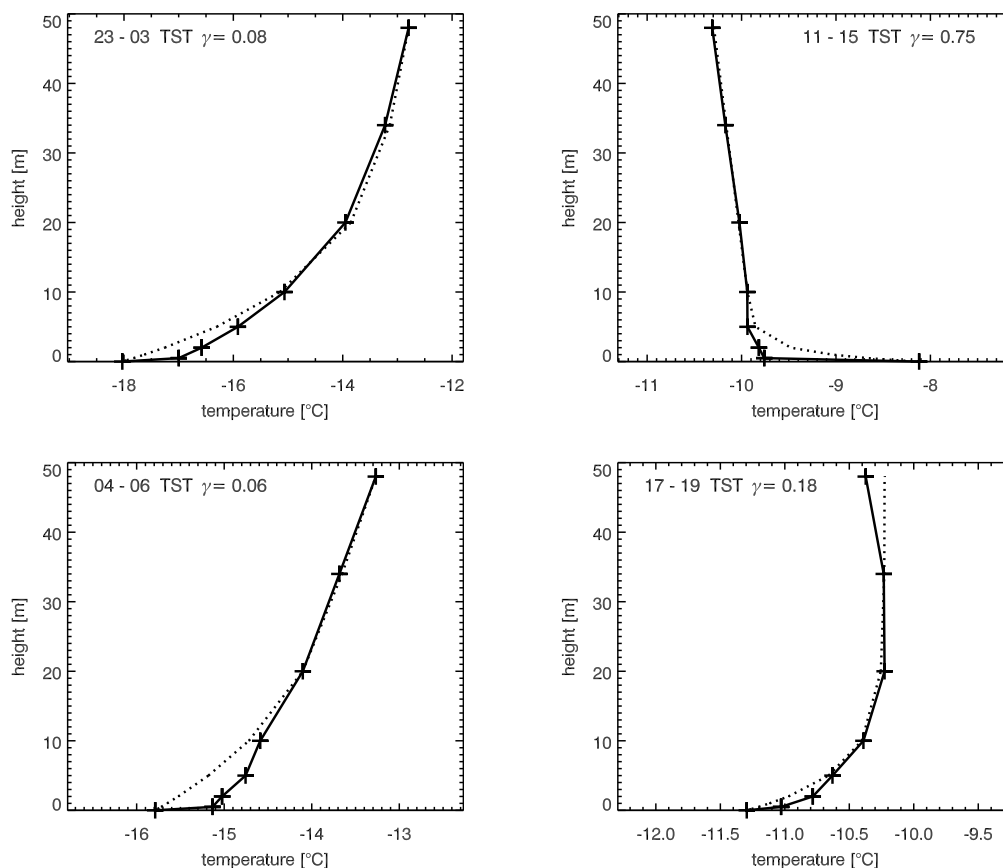


Figure 8.2: Mean summer temperature profiles for 23-3 TST, 11-15 TST, 4-6 TST and 17-19 TST. Dotted line represents a fit using Equation 6.1. The temperature profiles are best represented using different values of γ . Some levels with measurements were omitted.

8.7 Flux divergence under different meteorological conditions

The dataset of longwave radiative flux divergence which was collected between May 19th and July 18th, 2002, was analyzed for four different meteorological conditions. 'Cloud free' conditions (opacity below or equal to three tenths, low and middle cloud amount below or equal to one tenth, high cloud amount less or equal to five tenths) could be compared to overcast situations (low cloud amount nine tenths or higher) and offer information on the influence of clouds on longwave radiative flux divergence. Calm conditions (2m wind speed below 2 m s^{-1}) and windy situations (2m wind speed above 5.5 m s^{-1}) illustrate the role of the wind speed. The bulk cooling between 2 m and 50 m is about one third larger (-15 Kd^{-1}) during overcast night than during clear nights (-10 Kd^{-1}). This is surprising in the first moment, as the differences in the temperature profiles are very small, as can be seen in Figure 8.3. The answer can be seen in the components of longwave radiative flux divergence. The cooling rates due to the outgoing component are the same during the night (-8 Kd^{-1} and -7 Kd^{-1} for clear and overcast conditions, respectively). The

contribution of the divergence of the incoming flux, however, results in a stronger cooling (-8 Kd^{-1}) during the overcast conditions than during clear nights. The cause must be the inclusion of nights with fog into the overcast class, as a diverging incoming flux during stable conditions is a clear sign of fog.

The difference between the profiles of longwave radiative flux divergence are much larger between calm and windy conditions than between clear and cloudy skies. Under calm conditions, the absolute values of longwave radiative flux divergence are generally larger than under windy conditions. The obvious reason is seen in the difference of the two temperature profiles (Figure 8.3). While a stable stratification develops in the lowest 30 m of the boundary layer during calm nights, turbulent mixing avoids the formation of a distinct inversion layer at stronger wind speeds. During the calm nights, the inversion is distinct enough that the sign change of longwave radiative flux divergence is resolved in the measurements, and a heating within the 0.5-2 m layer is observed. The inversion layer under windy conditions lies very close to the surface, and a sign change in the radiative flux divergence can not be resolved by the observations.

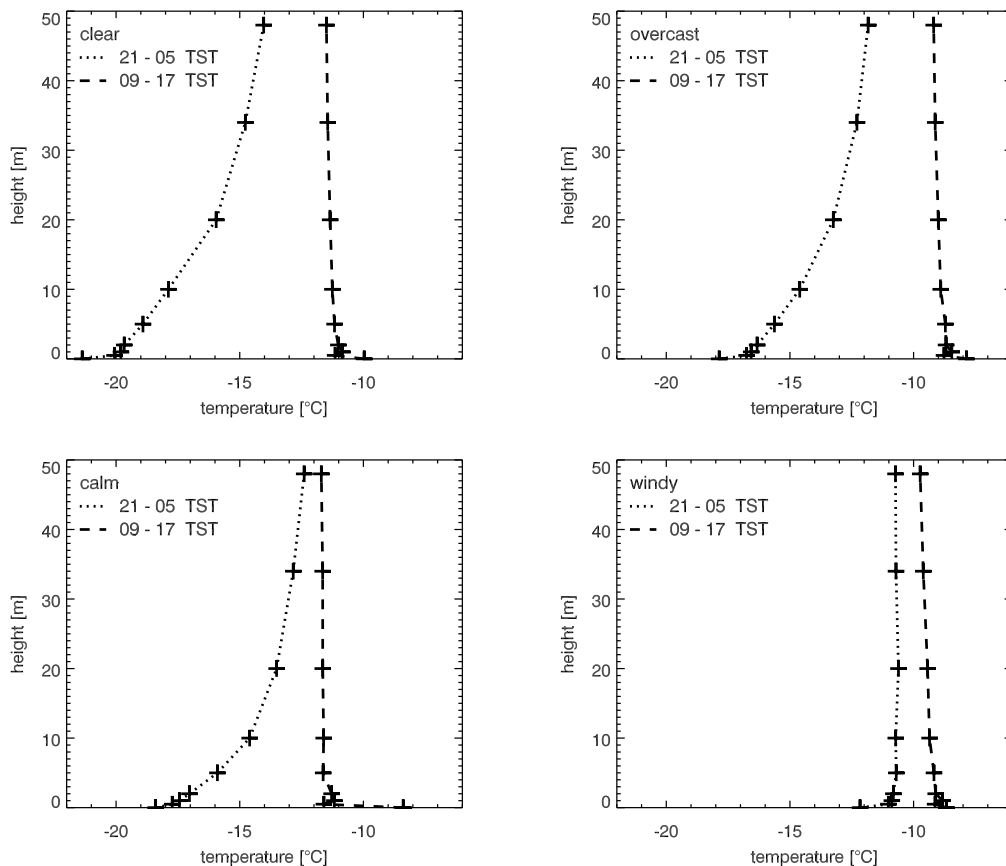


Figure 8.3: Mean nighttime (dotted) and daytime (dashed) temperature profiles within the lowest 50 m for clear sky (top left), overcast (top right), calm (bottom left) and windy (bottom right) conditions.

8.8 Longwave radiative flux divergence and the fine structure of the temperature profile

This section is an attempt to explain the possible influence of longwave radiative flux divergence on the vertical temperature distribution. To this point, the role of vertical temperature stratification for the profile of longwave radiative flux divergence was discussed. A vertically varying radiative flux divergence, however, will induce a differential heating and cooling within the air layers, and is suggested to alter the temperature profile. The discussion here is based on the observed fine structure of the temperature profile above the snow surface. Information on this fine structure is available from measurements with thermocouples in high vertical resolution (0.0 m, 0.1 m, 0.2 m, 0.5 m and 1 m). A mean daytime (11-15 TST) temperature profile for clear sky conditions, assembled from 86 15-minute mean temperature profiles, is shown in top left panel of Figure 8.4. Above a highly unstable near-surface layer (0.0-0.2 m), an inversion layer is identified, which reaches up to a height of 1 m. Above 1 m, a neutral to unstable stratification is found (Figure 8.4). Daytime profiles of temperature collected over the Antarctic shelf ice have been shown to develop a similar shape. Sodemann and Foken (2004) report an inversion layer in the lowest 2 m above ground that often persists during daytime. Above this inversion, a neutral to unstable layer is observed to a height of about 5 m. Measurements with an infrared thermometer show a surface temperature that is higher than the air temperature in their lowest measurement level at 0.5 m (Sodemann, 2002). This indicates that this inversion layer is as well underlain by an unstable layer in contact with the surface. The near surface inversion observed at Summit is somewhat thinner than the one observed by Sodemann and Foken (2004) and the increase in temperature towards the snow surface is better resolved in our observations.

During nighttime, a special shape of the temperature profile can be observed as well. A strong stable layer is seen very close to the surface, up to about 0.2 m. Above, a remarkably less stable temperature gradient is observed to a height of about 2 m to 5 m. Above 10 m, the profile agrees well with a temperature curve that may be described with Equation 6.1 (Figure 8.4, bottom left panel).

In Figure 8.4 the mean temperature profiles for clear sky daytime and nighttime conditions are shown together with their approximations based on Equation 6.1. The panels on the right-hand side show the corresponding observed profiles of longwave radiative heating.

During daytime, it is exactly the layer where a strong longwave radiative cooling rate is observed that shows a stable stratification. The elevated surface inversion between approximately 0.2 m and 1 m during daytime could thus be attributed to the radiative cooling in the air just above the warmer snow surface (0.5-1.0 m). Strong radiative heating is observed above (2-10 m), which further strengthens the underlying inversion. A buildup of a warm air pool in this layer is avoided by a downward erosion due to convection. The highly unstable layer in contact with the snow surface observed between 0.0-0.2 m is the result of shortwave heating of the snow surface. It is worth mentioning that the elevated inversion layer decouples the ground from the atmosphere. Thus, heating of the air during the diurnal temperature

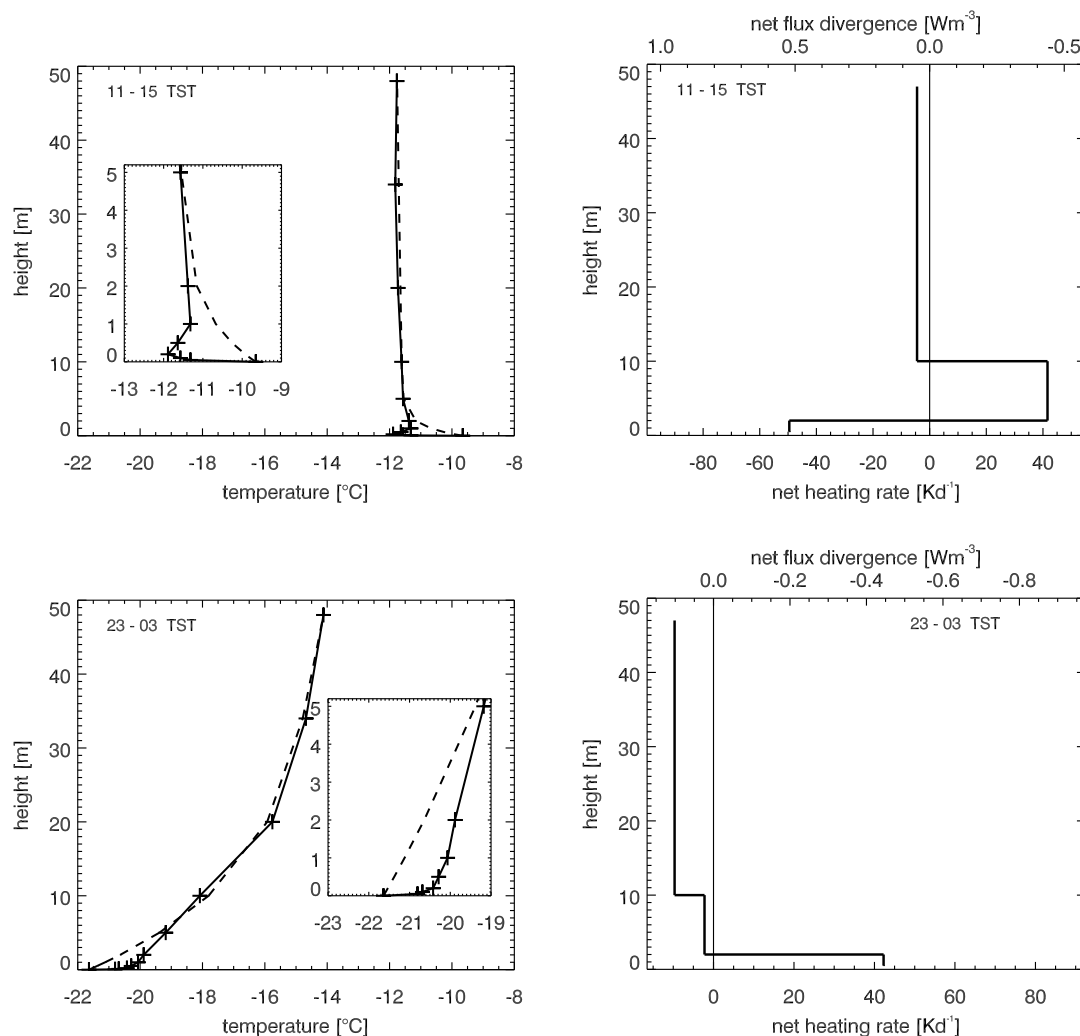


Figure 8.4: Mean temperature (left) and longwave radiative heating rate (right) profiles during clear sky day (top panels) and night (bottom panels). Number of 15-minute profiles included in the mean are $n=86$ for the daytime and $n=64$ for the nighttime profile.

cycle may be controlled to the largest part by radiative processes.

During nighttime, on the other hand, the longwave radiative heating just above the cold surface leads to a destabilization of the air. This effect is seen between 0.2 m and about 5 m in the observed temperature profile. The snow surface itself cools due to longwave emission, and the strong stability in the thin layer in contact with the surface (0.0-0.2 m) is maintained.

The shape of the temperature profile is, however, the integrated result of more processes than radiative flux divergence alone. Sensible heat flux divergence equally depends upon, and influences, the temperature stratification. Note that the turbulent heat transfer tends to suppress the temperature gradient on which it feeds. That is to say, that turbulence alone is not able to maintain a strong inversion over a long time. The persistence of strong inversions at Summit underlies thus the importance of radiative flux divergence and its interactions with turbulence.

A fundamental assumption in micrometeorology has been that the turbulent vertical heat flux is constant with height in the surface boundary layer (Munn, 1966). The justification for this assumption is that during the middle of the night and during a short period in the afternoon, air temperatures remain constant with time (steady-state), and that during these times the vertical flux divergence must thus be negligible. Fundamental theories on turbulent heat exchange such as the Monin-Obukhov similarity theory (Monin and Obukhov, 1956) are based on this concept of a constant flux layer. They are, however limited to near-neutral conditions.

The observations presented in this thesis clearly show that under stable nighttime and unstable daytime conditions at Summit, a strong heating or cooling due to longwave radiative flux divergence acts upon the temperature profile. The longwave radiative heating or cooling is shown to be especially large during the near steady-state situations in the early afternoon and around midnight. The largest values of radiative heating and cooling are observed within the lowest several meters above the surface. This suggests diverging and converging sensible heat fluxes within the surface layer.

Part IV

Summary and conclusions

The goal of this study was twofold. In the first part, the meteorological and climatic conditions of the dry snow zone at Summit, Greenland, were investigated. This analysis is based on measurements from the 14-month ETH Summit Project field campaign that took place between May 2001 and July 2002. The annual cycle as well as the diurnal variation of the energy balance components were presented.

The second part of this study focused on the process of longwave radiative flux divergence in the atmospheric boundary layer. A unique dataset was collected during the ETH Summit Project. Longwave radiative flux divergence was derived in up to five layers within the lowest 50 m of the boundary layer from measurements of incoming and outgoing longwave fluxes. In addition to the observations, model calculations with the radiative transfer model MODTRAN proved helpful to interpret the observed features in the profile of longwave radiative flux divergence and to examine the spectral characteristics. The model was driven by observed profiles of temperature and humidity from a 50 m meteorological tower and from upper air soundings. Both, observations and model calculations lead to a thorough understanding of the process of radiative flux divergence and its vertical structure. In the following, the most important features and findings are summarized.

Climatic conditions at Summit, Greenland

Annual net radiation is negative at Summit, Greenland, with -6 Wm^{-2} . In the summer months May, June and July, however, net radiation is positive. A maximum of 17 Wm^{-2} was observed in July 2002. In February 2002, the lowest net radiation of -22 Wm^{-2} was recorded.

Cloudiness exhibits an annual cycle. Total cloud amount is lower in spring than in late summer. In April and May, global radiation is therefore dominated to 60% by the direct component, while the diffuse radiation is the larger component (60%) of global radiation in July and August. Monthly mean global radiation reaches 380 Wm^{-2} in June.

Annual mean albedo amounts to 0.82. In March and April, monthly mean albedo is slightly lower, and an increase is seen towards the end of the year. This is due to the combination of a rougher surface in spring, an increase in precipitation in fall, and the increase in total cloud amount.

The lowest monthly mean incoming longwave flux of 114 Wm^{-2} was recorded in February 2002, which was with -47.3°C also the coldest month on our record. A maximum incoming longwave flux of 229 Wm^{-2} was observed in July 2002.

The energy balance shows no significant diurnal variation from October to February. During the winter months, the negative net radiation of -20 Wm^{-2} is balanced to 2/3 by the sensible heat flux and to 1/3 by the subsurface heat flux.

From April to August, sensible heat flux is negative during parts of the day. This indicates unstable conditions near the surface. Averaged over the summer months, sensible heat flux amounts to only 1 Wm^{-2} . Latent heat flux becomes important only in summer. Half of the available energy from the positive net radiation (11 Wm^{-2}) is used for sublimation. The other half is used to heat the snow cover (negative subsurface heat flux).

The annual mass gain at Summit between the summers of 2001 and 2002 was 242 mmWE. Annual sublimation amounted to 12% of the precipitation. In summer, however, nearly 30% of the precipitation is lost by sublimation. Due to a large negative subsurface heat flux, an even greater sublimation is avoided. In the dry snow zone at Summit, 70% of the net accumulation takes place in fall and winter. Net accumulation is smallest in spring.

Profile measurement of longwave radiative flux

Measurements of longwave radiative fluxes with Eppley PIR pyrgeometers were accurate enough to determine longwave radiative flux divergence in air layers with a thickness of several meters. Instruments were equipped with three dome thermistors and ventilated with air warmer than the ambient temperature. A relative calibration of the pyrgeometers at the field site was necessary to reduce the standard deviation in the measurements of flux differences between the individual instruments. This relative calibration was performed for both up-facing and down-facing pyrgeometers. During the 2002 summer field season, flux differences between incoming and outgoing fluxes at different levels could be determined with an uncertainty of only ± 0.60 and $\pm 0.45 \text{ Wm}^{-2}$, respectively. A correction of the measurements for the influence of the tower structure was shown to be necessary.

Radiative flux divergence in the bulk 2-50 m layer

During an average summer night which is stably stratified, longwave radiative flux divergence within the bulk layer between 2 m and 50 m reaches a maximum of 0.15 Wm^{-3} . This corresponds to a heating rate of -15 Kd^{-1} . A minimum of about 0.05 Wm^{-3} (-5 Kd^{-1}) is observed during summer mean daytime conditions. During stable conditions in winter, daily means of longwave radiative flux divergence as large as 0.31 Wm^{-3} (-30 Kd^{-1}) were recorded. During summer nights with fog formation, longwave radiative flux divergence of up to 0.6 Wm^{-3} (-55 Kd^{-1}) are observed. Monthly means of longwave radiative flux divergence vary between 0.03 Wm^{-3} (-3 Kd^{-1}) during summer and 0.13 Wm^{-3} (-12 Kd^{-1}) in fall, winter and early spring.

Divergence of incoming and outgoing flux

In the bulk layer between 2 m and 50 m, the divergence of the outgoing flux usually dominates the net longwave flux divergence. It is often opposed by a converging incoming flux.

A relationship between temperature gradient and longwave radiative flux divergence is suggested by the measurements. For the 2-50 m bulk layer, an increase in longwave radiative flux divergence (increased cooling) is observed with increasing stability. This relationship is dominated by a strong relationship between the divergence of the outgoing flux and temperature gradient.

The vertical profile of longwave radiative flux divergence

Longwave radiative flux divergence changes with height. If stratification is not neutral, there is always a height within the first meters of the atmosphere where a sign change in longwave radiative flux divergence is observed. In the layer in contact with a cold (warm) surface, a negative (positive) divergence results. In this layer, which often falls within the 0.5-2 m layer covered by our measurements, extreme cooling or heating rates due to the divergence or convergence of the incoming and outgoing longwave fluxes on the order of $\pm 200 \text{ Kd}^{-1}$ are observed. Due to the compensating behavior of the two components, the net longwave radiative flux divergence in this layer is one order of magnitude smaller. It is positive during the day (heating rate of -10 Kd^{-1}) and negative at night (heating rate of 40 Kd^{-1}).

Model calculations show that the sign change of radiative flux divergence results from a shift in the balance between the divergence of the incoming and outgoing flux. While the absolute value of the divergence of the incoming flux component increases towards the surface, a decrease in the divergence of the outgoing flux is seen. Above this near-surface layer, a radiative cooling (positive divergence) results above a cold surface, and a radiative heating (negative divergence) is seen above surfaces warmer than the atmosphere. This cooling or heating, which is caused by the dominating effect of the divergence of the outgoing flux, reaches a maximum at a level near the top of the inversion or unstable layer. Model calculations with idealized temperature profiles show that this height corresponds to the height where the temperature difference (from the surface) has reached approximately 85-90 % of the overall inversion strength.

During mean summer daytime conditions the layer of maximum convergence falls within the layer between 2 m and 10 m. This corresponds to a heating of 25 Kd^{-1} . During the night, when the inversion layer is thicker, the height of maximum cooling falls within a height of approximately 10 m. The resulting cooling within the 2-10 m layer and the 10-50 m layer is then equally strong and amounts to -10 Kd^{-1} .

Model calculations based on idealized measured temperature and humidity profiles are in qualitative agreement with observations. The observed overall shape of the profile of net longwave radiative flux divergence, including the change of sign within the first several meters above the ground is well represented in the model calculations for day- and nighttime conditions, as well as for situations with fog. There remain, however, some discrepancies in relation to the conditions within the first few meters of the profile. Observed heating rates of the incoming and outgoing components are usually stronger than modeled. These discrepancies may arise from the idealized representation of the temperature and humidity profile close to the surface. The magnitude of the measured heating rates agrees well with the observations published by Eliseev et al. (2002).

The presented measurements and model calculations clearly show that the theoretical considerations by Fleagle (1953) and the vertically highly resolved numerical calculations by Räisänen (1996) correctly reflect the phenomenon of a sign change in the radiative flux divergence profile close to the surface.

Radiative flux divergence, temperature gradient and humidity

The characteristic profile of longwave radiative flux divergence explains why it is not possible to link radiative flux divergence directly with the temperature gradient. The strength and sign of longwave radiative flux divergence depends not only on temperature gradient but also on the shape and total height of the temperature inversion or superadiabatic layer, and on the height of the considered layer above the surface. This explains why measurements indicate an increasing heating rate with increasing stability for the layer below 2 m and an increasing cooling in the layers above 2 m. For individual layers within a typical shape of temperature profile however, radiative flux divergence is mainly a function of the temperature gradient. It could be shown from model calculations, that the increase in humidity has an enhancing effect on longwave radiative flux divergence.

Spectral distribution of radiative flux divergence and the influence of fog

Model calculations with MODTRAN offer a spectral viewpoint on longwave radiative flux divergence. The strong radiative flux divergence under fog free conditions can be shown to occur mainly within the strong absorbing bands of water vapor and carbon dioxide. The partitioning of the modeled outgoing flux into its three components path thermal, surface emitted and ground reflected helps to understand the profile of the outgoing flux close to the surface.

When fog forms under stable nighttime conditions, some of the strongest cooling rates are observed. Measurements show that this enhanced cooling is caused by a change from a heating to a cooling contribution of the incoming flux. While a converging incoming flux generates a heating under fog free conditions, a strong cooling is induced by a diverging incoming flux under conditions with fog. Spectral calculations illustrate that this strong cooling originates within the atmospheric window region of the spectrum and is caused by the radiative exchange between the fog droplets. This cooling is stronger than the heating which is induced in the strong absorption bands of water vapor and carbon dioxide and which dominates under fog-free conditions.

Feedback of longwave radiative flux divergence on temperature

Furthermore, a link between the measured profile of longwave radiative flux divergence and the fine structure of the temperature profile is suggested. The deviations of the mean daytime and nighttime temperature profiles from an idealized shape may be attributed to the influence of longwave radiative flux divergence. During daytime, the observed elevated surface inversion between 0.3 and 1 m is most likely caused by the observed strong cooling due to longwave radiative flux divergence in the air layer close to the surface and by the observed strong heating above. During nighttime, a layer of reduced stability between 0.3-5 m can be attributed to the observed heating effect of a negative radiative flux divergence.

Appendices

Appendix A

Shortwave radiative heating

The divergence of shortwave radiation is always negative. The resulting heating effect, however, is rather small. A simple parameterization of the shortwave radiative heating is developed from model results using MODTRAN. Four combinations of temperature and humidity profiles are chosen that cover the entire range of specific humidities expected during summer conditions at the field site. Once, the observed temperature and humidity profiles from 1540 LT July 8th, 2002, once those from 2140 LT July 10th, 2002, were used as model input. A third temperature profile (1540 LT July 9th, 2002) was combined with theoretical specific humidities of 10% and 99% in the lowest 200 m of the atmosphere. The mean specific humidities in the lowest 50 m for the four cases are 0.32, 1.27, 2.24 and 3.20 g kg⁻¹. Heating rate calculations are performed for five solar elevation angles, ranging between 6 and 40 degrees. A linear dependence of the heating rate on the elevation angle is observed for all profiles (not shown). The slope of this dependence is assumed to only depend on specific humidity. An empirical relationship is then formulated:

$$sw \text{ heating rate} = \text{elevation angle} \cdot (c_1 \cdot q + c_2) , \quad (\text{A.1})$$

with the specific humidity q in g kg⁻¹, the shortwave radiative heating rate in Kd⁻¹, and c_1 of 0.031 Kd⁻¹ deg⁻¹g⁻¹ kg and c_2 of 0.03 Kd⁻¹ deg⁻¹. In Figure A.1 the comparison of parameterized and modeled shortwave radiative heating rates is shown.

The parameterization is very simple and based on only a few model calculations. A more detailed parameterization scheme is presented by Savijärvi (1990). His parameterization is based on the work of Chou (1986). He also recommends the scheme by Lacis and Hansen (1974) which is based on absorption data by Yamamoto (1962).

Figure A.2 illustrates the clear sky summer mean diurnal cycle of shortwave radiative flux divergence. It is calculated using the above developed parameterization and the humidity measurements taken at the 10 m level. The maximum shortwave radiative heating of 4 Kd⁻¹ (divergence of -0.04 Wm⁻³) is reached during the high solar elevation angles at noon.

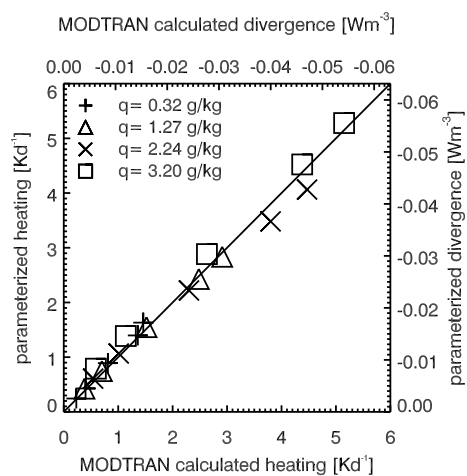


Figure A.1: Comparison of parameterized and modeled shortwave radiative heating rates. Four different profiles with specific humidities between 0.32 and 3.20 g kg^{-1} were used at five different zenith angles.

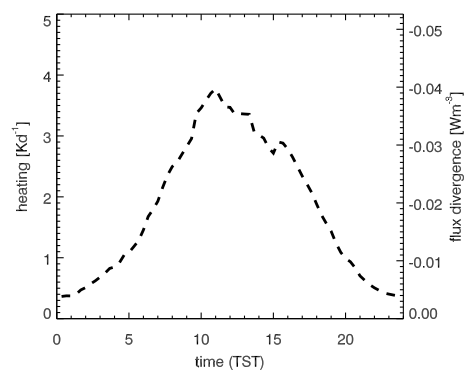


Figure A.2: Clear sky summer mean diurnal cycle of shortwave radiative flux divergence at Summit.

Appendix B

Temperature measurements

Ventilated and thermocouple air temperatures

Different sensors were used to monitor air temperature. The ventilated Vaisala HMP35A sensors were mounted on eight levels of the tower (0.5, 1, 2, 5, 10, 19, 34, 48 m), while thermocouples were installed at a distance of 15 m away from the tower structure at heights of 0.0, 0.05, 0.1, 0.2, 0.5 and 1 m. Thermocouples measurements exhibit a radiation error which is seen during daytime. A possibility to correct for the radiation error is to assume that this error is the same for all thermocouples. The difference between a thermocouple and a ventilated HMP35A sensor can then be used to correct all thermocouple measurements. This is complicated by the fact that this correction is not the same for the two heights where overlapping measurements are available. While nighttime differences (with the sun at large zenith angles) are the same, daytime corrections differ. It was decided to use the lower overlapping measurement at 0.5 m above the surface to determine the correction for the radiation effect on the thermocouples, as the thermocouple at 1 m broke during the experiment.

Surface temperature

Surface temperature is a crucial variable. A lack of a reliable infrared thermometer needs to be compensated. Surface temperature is monitored with a thermocouple placed on the snow surface, which is checked twice daily. The thermocouple shows a radiation error is observed during the day. In addition, a certain distance of the thermocouple from the true snow-air interphase may be caused either through wind, sublimation or due to a light cover of rime or drifting snow. An second estimate of the surface temperature is also available from the pyrgeometer measurements at 0.5 m. The assumption of zero flux divergence, however, will introduce an error. Under stable conditions, the temperature estimate will be too high, as the outgoing flux decreases with height (increases in absolute values), giving an upper bound of the surface temperature estimate. Under unstable conditions, the opposite will result. The temperature estimate will give a lower boundary estimate, as the outgoing flux increases with height (decreases in absolute values).

Appendix C

Shortwave leaking and down-facing pyrgeometers

The problem of radiation with shorter wavelengths than $4\ \mu\text{m}$ leaking through the pyrgeometer domes was discussed in Section 5.1.3. This effect is corrected through the use of a compensation term which includes the f -factor in the pyrgeometer formula (Equation 5.20). This correction is, however, only applied to measurements of up-facing instruments. In the field program, the instruments that had shown the strongest shortwave leaking during shading experiments were used to monitor the up-welling longwave fluxes, to avoid large correction terms.

The question arises whether the down-facing pyrgeometer measurements may overestimate the up-welling longwave flux due to a shortwave leaking of reflected shortwave radiation through the dome. Such leakage may have led, for example, to the large change of the outgoing longwave on July 10th, 21.30 UTC. The strong decrease of the outgoing flux between 2 m and 0.5 m (increase in absolute values) does not correspond with the model calculations (Figure 7.3). As the f -factor of the 0.5 m instrument is larger than the f -factor of the 2 m instrument, a shortwave leaking could potentially explain this discrepancy.

The shortwave leaking of the individual pyrgeometer domes may differ. The efficiency of the interference filter and its cut-on may vary. Also, the angular distribution of the radiation onto the dome may play a role due to different characteristics (density, thickness) of the vacuum-deposited interference filter on the inside of the silicon dome. Due to the small spectral albedo of snow at wavelengths above $2\ \mu\text{m}$, however, the leakage effects should be smaller for down-facing instruments than for the up-facing ones.

A model calculation with the MODTRAN radiative transfer model is used to evaluate the spectral distribution of the incoming and outgoing flux for clear sky conditions. Table C.1 summarizes the results. It becomes obvious why the direct shortwave component is used in the correction term of the pyrgeometer formula. The direct solar component is the main component in the spectral region in which the leaking takes place. The transmission of a pyrgeometer silicon dome without interference filter starts at about $1\ \mu\text{m}$. The vacuum-deposited interference filter on the inside of the dome is supposed to block radiation at wavelengths shorter than 3.5-

Table C.1: Modeled downward diffuse, upward diffuse and direct solar radiation in Wm^{-2} for selected spectral intervals, for July 9th, 2002, 12.40 LT ($z_{solar} = 51^\circ$) under clear sky conditions.

frequency range	direct solar	downward diffuse	upward diffuse
0.3-4.0 μm	610.8	121.4	529.3
1.0-1.5 μm	108.9	3.9	52.6
1.5-2.0 μm	44.0	0.5	4.6
2.0-2.35 μm	16.4	0.1	1.4
2.35-2.4 μm	1.7	0.0	0.1
2.4-2.5 μm	2.4	0.0	0.1
2.5-3.0 μm	1.3	0.0	0.0
3.0-3.5 μm	3.4	0.0	0.2
3.5-4.0 μm	3.2	0.0	0.3
4.0-500 μm	2.4	175.9	270.8

4 μm . The onset of the filter, however, varies from dome to dome. In the worst case, an instrument with an average dome transmission of 35 % may still transmit 25 % at a wavelength of 2.5 μm . A worst case scenario, with instruments of uniform spectral transmission that differ only in the onset of filter, may be considered. Theoretical amounts of shortwave-leaking can then be estimated using available f -factors and modeled spectral radiative fluxes. Let us consider the 0.5 m PIR, which showed the largest f -factor of 20.1 when pointing upward during shading experiments. The downward diffuse flux contains no radiation between 4.0 μm and 2.0 μm (Table C.1). Only the direct solar can be a source of shortwave-leaking. From the modeled direct solar, we estimate the amount of shortwave-leaking R_{leak} into the 0.5 m instrument:

$$R_{leak} = f \cdot D/1000. = 20.1 \cdot 610.8/1000. = 12.3 Wm^{-2}. \quad (C.1)$$

By adding the contributions from the spectral intervals of the direct beam, we find that the shortwave-leaking is due to radiation at wavelengths of 2.4 μm on higher, as they add up to 12.8 Wm^{-2} . Now we can estimate from our calculations how much of the upward radiation is in the frequency range from 2.4 to 4.0 μm . It amounts to 0.6 Wm^{-2} . The unexplained flux differences in the outgoing fluxes however, are in the order of 3-5 Wm^{-2} . This clearly shows that it is justified to neglect an influence of the shortwave reflected radiation on the down-facing instruments. The influence of 0.6 Wm^{-2} represents the worst case scenario. The effect should be smaller with larger zenith angle, and the f -factor value of $f=20.1$ is the maximum determined for the pyrgeometers. As the other instruments have a non-zero f -factor as well, the flux difference would be further reduced, as both instruments would show a leakage. In our theoretical consideration we give the same weight to the radiation in this border region of dome transmittance spectrum as to spectral regions where flux densities are largest. The lower transmittance in the region of shortwave-leakage further reduces its potential influence. Angle dependent measurements of dome transmittance have shown an onset of non-zero transmittance at longer wavelengths with rising zenith angle. There is also a trend to lower transmittance with rising zenith angles. Assuming an isotropic radiation field, the integrating sphere gives the strongest weight to

radiation from the sector around 45° (50% in $30\text{-}60^\circ$ range). For all of these reasons, an effect shortwave leaking on down-facing pyrgeometers must be ruled out.

Bibliography

- Abdalati, W. and K. Steffen, 1995: Passive microwave-derived snowmelt regions on the Greenland ice sheet. *Geophys. Res. Lett.* **22**(7), 787–790.
- Abdalati, W. and K. Steffen, 2001: Greenland ice sheet melt extent: 1979-1999. *J. Geophys. Res.* **106**(D24), 33,983–33,988.
- Albrecht, B. and S. K. Cox, 1977: Procedures for Improving Pyrgeometer Performance. *J. Appl. Meteorol.* **16**(2), 188–197.
- Albrecht, B. A., M. Poellot, and S. K. Cox, 1974: Pyrgeometer measurements from aircraft. *Rev. Sci. Instrum.* **45**, 33–38.
- Ambach, W., 1963: Untersuchungen zum Energieumsatz in der Ablationszone des grönländischen Inlandeises. EGIG 1967-1968, 4 (4) Meddelelser om Grønland, Bd. 174 (4), Reitzels, Copenhagen, 311 pp.
- Ambach, W., 1977: Untersuchungen zum Energieumsatz in der Akkumulationszone des grönländischen Inlandeises. EGIG 1967-1968, 4 (7) Meddelelser om Grønland, Bd. 187 (7), Reitzels, Copenhagen, 44 pp.
- Ambach, W. and G. Markl, 1983: Untersuchungen zum Strahlungshaushalt in der Akkumulationszone des grönländischen Inlandeises. EGIG 1957-1960, 4 (6) Bianco Lunos Bogtrykkeri, a/s København, 61 pp.
- Ambartsumian, V., 1936: The effect of absorption lines on the radiative equilibrium of the outer layers of stars. *Publ. Astron. Obser. Leningrad* **6**, 7–18.
- Anderson, G., J. H. Chetwynd, J. Wang, L. A. Hall, F. X. Kneizys, L. M. Kimball, L. Bernstein, P. Acharya, A. Berk, D. C. Robertson, E. P. Shettle, L. W. Abreu, K. Minschwaner, and J. A. Conant, 1995: MODTRAN 3: Suitability as a Flux divergence Code. In *Proceedings of the Fourth Atmospheric Radiation Measurement (ARM) Science Team Meeting*, pp. 75–80. U.S. Department of Energy, Washington, DC.
- André, J. C. and L. Mahrt, 1982: The Nocturnal Surface Inversion and Influence of Clear-Air Radiative Cooling. *J. Atmos. Sci.* **39**, 864–878.
- Arking, A. and K. Grossman, 1972: The Influence of Line Shape and Band Structure on Temperatures in Planetary Atmospheres. *J. Atmos. Sci.* **29**, 937–949.
- Benson, C. S., 1962: Stratigraphic studies in the snow and firn of the Greenland ice sheet. Research Report. No. 70, Snow, Ice and Permafrost Research Establishment (SIPRE), 93 pp.
- Berk, A., G. P. Anderson, P. K. Acharya, J. H. Chetwynd, M. L. Hoke, L. S. Bernstein, E. P. Shettle, M. W. Matthew, and S. M. Adler-Golden, 1999,

- June) *MODTRAN4 Version 2 User's Manual* Hanscom Air Force Base, MA 01731-3010: Air Force Research Laboratory, Space Vehicles Directorate.
- Berk, A., G. P. Anderson, L. S. Bernstein, P. K. Acharya, H. Dothe, M. W. Matthew, S. M. Adler-Golden, J. H. Chetwynd, S. C. Richtsmeier, B. Pukall, C. L. Allred, L. S. Jeong, and M. L. Hoke, 1999: MODTRAN4 Radiative Transfer Modeling for Atmospheric Correction. *SPIE Proc.* **3756**, 348–353.
- Berk, A., L. S. Bernstein, G. P. Anderson, P. K. Acharya, D. C. Robertson, J. H. Chetwynd, and S. M. Adler-Golden, 1998: MODTRAN Cloud and Multiple Scattering Upgrades with Application to AVIRIS. *Remote Sens. Environ.* **65**, 367–375.
- Bernstein, L. S., A. Berk, P. K. Acharya, and D. C. Robertson, 1996: Very Narrow Band Model Calculations of Atmospheric Fluxes and Cooling Rates. *J. Atmos. Sci.* **53**(20), 2887–2904.
- Box, J. E. and K. Steffen, 2000: Greenland Climate Network (GC-NET Data Reference) Program for Arctic Regional Climate Assessment (PARKA) Cooperative Institute for Research in Environmental Sciences (CIRES), University of Colorado, Boulder, USA.
- Carlson, M. A. and R. B. Stull, 1986: Subsidence in the Nocturnal Boundary Layer. *J. Clim. Appl. Meteorol.* **25**, 1088–1099.
- Cerni, T. A. and T. R. Parish, 1984: A Radiative Model of the Stable Nocturnal Boundary Layer with Application to the Polar Night. *J. Clim.* **23**(11), 1563–1572.
- Charlock, T. P. and V. Ramanathan, 1985: The Albedo Field and Cloud Radiative Forcing Produced by a General Circulation Model with Internally Generated Cloud Optics. *J. Atmos. Sci.* **42**(13), 1408–1429.
- Chou, M.-D., 1986: Atmospheric Solar Heating in the Water Vapour Bands. *J. Appl. Meteorol.* **25**, 1532–1542.
- Chou, M.-D. and A. Arking, 1980: Computation of Infrared Cooling Rates in the Water Vapor Bands. *J. Atmos. Sci.* **37**, 855–867.
- Clough, S. A., M. J. Iacono, and J.-L. Moncet, 1992: Line-by-Line Calculations of Atmospheric Fluxes and Cooling Rates: Application to Water Vapor. *J. Geophys. Res.* **97**(D14), 15761–15785.
- Clough, S. A., F. X. Kneizys, and R. W. Davies, 1989: Line Shape and the Water Vapor Continuum. *Atmos. Res.* **23**(3-4), 229–241.
- Coantic, M. and B. Seguin, 1971: On the Interaction of Turbulent and Radiative Transfers in the Surface Layer. *Bound. Layer Meteorol.* **1**(3), 245–263.
- Drummond, A. J., W. J. Scholes, J. H. Brown, and R. E. Nelson, 1970: A New Approach to the Measurement of Terrestrial Long-wave Radiation. In *Radiation including Satellite Techniques. Proceedings of the WMO/IUGG Symposium held at Bergen, August 1968*, Technical Note No. 104, WMO - No. 248.TP.136, pp. 383–387. Secretariat of the World Meteorological Organization - Geneva - Switzerland.

- Dutton, E. G., J. J. Michalsky, T. Stoffel, B. W. Forgan, J. Hickey, D. W. Nelson, T. L. Alberta, and I. Reda, 2001: Measurement of Broadband Diffuse Solar Irradiance Using Current Commercial Instrumentation with a Correction for Thermal Offset Errors. *J. Atmos. Oceanic Technol.* **18**, 297–314.
- Eliseev, A. A., V. I. Privalov, N. N. Paramonova, and Z. M. Utina, 2002: Experimental Study of Heat-Flux Divergences in the Atmospheric Surface Layer. *Izvestiya, Atmospheric and Oceanic Physics* **38**(5), 649–657.
- Elliott, W. P., 1964: The Height Variation of the Vertical Heat Flux near the Ground. *Quart. J. Roy. Meteor. Soc.* **90**(385), 260–265.
- Elsasser, W. M., 1942: Heat transfer by infrared radiation in the atmosphere. *Harvard Meteor. Studies* **6**, 108.
- Enz, J. W., J. C. Klink, and D. G. Baker, 1975: Solar Radiation Effects on Pyrogeometer Performance. *J. Appl. Meteorol.* **14**(7), 1297–1302.
- Estournel, C. and D. Guedalia, 1985: Influence on Geostrophic Wind on Atmospheric Nocturnal Cooling. *J. Atmos. Sci.* **42**(23), 2695–2698.
- Fairall, C. W., P. O. G. Persson, E. F. Bradley, R. E. Payne, and S. P. Anderson, 1998: A New Look at Calibration and Use of Eppley Precision Infrared Radiometers. Part I: Theory and Application. *J. Atmos. Oceanic Technol.* **15**, 1229–1242.
- Faraponova, G. P., 1969: Radiative Heating of the Atmosphere due to Long-wave Radiation during Daylight Hours. *Izv. An. SSSR Fiz. Atm.* **5**, 494–495.
- Fleagle, R. G., 1953: A Theory of Fog Formation. *J. Marine Res.* **12**(1), 43–50.
- Fuggle, R. F. and T. R. Oke, 1976: Long-wave Radiative Flux Divergence and Nocturnal Cooling of the Urban Atmosphere. *Bound. Layer Meteorol.* **10**, 113–120.
- Funk, J. P., 1960: Measured Radiative Flux Divergence near the Ground at Night. *Quart. J. Roy. Meteor. Soc.* **86**(369), 382–389.
- Funk, J. P., 1961: A Numerical Method for the Computation of the Radiative Flux Divergence near the Ground. *J. of Met.* **18**, 388–392.
- Funk, J. P., 1962: Radiative Flux Divergence in Radiation Fog. *Quart. J. Roy. Meteor. Soc.* **88**(377), 233–248.
- Gaevskaya, G. N., K. Y. Kondratiev, and K. E. Yakushevskaya, 1963: Radiative Heat Flux Divergence and Heat Regime in the Lowest Layer of the Atmosphere. *Archiv Meteorol. Geophys. Bioklima. Ser. B* **12**, 95–108.
- Garratt, J. R. and R. A. Brost, 1981: Radiative Cooling Effects within and above the Nocturnal Boundary Layer. *J. Atmos. Sci.* **38**(12), 1307–1316.
- Goody, R. M., 1952: A statistical model for water vapour absorption. *Quart. J. Roy. Meteor. Soc.* **93**, 165–169.
- Gopalakrishnan, S. G., M. Sharan, R. T. McNider, and M. P. Singh, 1998: Study of Radiative and Turbulent Processes in the Stable Boundary Layer under Weak Wind Conditions. *J. Atmos. Sci.* **55**, 954–960.

- Gupta, S. K., W. F. Staylor, W. L. Darnell, A. C. Wilber, and N. A. Ritchey, 1993: Seasonal Variation of Surface and Atmospheric Cloud Radiative Forcing over the Globe Derived from Satellite Data. *J. Geophys. Res.* **98**(D11), 20761–20778.
- Ha, K. J. and L. Mahrt, 2003: Radiative and Turbulent Fluxes in the Nocturnal Boundary Layer. *Tellus* **55A**(4), 317–327.
- Kneizys, F. X., D. C. Robertson, L. Abreu, P. Acharya, G. P. Anderson, L. S. Rothman, J. H. Chetwynd, J. E. A. Selby, E. P. Shettle, W. O. Gallery, A. Berk, S. A. Clough, and L. S. Bernstein, 1996: The MODTRAN 2/3 Report and LOWTRAN7 Model. Technical report, Philips Laboratory, Geophysics Directorate PL/GPOS, 29 Randolph Road, Hanscom Air Force Base, MA 01731-3010.
- Kondo, J., 1971: Effect of Radiative Heat Transfer on Profiles of Wind, Temperature and Water Vapor in the Atmospheric Boundary Layer. *J. Meteorol. Soc. Jpn.* **49**(2), 75–94.
- Kondratyev, K. Y., 1969: *Radiation in the Atmosphere*, Volume 12 of *International Geophysics Series*. Academic Press.
- Konzelmann, T., 1994: *Radiation Conditions on the Greenland Ice Sheet* Ph. D. thesis, ETH Zürich.
- Konzelmann, T. and A. Ohmura, 1995: Radiative Fluxes and Their Impact on the Energy Balance of the Greenland Ice Sheet. *J. Glaciol.* **41**(139), 490–502.
- Kuhn, M., L. S. Kundla, and L. A. Stroschein, 1977: The Radiation Budget at Plateau Station, Antarctica, 1966-1967. In J. A. Businger (Ed.), *Meteorological Studies at Plateau Station, Antarctica. Antarctic Research Series Volume 25, 41-73*. American Geophysical Union.
- Lacis, A. A. and H. P. Hansen, 1974: A Parameterization for the Absorption of Solar Radiation in the Earth's Atmosphere. *J. Atmos. Sci.* **31**, 118–133.
- Lettau, H., A. Riordan, and M. Kuhn, 1977: Air temperature and two-dimensional wind profiles in the lowest 32 meters as a function of bulk stability. In J. A. Businger (Ed.), *Meteorological Studies at Plateau Station, Antarctica. Antarctic Research Series Volume 25, 77-91*. American Geophysical Union.
- Lieske, B. J. and L. A. Stroschein, 1967: Measurements of Radiative Flux Divergence in the Arctic. *Archiv Meteorol. Geophys. Bioklima., Ser. B* **15**, 67–81.
- Liou, K.-N., 1987: *An Introduction to Atmospheric Radiation*, Volume 26 of *International Geophysics Series*. Academic Press.
- Liou, K. N., 1992: *Radiation and Cloud Processes in the Atmosphere*, Volume 20 of *Oxford Monographs on Geology and Geophysics*. Oxford University Press.
- Long, C. N. and T. P. Ackerman, 2000: Identification of Clear Skies from Broadband Pyranometer Measurements and Calculation of Downwelling Shortwave Cloud Effects. *J. Geophys. Res.* **105**(D12), 15609–15626.
- Luther, F. M., R. G. Ellingson, Y. Fouquart, F. S. N. A. Scott, and W. J. Wiscombe, 1988: Intercomparison of radiation codes in climate models: Longwave clear sky results - a workshop summary. *Bull. Am. Meteorol. Soc.* **69**, 40–48.

- Marty, C., 2000: *Surface Radiation, Cloud Forcing and Greenhouse Effect in the Alps*. Ph. D. thesis, Swiss Federal Institute of Technology ETH, Zuerich.
- Marty, C., R. Philipona, J. Delamere, E. G. Dutton, J. Michalsky, K. Stamnes, R. Stordvold, T. Stoffel, S. A. Clough, and E. J. Mlawer, 2003: Downward longwave irradiance uncertainty under arctic atmospheres: Measurements and modeling. *J. Geophys. Res.* **108**(D12), ACL4,1–11.
- McArthur, L. J. B., 1998: Baseline Surface Radiation Network BSRN.Operations Manual. WMO/TD-No. 879, WRCP/WMO.
- Miscolzi, F. and R. Guzzi, 1995: Effect of Nonuniform Spectral Dome Transmittance on the Accuracy of Infrared Radiation Measurements Using Shielded Pyrrometers and Pyrgeometers. *Appl. Opt.* **32**(18), 3257–3265.
- Monin, A. S. and A. M. Obukhov, 1956: Fundamentale Gesetzmässigkeiten der turbulenten Vermischung in der bodennahen Schicht der Atmosphäre. In *Statistische Theorie der Turbulenz*, pp. 199–226. Akademie Verlag, Berlin.
- Munn, R. E., 1966: *Descriptive Micrometeorology*. Advances in Geophysics. Academic Press, New York.
- Nkendirim, L. C., 1978: A Comparison of Radiative and Actual Nocturnal Cooling Rates over Grass and Snow. *J. Appl. Meteorol.* **17**(11), 1643–1646.
- Nunez, M. and T. R. Oke, 1976: Long-wave Radiative Flux Divergence and Nocturnal Cooling of the Urban Atmosphere. ii: Within an Urban Canyon. *Bound. Layer Meteorol.* **10**, 121–135.
- Obleitner, F., 1995: On a preliminary evaluation of the energy budget at the summit of the Greenland Ice Cap In: Obleitner, F. and Olesen, O.B. (EDS.): Mass Balance and Related Topics of the Greenland Ice Sheet. Geol. Surv. Greenland Open File Ser. 95/5, 22-43.
- Ohmura, A., 1980: *Climate and Energy Balance on Arctic Tundra* Ph. D. thesis, ETH Zürich.
- Ohmura, A., P. Calanca, M. Wild, and M. Anclin, 1999: Precipitation, accumulation and mass balance of the Greenland ice sheet. *Zeitschrift für Gletscherkunde und Glazialgeologie* **35**(1), 1–20.
- Ohmura, A., E. G. Dutton, B. Forgan, C. Fröhlich, H. Gilgen, H. Hegner, A. Heimo, G. König-Langlo, B. McArthur, G. Müller, R. Philipona, R. Pinker, C. Whitlock, K. Dehne, and M. Wild, 1998: Baseline Surface Radiation Network (BSRN/WCRP): New Precision Radiometry for Climate Research. *Bull. Am. Meteorol. Soc.* **79**(10), 2115–2136.
- Ohmura, A., M. Wild, and L. Bengtsson, 1996: A Possible Change in Mass Balance of Greenland and Antarctic Ice Sheets in the Coming Century. *J. Clim.* **9**(9), 2124–2135.
- Philipona, R., E. G. Dutton, T. Stoffel, J. Michalsky, I. Reda, A. Stifter, P. Wendling, N. Wood, S. A. Clough, E. J. Mlawer, G. Anderson, H. E. Revercomb, and T. R. Shippert, 2001: Atmospheric Longwave Irradiance Uncertainty: Pyrgeometers Compared to an Absolute Sky-scanning Radiometer,

- Atmospheric Emitted Radiance Interferometer, and Radiative Transfer Model Calculations. *J. Geophys. Res.* **106**(D22), 28129–28141.
- Philipona, R., C. Fröhlich, and C. Betz, 1995: Characterization of Pyrgeometers and the Accuracy of Atmospheric Long-wave Radiation Measurements. *Appl. Opt.* **34**(9), 1598–1605.
- Philipona, R., C. Fröhlich, K. Dehne, J. DeLuisi, J. Augustine, E. Dutton, D. Nelson, B. Forgan, P. Novotny, J. Hickey, S. P. Love, S. Bender, B. McArthur, A. Ohmura, J. H. Seymour, J. S. Foot, M. Shiobara, F. P. J. Valero, and A. W. Strawa, 1998: The Baseline Surface Radiation Network Pyrgeometer Round-Robin Calibration Experiment. *J. Atmos. Oceanic Technol.* **15**(3), 687–696.
- Putnins, P., 1970: The Climate of Greenland. In S. Orvig (Ed.), *Climates of the Polar Regions*, Volume 14 of *World Survey of Climatology*, pp. 3–128. Elsevier.
- Räisänen, P., 1996: The Effect of Vertical Resolution on Clear-sky Radiation Calculations: Tests with Two Schemes. *Tellus* **48A**(3), 403–423.
- Ramanathan, V., 1987: The Role of Earth Radiation Budget Studies in Climate and General Circulation Research. *J. Geophys. Res.* **92**(D4), 4075–4095.
- Riordan, A. J., 1977: Variations of temperature and air motion in the 0- to 32-meter layer at Plateau Station, Antarctica. In J. A. Businger (Ed.), *Meteorological Studies at Plateau Station, Antarctica. Antarctic Research Series Volume 25, 113-127*. American Geophysical Union.
- Roach, W. T., R. Brown, S. J. Caughey, J. A. Garland, and C. J. Readings, 1976: The physics of radiation fog: I - a field study. *Quart. J. Roy. Meteor. Soc.* **102**, 313–333.
- Robinson, G. D., 1950: Notes on the measurement and estimation of atmospheric radiation. 2. *Quart. J. Roy. Meteor. Soc.* **76**, 37–51.
- Rodgers, C. D. and C. D. Walshaw, 1966: The computation of infra-red cooling rate in planetary atmospheres. *Quart. J. Roy. Meteor. Soc.* **92**(391), 67–92.
- Roeckner, E., K. Arpe, L. Bengtsson, M. Christoph, M. Claussen, L. Dümenil, M. Esch, M. Giorgetta, U. Schlese, and U. Schulzweida, 1996: The Atmospheric General Circulation Model ECHAM-4: Model Description and Simulation of Present-day Climate. Technical Report 218, Max Planck Institut for Meteorology.
- Rothman, L. S., C. P. Rinsland, A. Goldman, S. Massie, D. P. Edwards, J. M. Flaud, A. Perrin, C. Camy-Peyret, V. Dana, J. Y. Mandin, J. Schroeder, A. McCann, R. R. Gamache, R. B. Wattson, K. Yoshino, K. V. Chance, K. W. Jucks, L. R. Brown, V. Nemtchinov, and P. Varanasi, 1998: The HITRAN molecular spectroscopic database and HAWKS (HITRAN Atmospheric Workstation): 1996 edition. *J. Quant. Spectrosc. Radiat. Transfer* **60**(5), 665–710.
- Sala, A., 1986: *Radiant properties of materials : tables of radiant values for black body and real materials*. Elsevier.
- Savijärvi, H., 1990: Fast Radiation Parameterization Schemes for Mesoscale and Short-Range Forecast Models. *J. Appl. Meteorol.* **29**, 437–447.

- Sodemann, H., 2002: Evaluation of a Parameterisation for Turbulent Fluxes of Momentum and Heat in Stably Stratified Surface Layers Master's thesis, University of Bayreuth.
- Sodemann, H. and T. Foken, 2004: Special characteristics of the temperature structure near the surface. *Theor. Appl. Climatol.* **80**(2-4), 81–89.
- Staley, D. O. and G. M. Jurica, 1970: Flux emissivity tables for water vapor, carbon dioxide and ozone. *J. Appl. Meteorol.* **9**, 365–372.
- Stammes, K., S. Tsay, W. Wiscombe, and K. Jayaweera, 1988: A Numerically Stable Algorithm for Discrete-Ordinate-Method Radiative Transfer in Multiple Scattering and Emitting Layered Media. *Appl. Opt.* **27**, 2502–2509.
- Steffen, K. and J. E. Box, 2001: Surface climatology of the Greenland ice sheet: Greenland Climate Network 1995-1999. *J. Geophys. Res.* **106**(D24), 33951–33964.
- Steffen, K., J. E. Box, and W. Abdalati, 1996: Greenland Climate Network: GC-Net US Army Cold Regions Research and Engineering (CRREL), CRREL monograph, trib. to M. Meier.
- Stephens, G., 1984: Parameterization of Radiation for Numerical Weather Prediction and Climate Models. *Mon. Weather Rev.* **112**, 826–867.
- Stull, R. B., 1988: *An Introduction to Boundary Layer Meteorology*. Kluwer Academic Publishers.
- Sun, J., S. P. Burns, A. C. Delany, S. P. Oncley, T. W. Horst, and D. H. Lenschow, 2003: Heat Balance in the Nocturnal Boundary Layer during CASES-99. *J. Appl. Meteorol.* **42**, 1649–1666.
- Timanovskaya, R. G. and G. P. Faraponova, 1967: Measurement of the Radiative Heat Influx in the Atmospheric Ground Layer. *Izv. An. SSSR Fiz. Atm.* **3**(12), 1259–1270.
- Tjemkes, S. A. and P. G. Duynkerke, 1989: The Nocturnal Boundary Layer: Model Calculations Compared with Observations. *J. Appl. Meteorol.* **28**, 161–175.
- Weidick, A., 1995: Greenland. Satellite Image Atlas of Glaciers of the World. Professional Paper, 1386-C. U.S. Geological Survey, U.S. Gov. Printing Office, Washington, D.C., 141 pp.
- Weiss, A., 1981: On the Performance of Pyrgeometers with Silicon Domes. *J. Appl. Meteorol.* **20**, 962–965.
- Wild, M., P. Calanca, S. C. Scherrer, and A. Ohmura, 2003: Effects of polar ice sheets on global sea level in high-resolution greenhouse scenarios. *J. Geophys. Res.* **108**(D5), Art. No. 4165.
- Wild, M., A. Ohmura, H. Gilgen, J.-J. Morcrette, and A. Slingo, 2001: Evaluation of Downward Longwave Radiation in General Circulation Models. *J. Clim.* **14**(15), 3227–3239.
- Wild, M., A. Ohmura, H. Gilgen, E. Roeckner, M. Giorgetta, and J.-J. Morcrette, 1998: The Disposition of Radiative Energy in the Global Climate System: GCM-calculated versus Observational Estimates. *Clim. Dyn.* **14**, 835–869.

- Wu, M.-L., 1980: The Exchange of Infrared Radiative Energy in the Troposphere. *J. Geophys. Res.* **85**(C7), 4084–4090.
- Yamamoto, G., 1952: On a radiation chart. *Sci. Rept. Tohoku Univ., Ser. 5, Geophys.* **4**, 9–23.
- Yamamoto, G., 1962: Direct Absorption of Solar Radiation by Atmospheric Water Vapour, Carbon Dioxide and Molecular Oxygen. *J. Atmos. Sci.* **19**, 182–188.

Curriculum Vitae

Name: Sebastian Wilhelm Hoch
Date of birth: November 17th, 1973
Place of birth: Müllheim, Germany
Citizenship: German
Current address: Bülachstr. 7 g
8057 Zürich

Education

1980-1984: Primary school Höllstein, Germany
1984-1991: Gymnasium Schopfheim, Germany
1991-1992: Steller Secondary School, Anchorage, Alaska, USA
1992-1994: Gymnasium Lörrach, Germany
1994: Graduation: Abitur
1994-1999: Studies in Earth Science at the Swiss Federal Institute of Technology, ETH Zürich.
8/1997-9/1997: Internship at CMDL/NOAA in Boulder, Colorado, USA
1999: Master Thesis at the Institute for Atmospheric and Climate Science, ETH Zürich:
"Untersuchung der Absorption in stratiformer Bewölkung".
11/1999: Graduation: Dipl. Natw. ETH
since 2000: Ph.D. Student at the Institute for Atmospheric and Climate Science, ETH Zürich.
2000, 2001 and 2002 summer field seasons at Summit Camp, Greenland.

International Conferences

IUGG 2003, Sapporo, Japan
EGU General Assembly 2004, Nice, France
EGU General Assembly 2005, Vienna, Austria